Advances in High-speed Rail Technology

Zhigang Liu

Detection and Estimation Research of High-speed Railway Catenary

Springer

Advances in High-speed Rail Technology

More information about this series at http://www.springer.com/series/13506

Zhigang Liu

Detection and Estimation Research of High-speed Railway Catenary

Springer

Zhigang Liu
School of Electrical Engineering
Southwest Jiaotong University
Chengdu
China

ISSN 2363-5010 ISSN 2363-5029 (electronic)
Advances in High-speed Rail Technology
ISBN 978-981-10-2752-9 ISBN 978-981-10-2753-6 (eBook)
DOI 10.1007/978-981-10-2753-6

Library of Congress Control Number: 2016953286

Printed on acid-free paper

This Springer imprint is published by Springer Nature
The registered company is Springer Nature Singapore Pte Ltd.
The registered company address is: 152 Beach Road, #22-06/08 Gateway East, Singapore 189721, Singapore

Foreword

Since high-speed railway that generally adopts electric traction has many advantages such as fast speed, high efficiency, energy saving, environmental friendly, ensured safety and comfort, etc., it has become the main development trend of the world's rail transit. In 2015, the total mileage of China's high-speed railway has exceeded 19,000 km, and China has the world's largest high-speed railway network.

It is known that pantograph-catenary system is the only way for trains to obtain a stable power supply. When the train is running at high speed, the electric power can be obtained by the sliding contact between the pantograph and the catenary. So, the favorable interactive characteristic of the pantograph-catenary system is the basic requirement of current collection. In the actual operation, the bad condition of catenary will directly influence the train's safe operation in high-speed railway. Therefore, the "Technical requirements of high-speed railway power supply safety detection and monitor system" is published by the Railway Ministry of China in 2012. However, a great deal of research on pantograph-catenary system needs to be developed and performed first. The detection and estimation of pantograph-catenary system in high-speed railway are the research focuses now. Specially, the key point is to efficiently and automatically detect and estimate the catenary.

It is encouraging to find this book about the detection and estimation of catenary in high-speed railway. In this book, some important characteristics of pantograph-catenary system, such as the statistical characteristics of pantograph-catenary contact pressure including stationarity, periodicity, correlation, high-order statistical properties are presented and discussed. The wave motion velocity of contact line considering air damping is deduced and the influence factors are discussed. Some new methods and algorithms on the detections of geometric parameters of catenary, pantograph slipper fault, and catenary support system are presented and applied in real-life engineering. Furthermore, the estimation methods of pantograph-catenary contact pressure based on time–frequency distributions and power spectrum density are presented, developed and verified.

An important feature of this book is that many new technologies or ideas on the detection and estimation of high-speed railway catenary are presented and discussed. The presented experiments are based on real-life engineering problems, as well as problems that can be helpful to apply the new techniques in high-speed railway.

I believe that this book can provide important references to the researches and applications of detection and estimation of catenary in high-speed railway.

Chengdu, China
July 2016

Prof. Qingquan Qian
Academician of Chinese
Academy of Engineering

Preface

Catenary is one of the main components of the power supply system of high-speed railway, which mainly includes contact line, messenger, dropper, supporting device, suspension device, etc. It is responsible for transmitting the electric energy from traction substation to the EMUs (Motor Train Unit). Its working states directly influence the train's safe operation in high-speed railway. Therefore, efficient detection and estimation of catenary for high-speed railway are very important and necessary.

The book begins with an introduction of detection and estimation of high-speed railway catenary in Chap. 1. First, pantograph-catenary detection technologies are simply outlined. Second, the development of non-contact detection devices using image processing, including catenary image detection device and pantograph image detection device, are presented, respectively. Third, pantograph-catenary image recognition technology is introduced, where some recognition algorithms or methods are reviewed. Fourth, catenary estimation methods including static estimation and dynamic estimation are summarized and reviewed in detail. In the end, the future detection and estimation researches are given. In Chap. 2, the statistical characteristics of pantograph-catenary contact pressure are presented and discussed in detail. These statistical characteristics include stationarity, periodicity, correlation, high-order statistical properties of pantograph-catenary contact pressure. First, the stationarity test methods are introduced and the stationarity of actual pantograph-catenary contact pressure is analyzed in detail. Second, the periodicity of pantograph-catenary contact pressure data is discussed, including periodic trend feature, trend term extraction and evaluation of pantograph-catenary contact pressure data. Third, the correlation of pantograph-catenary contact pressure data is discussed based on EMD (Empirical mode decomposition). In the end, the high-order statistical properties of pantograph-catenary contact pressure data is discussed based on SK (Spectral Kurtosis). In Chap. 3, the wave motion velocity of contact line considering air damping is deduced in detail and the influence factors are discussed first. Then the static aerodynamic parameters of contact line are analyzed. The test experiment of static aerodynamic parameters of contact line is designed and carried out in the wind tunnel. In the end, the dynamic equations of

pantograph-catenary considering air damping is modified and discussed. In Chap. 4, the non-contact detection for the height and stagger of contact line is presented in detail, including the detection value correction of catenary geometric parameters based on Kalman filtering, the detection correction method of contact line height, and the detection method based on mean shift and particle filter algorithm. In Chap. 5, the features of pantograph slipper image including pantograph structure, slipper type and image features of slipper are given and discussed in detail. First, the characteristics of pantograph slipper image based on curvelet transform are analyzed. Second, the pantograph slipper crack extraction based on translational parallel window in curvelet transform domain is given. In the end, the extraction algorithm of cracks and experiment verification are performed and verified. In Chap. 6, some new detection methods of the working state of insulators, clevises, and diagonal tube are presented and discussed in detail. For the insulator detection, affine invariant moments, fast fuzzy matching and Harris corner points are adopted for insulator positioning. Grayscale statistic, wavelet singular value, Chan–Vese model and curvelet coefficients morphology are adopted for insulator fault detection. For the clevis fault detection, SIFT (Scale-invariant Feature Transform) and SUFT (Speed-up Robust Features) are adopted for clevis matching. HOG (Histogram of Oriented Gradient) features, curvature, Hough transform, Gabor wavelet transform and second-generation curvelet are adopted for clevis fault detection. In addition, the detection of clevis pins is presented and discussed. In the end, the diagonal tube fault detection is presented including the diagonal tube detection based on cascaded AdaBoost classifier and detection of loosening and missing of screws from the diagonal tube. In Chap. 7, the time–frequency distributions of pantograph-catenary contact force based on different time–frequency representations are analyzed and discussed in detail. The detection of contact wire irregularity in railway catenary is presented. The ZAMD (Zhao–Atlas–Mark distribution) is presented and discussed as the best candidate for the quadratic time–frequency representation of pantograph-catenary contact force. In Chap. 8, the catenary estimation based on the PSDs (Power Spectrum Density) of dynamic data is presented and discussed. First, the selection of AR (Autoregressive) model order for catenary data is discussed. Then, the correlations between the PSDs and some crucial operation conditions are investigated and a cross-correlation coefficient is presented for evaluating the pantograph-catenary coupling performance. In the end, the quantification method of PSDs is developed based on the second-order polynomial.

In this book, we try to indicate an increasing interest in detection and estimation of high-speed railway catenary for real-life engineering applications. It is hopeful to provide some references and help for other researchers around the world who engage in detection and estimation of high-speed railway.

Chengdu, China Zhigang Liu
July 2016

Acknowledgments

This book is partly supported by the National Natural Science Foundation of China (51007074, 51377136, U143420), the New Century Excellent Talent Project of China Education Ministry (NECT-08-0825), the Sichuan Province Youth Science and Technology Innovation Team under Grant (2016TD0012), the Key Project of Science and Technology Research and Development Program of Ministry of Railways (2011J016-B, 2013J010-B). It is also a summary of the achievements of our team for many years, including doctoral and master graduate researches, such as the works of Dr. Zhiwei Han, Dr. Candidate Hongrui Wang, Ye Han, Guinan Zhang, M.A. Hongmei Yang, Kunfeng Chen and Xiaoxiao Zhang.

Furthermore, the author would like to thank Dr. Candidate Hongrui Wang, Ye Han, Zongsheng Zheng, and M.A. Candidate Junwen Chen for their helpful proofreading.

Contents

Chapter 1
Overview of Detection and Estimation of High-Speed Railway Catenary

1.1 Introduction

In 2012, "Technical requirements of high-speed railway power supply safety detection and monitor system" is published by the Railway Ministry of China. The key idea of this system is to achieve the non-contact detection of safety-threatening operation state of pantograph-catenary system and its fittings based on the images and videos captured by inspection vehicles or devices. However, the level of automatic recognition of the image needs to be highly improved at present.

Furthermore, pantograph-catenary system is a random vibration system in high-speed railway, and its dynamic characteristic is always the hot topic and difficult topic in the research of high-speed railway pantograph-catenary system. At present, the evaluation of dynamic characteristics of pantograph-catenary system is generally based on the statistical parameters, such as the time domain stationary mean, variance and so on. These evaluation indexes are adopted based on the assumption that the data have generalized stability, and cannot meet the requirements of high-speed pantograph-catenary dynamic data analysis. It is difficult to evaluate the performance of the pantograph-catenary system effectively.

Therefore, efficient detection and estimation of catenary for high-speed railway are very important and necessary. In this chapter, the overview of current catenary detection and estimation is presented and discussed.

1.2 Pantograph-Catenary Detection Technologies

Non-contact image detection has been applied more and more widely in the pantograph-catenary comprehensive inspection vehicle, stationary pantograph-catenary inspection devices, mobile pantograph-catenary inspection devices and hand-held pantograph-catenary inspection devices owing to its advantages of few

Z. Liu, *Detection and Estimation Research of High-speed Railway Catenary*,
Advances in High-speed Rail Technology, DOI 10.1007/978-981-10-2753-6_1

operation interference, good generality and easy installation. To ensure the security of the pantograph-catenary system, the essence is to carry out efficient, accurate, real-time monitoring and detection of the pantograph-catenary system, master its real-time operating conditions, and timely perform the maintenance corresponding to bad conditions. The development of pantograph-catenary detection mainly has gone through four stages [1] as follows.

1. Manual detection

The traditional pantograph-catenary detection is mainly based on manual work. The advantage of manual detection is more flexible, and it can manually identify various failure types. Its disadvantage is low efficiency and poor security. In addition, the detection operation must be carried out during the train operation interval to avoid influences on the railway traffic. The human factors, such as the staff's experience can also influence the detection results.

2. Contact detection

The contact pantograph-catenary parameter measurement is developed with the development of railway electrification. The contact detection is generally performed in the actual situations of electrical railway. In Germany, the pantograph-catenary contact pressure is regarded as the key detection parameter, which is mainly obtained through the pressure sensors and acceleration sensors in the pantograph. In Japan, the disconnection of pantograph-catenary system and the contact wire wear are focused on as the key detection parameters. It is mainly due to the extensive use of metallurgical powder for the pantograph slide, which leads to severe contact wear. For different detection parameters, some pantograph-catenary detection devices with multiple usages have been developed. In [2, 3], the design for the wear detection vehicle of contact wire was proposed. The real-time stress variation and pantograph impact were detected by embedding optical fiber sensors in pantograph in [4]. In China, the catenary detection vehicle is used to detect the pantograph-catenary parameters [5, 6]. In [7], the detection method through adding the fiber in pantograph was proposed, which could determine the wear based on the amount of light under wear. The sensors were set on the pantograph's slide to detect the stagger of contact wire in [8]. The contact resistance method and current loop measurement method were adopted to detect the pantograph-catenary disconnection ratio in [9].

The contact detection methods have been greatly improved in the detection accuracy and detection efficiency. However, the integrated detection vehicles need to occupy the railway line, which will interfere with the normal train's operation. The detection object of different devices is single, so the different devices must be installed for different detection parameters. In addition, some detection devices are required to modify the pantograph's frame, which will affect the pantograph dynamic performance, and ultimately may affect the detection results.

3. Non-contact detection using ranging technology

With the development of laser and ultrasonic ranging technology, many non-contact detection methods are widely used in the detection of pantograph-catenary system. For the laser ranging technology, the catenary geometry parameter detection method using the high accuracy laser pulse phase ranging technique and incremental grating angle measurement technique was proposed in [10]. Using the pulse phase laser measuring principle, the detection of high precision height and stagger of catenary was realized in [11–13]. The detection for pantograph slide wear using laser beams was proposed in [14]. For the ultrasonic ranging technology, the East Japan Railway Company has developed the pantograph-catenary parameter detection system using the ultrasonic in 1993 [15]. SIEMENS, Germany, has also developed a contact wire height and stagger detection instrument using the ultrasonic [16]. In [17, 18], the apparatus for measuring the pantograph wear using ultrasonic sensor as the detection element was designed.

The advantage of non-contact measurement is that the detection efficiency is high, and the traffic disturbance is small. However, the relative functions of laser detection are relatively simple, and the accuracy of ultrasonic testing is relatively poor.

4. Non-contact detection using image detection technology

Since 1990s, with the rapid development of computer and image processing technology, the use of image acquisition and processing technology for the pantograph-catenary detection has shown unparalleled advantages.

- The image detection technology can detect a variety of pantograph-catenary components at the same time only using a single device, and reduce the number of equipment.
- The equipment's intelligent level is high, which can automatically identify the parameters and fault of pantograph-catenary system.
- The pantograph-catenary detection device can avoid the interferences from the train's operation.
- The equipment size is flexible, from small handheld devices, track mobile devices, to large pantograph-catenary vehicle, and can be widely used.

The many advantages of non-contact detection using image processing technology make it more and more applicable in the pantograph-catenary detection. In this chapter, the detection and identification of pantograph-catenary parameters are presented from the detection equipment development and intelligent image recognition algorithms.

1.3 Development of Non-contact Detection Devices Using Image Processing

The non-contact image detection is firstly to use the camera equipment to sample the pantograph-catenary remote images, secondly to analyze the pantograph-catenary element through the intelligent image recognition algorithm, and lastly to achieve the parameters detection and fault identification of pantograph-catenary system.

In addition, in order to achieve all-weather detection or special state detection (such as arc, etc.), the multi spectral camera for infrared, ultraviolet image analysis is adopted. For different detection objects, the equipment will adopt different sampling strategies, such as camera looking up, looking down, fixed angle and reflection type. In this section, the research progress of pantograph-catenary detection equipment is introduced.

1.3.1 Catenary Image Detection Device

At present, there are two main aspects of application in the detection of catenary images, namely the detection of catenary parameters and catenary bad state.

1. Catenary parameter detection device

The catenary parameter detection is mostly realized through the camera mounted on the vehicle roof. These parameters mainly include contact wire height, stagger, location gradient, wire wear and so on.

(a) Catenary suspension parameter detection

The catenary suspension parameters are the most basic technical indicators that can ensure the catenary performance. Hence they are the most important detection objects. For example, DB Company developed the contact wire location recognition and location gradient detection system, shown in Fig. 1.1. In order to avoid the influence of environmental light on the image capture, the infrared was used to detect the gradient of the locator, as shown in Fig. 1.2 [1].

In [19], the optical triangle location method was adopted to automatically detect the contact wire stagger. These detection devices need to be mounted in the specific catenary detection vehicle and will occupy the railway line. In 2007, a new equipment for the pantograph-catenary detection was developed, which was based on the technique of continuous image processing in [20]. The equipment can be installed in the commercial operation vehicle to achieve the daily pantograph-catenary detection.

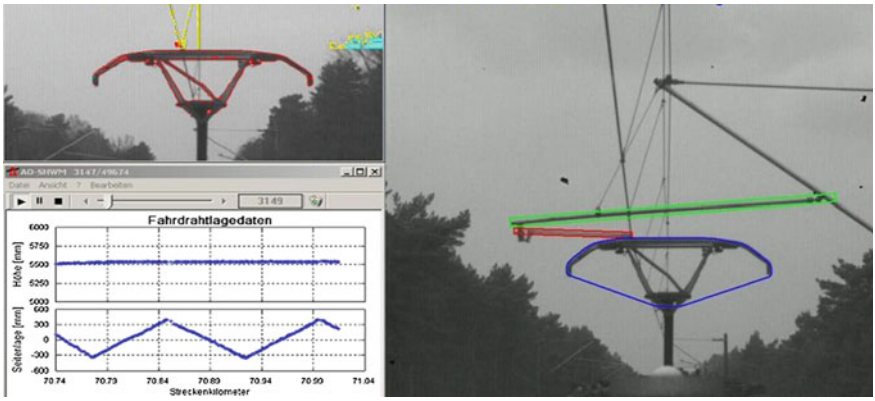

Fig. 1.1 Contact wire location and locator gradient detection system

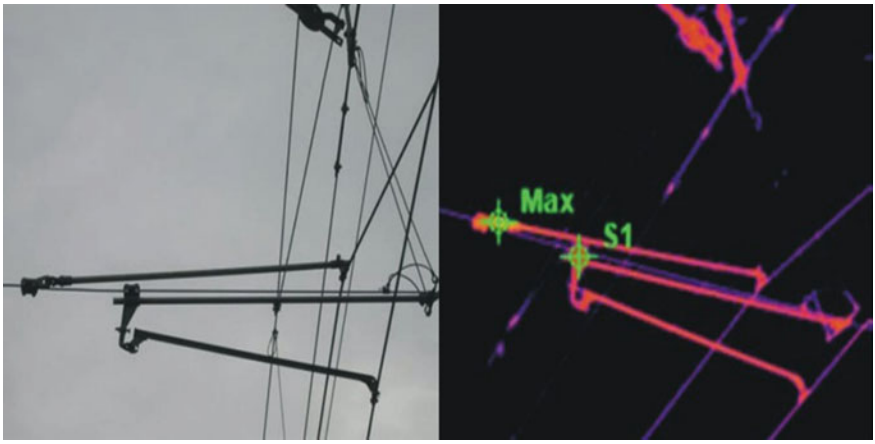

Fig. 1.2 Locator gradient detection system using infrared

(b) Catenary geometry parameter detection

In order to ensure the current collection ability of catenary, regularity of catenary and sufficient mechanical strength to prevent wire breakage, the contact wire wear must be detected. The CCD (Charge-coupled Device) camera was used to design the contact wire wear detection device, which was installed in the commercial operation vehicle. The wear of the contact line was identified by the position of the incident light reflected from the CCD camera [21], as shown in Fig. 1.3.

2. Catenary bad state detection device

If the pantograph-catenary system is running in a bad condition, the disconnection arc and overheated contact point will severely influence the catenary current

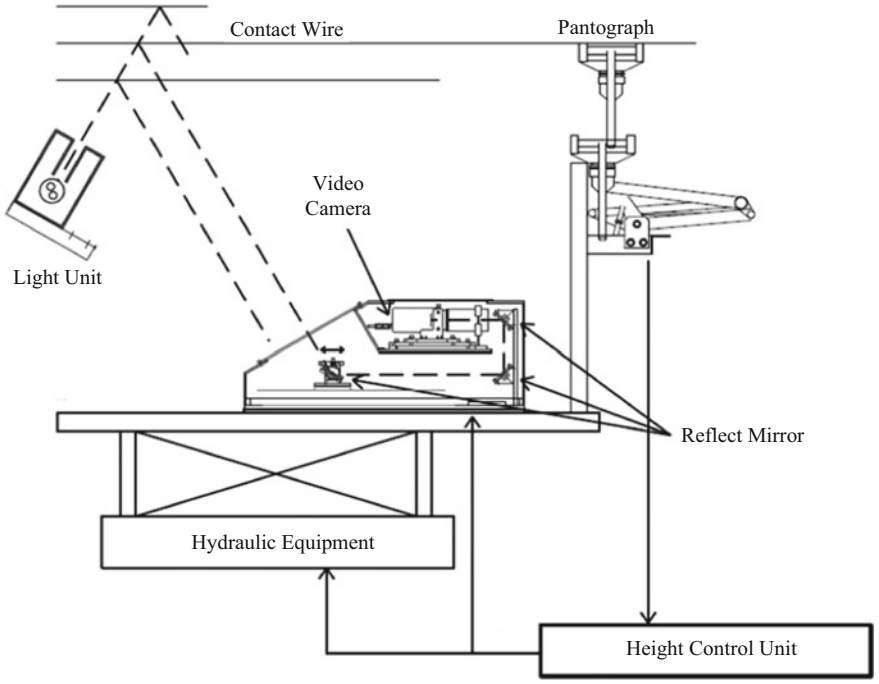

Fig. 1.3 Contact wire wear detection system in Japan

collection, even damage the catenary itself. The catenary faults, such as foreign body invasion, tree intrusion or fitting missing, will result in significant influences on the normal train operation. Hence, it is very necessary to detect and maintain the bad state of catenary.

(a) Pantograph-catenary disconnection arc detection

In [22], a light receiver was arranged in the lens system, and the photoelectric diode was placed in the focal point of the lens system. The off line electric spark can be transformed to the amplified electrical signal, and realize the arcing detection. This method was easily influenced by the surrounding environment in practice. The research results in [23] show that when the arc is generated, a large number of ultraviolet rays are emitted, whose wavelengths are lower than the visible wavelengths of 200–400 nm. Through the ultraviolet ray images, the arc information can be obtained. When the pantograph-catenary arc is clearly seen from the ultraviolet ray sensor data, the ultraviolet ray data appears to be mutated, which can determine the arc initiation.

(b) Pantograph-catenary contact point heat state detection

In order to overcome the problem that the image can be easily contaminated by the environmental light in the visible light image acquisition system, which results

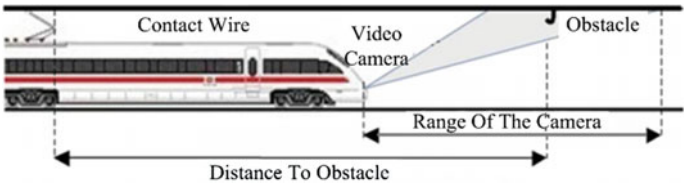

Fig. 1.4 All-weather catenary detection system

in the image information loss caused by the overexposure or insufficient exposure, the detection plan was proposed in [24]. The infrared camera was adopted to monitor the contact hot point, disconnection arc of pantograph-catenary system and the contact wire location.

(c) Catenary foreign body detection

The foreign body among the catenary suspension components can result in hitting pantograph and pulling catenary, which will severely influence the train's operation. In [25], the catenary foreign body detection system was designed, where three cameras are used to capture the stereo image 70 m in front of the train. In order to realize the automatic detection, all-weather image capture is realized based on the spectrum characteristics of ultraviolet, visible light and infrared, shown in Fig. 1.4.

(d) Catenary tree intrusion detection

In order to prevent the tree intrusion from influencing the pantograph's operation, DB Company developed the tree intrusion detection device based on image processing, which used the multi spectral camera to realize the three-dimensional data detection of trees, and then compared with the predefined contour template to determine whether there are tree intrusions.

(e) Contact wire wind deviation detection

In [26], the CCD (Charge-coupled Device) camera was adopted to detect the multi detection marks at the same time, which can be used to compute the contact wire wind deviation through the identification of width ratio. The method can monitor the contact wire wind deviation in real time and provide the overrun alarm.

1.3.2 Pantograph Image Detection Device

1. Pantograph wear detection

The sliding wear of pantograph will decrease the capability of current collection. The heavy wear perhaps results in the slide plate breaking and seriously harming the catenary. In [27], the pantograph wear detection system using 4 CCD cameras

was designed. After the edge cutting, detection and extraction, the upper and lower edges of contact wire can be located in the image, then the pantograph sliding wear can be computed and the wear curve can be drawn.

2. Pantograph dynamic envelope detection

The dynamic envelope of pantograph is formed by the maximum amplitudes in the vertical direction, and the horizontal direction. The dynamic envelope plays an important role for the safety, maintenance, inspection, construction of pantograph-catenary system. In [28], the high pressure sodium lamp was adopted as the light source, whose spectral lines are in the vicinity of 589 and 589.6 nm. The specially tailored narrowband filter is used to filter out the vast majority of other wavelengths of light. A stable image is obtained on the CCD target surface, and the detection and recognition of the dynamic envelope of pantograph is achieved.

3. Pantograph fault detection

The pantograph fault detection needs to process complex images. In [29], a wireless video monitoring system for locomotive pantograph was designed, shown in Fig. 1.5.

1.4 Pantograph-Catenary Image Recognition Technology

Because the pantograph-catenary components are complex, and the image ambient light and the clearance condition are poor, the image recognition algorithms mostly focus on the simplest edge detection and line detection.

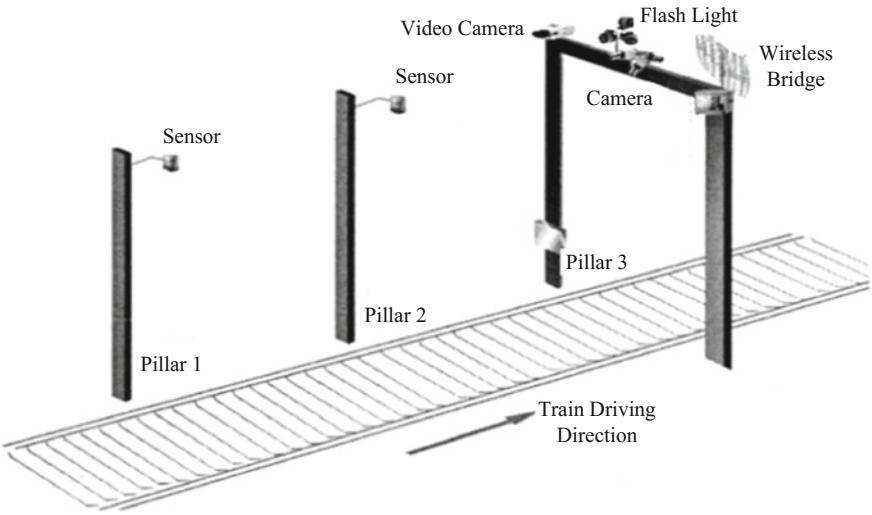

Fig. 1.5 Wireless video monitoring system for locomotive pantograph

1. Radon transform

For the gradient detection of contact wire locator, the combination method of chain code and Radon transform was proposed to detect the gradient of contact wire locator in [30]. The chain code was used to locate the region of the target line segment in the image and determine the rough angle of the line segment. The Radon transform was used to precisely locate the locator's gradient in the small region, shown in Fig. 1.6.

2. Hough transform

In [24], when the catenary parameters were extracted from the infrared ray image, Hough transform was adopted to detect the line information in order to locate the pantograph frame and contact wire. In [31], in order to detect the wear of pantograph slide plate, the Sobel operator and Canny operator were adopted to extract the image edge. The Hough transform was adopted to detect the upper and lower boundaries of pantograph slide plate. The fuzzy C-mean clustering was adopted to analyze the detected lines. Then the actual wear height of pantograph slide can be computed from the analyzed image, shown in Fig. 1.7.

3. Template matching

In [26], in order to detect the wind deviation, the special detection marks were adopted as the location feature information. Through the object feature template matching, the contact wire was located, and its wind deviation was determined. The method needs to install a special logo for image calibration, so its application is limited.

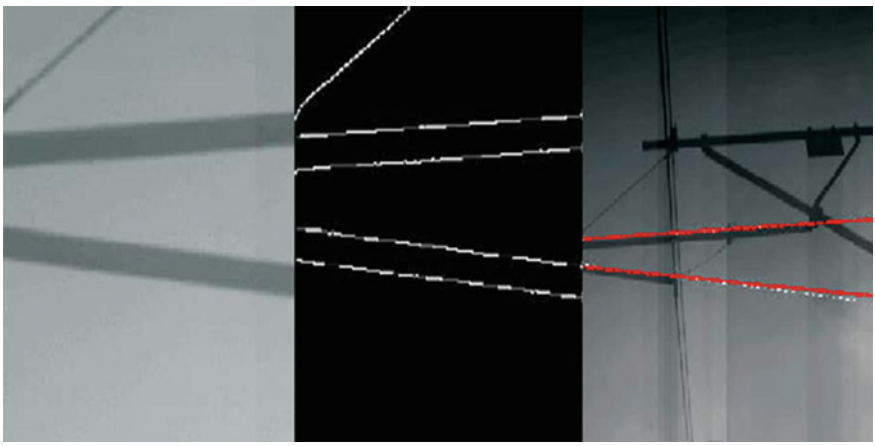

Fig. 1.6 Locator gradient detection using chain code and Radon transform

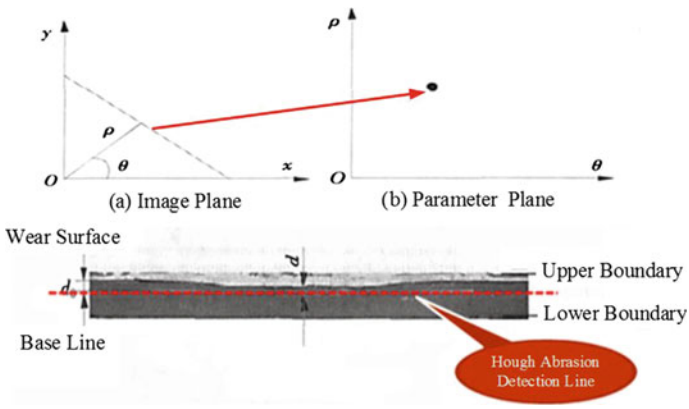

Fig. 1.7 Pantograph slide plate wear detection with Hough transform

In order to overcome the limitations of the straight line detection algorithms in the detection and fault identification of pantograph-catenary parameters, and to analyze and identify the fault image, some new image detection and recognition methods should be adopted and developed for the complex pantograph-catenary images, such as image sparse decomposition and anisotropic filtering.

4. Wavelet transform

In [27], based on the singularity analysis of wavelet transform, the image was analyzed after extracting the edge of pantograph, and the wear degree was judged. Aiming at the detection of foreign body in the catenary insulator, the insulator was located based on the template matching and the characteristics of the reflection point of light [32]. The detection of insulator foreign body was realized by using the singularity of the wavelet.

5. Curvelet transform

The pantograph slide plate cracks easily cause the fracture loss, even contact wire breakages. Based on the second generation curvelet sparse decomposition theory, the anisotropic curvelet "atom" was adopted to decompose the image. In [33], a new method of extracting the correlation information of each directional image was proposed by applying CCDP (Curvelet Coefficients Directional Projection) transform to the curvelet decomposition coefficient matrix, which can realize the crack extraction of pantograph surface.

A new method based on the curvelet coefficient of the parallel joint of pantograph metal plate, was designed in [34]. Utilizing the multi-direction and anisotropic property of curvelet transform, the spot, linear and nonlinear characteristics of the pantograph slide plate images are classified. Translational parallel windows are used in the direction matrixes of curvelet decomposition, and then the energy

values of translational windows are calculated. The different image features between the linear parallel joints and other nonlinear images such as rivets, scratches, and cracks are distinguished according to the energy values of the curvelet coefficients, so the slide plate cracks information can be obtained finally.

In [35], the curvelet was adopted to carry out directional filtering, and the curvelet clustering coefficients were enhanced by using mathematical morphology. Finally, with the zonal energy, the fault location can be accurately identified.

6. Invariant moment

The catenary insulators have different types and different suspension angles, which results in the difficulties in locating and identifying them. In view of the problem of foreign body detection, 6 different kinds of affine invariant moment templates for insulator identification were proposed in [36]. Firstly, the Hough transform line detection is adopted to classify the shaft and insulator of the global image after preprocessing. Secondly, the porcelain bottles of the insulator is recognized and located with the affine moment invariant. Thirdly, the gray statistical curves of the insulators are obtained after the morphological dilation operation and edge adjustment. Comparing the band width of the Gray statistical curves, whether the foreign body exists can be distinguished.

7. SIFT (Scale Invariant Feature Transform)

In the SIFT, the feature points are matched with the local invariant features (SIFT feature) of the image, which is invariant to scale, rotation and illumination changes. In [37], for the fracture failures of ear pieces of rotary double ears in the catenary support structure, a new detection method based on SIFT was proposed. To realize the positioning and extracting of rotary double ears, the matching of local feature points between catenary image and the standard image of rotary double ears is utilized. And the analysis of the bending degree of each point of the upper boundary curve of the rotary double ears is used to judge whether a fracture failure exists.

8. SURF (Speeded-Up Robust Features)

SURF is a feature extraction algorithm, which includes feature point detection and description. The algorithm can improve the computation speed by combining the integral image, Hessian matrix and 2D Haar wavelet response. In [38], a detection method based on feature matching of SURF was proposed. Firstly, the feature extraction and matching of insulator in the image are performed by SURF. Secondly, the pre-processing of insulator image such as angle correction and morphological operation is carried out. Finally, the longitudinal statistics of insulator grayscale is implemented, and according to the distribution regularity of the minimal value of the grayscale, the defective insulator can be identified and located.

1.5 Catenary Estimation

In electrified railway industry, the catenary estimation generally refers to the qualitative and quantitative characterization of the level of feasibility and applicability that the catenary infrastructure fulfills the corresponding operation requirement. It serves an important role in the whole stage of catenary life circle, including the design, acceptance and operation of catenary infrastructure. The catenary estimation takes into consideration of not only the overall condition of infrastructure, but also the influences of catenary defects on the condition of infrastructure. Therefore, it generally utilizes a variety of simulation and real-life measurement that are relevant to the function of catenary infrastructure. Traditionally, the catenary estimation for conventional railway is accomplished by threshold criterion and simple statistics of relevant data, such as mean, standard deviation, maximum, minimum and so forth. For the catenary infrastructure in high-speed railway, the estimation requires upgrade to meet the high-level demand of safe and stable operation. With the massive construction of high-speed railway lines all over the world, the increasing total mileage of catenary infrastructure makes the research on catenary estimation necessary now more than ever.

Basically, the simulation or measurement data adopted for catenary estimation can be classified into two categories, namely the static data and the dynamic data, according to the type of catenary status that the data describe. The static data describe the static status of catenary infrastructure, which refer to the catenary itself without external excitation. It mainly includes the structural parameters of catenary, such as span, inter-dropper distance, encumbrance and line tension, and the geometrical parameters of contact line, such as height, stagger and wear. Correspondingly, the dynamic data describe the dynamic status of catenary infrastructure, namely the dynamic response of catenary under external excitation. The excitation primarily refers to the pantograph contact. Thus, the dynamic data mainly include the pantograph-catenary contact force, the dynamic lifting displacement of contact line and pantograph, the frequency of pantograph arcing, the number of hard points and the acceleration of pantograph.

Based on the type of data adopted for catenary estimation, the estimation can be divided into two types, namely the static estimation and the dynamic estimation. The two types of estimation have certain relevance in their effects, while each has its superiority under certain circumstances. Generally speaking, catenary estimation should be accomplished by the combination of static and dynamic estimation in reality. Concretely, in the acceptance stage of catenary infrastructure, static estimation applies to the acceptance of construction quality, while dynamic estimation applies to the acceptance of designing scheme. For daily operation and maintenance, static estimation is the dominated estimation method, particularly in conventional railway lines for two main reasons. On one hand, static data measurements and static indicators are easy to be implemented at a relatively low cost in reality. On the other hand, because static data can be regarded as the input of pantograph-catenary dynamic interaction and the pantograph-catenary interaction is

highly sensitive to the static state of catenary, static estimation can reflect the dynamic characteristics of catenary at some level. Thus, dynamic estimation is usually the supplementary for static estimation and infrequently performed since its function can be partly substituted by static estimation with a low cost. However, as the increase of operation speed, current estimation method is falling behind and could not fully meet the operation and maintenance requirement of high-speed railway catenary. Considering that dynamic data are the direct reflections of pantograph-catenary interaction, it is believed that dynamic estimation is more suitable for the characterization of catenary dynamic performance. Meanwhile, relevant measurement techniques are developed accordingly for high-speed railway catenary, which provide sufficient data source for the developments and applications of novel estimation methods. Overall, more advanced estimation method and extensive dynamic estimation are the inexorable trend for achieving better performances of high-speed railway catenary.

1.5.1 Static Estimation

As defined, the static data of a catenary infrastructure can be precisely determined by the corresponding design as the nominal values. After completed construction based on the design, static data of the catenary will be measured to check if the actual structure matches the design and to what extent. In practice, the actual static data is inevitable deviated from the design due to many causes, especially in a long-term operation. But as long as the deviations remain within an acceptable range, the catenary will be recognized as functional. Therefore, estimation methods based on threshold criterion and lower-order statistics are developed accordingly.

Concretely, among all static data, the contact line height, stagger and wear are believed to be the most important static data that determine the catenary performance as shown in Fig. 1.8. The contact line height and stagger largely influence the spatial position and pressure of the contact point between contact line and

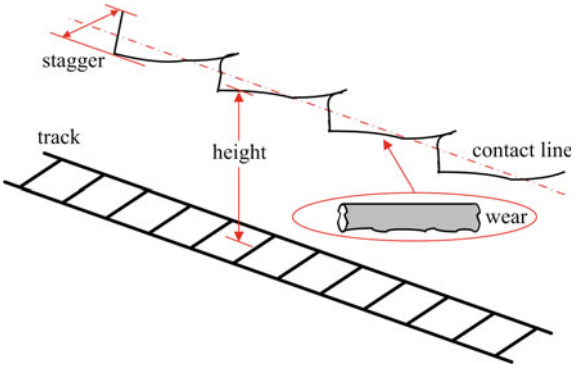

Fig. 1.8 Schematic of the contact line height, stagger and wear

pantograph. The contact line wear is uneven and has direct impact on the pantograph slide plate. Meanwhile, these data are relatively vulnerable and changeable under excitations in practice. Thus, static estimation is mainly realized based on corresponding static measurements.

For measurement data of contact line height and stagger, there are certainly nominal values to compare with. Thresholds can be set according to the acceptable deviation from nominal values. Different levels of deviation can be established to facilitate making maintenance decisions and taking actions such as adjusting the tension compensator, replacing the dropper and so on. In the case of contact line height, the sag of a span is sometimes computed and adopted as additional indicator.

For measurement data of contact line wear, which usually refers to the loss of line section or line thickness, there is an allowed maximum loss for certain type of line based on experimental and empirical conclusions. The percentage of loss of line thickness is usually adopted as the indicator to determine the line will be replaced or not. Meanwhile, some singular points with exceedingly high or low thickness loss will also be judged and handled.

Another concept, namely the contact line irregularity or unevenness is proposed in recent decades, which is another type of static data of catenary. It is generally defined as the combination of the geometry deformation of contact line and the wear and manufacturing defect of contact line surface. In some cases, the geometry deformation and wear are separately considered due to different orders of magnitude. The influence of contact line irregularity on catenary performance is not fully revealed yet. But its impact is considered to be high and important, especially for high-speed railway catenary. Thus, valid estimation methods need to be developed accordingly.

The concept of contact line irregularity was put forward in 2000 [39, 40], which has been widely concerned by scholars in recent years. According to the actual experiment and simulation model, the influence of contact line irregularity on the pantograph-catenary system was analyzed by Collina et al. [41]. According to the vibration of pantograph-catenary system, the contact line wear prediction method was put forward and the line test verification was carried out [42]. The influences of geometric irregularity and contact wire wear on dynamic characteristics were researched, respectively in [43]. The power spectrum was adopted to analyze the relationship between contact line wear and pantograph-catenary disconnection in Shinkansen of Japan in [44]. The irregularity power spectrum of contact line of Shinkansen was constructed in [40, 45]. The influence of contact line irregularity on the contact pressure was studied by the Hardware-in-the-loop platform [46]. The influence of vertical irregularity on the contact pressure of the measured high speed railway contact line was discussed in [47]. The influence of catenary irregularity on the flow quality of pantograph catenary system was analyzed by the pantograph catenary dynamic model in [48].

PSD (Power Spectrum Density) analysis is the main method for the representation of contact line irregularity, and the spectrum estimation is mostly based on the traditional periodogram method and the maximum entropy method. Suppose

that there are N data samples $x(0), x(1), \cdots, x(N-1)$, and the periodogram method means the Fourier transform, namely

$$X(\omega) = \sum_{n=0}^{N-1} x(n) e^{-j\omega n} \tag{1.1}$$

The power spectrum is obtained, as follows.

$$P_x(\omega) = \frac{1}{N} |X_N(\omega)|^2 = \frac{1}{N} \left| \sum_{n=0}^{N-1} x(n) e^{-j\omega n} \right|^2 \tag{1.2}$$

To overcome the disadvantages of traditional spectrum estimation, the concept of catenary line spectrum based on track spectrum was put forward in [49]. AR (autoregressive) spectrum was adopted to estimate the contact line irregularity [50].

To characterize the trend of contact line uneven spectrum, actual speed railway contact line irregularity spectrum fitting formula was presented in [51].

$$S_1(k) = \frac{A + Bk}{1 + Ck + Dk^2} \tag{1.3}$$

where A, B, C and D are the fitting parameters.

The fitting formula of vertical irregularity of high-speed railway contact line was presented as follows [47].

$$S_2(k) = \exp\left(\sum_{i=1}^{n} a_i (\ln(k))^i - a_0 \right) \tag{1.4}$$

where a_i is the fitting parameter, which is determined by the contact line type and state.

In addition, according to the spectrum fitting results and operation conditions of different lines, the inversion method of fitting spectrum based on inverse Fourier transform [43] or trigonometric series [51] has become the main method for catenary numerical simulation.

1.5.2 Dynamic Estimation

Because the geometrical shape of catenary is changeable under external excitations such as pantograph contact and aerodynamic force, static estimation cannot fully reveal the dynamic performance of catenary. Dynamic estimation based on dynamic data shows the catenary dynamic performance in actual operations. The major data commonly adopted for dynamic estimation are pantograph-catenary contact force

and the number of hard points, among which the hard point is defined as where the contact force experiences abrupt change on the contact line.

For the pantograph-catenary contact force, low-order statistics including the mean, standard deviation, maximum and minimum are adopted as the indicators for dynamic estimation. Thresholds are accordingly set for all indicators to estimate the catenary dynamic performance in simulation and reality. Another indicator calculated by the contact force is the percentage contact loss

$$\text{Contact loss} = \frac{\text{Number of samples indicating contact loss}}{\text{Total number of sample points}} \times 100\ \% \tag{1.5}$$

where the sample indicating contact loss is the sample points with zero or too small value of force. Similarly, if the contact loss exceeds certain threshold, the catenary performance is unacceptable and requires improvement.

For the hard point in contact line, it can be obtained by the pantograph-catenary contact force or other contact force measured through other form of sliding contact. Generally, the contact point with exceedingly high contact force can be regarded as hard point and be classified by different severity. There are many causes of hard point such as restriction arm, severe wear and so on. Thus, once a hard point is found, it must be handled depending on the cause of it.

Based on the frequency domain characteristics of pantograph-catenary system, band limited time domain index [52] and power spectrum density estimation [40] were proposed to estimate the contact force and catenary irregularity. Pantograph catenary contact pressure is the most capable of reflecting the dynamic characteristics of catenary data, the majority of research in the pantograph catenary contact pressure were used to observe the power spectrum characteristics in the frequency domain [53]. The catenary line spectrum based on AR model was proposed to evaluate the catenary dynamic characteristics, and the spectral characteristics of different lines, train speed, pantograph type and wind speed were analyzed in [50]. The fitting method of contact pressure spectrum trend was proposed, and the catenary dynamic characteristic was evaluated by the extraction of spectrum peak value in [51].

In addition, the waveform features of contact pressure power spectrum were analyzed, and their feature change was used to diagnose the contact line condition in [55]. The AR spectrum of contact line dynamic uplift was used to evaluate the dynamic vibration frequency of catenary in [56]. The low frequency component of contact pressure was analyzed by using the double spectrum in [57]. In [58], the dynamic response of pantograph-catenary system was analyzed, and the different frequency components of contact pressure were related to the catenary structure and the natural frequency of pantograph. In [59], based on the dynamic uplift of contact line and pantograph, the dynamic uplift spectrum was constructed to evaluate dynamic characteristics of pantograph-catenary, and EEMD (Ensemble Empirical Mode Decomposition) was used to eliminate the error data of contact pressure in different frequency bands [60]. Based on multiple EEMD, the wavelength components in pantograph-catenary contact pressure were analyzed, and the dynamic

characteristics of pantograph-catenary were evaluated based on the wavelength number in the range of different wavelengths in [61].

At present, time-frequency analysis is seldom used in the study of pantograph catenary system. STFT (Short Time Fourier Transform) was used to analyze the vibration frequency of dynamic uplift in [62]. The combination of STFT and neural network was presented to predict the actual wear of contact line in [63]. Through analyzing the time frequency characteristics of contact line current, the current collection quality of pantograph-catenary system was analyzed in [64].

1.6 Future Detection and Estimation Research

From the research and development of the pantograph-catenary detection, the detection equipment based on non-contact image processing is more and more widely used. However, it is restricted by the image recognition development. Therefore, the future detection technology research can focus on the following issues [65].

1. For the noncontact detection technologies of pantograph and catenary system, the image acquisition approach is mainly through the cameras mounted on the catenary inspection vehicle roof, which is influenced by the various forms of vibration. Though some compensation methods are presented, due to the complexity of vehicle body vibration and the precision control of sensor detection, how to realize the full compensation for the body vibration is still an urgent problem to be solved.
2. The fault detection algorithms of key components of catenary suspension system are mainly based on image processing technologies. Due to the weather, light and other restriction conditions, they cannot meet the requirements of the all-weather real-time online detection. Therefore, how to improve the existing detection algorithms to achieve the performance of image acquisition equipment is the main problem in the future.
3. The fault identification and detection algorithms are mainly based on the simple pattern recognition and machine learning algorithms, which do not fully exploit and utilize the existing image data. It can be assumed that the detection technology based on deep learning theory will become the trend of detection technology research of high-speed railway pantograph and catenary system.
4. At present, the estimation methods based as single assessment and single indicator cannot dig the hidden information in the data. Therefore, time frequency evaluation method has become the development trend of catenary estimation. However, the spectrum evaluation method needs to consider the full complex operating conditions and bad state of catenary. In addition, a large number of experiments and field data are needed to verify the physical meaning of each wavelength component, and improve the corresponding diagnostic methods.

5. For the various evaluation method and evaluation index, how to integrate them, construct the corresponding spectrum evaluation system aiming at actual high-speed railway, and guide the actual high-speed catenary operation and maintenance work, are their implementation trend.
6. Regardless of the static or dynamic evaluation, the evaluation methods of catenary depend on the establishment and improvement of safety inspection and monitoring system. For the big data provided by the system, intelligent analysis technologies such as data mining and data fusion will become an important research content of future contact network state evaluation.

References

1. Han Z, Liu Z, Zhang G, Yang H (2013) Overview of non-contact image detection technology for the pantograph-catenary monitoring. J China Railway 35(6):40–47
2. O' Donnell C, Palacin R, Rosinski J (2006) Pantograph damage and wear monitoring system. In: The Institution of engineering and technology international conference on railway condition monitoring, pp 178–181
3. Shing AWC, Pascoschi G (2006) Contact wire wear measurement and data management. In The institution of engineering and technology international conference on railway condition monitoring, pp 182–187
4. Boffi P, Cattaneo G, Amoriello L et al (2009) Optical fiber sensors to measure collector performance in the pantograph-catenary interaction. IEEE Sens J 9(6):635–640
5. Liu J (1998) Non-contact inspection of parameter of overhead contact system. Electr Railway 02:43–45
6. Liu F, Wang L, Gao X et al (2006) Study of measuring the contact force between pantograph and catenary. Electr Locomotives Mass Transit Veh 06:19–21
7. Ren S (2000) New pantograph wear detection and auto descending device. Railway Oper Technol 6(04):139–141
8. Wu J (1996) The system for detecting pull-out value of contact wire in electrified railway. J China Railway Soc 18(02):78–81
9. Liu H, Wang L, Gao X (2004) Current situation and prospects of the detection technology for the contact-loss of pantograph on electric locomotive. Locomotive Rolling Stock Technol 6:1–4
10. Liu Z, Liu S, Wu D et al (2004) The catenary geometric parameters measuring. Shandong Sci 17(01):67–69
11. Hofler H, Dambacher M, Dimopoulos N et al (2004) Monitoring and inspecting overhead wires and supporting structures. Institute of Electrical and Electronics Engineers Inc., Parma, Italy
12. Liu Y, Liu Z, Wen X et al (2002) A laser detecting device for measuring position of contact wire in OCS. Electr Railway 4:29–30
13. Peng C, Wang L, Gao X et al (2004) Dynamic detection for the height of contact wire. Opto Electron Eng S1:91–93
14. Kuen LK, Lee TKY, Ho SL et al (2006) A novel intelligent train condition monitoring system coupling laser beam into image processing algorithm. Trans Hong Kong Inst Eng 13(1):27–33
15. Kimura S (1993) Development of an automated consumables control system. Japan Railway Eng 32(3):21–24
16. Puschmann R, Wehrhahn D (2011) Ultrasonic measurement of contact wire position. eb—Elektrische Bahnen 109(7):323–324

17. Yin B, Wang B (2008) Application of ultrasonic ranging principle in monitoring abrasion of pantograph slider. Electr Drive Locomotives 05:57–59
18. Sun F, Wang B (2011) Ultrasonic detection method of abrasion of double slippers pantograph. Dev Innovation Mach Electr Prod 24(03):129–131
19. Zhang T (2008) Study and improvement on the OCS inspection system based on image processing. Railway Locomotive Car 28(6):68–71
20. Niwakawa M, Onda T, Kinoshita N (2007) Stereo vision based measurement of intersections of overhead contact wires and pantograph of Kyushushinkansen. IEEJ Trans Ind Appl 127 (2):118–123
21. Kusumi S, Nezu K, Nagasawa H (2000) Overhead contact line inspection system by rail-and-road car. Q Rep RTRI 41(4):169–172
22. Nakama F, Ichikawa M, Nagasawa H (1984) Measurement of contact loss by detection spark. Q Rep RTRI 25(3):95–98
23. Hayasaka T, Shimizu M, Nezu K (2009) Development of contact-loss measuring system using ultraviolet ray detection. Q Rep RTRI 50(3):131–136
24. Landi A, Menconi L, Sani L (2006) Hough transform and thermo-vision for monitoring pantograph-catenary system. Proc Inst Mech Eng Part F J Rail Rapid Transit 220(4):435–447
25. Hulin B, Schussler S (2007) Concepts for day-night stereo obstacle detection in the pantograph gauge. In: 2007 5th IEEE international conference on industrial informatics, pp 449–454
26. Jiang J (2009) The design and realization of catenary wind deviation. Central South University, Changsha
27. Yang K, Wang L, Gao X et al (2009) Application of CCD measurement technique for wear on pantograph sliding plates. In: 4th international symposium on advanced optical manufacturing and testing technologies, pp 728334–728334-7
28. Zhang Y, Wu W, Xu K (2007) Detection system of dynamic envelope line of pantograph based on machine vision. Electr Railway 6:29–30
29. Chen K (2009) Development and implementation of wireless video monitoring system for locomotive pantograph. Southwest Jiaotong University, Chengdu
30. Fan H, Bian C, Zhu T et al (2010) Automatic detection of positioning line in contactless overhead contact system. J Comput Appl 30(S2):102–103
31. Feng Q, Chen W, Wang Y et al (2010) Research on the algorithm to measure the pantographic slipper abrasion. J China Railway Soc 32(01):109–113
32. Zhang G, Liu Z, Han Y et al (2013) A fast fuzzy matching method of fault detection for rod insulators of high-speed railways. J China Railway Soc 35(05):27–33
33. Han Z, Liu Z, Chen K et al (2011) Pantograph slide cracks detection technology based on curvelet coefficients directional projection (CCDP). J China Railway Soc 33(11):63–69
34. Chen K, Liu Z, Han Z (2012) Pantograph slipper cracks identification based on translational parallel window in curvelet transform domain. J China Railway Soc 34(10):44–46
35. Han Z, Liu Z, Yang H et al (2013) Insulator fault detection based on curvelet coefficients morphology and zonal energy methods. J China Railway Soc 35(03):37–40
36. Yang H, Liu Z, Han Z et al (2013) Foreign body detection between insulator pieces in electrified railway based on affine moment invariant. J China Railway Soc 35(04):30–36
37. Han Y, Liu Z, Han Z et al (2014) Fracture detection of ear pieces in catenary support devices of high-speed railway based on SIFT feature matching. J China Railway Soc 36(02):31–36
38. Yang H, Liu Z, Han Y et al (2013) Defective condition detection of insulators in electrified railway based on feature matching of speeded-up robust features. Power Syst Technol 37 (8):2297–2302
39. Zhang W, Mei G, Chen L (2000) Analysis of the influence of catenary's sag and irregularity upon the quality of current-feeding. J China Railway Soc 22(6):50–54
40. Aboshi M, Manabe K (2000) Analyses of contact force fluctuation between catenary and pantograph. Q Rep RTRI 41(4):182–187

41. Collina A, Fossati F, Papi M et al (2007) Impact of overhead line irregularity on current collection and diagnostics based on the measurement of pantograph dynamics. Proc Inst Mech Eng Part F: J Rail Rapid Transit 221(4):547–559
42. Bucca G, Collina A (2009) A procedure for the wear prediction of collector strip and contact wire in pantograph–catenary system. Wear 266(1):46–59
43. Van Vo O, Massat JP, Laurent C et al (2014) Introduction of variability into pantograph–catenary dynamic simulations. Veh Syst Dyn 52(10):1254–1269
44. Howa F (1995) Research on the high speed of the flow system of the new main line. Electr Traction Express 10:20–25
45. Aboshi M (2004) Precise measurement and estimation method for overhead contact line unevenness. IEE J T Ind Appl 124:871–877
46. Zhang W, Mei G, Wu X et al (2002) Hybrid simulation of dynamics for the pantograph-catenary system. Veh Syst Dyn 38(6):393–414
47. Huan R, Jiao J, Su G et al (2012) Dynamics of pantograph-catenary coupled system with contact wire vertical irregularities. J China Railway Soc 34(7):15–21
48. Xie J, Liu Z, Han Z et al (2009) Pantograph and overhead contact line coupling dynamic model simulation and analysis of imbalance of overhead contact line. Electr Railway 6:23–26
49. Liu Z, Han Z (2011) Review of researches on catenary spectrum in electrified railway. Electr Railway 1:1–3
50. Liu Z, Han Z (2013) Study on electrical railway catenary line spectrum based on AR model. J China Railway Soc 35(12):24–29
51. Jiang Y, Zhang W, Song D (2015) Study on the contact wire unevenness of high-speed railway. J China Railway Soc 37(2):34–38
52. Bruni S, Ambrosio J, Carnicero A et al (2015) The results of the pantograph–catenary interaction benchmark. Veh Syst Dyn 53(3):412–435
53. Kim JW, Chae HC, Park BS et al (2007) State sensitivity analysis of the pantograph system for a high-speed rail vehicle considering span length and static uplift force. J Sound Vib 303 (3):405–427
54. Wang H, Liu Z, Han Z et al (2014) Feature extraction of pantograph-catenary contact force power spectrum of electrified railway. J China Railway Soc 36(11):23–28
55. Kusumi S, Fukutani T, Nezu K (2006) Diagnosis of overhead contact line based on contact force. Q Rep RTRI 47(1):39–45
56. Rønnquist A, Nåvik P (2015) Dynamic assessment of existing soft catenary systems using modal analysis to explore higher train velocities: a case study of a Norwegian contact line system. Veh Syst Dyn 53(6):756–774
57. Kudo S, Honda S, Ikeda M (2002) Contact force signal analysis of current collecting with bispectrum and wavelet. In: Proceedings of the 41st SICE annual conference, IEEE, vol 4, pp 2478–2482
58. Kim JS (2007) An experimental study of the dynamic characteristics of the catenary-pantograph interface in high speed trains. J Mech Sci Technol 21(12):2108–2116
59. Han Z (2013) The dynamic characteristics assessment of high-speed catenary-pantograph based on modern spectrum analysis and intelligent fault image identification. Southwest Jiaotong University Graduate Thesis, Chengdu
60. Han Z, Liu Z, Zhang X et al (2013) Pantograph-catenary contact force data analysis based on data correlation decomposed by EEMD. J China Railway Soc 35(9):25–30
61. Wang H, Liu Zhigang, Song Yang (2015) Analysis on wavelength components in pantograph-catenary contact force of electric railway based on multiple EEMD. J China Railway Soc 37(5):34–41
62. Rønnquist A, Nåvik P (2015) Dynamic assessment of existing soft catenary systems using modal analysis to explore higher train velocities: a case study of a Norwegian contact line system. Veh Syst Dyn 53(6):756–774
63. Usuda T (2007) Estimation of wear and strain of contact wire using contact force of pantograph. Q Rep RTRI 48(3):170–175

64. Mariscotti A, Marrese A, Pasquino N et al (2013) Time and frequency characterization of radiated disturbance in telecommunication bands due to pantograph. Measurement 46 (10):4342–4352
65. Liu Z, Song Y, Han Y et al (2016) Advances of research on high-speed railway catenary. J Southwest Jiaotong Univ 51(3):495–518

Chapter 2
Statistical Characteristics of Pantograph-Catenary Contact Pressure

2.1 Introduction

At present, the studies on statistical characteristics of pantograph-catenary data generally concern the simple statistical properties, such as mean value and variance of contact pressure between pantograph and catenary. However, it is obviously insufficient to realize the efficient fault detection and state estimation of catenary. In this chapter, the statistical characteristics including stationarity, periodicity, correlation, high-order statistical properties of pantograph-catenary data are analyzed and discussed in detail.

2.2 Stationarity of Pantograph-Catenary Contact Pressure

2.2.1 Definition of Random Signal Stationarity

In general, if the joint probability distribution of a random process $\{x(t_1), \ldots, x(t_n)\}$ is same as that of the random process $\{x(t_1 + \tau), \ldots, x(t_n + \tau)\}$ after delaying τ, $\{x(t),\ t \in T\}$ is called the narrow sense stationary processes or strictly stationary process. This means that the statistical properties of stationary random signals are not related to the selection of start and end time. That is to say, the statistical properties of the random process do not change with the time. In many cases, it is very difficult to obtain a joint distribution function of a random process, so it is also difficult to judge the stability of a random signal according to the above definition in practice.

Z. Liu, *Detection and Estimation Research of High-speed Railway Catenary*,
Advances in High-speed Rail Technology, DOI 10.1007/978-981-10-2753-6_2

The random process $\{x(t),\ t \in T\}$ is called a generalized stationary process, if

(1) The expected function, namely, the first order moment function $E\{x(t)\} = m$, m is the constant.
(2) The mean square value function, namely, the second order origin moment function $E\{|x(t)|^2\} < \infty$.
(3) The covariance function, namely, the second order mixed center distance function $E\{[x(t) - m][x(\tau) - m]^*\} = R_x(t - \tau) - |m|^2$, where $R_x(t - \tau) = E\{x(t)x(\tau)^*\}$ is the auto correlation function of random process.

The essence of the definition means that, for a generalized stationary process, its expectation function is constant, its mean square function exists, and its covariance function does not change with the time, i.e. is not related to the start time, and only depends on the time difference $t - \tau$. So, the generalized stationary process is also called the covariance difference stationary process or second order stationary process. The random signal can be divided into stationary signal and non-stationary signal. If a signal is a stationary signal, it can be very simple. If a signal is not a generalized stationary process, it is called the non-stationary signal.

2.2.2 *Stationarity Test Methods of Pantograph-Catenary Contact Pressure*

According to European Standard EN50318, EN50367 and China Railway Standard, the technical indicators of performance evaluation for pantograph-catenary contact pressure mainly include the contact pressure average value F_m, standard deviation σ, statistical minimum value, statistical maximum value, etc.

These indicators can be computed directly using the sampled time series, which practically mean that the sampled data of contact pressure is stationary and has the ergodicity. However, the catenary system is a soft cable structure system with the cycle spans along the railway line. The supporting devices, droppers, and uneven tension, can cause the inhomogeneous elasticity in a span. At a low speed, this impact is relatively small, but at a high speed, the uneven elasticity may cause the increasing instability of pantograph-catenary contact pressure, which influences the accuracy of catenary performance evaluation. Therefore, it is very important to choose the appropriate analysis method to reveal the dynamic characteristic of contact pressure. The essence of signal stationarity test is whether the basic physical factors of random signal are changed with the time. At present, the usual method of stationarity test includes non-parametric detection and parametric test.

The non-parameter test method mainly includes run length (round) test, which is also called the random test of single sample variable value. This method only involves a set of the measured data, and does not require the assumption of the signal distribution, so it has a good practicability.

The parametric test methods include DF (Dickey-Fuller), ADF (Augment Dickey Fuller), PP (Phillips-Perron), Holzer instrumental variable method, DF-GLS (Dickey-Fuller Generalized Least Square), KPSS (Kwiatkowski, Phillips, Schmidt, and Shin), LMC (Leybourne and McCabe) test methods, etc.

For the irregularity test of railway track geometry, the round test method is most commonly used. In [1], the round test method was adopted to check the long wave irregularity of Maglev track. The results showed that the random data of magnetic levitation track vertical irregular signal has high non-stationarity. In [2], the round test method was adopted to check the track irregularity of Qinhuangdao-Shenyang Passenger Railway of China. The results showed that the majority of rail irregular samples were smooth or weakly stationary and could be approximately treated as stationary random process. In [3], the round test method was adopted to check the irregular samples of the welded joint rail surface in Jingshan Line and Guangshen Line of China. The results showed that the irregular sample function of single welded joint surface had the non-stationarity, and the whole sample space of a large number of welded joints in the same railway line was stationary.

1. Round test method

Round test method is a non-parametric test method. Because it does not need an assumption of data distribution, and only relates to a set of measured data, it has some applications in practical engineering.

The test steps are listed as follows.

(1) The tested data sequence $\{x_i\}$ is divided into m parts, and their variances σ_i^2 are respectively computed.

(2) Compute $\sigma^2 = \frac{\sigma_{i\max}^2 + \sigma_{i\min}^2}{2}$, where $\sigma_{i\max}^2$ and $\sigma_{i\min}^2$ are the maximum and minimum value of σ_i^2, respectively.

(3) If $\sigma_i^2 < \sigma^2$, the division is marked with "+". If $\sigma_i^2 > \sigma^2$, the division is marked with "−".

(4) The m sections form an observation sequence according to "+" and "−", and the sequences with same mark are defined as a round (run length). The number r of rounds is the test statistic.

(5) Let the number of "+" be N_1, and the number of "−" be N_2.

(6) When $N_1 \ll 15$ and $N_2 \ll 15$, they are considered as the small samples. Check the round (run length) test distribution table, then the upper and lower limit r_u, r_l can be obtained at $\alpha = 0.05$.

(7) If $r_1 < r < r_u$, where r is the tested data, the tested data is considered as the stationary data.

(8) When $N_1 > 15$ or $N_2 > 15$, they are considered as the large samples, and can be approximated with normal distribution.

(9) The statistic can be computed by $Z = \frac{r-u}{\sigma}$.

Where $N = N_1 + N_2$, $u = \frac{2N_1N_2}{N} + 1$, and $\sigma = \sqrt{\frac{2N_1N_2(2N_1N_2 - N)}{N^2(N-1)}}$.

(10) When $\alpha = 0.05$, and $|Z| \leq 1.96$, the tested data is stationary.

2. Surrogate-data test method

Since the correlation function and power spectrum of a signal are a Fourier transform pair, it can be considered that the spectrum of stationary random signal is invariant with the time and that of non-stationary signals is variant with the time. Therefore, the stationarity of the signal can be judged by comparing the similarity of the spectrum at different time instants.

For the same marginal spectrum, the difference between the non-stationary signal and the stationary signal is reflected in the frequency spectrum changing with the time. So, in order to test the signal stationarity, a stationary signal needs to be introduced as a reference. The signal is called a surrogate signal and generated by the test signal, which retains some statistical properties of the original signal.

The test steps are listed as follows.

(1) Produce the surrogate data S_J.
The produced surrogate data is stationary using Fourier transform. The algorithm can ensure that the power spectrum's amplitude of original signal is unchanged. The signal's phases become the random ones φ_f that uniformly distribute in $[-\pi, \pi]$. The Fourier inverse transform of the random distribution is the surrogate data $S(t)$.

$$S(t) = \int e^{i2\pi ft}|X(f)|e^{i\varphi f}df \tag{2.1}$$

(2) Solve the time-frequency representation of original and surrogate signals.
For signal $x(t)$, considering the computation time and estimation accuracy of the spectrum, the time-frequency representation is described through the multi window of signal.

$$S_{x,k}(t,f) = \frac{1}{k}\sum_{k=1}^{k}\left|\int_{-\infty}^{+\infty} x(s)h_k(s-t)e^{-i2\pi fs}ds\right|^2 \tag{2.2}$$

$h_k(t)$ is the kth Hermite function as follows.

$$h_k(t) = \frac{1}{\sqrt{k!2^k\sqrt{\pi}}}e^{-t^2}H_k(t) \tag{2.3}$$

(3) Compute the distance $C_n^{(x)}$ and $C_n^{(S_J)}$ between the local spectrum and the global spectrum of original signal and surrogate signal.

$$\{c_n^{(x)} := K(S_{x,k}(t_n,.)\ \langle S_{x,k}(t_n,.)\rangle_{n=1,\ldots,N})\} \tag{2.4}$$

where $\langle S_{x,k}(t_n,f)\rangle_{n=1,\ldots,N}$ is the mean of power spectrum at all time instants.

$$\langle S_{x,k}(t_n,f)\rangle_{n=1,\ldots,N} = \frac{1}{N}\sum_{n=1}^{N} S_{x,k}(t_n,f) \tag{2.5}$$

The above distance can be obtained based on Ref. [4].

$$K(G,H) = \left(1 + \int \left|\log\frac{G(f)}{H(f)}df\right|\right) \cdot \int (\tilde{G}(f) - \tilde{H}(f)) \log\frac{\tilde{G}(f)}{\tilde{H}(f)}df \tag{2.6}$$

where "$\sim$" means the normalized function of corresponding function, such as $\tilde{f}(x) = f(x)/\max(f(x))$.

(4) Compute the fluctuation θ of the distance $C_n^{(x)}$ with time.
The fluctuation of distance $C_n^{(x)}$ with the time of original signal is θ_1, and the fluctuation of distance $C_n^{(S_J)}$ with the time of surrogate signal is θ_0.

$$\theta = \frac{1}{N}\sum_{n=1}^{N} (C_n^{(x)} - \langle C_n^{(x)}\rangle)^2 \tag{2.7}$$

(5) Solve the probability distribution curve of θ_0, set the threshold γ, and judge the stationarity.
θ_0 obeys the Gamma distribution in [5]. Based on the fitting Gamma distribution curve, the test threshold γ can be determined, and the stationarity of data can be tested as follows.

$$\begin{cases} \theta_1 > \gamma: \text{ non-stationary} \\ \theta_1 < \gamma: \text{ stationary} \end{cases} \tag{2.8}$$

(6) Define the non-stationary measurement *INS*.

$$INS = \sqrt{\frac{\theta_1}{\frac{1}{J}\sum_{j=1}^{J}\theta_0(j)}} \tag{2.9}$$

Based on the expression of non-stationary measurement, if the *INS* value further deviates from 1, the signal is more stationary.

3. Mean function

If $\{X_t\}$ is a stationary signal with mean value μ, the segment of the signal should also be stationary. Suppose that $\bar{X}_{N_i}$, $i = 1, 2, \ldots, s$ is the mean value of each segment in the signal, then $\sqrt{N_i}(\overline{X_{N_i} - \mu})$ obeys the normal distribution [6]. The test of mean value can be transform into the test of whether $\sqrt{N_i}(\overline{X_{N_i} - \mu})$ is coming from the normal distribution $N(0, 2\pi S_{xx}(0))$.

Based on the 3σ rule [7], it can be obtained as follows.

$$p_1 = P\{-\sqrt{2\pi S_{xx}(0)} < \sqrt{N_i}(\overline{X_{N_i}} - \mu) < \sqrt{2\pi S_{xx}(0)}\} = 0.638 \tag{2.10}$$

where p is the proportion of $\sqrt{N_i}(\overline{X_{N_i}} - \mu)(i = 1, 2, \ldots s)$ in $(-\sqrt{2\pi S_{xx}(0)}, \sqrt{2\pi S_{xx}(0)})$, and $p \sim N(p_1, p_1(1-p_1)/s)$ can be obtained according to the central limit theorem.

For the significant level α, the test statistic is adopted.

$$Z = (p - p_1)/\sqrt{p_1(1-p_1)/s} \tag{2.11}$$

For $Z \sim N(0,1)$, the rejection region is $Z > z_{\alpha/2}$, and $z_{\alpha/2}$ is the upper section point $\alpha/2$ in the standard normal distribution.

4. Auto covariance function

Based on the definition of signal stationarity and Wiener-Khinchin theorem, the auto covariance function can be used to test the signal's stationarity. The spectral density of each segment of signal can be considered to be determined by each segment location and frequency. If the signal is stationary, the spectral density of each segment should be related to the frequency, instead of its location.

The model is given below.

$$S_{xx}(\omega) = \alpha + \beta + \varepsilon \tag{2.12}$$

where α is the location factor, β is the frequency factor and ε is the random factor. The covariance test can be considered as the variance analysis problem of two factors. $H_0 : \alpha_1 = \alpha_2 = \cdots = \alpha_s$, $H_1 : \alpha_1, \alpha_2, \ldots, \alpha_s$, and they are not all equal.

Suppose,

$$Y_{\cdot\cdot} = \frac{1}{sn}\sum_{i=1}^{s}\sum_{j=1}^{n} Y_{ij}, \quad Y_i = \frac{1}{n}\sum_{i=1}^{s} Y_{ij}, i = 1, 2, \ldots, s, \quad Y_{\cdot j} = \frac{1}{s}\sum_{i=1}^{s} Y_{ij}, j = 1, 2, \ldots, n$$

$$S_A = n\sum_{i=1}^{s}(Y_i - Y_{\cdot\cdot})^2, \quad S_B = s\sum_{j=1}^{n}(Y_{\cdot j} - Y_{\cdot\cdot})^2,$$
$$S_E = \sum_{i=1}^{s}\sum_{j=1}^{n}(Y_{ij} - Y_i - Y_{\cdot j} + Y_{\cdot\cdot})^2$$

The test statistic is given below.

$$F = \frac{S_A/(s-1)}{S_E/(s-1)(n-1)} \overset{H_0}{\sim} F(s-1, (s-1)(n-1)) \tag{2.13}$$

At the significant level α, the rejection region is $F > F_\alpha(s-1,(s-1)(n-1))$, $F_\alpha(s-1,(s-1)(n-1))$ is the upper section point α in F distribution. In the actual application, F value method is adopted in general.

2.2.3 *Stationarity Analysis of Actual Pantograph-Catenary Contact Pressure*

The actual contact pressure data is from the up and down lines of Jingguang Line and Hukun Line in China. The speeds are 115, 140, 150 and 120 km/h, respectively. The sampling interval is 2 data points each meter [8]. The stationarity analysis of contact pressure signal with surrogate-data is described as follows.

1. Stationarity test process of contact pressure

The contact pressure data is from a certain section of the up line of Hukun Line, and the sampling number is 3000.

(a) The surrogate signal is produced with Fourier transform of the original signal. Considering the fitting accuracy and computational quantity, 500 surrogate signals are chosen. The contact pressure signal and its surrogate signal of Hukun Line are shown in Fig. 2.1.
(b) The original signal and surrogate signal are represented with time-frequency distribution. The distances between their local and global spectrums can be computed based the distance formula, shown in Fig. 2.2.
(c) The fluctuation θ_1 of spectrum distances of contact pressure and surrogate signals with time can be solved, while the number of θ_0 is 500. Based on the distribution histogram of θ_0, the gamma distribution curve of θ_0 can be fitted. The relationship between θ_0 and θ_1 can be obtained, as shown in Fig. 2.3.

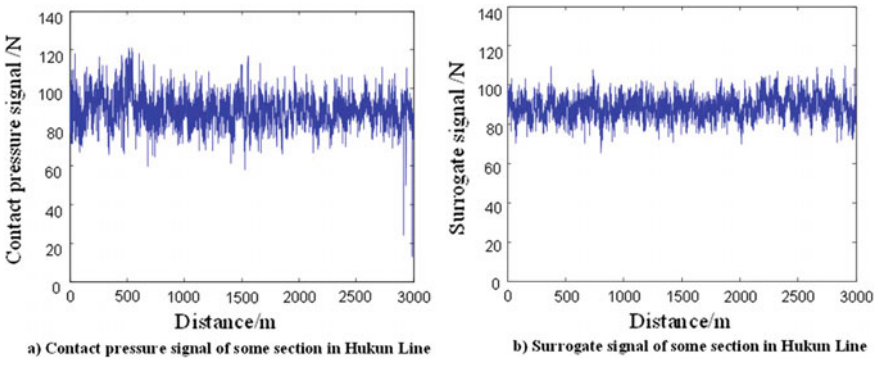

Fig. 2.1 Contact pressure signal and its surrogate signal of Hukun Line

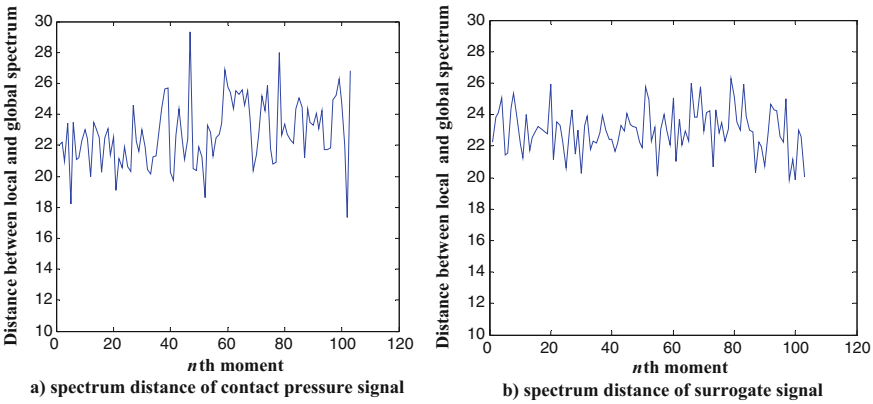

Fig. 2.2 Spectrum distances of contact pressure and its surrogate signal

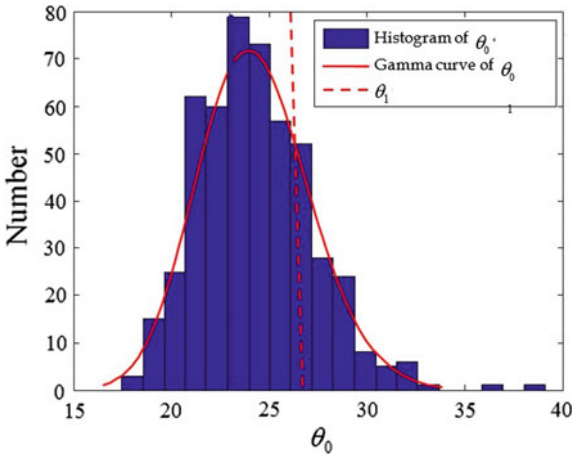

Fig. 2.3 Results of stationarity test analysis

Based on Fig. 2.3, it can be found that θ_1 is in the probability distribution of θ_0. The spectrum distances of the tested data at each time are in the range of the stationary surrogate data. Therefore, the contact pressure signal in the section can be judged to be stationary.

2. Contact pressure stationarity analysis for different distances

The contact pressure signals from different distances are adopted for their stationarity analysis. The analysis results are listed in Table 2.1.

Because the signal's time-frequency spectrum should be first computed using the surrogate data method, considering that the signal's length can influence the estimation accuracy of time-frequency spectrum, the minimum length of contact pressure data is 400 points, and that is to say that the sampling distance is 200 m. Based on the analysis results, it can be found that the data between 1000 and

Table 2.1 Contact pressure signal stationarity analysis for different distances

Line name	Sampling distance (m)	Stationarity pass rate (%)
Up line of Hukun Line	1000–3000	100
	500–1000	96
	200–500	80
Down line of Hukun Line	1000–3000	100
	500–1000	92
	200–500	82
Up line of Jingguang Line	1000–3000	100
	500–1000	95
	200–500	87
Down line of Jingguang Line	1000–3000	100
	500–1000	96
	200–500	90

3000 m is almost stationary. With the decreasing of sampling distance, especially between 200 and 500 m, some data segments show obvious non-stationarity. Therefore, for these contact pressure signals, the non-stationary signal processing method should be adopted. In addition, it is found that the data are sampled from the joint of the anchor section, track turning, mountain area and tunnel area.

The round test method is also adopted to test the stationarity of actual sampling data of pantograph-catenary contact pressure. The test results are listed in Table 2.2. It can be found that for the contact pressure signal' stationarity, in the long term, it basically satisfies the condition of stationarity, and can be used to study the stability analysis, but there may be some non-stationary in the local, especially in the position of the support and so on.

2.3 Periodicity of Pantograph-Catenary Contact Pressure

2.3.1 Periodic Trend Feature of Pantograph-Catenary Pressure

The catenary is constructed along the railway line through the suspension and supporting devices, and the structure "span" as a unit is repeated. In a span, the contact line is hanged through the droppers, so the dropper is equivalent to a concentrated mass point, which influences the catenary's elasticity. At a low speed, the pantograph can have better dynamic performance, since the structural concentrated mass point has little effect on the pantograph. At a high speed, the uneven elasticity of the structural concentrated mass point becomes larger, and the contact pressure highlights the more obvious periodic feature, and namely the contact pressure fluctuates with the span and dropper interval.

Table 2.2 Contact pressure signal stationarity analysis using round test method

Line Name	Data point	Group number	Confidence coefficient (%)	Stationarity
Up line of Hukun Line	3200	100	95	Yes
		160		Yes
		200		Yes
		320		No
Low line of Hukun Line	3200	100	95	Yes
		160		Yes
		200		Yes
		320		No
Up line of Jingguang Line	3200	100	95	Yes
		160		Yes
		200		Yes
		320		No
Down line of Jingguang Line	3200	100	95	Yes
		160		Yes
		200		Yes
		320		No

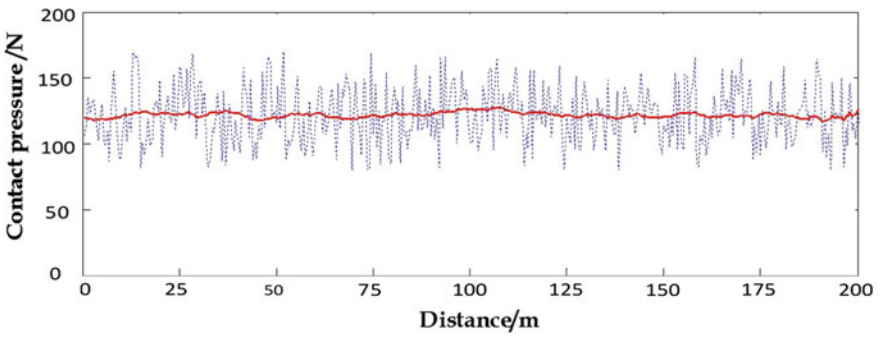

Fig. 2.4 Actual contact pressure signal at 100 km/h

The contact pressure signals at 100 and 300 km/h are shown in Figs. 2.4 and 2.5, in which the dotted line is the time series, and the solid line is the fluctuation trend of contact pressure. It can be found that the trend of contact pressure at high speed shows obvious periodicity. The statistics results show that at low speed, the standard deviation of contact pressure is less than 3 N, and the standard deviation at high speed is more than 10 N. Therefore, at high speed, the contact pressure has become a mean time varying data, and does not conform to the definition of the generalized stationary, which is not suitable for the use of stationary data mean variance analysis.

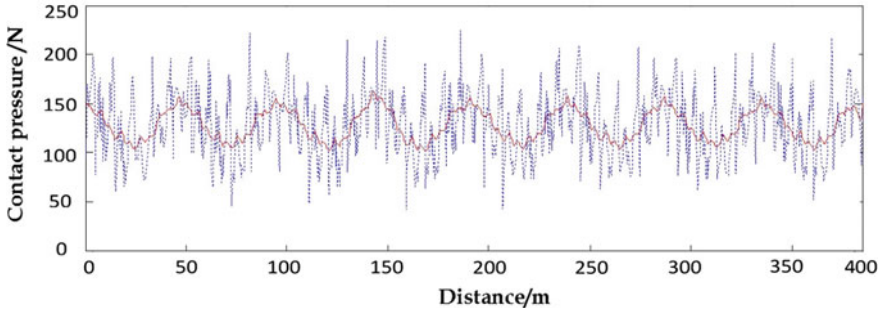

Fig. 2.5 Actual contact pressure signal at 300 km/h

The second order auto-correlation functions of simulation data and different line actual measurement data from Jiaoliu Line, Jingguang Line, and Guangshen Line are shown in Fig. 2.6. It can be found that the second order auto-correlation functions of different contact pressure data have obvious period correlation characteristics.

According to the definition, if the mean value and the autocorrelation function of a random signal are periodic, the signal can be defined as a periodic stationary random signal. The above research results show that the average and the correlation function of pantograph-catenary contact pressure data at high speed are more obviously periodic, so the contact pressure data tend to be a periodic stationary random signal.

According to Cramer decomposition theorem, the time series can be decomposed into two parts. One is the deterministic trend component, and the other is the stationary zero mean random component. Cramer decomposition theorem guarantees that the deterministic information of time series can be sufficiently extracted through the difference of proper order number. Since the change of the pantograph-catenary contact pressure is determined by the structure of catenary suspension, the time series has strong determinacy. Therefore, for the pantograph-catenary contact pressure with periodic time-varying mean characteristics at high speed, an effective method is to extract the trend term first, then analyze the stationary random vibration components by the several times of trend differential elimination.

2.3.2 Trend Term Extraction of Pantograph-Catenary Contact Pressure

Aiming at the periodicity of pantograph-catenary contact pressure, the moving mean, data fitting and low-pass filtering methods are adopted in this section.

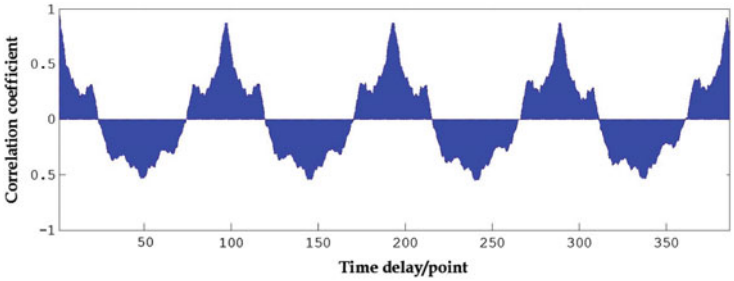

(a) Auto-correlation function of contact pressure simulation data

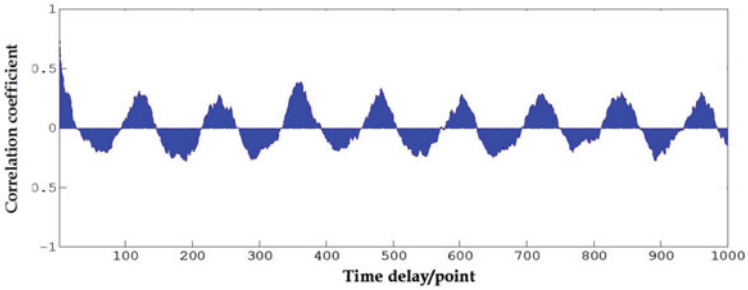

(b) Auto-correlation function of contact pressure of Jiaoliu Line

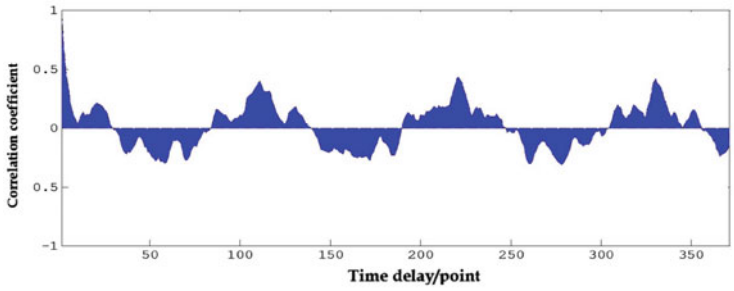

(c) Auto-correlation function of contact pressure of Jingguang Line

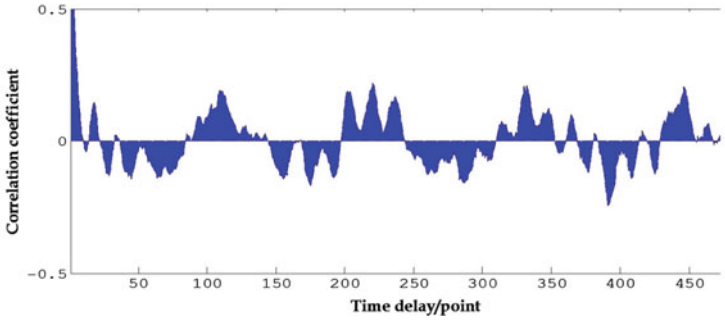

(d) Auto-correlation function of contact pressure of Guangshen Line

Fig. 2.6 Auto-correlation functions of contact pressure data

1. Moving mean method

The most direct method to extract the trend term is to segment the data and extract the local mean value of the continuous movement.

The center moving mean value of contact pressure data is defined as follows.

$$M_w(n) = \begin{cases} \frac{1}{n}\sum_{i=1}^{n+w/2} F(i) & n \geq w/2 \\ \frac{1}{w}\sum_{i=n-w/2}^{n+w/2} F(i) & w/2 < n \leq N - w/2 \\ \frac{1}{N-n}\sum_{i=n-w/2}^{N} F(i) & n > N - w/2 \end{cases} \tag{2.14}$$

where M_w is the center moving mean value, w is the length of moving window, $F(i)$ is the contact pressure, and N is the sampling data length of contact pressure.

Since the catenary elasticity is symmetrical within its span, the quarter of sampling point number in a span can be chosen as the window length moving average window in general.

2. Data fitting method

The pantograph-catenary contact pressure can be described in general below.

$$P = P_0\delta(x - vt) \tag{2.15}$$

The formula means that the contact pressure P_0 moves at v speed along x direction. $\delta(\cdot)$ function can be expended as follows.

$$P = P_0 \cdot \frac{2}{l}\sum \sin(k\pi vt) \cdot \sin\left(\frac{k\pi x}{l}\right) \tag{2.16}$$

where l is the cycle period.

Because the contact pressure data has triangle periodicity, the sine polynomial can be adopted to fit the data, as shown below.

$$P = \sum_{i=1}^{n} A_i \sin(\omega_i x + \varphi_i) \tag{2.17}$$

where n is the order of fitting.

The effect of the trend term extraction using a sine polynomial fitting is shown in Fig. 2.7. In Fig. 2.7a, the forth order sine fitting is adopted, and the trend of the span as period can be extracted. In Fig. 2.7b, the fifth order sine fitting is adopted, and the trend of the dropper as period can be extracted.

The extracted trend term using the fitting method is more smooth and easy to analyze the impact of different equipment on the contact pressure. But for the

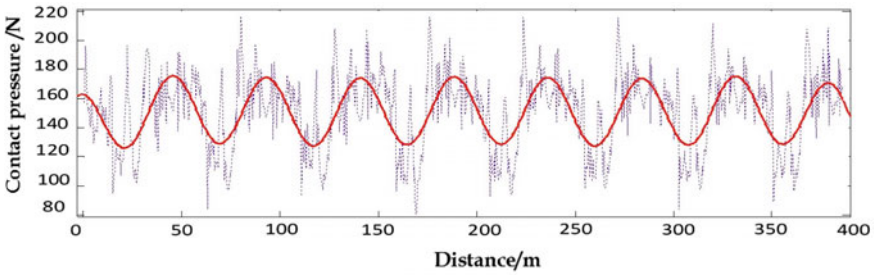

(a) Forth order sine fitting

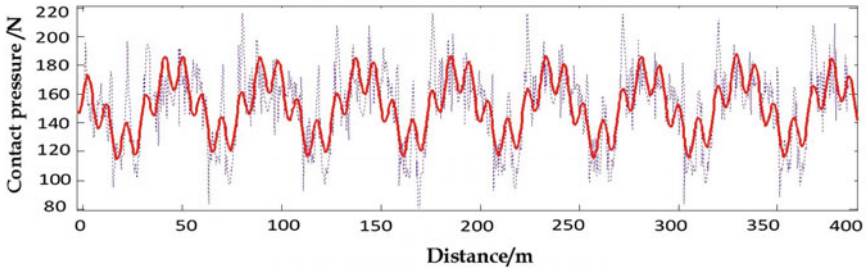

(b) Fifth order sine fitting

Fig. 2.7 Trend term extraction with data fitting

catenary with different droppers and design structures, the order selection for extracting the same trend is different, and the application is inconvenient. In general, the order number of fitting increases from low order, and the fitting ends when the periodic length of fitting term approximates the length of sampling data in a span of catenary.

3. Low pass filtering method

The trend term of contact pressure is caused by low frequency vibration. Finite Impulse Response (FIR) filter can be adopted conveniently. The Z transform form of FIR filter is listed below.

$$P_{tend}(z) = (b_1 + b_2 z^{-1} + \cdots + b_{n_b+1} z^{-n_b}) P(z) \tag{2.18}$$

The trend term extraction with FIR filter is shown in Fig. 2.8. It can be found that the correlation between the trend term and data is strong, and the trend term is more sensitive to the data fluctuation.

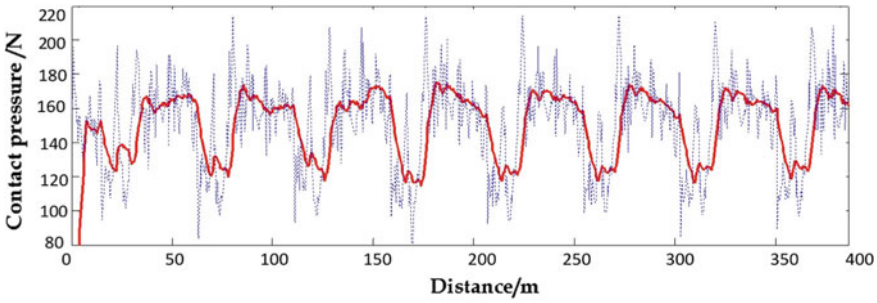

Fig. 2.8 Trend term extraction with FIR filter

2.3.3 Evaluation of Pantograph-Catenary Contact Pressure

The moving average is not required to select the model order, and it is not sensitive to the data fluctuation, so the moving average method can be used to eliminate the trend term. The Cramer decomposition theorem cannot determine the order that accords with the stability of random component. The standard deviation of each trend term is calculated by iteration. When the nth trend term standard deviation is less than the threshold, the stationary random term can be obtained with the $n-1$th difference. The research results based on the measurement and the simulation data show that the stationary condition can be satisfied by the second order difference.

In Fig. 2.9, it can be found that the contact pressure data basically satisfies the random vibration component of stationary condition after the second order difference, and the time sequence mean value and standard deviation can be computed directly.

For the different pantograph type for different speed, the data of pantograph-catenary contact pressure can be obtained through the simulation at 350 km/h. The matching performance of pantograph-catenary interaction for the different type is estimated with the second order moving mean difference standard deviation.

Based on the comparison results in Table 2.3, it can be found that the direct time sequence standard deviations of SBS81 and SSS400+ are basically consistent, as well as DSA250 and DSA380. But SBS81 and DSA250 are the low-speed pantographs and SSS400+ and DSA380 are the high-speed pantographs. Therefore, the results are not consist with the actual operation experiments. The main reason is that the computation process ignores the influence of time-variant mean value. When the second order moving mean difference standard deviation is computed after the time-variant trend term is amended, it can be found that the matching performance of pantograph-catenary for DSA380 and SSS400+ is far better than that for SBS81 and DSA250.

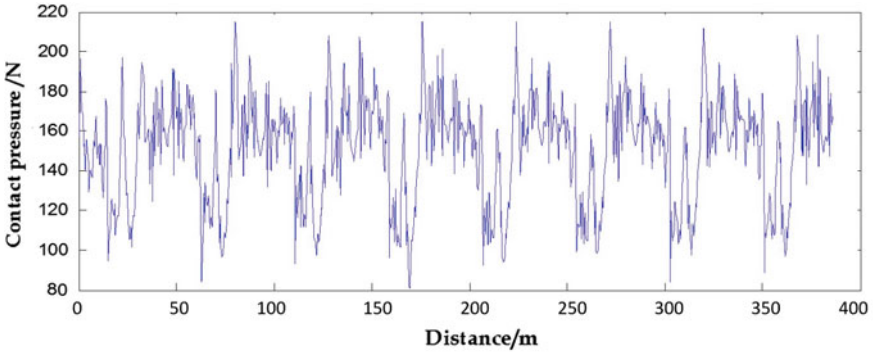

(a) Contact pressure data at 350km/h

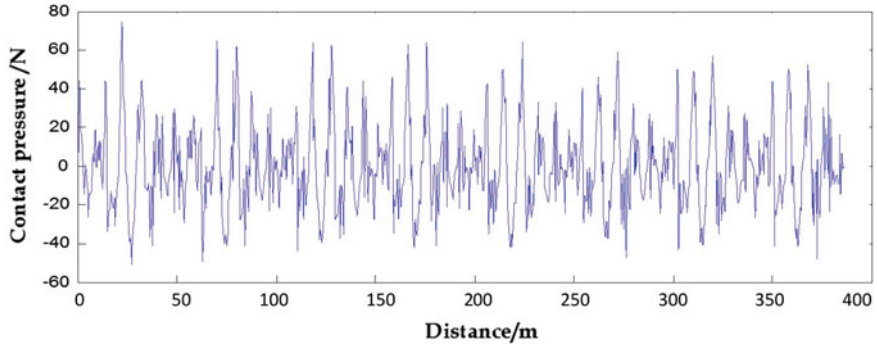

(b) Contact pressure data after eliminating the trend term

Fig. 2.9 Contact pressure data after eliminating trend term with second order moving average method

Table 2.3 Evaluation of second order differential standard deviation of pantograph-catenary contact pressure

Method	Pantograph Type			
	SBS81	DSA250	DSA380	SSS400+
Direct time sequence standard deviation	35.59	32.82	32.04	35.55
Second order difference standard deviation	29.57	28.06	25.96	25.28

2.4 Correlation of Pantograph-Catenary Contact Pressure

Under the high voltage and strong interference environment, the parameters of the electric railway pantograph-catenary system may cause the abnormal changes of the measured data, which seriously pollute the data. Therefore, the data must be pre-processed before analyzed.

The common methods for processing the over-standard data include Wright (3σ criteria) criteria, Romanovsky criterion [9], Dixon criterion [10], Chauvenet criterion [11], Grubbs criterion [12], etc. These methods are threshold filtering based on the statistical properties of observed data. In addition, the field value is judged and processed by information processing and feature extraction, such as wavelet method, time series feature extraction method [13], etc. In [14], 3σ criteria was adopted to determine the random parameter distribution of ballast bed stiffness in the ballasted track. For the research of railway track irregularity data in China, the method through observing the data spectrum density was used to eliminate the error in [15]. In [16], the measured pantograph-catenary data was considered to meet Gauss distribution and the 3σ criteria was adopted to eliminate the abnormal pantograph-catenary contact pressure data. For the pantograph-catenary pressure data, the abnormal mutation of the data is not necessarily caused by the measurement. For example, the hard point, the parameter mutation of catenary or track [17, 18], could cause the intense variance of contact pressure. Therefore, it is very necessary to analyze the correlation of different measured data to judge the data mutation reason, which can avoid eliminating the true fault data. The EEMD will be adopted to analyze the correlation of pantograph-catenary contact pressure data.

2.4.1 HHT and EEMD

HHT (Hilbert-Huang Transform) is a kind of signal processing methods, which includes EMD (Empirical mode decomposition) and Hilbert transform. EMD is a multi-resolution signal decomposition technique, which is originally introduced by N. E. Huang et al. in 1998 [19]. The purpose of EMD is to decompose complex signals into several IMF (Intrinsic Mode Function) components. The decomposition process is based on the local characteristics of signals and adaptive to the signal itself. IMF is generally stationary signal, and it contains the local information of signals. EMD has strong ability on analyzing the non-linear and non-stationary signals. In HHT, the IMF concept makes instantaneous frequency defined by Hilbert transform have the actual physical meaning. It is easy to obtain the precise expression of frequency variations [20].

(1) EMD

EMD is a process to decompose the time series signal into some time series components. EMD method is adaptive and very suitable to analyze the non-linear and non-stationary signal. The steps of extracting IMFs from a signal $s(t)$ are listed as follows [21].

- Make $x(t)$ equal to the value of original signal $s(t)$.
- Spline interpolates between local maxima (minima) of $x(t)$ to obtain the upper (lower) envelope, and calculate the mean $m(t)$ of the upper and lower envelope.
- Subtract $m(t)$ from $x(t)$, and get the result $h(t)$.

- Test whether $h(t)$ satisfies IMF conditions or not. If yes, take $h(t)$ as the first IMF; if not, replace $x(t)$ with $h(t)$.
- And then repeat the steps above. This process can be repeated up to k times until satisfies the IMF conditions. Then the IMF component is separated from the data.
- Subtract the IMF from original signal to obtain the residual. Use the remainder to extract the new IMF, until the residual becomes a monotonic function. At last, the original signal is represented as:

$$s(t) = \sum_{i=1}^{n} c_i + r_n \tag{2.19}$$

where r_n is the residual of signal $s(t)$, and c_i is the ith IMF of signal $s(t)$.

(2) EEMD

Sometimes EMD cannot decompose the original data sequence correctly because of the mode mixing problem, which makes the IMFs lose their physical meanings. In order to avoid this problem, a new method called EEMD [22] is proposed. The process of EEMD is shown as follows.

- Add a random white noise series to the target data.
- Decompose the data into IMFs by EMD.
- Repeat the steps above for N times with different white noise series each time.
- Obtain the mean value of corresponding decomposed IMFs as the final result.

$$\overline{C_j(t)} = \frac{1}{N}\sum_{n=1}^{N} C_{jn}(t) \tag{2.20}$$

where $\overline{C_j(t)}$ is the jth IMF decomposed from the original signal by EEMD, $C_{jn}(t)$ is the jth IMF decomposed by the data adding the nth noise, and N is the number of the added white noise series.

The white noise with minimal amplitude has the characteristics of uniform distribution [23]. With the increase of noise, the signal will be continuous in different scales.

Because of the non-stationary and nonlinear characteristics of pantograph-catenary data, the frequency components are complex, and the data correlation analysis is difficult to obtain the reliable results. Therefore, EEMD decomposition method is adopted to decompose the measured data firstly, and then calculate the correlation of the IMF components, which can obtain more clear correlation information.

Table 2.4 Actual data detection item

No	Data	Unit	No	Data	Unit
1	Rail gauge	mm	8	Contact pressure	N
2	Super high	mm	9	Vertical acceleration	g
3	Horizontal irregularity	mm	10	Longitudinal acceleration	g
4	Curvature	rad/km	11	Height of contact line	mm
5	Slope	m/km	12	Stagger of contact line	mm
6	Irregularity of left track surface	mm	13	Catenary voltage	V
7	Irregularity of right track surface	mm	14	Wear of contact line	mm

2.4.2 *Basic Correlation Characteristics of Pantograph-Catenary Contact Pressure*

In Table 2.4, the item 1–7 means the actual data of track measurement, which is used to analyze the correlation of track and wheel. The item 8–14 means the actual data of pantograph-catenary system. Through the analysis of these data, it can be found that the rail gauge, slope, irregularity of left track surface, irregularity of right track surface, catenary voltage, and wear of contact line can influence the characteristic of pantograph-catenary system, but the correlation between them and the mutation point of contact pressure is not obvious. This shows that the variance of track parameters can be filtered to some extent through the damping spring of bogie, vehicle body and the transfer of pantograph. Therefore, the rest of item data will be analyzed in this section.

The measurement data of pantograph-catenary system in a certain distance is shown in Fig. 2.10. It can be found that the trends of the curves (super elevation, curvature, horizontal irregularity and stagger of contact line) are obviously consistent, shown in the oval marked sections. The trend variance means that there are curve sections in the line. The statistical results show that there is no obvious correlation between the 4 types of measurement data and the pantograph-catenary contact pressure, as well as the vertical acceleration, longitudinal acceleration, height of contact line, catenary voltage and wear of contact line.

In Fig. 2.10, the measurement data (contact pressure, vertical acceleration, longitudinal acceleration, height of contact line) has complex frequency components. The contact pressure data as the most data for characterizing the pantograph-catenary dynamic features has two parts, namely the pressure value obtained from the pressure sensors and the dynamic emended pressure value using the acceleration sensors in pantograph. The contact pressure is represented as follows.

$$F = F_S + F_a = F_S + \ddot{z} \cdot m_s \tag{2.21}$$

where F_s is the sum force of four pressure sensors, $\ddot{z}$ is the mean value of four pressure sensors, and m_s is the mass of slide plate of pantograph.

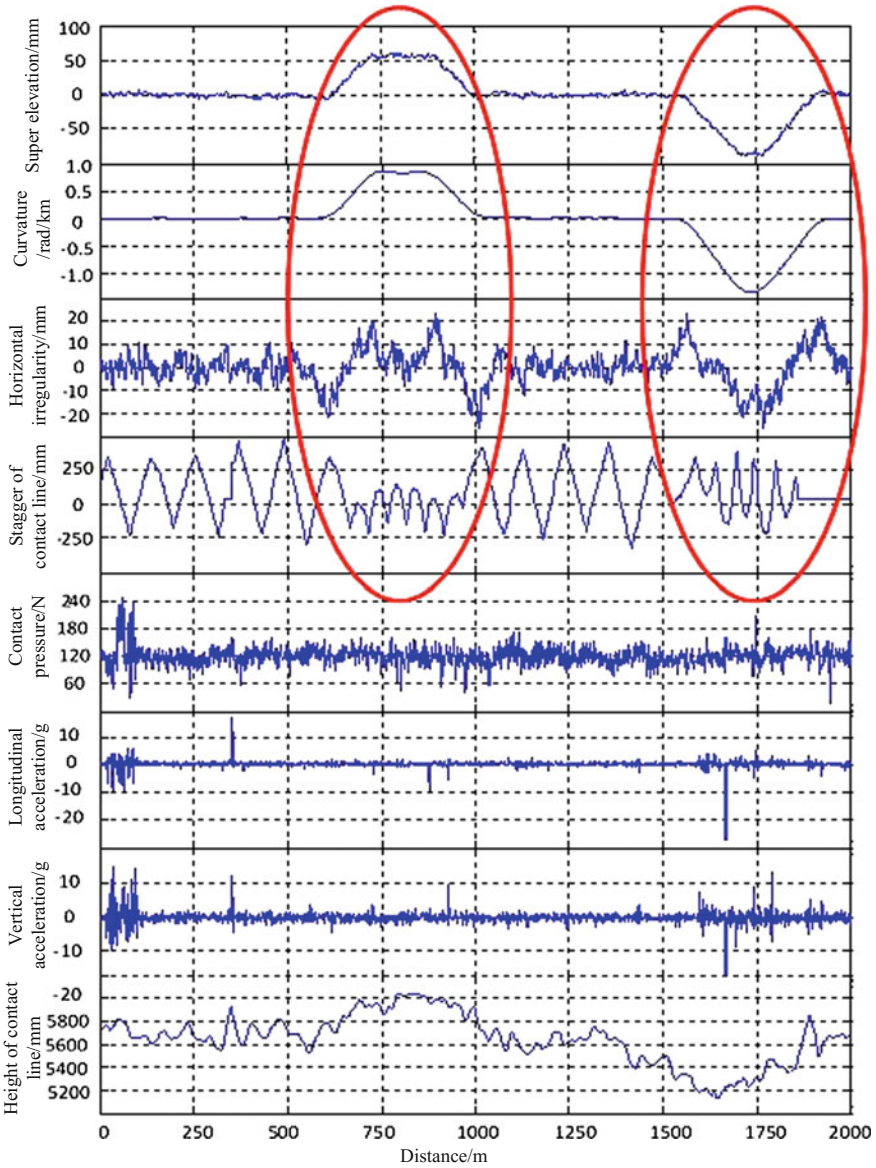

Fig. 2.10 Measurement data curves of a certain distance in the actual line

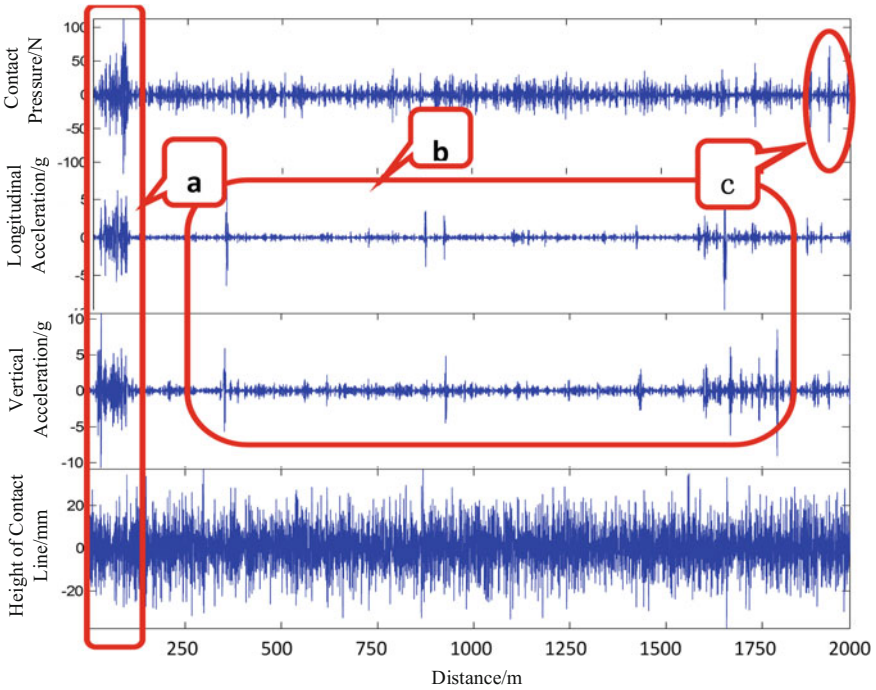

Fig. 2.11 IMF1 components of actual measurement data

2.4.3 IMFs Correlation Characteristics of Pantograph-Catenary Contact Pressure

It is very difficult to directly analyze the characteristics for the measurement data with complex frequency components. Because the frequency and amplitude features of singular components are very different, the singular correlation between multiple data sets is difficult to be directly compared. EEMD is adopted to decompose the data of contact pressure, height of contact line, vertical acceleration, and longitudinal acceleration to obtain their IMFs correlation. The high-frequency IMF component is shown in Fig. 2.11.

In Fig. 2.11, there are three parts where the IMF1 is more than 3σ.

(1) In region "a" of Fig. 2.11, the mutation of contact pressure corresponds to the over-standard of acceleration, but there are no mutations of catenary parameters. The contact pressure in region "a" has important physical meaning and cannot be eliminated using the 3σ criteria.
(2) The other over-standard of acceleration curve, namely region "b" of Fig. 2.11, has not cause the contact pressure over-standard. It can be seen that the impulse

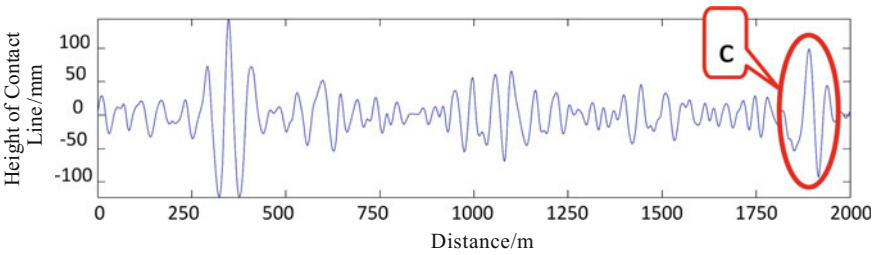

Fig. 2.12 IMF5 component of contact line height

of acceleration may not directly cause the mutation of contact pressure because the influence factors of pantograph-catenary contact pressure are very complex.

(3) The over-standard part of contact pressure, namely region "c" of Fig. 2.11, does not correspond to the variant parts of acceleration or other parameters. For the IMF5 components, it can be found that the over-standard of contact line height occurs in region "c" of Fig. 2.11. Therefore, the mutation of contact pressure in region "c" is caused by the parameter variance of catenary, shown in Fig. 2.12.

The IMF2 components of actual measurement data is shown in Fig. 2.13. There is a new mutation in region "d" of Fig. 2.13, which does not correspond to any over-standard part of acceleration. After the analysis of all IMF components, the consistent over-standard points are not found. Therefore, the mutation in region "d" of Fig. 2.13 can be considered as the error record and eliminated.

2.4.4 *IMFs Correlation Measurement of Pantograph-Catenary Contact Pressure*

1. Pre-processing of detection data

Because of the influence of local fluctuations of data, it is difficult to accurately characterize the correlation between the IMF components of measurement data. Specially, for the pantograph-catenary data with singular mutations, the scope of mutation is small and the mutation degree is high. Therefore, the 3σ criteria are adopted to find the mutation's location and the data singularity mutation ratio (SMR) is defined to describe the mutation degree of measurement data in all channels as follows.

$$SMR(i) = \begin{cases} \dfrac{x(i)}{\sqrt{\frac{1}{N}\sum_{i=1}^{N}\left(x(i)-\frac{1}{N}\sum_{i=1}^{N}x(i)\right)^2}} & , \quad x(i) > 3\sigma \\ 0 & , \quad x(i) \le 3\sigma \end{cases} \tag{2.22}$$

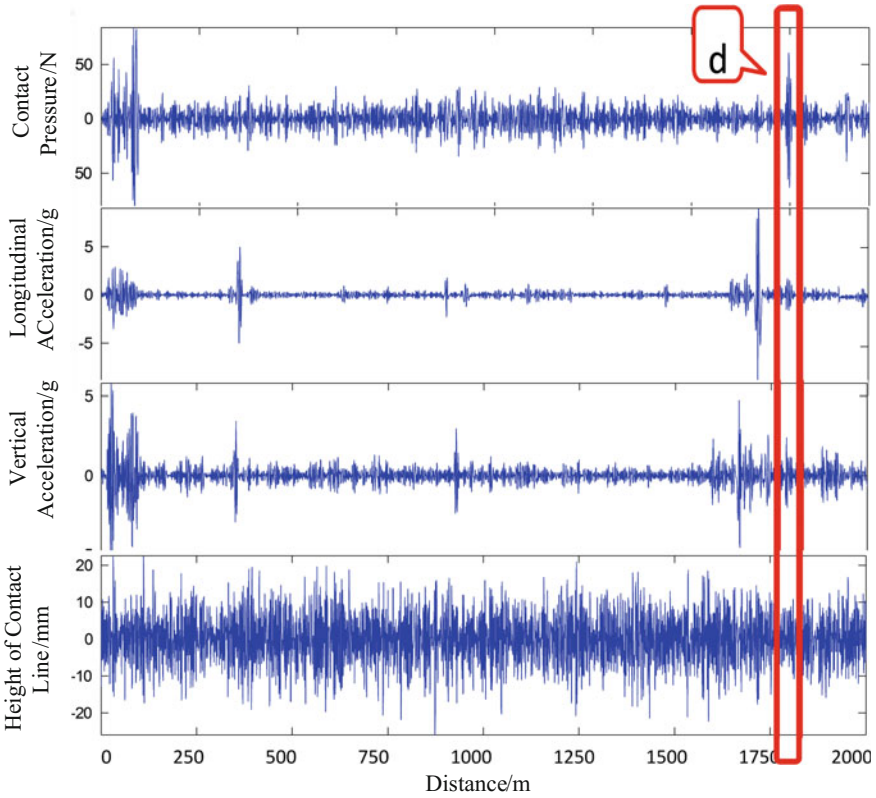

Fig. 2.13 IMF2 component figures of over-standard points

where $x_c(i)$ is the ith value of measurement data, N is the number of measurement data and σ is the standard deviation of detection data.

In Formula (2.22), the ratio of singularity mutation means the times of data value to its standard deviation. This definition can better eliminate the difference between different data absolute value, and quantify the variation of the mutation over-standard part comparing with the normal vibration.

2. Pearson correlation coefficients of local IMF components

The correlation coefficient is commonly adopted to measure the correlation of data, and the Pearson correlation coefficient is the usual method. In order to judge the correlation between the contact pressure mutation points and other measurement data, SMR is adopted to measure the data correlation of over-standard locations and analyze the over-standard point types of contact pressure data.

$$r_{\mathrm{ab}(\mathrm{I}MF_k)}=\frac{\sum_{i=\mathrm{s}}^{\mathrm{e}}\left(SMR_a(i)-\overline{SMR_a(i)}\right)\cdot\sum_{i=\mathrm{s}}^{\mathrm{e}}\left(SMR_{\mathrm{b}}(i)-\overline{SMR_b(i)}\right)}{\sqrt{\sum_{i=\mathrm{s}}^{\mathrm{e}}\left(SMR_a(i)-\overline{SMR_a(i)}\right)^2}\cdot\sqrt{\sum_{i=\mathrm{s}}^{\mathrm{e}}\left(SMR_b(i)-\overline{SMR_b(i)}\right)^2}} \tag{2.23}$$

where $r_{\mathrm{ab}(\mathrm{I}MF_k)}$ means the correlation coefficient between the kth IMF of measurement data series a and b. s and e mean the local window of SMR data with over-standard mutation.

There are 4 types of the correlation coefficients.

(a) The correlation coefficient is 0, which means the data is not relevant with each other.
(b) The absolute value of correlation coefficient is 1, which means the data is complete linear relevant.
(c) The absolute value of correlation coefficient is between 0 and 1, which means the data is relevant with each other.
(d) For the SMR data, there is full zero data in local scope, which will produce the indefinite form of zero over zero. Because there is no over-standard for full zero SMR data, the type means that there is no mutation data with the correlation.

3. Measurement data correlation coefficient matrix

Through calculating the correlation coefficient of all IMF components of measurement data, the correlation coefficient matrix of contact pressure data and other measurement data can be produced. In order to facilitate the analysis of data correlation, only the correlation coefficient between 1 and 0 is preserved, and the correlation coefficient of type c is not considered.

The correlation coefficients of IMF components between the contact pressure data and the measurement data in mutation region are shown in Fig. 2.14. It can be found that in the high frequency range, the mutation of contact pressure is mainly affected by the vertical acceleration, the middle frequency part is mainly affected by the longitudinal acceleration, and the low frequency part has no abnormal mutation points. It can be proved that the mutations are found mainly in the middle and high frequency parts, which are caused by the acceleration shock of pantograph.

In the region "b" of Fig. 2.11, since there are no abnormal mutation points, it is not necessary to calculate the correlation coefficient matrix. Because the region "d" of Fig. 2.11 does not correspond to any mutations of acceleration or parameters, all of correlation coefficients are zero, which shows that the mutations of contact pressure have no correlation with other data and these mutations are the error record outliers.

The SMR curves of mutation points in region "c" of Fig. 2.11 for contact pressure and height data is shown in Fig. 2.15. All correlation coefficients are less than 0.1, which shows there are no obvious correlations. However, the change trend of contact pressure and height is very consistent, and has some time delay correlation. Because the correlation coefficients are very small, it is very difficult to measure the correlations. Therefore, the time delay correlation coefficients are defined as follows.

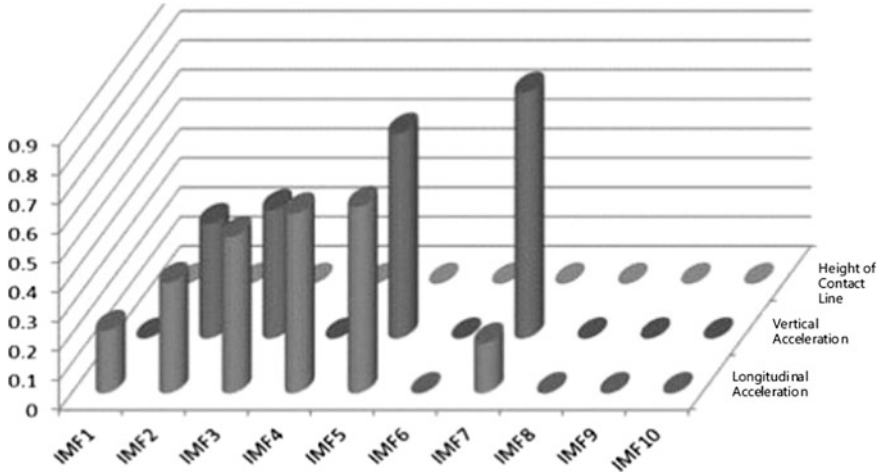

Fig. 2.14 Correlation coefficients in the mutation region "a"

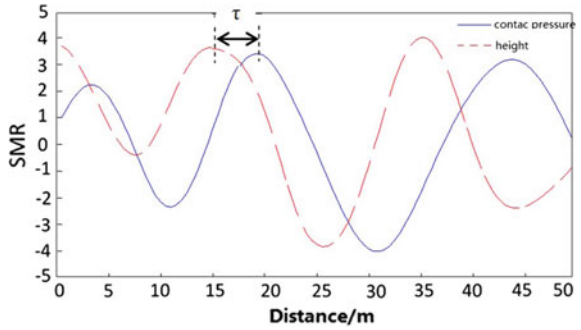

Fig. 2.15 SMR curves of mutation points in region "c" of IMF4

$$r_{\mathrm{ab}(\mathrm{IMF}_k)}(\tau)=\frac{\sum_{i=\mathrm{s}}^{\mathrm{e}}\left(SMR_a(i-\tau)-\overline{SMR_a(i-\tau)}\right)\cdot\sum_{i=\mathrm{s}}^{\mathrm{e}}\left(SMR_{\mathrm{b}}(i)-\overline{SMR_b(i)}\right)}{\sqrt{\sum_{i=\mathrm{s}}^{\mathrm{e}}\left(SMR_a(i-\tau)-\overline{SMR_a(i-\tau)}\right)^2}\cdot\sqrt{\sum_{i=\mathrm{s}}^{\mathrm{e}}\left(SMR_b(i)-\overline{SMR_b(i)}\right)^2}} \tag{2.24}$$

where τ is the time delay variant and its value can be determined by the adjacent peak value distance of SMR data.

The time delay correlation coefficients matrix of IMF components in mutation region "c" are shown in Fig. 2.16. It can be found that the correlations of height in mutation region "c" are very high, which can justify that the mutations in region "c" are caused by the contact line height. The time delay characteristics show that the change of height causes the mutation of contact pressure and the change in time is not consistent. There is some time delay from the parameter change to contact pressure change.

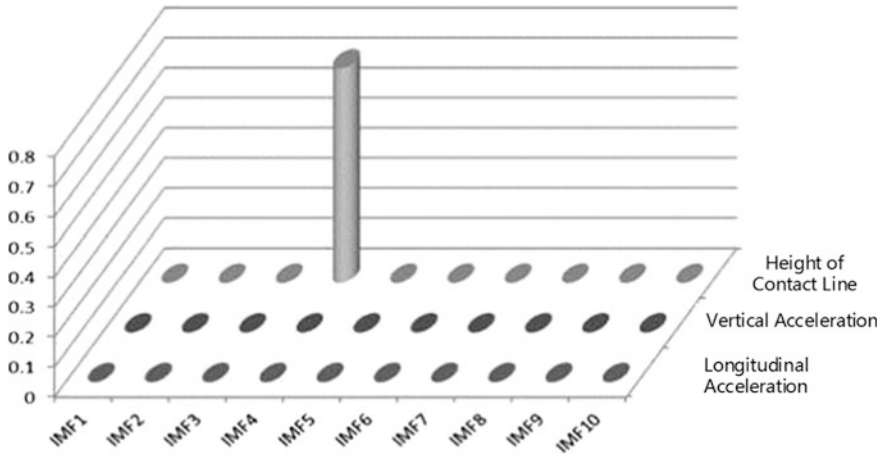

Fig. 2.16 Time delay correlation coefficients matrix in mutation region "c"

2.5 High-Order Statistical Properties of Pantograph-Catenary Contact Pressure

In general, if a signal and a noise obey the Gaussian distribution, their statistical characteristics can be easily described only by using the second-order and first-order statistics. If the distribution of signal is non-Gaussian, the high-order statistics should be adopted. High-order statistics mainly include four kinds, such as high-order moment, high-order cumulant, high-order moment spectrum, and high-order cumulant spectrum. In practical applications, the high-order cumulant of random process is frequently used.

Spectral kurtosis (SK) is a kind of transient signal analysis method, which belongs to the high-order statistics, and can contain all the features of high-order statistics. The power spectrum method cannot effectively detect and extract the transient components of the signal, but SK has a strong ability to characterize the non-stationary components of signal.

Dwyer first introduced spectral kurtosis as a statistical tool, which can indicate not only the non-Gaussian components in a signal, but also their locations in the frequency domain [24]. Vrabie et al. [25] considered that SK means the deviation of some process to Gaussian distribution, and applied SK in the diagnosis of bearing faults. Antoni [26] systematically defined SK and gave the proof about the SK's abilities with the detection of nonstationary and non-Gaussian signals containing the colored noise. Further, he proposed the fast SK computation algorithm and realized its applications in the detection of rolling-element bearing vibrations [27].

2.5.1 Definition and Computation Method of SK

1. Definition of SK

If we consider the Wold-Cramer decomposition of non-stationary signals, we can define signal $Y(t)$ as the response of the system with time varying impulse response $h(t,s)$, excited by a signal $X(t)$. Then, $Y(t)$ can be shown below.

$$Y(t) = \int_{-\infty}^{+\infty} e^{2\pi ft} H(t,f) dH(f) \tag{2.25}$$

where $H(t,f)$ is the time varying transfer function of the considered system and can be interpreted as the complex envelope of the signal $Y(t)$ at frequency f. SK is based on the fourth order spectral cumulant of a conditionally non-stationary process:

$$C_{4Y}(f) = S_{4Y}(f) - 2S_{2Y}^2(f) \tag{2.26}$$

where $S_{2nY}(f)$ is the second order instantaneous moment, which is the measure of the energy of the complex envelope. Thus, SK can be defined as the energy normalized cumulant, which is a measure of the peakiness of the probability density function H:

$$K_Y(f) = \frac{S_{4Y}(f)}{S_{2Y}^2(f)} - 2 \tag{2.27}$$

2. Computation methods of SK [28]

According to the definition of SK, for the computation of SK, STFT (Short Time Fourier Transform) and WT (Wavelet Transform) are generally adopted [26].

(1) Based on STFT

For a given random process $y(u)$, its STFT can be described as follow.

$$Y_w(u,f) = \sum_{-\infty}^{\infty} y(m) w(m-u) e^{-j2\pi mf} \tag{2.28}$$

where $w(m)$ is a window function, and N_w is the window's length. The second order spectral moments of $Y_w(u,f)$ can be defined as follows.

$$\hat{S}_{2n}(f) = \left\langle |Y_w(u,f)|^{2n} \right\rangle_k \tag{2.29}$$

where $\langle\cdot\rangle$ is the mean on the kth order. If $n = 1$ and 2, the SK estimation based on STFT can be computed as follows.

$$\hat{K}_Y(f) = \frac{\hat{S}_{4Y}(f)}{\hat{S}_{2Y}^2(f)} - 2, \quad |f - \mathrm{mod}(1/2)| > N_w^{-1} \tag{2.30}$$

(2) Based on WT

The wavelet transform of signal $x(t)$ is expressed below.

$$W_x(a,b) = \int_{-\infty}^{\infty} x(t)\varphi_{a,b}(t)dt \tag{2.31}$$

where $\varphi_{a,b}(t) = \frac{1}{\sqrt{a}}\varphi\left(\frac{t-b}{a}\right)$ is the sub-wavelet, and a is scale shift factor, b is time shift factor. The SK based WT can be computed with the equation below.

$$K_x(a) = \frac{E\left\langle |W_x(a,b)|^4 \right\rangle}{E\left\langle |W_x(a,b)|^2 \right\rangle} - 2 \tag{2.32}$$

For a given scale a, the wavelet coefficients of signal can be obtained through wavelet transformation, and the SK based WT can be obtained through calculating the kurtosis of wavelet coefficients.

2.5.2 SK of Pantograph-Catenary Contact Pressure

Based on the definition of SK, its value can represent the deviation degree from Gaussian distribution for the signal's frequency components with time. At a certain frequency, higher SK value means more non-uniform distribution of the frequency components with time. All frequency components at some moment consist of the spectrum of signal at the moment. If the SK value of each frequency component is small, the change of each frequency component with time is relatively uniform. That is to say that the nonstationary degree of signal is also small.

Because there are no signals that can satisfy the conditions of the strict definition of signal stationarity in the actual engineering, the signal's stationarity can be determined in a more generalized sense. In this section, SK is adopted to detect the non-stationary components of contact pressure signals. The qualitative judgement of contact pressure signal stationarity can be made. In addition, according to the amount of stationary components of contact pressure signals, the state of contact line irregularity can be evaluated.

The contact pressure signals in two sections of Hukun Line and Jingguang Line and their SK curves based on STFT are shown in Figs. 2.17 and 2.18. It can be found that the SK's value at some frequencies is zero or very small. Based on the stationarity analysis in Sect. 2.2.3, the signals in these sections are stationary. Therefore, SK can efficiently characterize the stationary components in signals. In the SK curves of contact pressure, the SK value is very low for the wavelength components from 1 to 5 m, which can reflect that the contact pressure at two sections is suitable to collect the current.

The contact pressure signals in two sections of Hukun Line and Jingguang Line and their SK curves based on STFT are shown in Figs. 2.19 and 2.20. It can be found that the SK value at some frequencies is high, even more than 20, which means that the contact pressure signals contain many nonstationary components. In Fig. 2.19, the SK's value is very high for the wavelength components from 1 to

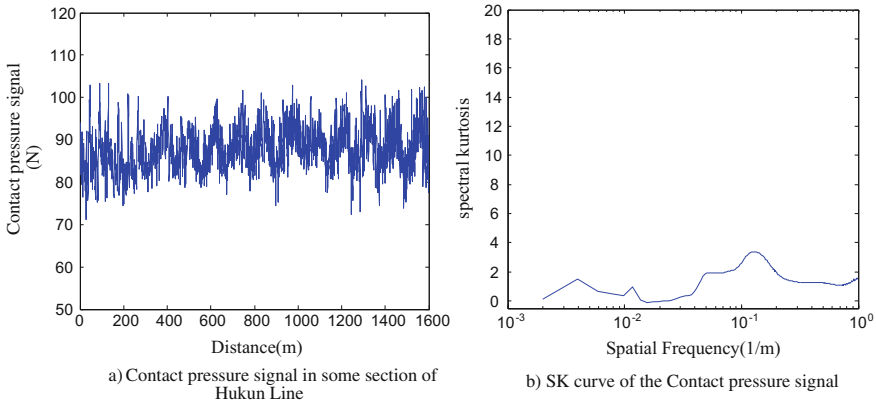

a) Contact pressure signal in some section of Hukun Line

b) SK curve of the Contact pressure signal

Fig. 2.17 Contact pressure signal in a certain section of Hukun Line and its SK curve

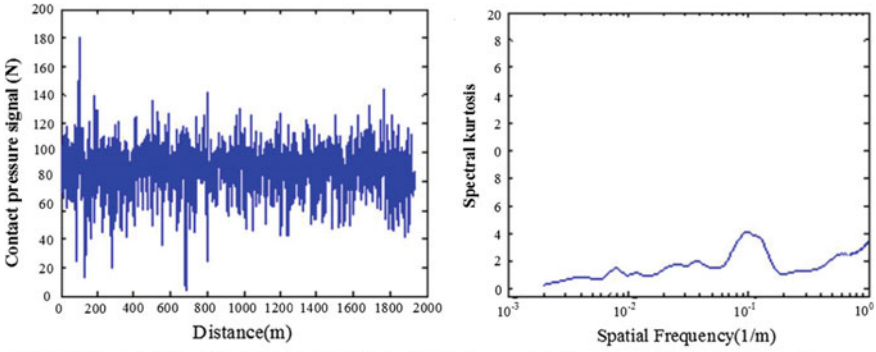

a) Contact pressure signal in some section of Jingguang Line

b) SK curve of Contact pressure signal

Fig. 2.18 Contact pressure signal in a certain section of Jingguang Line and its SK curve

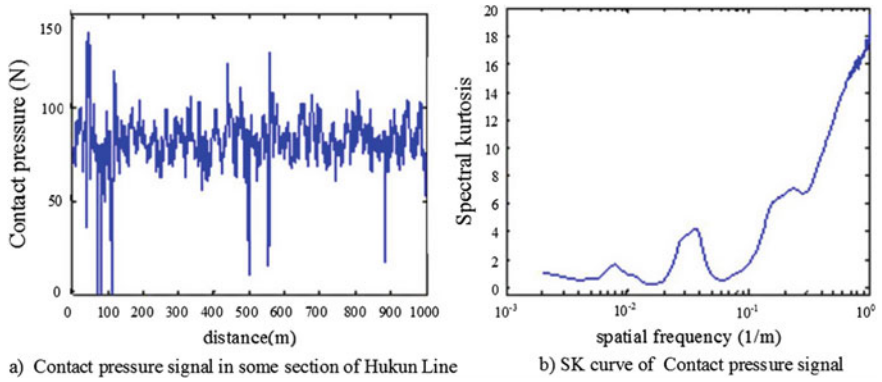

Fig. 2.19 Contact pressure signal in a certain section of Hukun Line and its SK curve

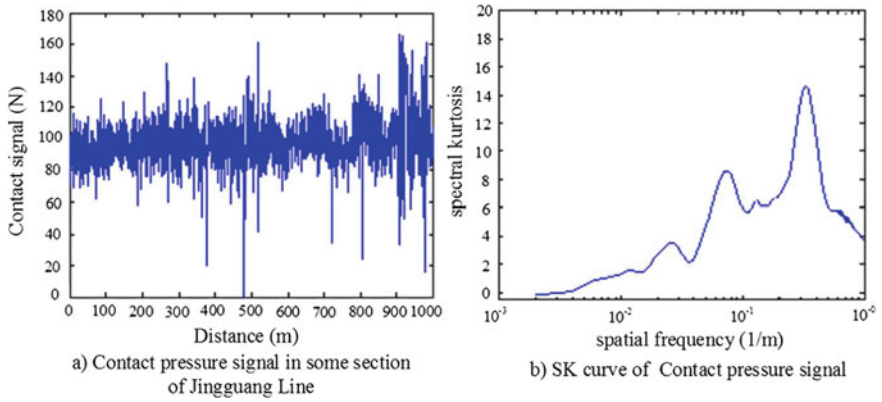

Fig. 2.20 Contact pressure signal in a certain section of Jingguang Line and its SK curve

5 m, which can reflect that the contact pressure in this section is not suitable for the current collection. In Fig. 2.20, the SK value is high for some wavelength components, but the value is low for the wavelength components from 1 to 5 m, which can reflect that the contact pressure at the two sections is suitable to get the current. Therefore, compared with the SK value in Fig. 2.19, the contact pressure at this section is more suitable for the current collection.

2.6 Summary

The simple characteristics of pantograph-catenary contact pressure data are insufficient to analyze their dynamic relationship, and difficult to realize the efficient fault detection and state estimation of catenary. In this chapter, more statistical

characteristics including stationarity, periodicity, correlation, high-order statistical properties of pantograph-catenary contact pressure data are analyzed and discussed in detail. In the first section, the stationarity of pantograph-catenary contact pressure data is discussed, including the stationarity check methods of pantograph-catenary contact pressure data and stationarity analysis of actual pantograph-catenary contact pressure data. In the second section, the periodicity of pantograph-catenary contact pressure data is discussed, including periodic trend feature, trend term extraction and evaluation of pantograph-catenary contact pressure data. In the third section, the correlation of pantograph-catenary contact pressure data is discussed based on EMD, including basic correlation characteristics, IMFs correlation characteristics, IMFs correlation measurement of pantograph-catenary contact pressure data. In the fourth section, the high-order statistical properties of pantograph-catenary contact pressure data is discussed based on SK, including the definition and computation method of SK and the SK of pantograph-catenary contact pressure data.

References

1. Gao Y, Lin JH, Li C (2009) Pretreatment and time-domain analysis of long-wave irregular data of Maglev track. J Comput Appl 29(6):353–355
2. Xiufang C, Shouhua J, Hualiang Z (2008) PSD analysis on track irregularity of railway line for passenger transport. Eng Sci 10(04): 56–59, 83
3. Xiubo L, Wu W (2000) PSD analysis of short wave irregularity on welded joints. China Railw Sci 21(02):26–34
4. Borgant P, Flandrin P (2009) Stationarization via surrogate. J Stat Mech Theory Exp 01:1–13
5. Borgnat P, Flandrin P, Honeine P et al (2010) Testing stationarity with surrogates: a time-frequency approach. IEEE Trans Signal Process 58(7):3459–3470
6. Shuyuan H (2003) Application of time series analysis. Peking University Press, Beijing
7. Schlitzer G (1995) Testing the stationarity of economic time series: further Monte Carlo evidence. Ricerche Econ 49(95):125–144
8. Xiaoxiao Z (2010) The analysis of contact force between the pantograph and contact line in electrified railway via signal processing methods. Southwest Jiaotong University, Chengdu
9. Yi D, Wang Z (1996) Measurement data modeling and parameter estimation. National University of Defense Technology Press, Changsha
10. Kalamkar SS, Banerjee A, Roychowdhury A (2012) Malicious user suppression for cooperative spectrum sensing in cognitive radio networks using Dixon's outlier detection method. In: 2012 national conference on IEEE communications, pp 1–5
11. Pop S, Ciascai I, Pitica D (2010) Statistical analysis of experimental data obtained from the optical pendulum. In: IEEE 16th international symposium for 2010 design and technology in electronic packaging (SIITME), pp 207–210
12. Grubbs FE (1950) Sample criteria for testing outlying observations. Ann Math Stat 21 (1):27–58
13. Angiulli F, Basta S, Pizzuti C (2006) Distance-based detection and prediction of outliers. IEEE Trans Knowl Data Eng 18(2):145–160
14. Li B, Liu X (2010) Study on designed dynamic wheel loads of middle speed and high speed railways in China based on theory of random vibration. J China Railw Soc 32(05):114–118
15. Ma W, Luo S, Song R (2006) Influence of track irregularity on longitudinal vibration of wheelset and correlation performance. J South Jiaotong Univ 03:238–251

16. Xie J (2010) Analysis and power spectrum research on catenary irregularities of electric railway. Southwest Jiaotong University, Chengdu
17. Cho YH, Lee K, Park Y et al (2010) Influence of contact wire pre-sag on the dynamics of pantograph-railway catenary. Int J Mech Sci 52(11):1471–1490
18. Zhai WM, Cai CB (1998) Effect of locomotive vibrations on pantograph-catenary system dynamics. Veh Syst Dyn 29:47–58
19. Huang NE, Shen Z, Long SSR et al (1971) The empirical mode decomposition and Hilbert spectrum for nonlinear and non-stationary time series analysis. Proc R Soc Lond Ser A 1998 (454):903–995
20. Liu Z, Sun W, Zeng J (2014) A new short-term load forecasting method of power system based on EEMD and SS-PSO. Neural Comput Appl 24(3–4):973–983
21. Huang N, Wu M, Long S et al (2003) A confidence limit for the empirical mode decomposition and Hilbert spectral analysis. Proc R Soc Lond A Math Phys Eng Sci 459 (2037):2317–2345
22. Wu Z, Huang N E (2004) A Study of the characteristics of white noise using the empirical mode decomposition method. Proc R Soc Lond A Math Phys Eng Sci 460(2046):1597–1611
23. Bao Y, Xie J (2011) Contrast study on power quality detection using EMD and EEMD. In: 2011 international conference on consumer electronics, communications and networks, pp 2074–2077
24. Dwyer RF (1983) Detection of non-Gaussian signals by frequency domain kurtosis estimation. In: Proceedings of the international conference on acoustics, speech, and signal processing. Boston, MA, USA, pp 607–610
25. Vrabie V, Granjon P, Servière C (2003) Spectral kurtosis: from definition to application. In: Proceedings of the 6th IEEE international workshop on nonlinear signal and image processing. Grado-Trieste, Italy, pp 1–3
26. Antoni J (2006) The spectral kurtosis: a useful tool for characterizing non-stationary signals. Mech Syst Signal Process 20(3):282–307
27. Antoni J (2007) Fast computation of the kurtogram for the detection of transient faults. Mech Syst Signal Process 21(2):108–124
28. Liu Z, Zhang Q (2014) An approach to recognize the transient disturbances with spectral kurtosis. IEEE Trans Instrum Meas 63(1):46–55

Chapter 3
Wave Motion Characteristic of Contact Line Considering Wind

3.1 Introduction

At present, the maximum operation speed of train can be determined by the wave motion velocity of contact line in general, namely the maximum operation speed of train is about the 70 % of wave motion velocity, which is also provided in EN50119 standard [1]. Therefore, it is of great practical significance to determine the wave motion velocity of contact line.

It is believed that when the contact line frequency is low, the contact line can be considered as a string. So, the wave motion velocity can be expressed as the square root of the ratio of tension and line density. When the contact line stiffness is considered, it will lead to the wave propagation of contact line at the high frequency. Thus, the contact line should be considered as the beam, and the contact line stiffness EI and vibration frequency f should be considered. If the contact line is considered as a tensile beam, the wave motion velocity of contact line should be amended.

The tension is one of the most important physical parameters in the catenary suspension system. There are a lot of researches considering its influences on catenary characteristics and pantograph-catenary coupling performance. The influence of messenger wire tension on pantograph-catenary collection current was analyzed in [2]. The relationships between contact wear, wave motion velocity, contact line tension and safe coefficient were discussed, and the contact line tension design for the 350 km/h railway was presented in [3]. The influence factor of curve section on the messenger wire tension was analyzed and the tension difference formula was obtained in [4]. Then the tension of messenger wire was determined during the dropper calculation, which could improve the accuracy of dropper calculation. In [1], the relationship between tension and wave propagation in the catenary suspension system was studied, and it could be considered that if the

Z. Liu, *Detection and Estimation Research of High-speed Railway Catenary*,
Advances in High-speed Rail Technology, DOI 10.1007/978-981-10-2753-6_3

tension was reduced by 1.46 kN, the wave motion velocity would decrease by 18 km/h. As the main factor, the contact line tension was adopted to simulate the catenary, and the influence of tension on the catenary characteristics was analyzed in [5]. Based on the catenary characteristics of high-speed railway, the mechanics model and motion differential equation were constructed in [6].

Although the different forms of wave motion velocity have been studied for the different models of catenary, the formula correction and verification for wave motion velocity in large tension of high-speed railway considering the air damping have not been developed. However, the practical operation experiences show that when the contact line is affected by the environment wind, the wave motion velocity of contact line will change, which seriously affects the current collection of pantograph. Therefore, the wave motion velocity of contact line considering air damping should be amended and verified by the actual data.

3.2 Wave Motion Equation of Catenary

If the catenary suspension can be considered to have certain stiffness, the tensile beam model of contact line can be considered as the study object [7]. For the convenience of study, a small differential segment dx of tensile beam is chosen, as shown in Fig. 3.1. The static stress diagram is shown in Fig. 3.1a, as well as the dynamic stress diagram in Fig. 3.1b. Suppose that the flexural strength of differential segment dx is EI, and the mass of unit length is ρ. The vertical force caused by the lift force of pantograph exerting on the contact line can be described as $P = f(x,t)$. The displacement caused by contact line suspension is $y(x,t)$. The vertical force P and its vertical displacement will change with the time and location. Also, the weight $\rho g \cdot dx$ of differential segment dx should be considered. In addition, the contact line damping f_0 should be considered as the weight $\rho g \cdot dx$ of differential segment dx moves along the vertical direction, which is related to the damping coefficient of contact line structure. In Fig. 3.1b, the shear stress Q at both ends of the differential section forms the bending moment M. The differential segment dx forms the inertial force f_1 during its movement. Based on the principle of force balance, the resultant in the vertical direction should be zero, namely

$$Q + f(x,t)dx - \left(Q + \frac{\partial Q}{\partial x}dx\right) - f_1 \cdot dx - f_0 \cdot dx - \rho g \cdot dx = 0 \tag{3.1}$$

where $f_1 \cdot dx$ represent the transverse inertia force, and its value is equal to the product of mass and accelerator of the differential segment, namely

$$f_1 \cdot dx = \rho \cdot dx \cdot \frac{\partial^2 y(x,t)}{\partial t^2} \tag{3.2}$$

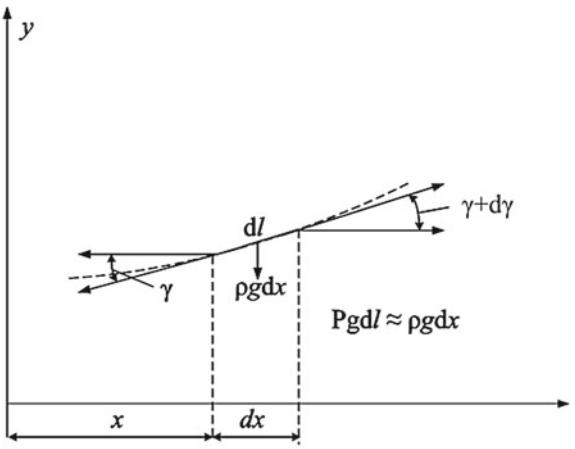

(a) Static stress diagram of contact line

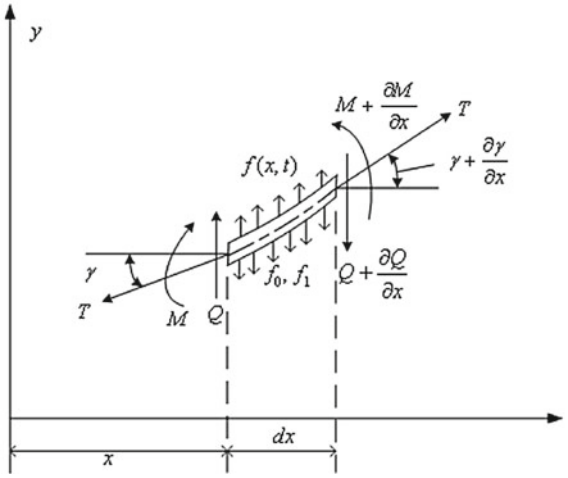

(b) Dynamic stress diagram of contact line

Fig. 3.1 Stress analysis of a differential segment of contact line with the stiffness

Formula (3.1) can be simplified as follows.

$$\frac{\partial Q}{\partial x} = f(x,t) - \rho \frac{\partial^2 y(x,t)}{\partial t^2} - f_0 - \rho g \tag{3.3}$$

In order to study the axial force, the tension and shear force should be mainly considered. Based on Fig. 3.1b, the balance equation can be obtained as follows.

$$M + Q \cdot dx + T\frac{\partial y(x,t)}{\partial x}dx - \left(M + \frac{\partial M}{\partial x} \cdot dx\right) = 0 \tag{3.4}$$

where M is the bending moment, and EI is the bending strength. Their relationship is shown below.

$$M = EI\frac{\partial^2 y(x,t)}{\partial x^2} \tag{3.5}$$

Formula (3.1) can be rearranged as follows.

$$Q = -T\frac{\partial y(x,t)}{\partial x} + \frac{\partial}{\partial x}\left[EI\frac{\partial y^2(x,t)}{\partial x^2}\right] \tag{3.6}$$

Substitute formula (3.6) into formula (3.3), it can be obtained below.

$$\frac{\partial}{\partial x}\left[-T\frac{\partial y(x,t)}{\partial x} + \frac{\partial}{\partial x}\left(EI\frac{\partial^2 y(x,t)}{\partial x^2}\right)\right] = f(x,t) - \rho\frac{\partial^2 y(x,t)}{\partial t^2} - f_0 - \rho g \tag{3.7}$$

where $f_0 = C\frac{\partial y(x,t)}{\partial t}$, and C is the damping coefficient.

$f(x,t)$ can be expressed with Dirac delta function, namely

$$f(x,t) = P_0\delta(x, vt) \tag{3.8}$$

then

$$EI\frac{\partial^4 y(x,t)}{\partial x^4} - T\frac{\partial^2 y(x,t)}{\partial x^2} + \rho\frac{\partial^2 y(x,t)}{\partial t^2} + C\frac{\partial y(x,t)}{\partial t} + \rho g = P_0\delta(x, vt) \tag{3.9}$$

Formula (3.9) is the vibration differential equation with a certain stiffness of contact line. Its corresponding homogeneous equation is shown as follows.

$$EI\frac{\partial^4 y(x,t)}{\partial x^4} - T\frac{\partial^2 y(x,t)}{\partial x^2} + \rho\frac{\partial^2 y(x,t)}{\partial t^2} + C\frac{\partial y(x,t)}{\partial t} = 0 \tag{3.10}$$

In order to solve the equation above, the dimension-reduction method is adopted. Let

$$y(x,t) = \phi(x) \cdot q(t) \tag{3.11}$$

where $\phi(x)$ is only related to x, and $q(t)$ is only related to t. Substitute formula (3.11) into formula (3.10), it can be obtained below.

$$\frac{EI\frac{d^4\phi(x)}{dx^4} - T\frac{d^2\phi(x)}{dx^2}}{\rho\phi(x)} = -\frac{\frac{d^2q(t)}{dt^2} + \frac{C}{\rho}\frac{dq(t)}{dt}}{q(t)} \tag{3.12}$$

The left side of Eq. (3.12) only depends on the spatial variables, and the right side only depends on the time. Thus, it determines that the two sides of the equation should be equal to the same constant only. The constant is denoted as w^2, and w is the circular frequency without damping for the contact line vibration. So, two equations can be obtained as follows.

$$\frac{d^2q(t)}{dt^2} + 2\xi w\frac{dq(t)}{dt} + w^2q(t) = 0 \tag{3.13}$$

$$EI\frac{d^4\phi(x)}{dx^4} - T\frac{d^2\phi(x)}{dx^2} - \rho w^2\phi(x) = 0 \tag{3.14}$$

where $\xi = \frac{C}{2\rho w}$. The solution of Eq. (3.13) is obtained below.

$$q(t) = \mathrm{e}^{-\xi wt}(A_1\cos w_r t + A_2\sin w_r t) = A\mathrm{e}^{-\xi wt}\cos(w_r t + \theta) \tag{3.15}$$

where $w_r = w\sqrt{1-\xi^2}$. Similarly, the solution of Eq. (3.14) is obtained below.

$$\begin{aligned}\phi(x) = {} & B_1\mathrm{e}^{\sqrt{\frac{\sqrt{T^2+4\rho w^2EI}+T}{2EI}}x} + B_2\mathrm{e}^{-\sqrt{\frac{\sqrt{T^2+4\rho w^2EI}+T}{2EI}}x} \\ & + B_3\cos\sqrt{\frac{\sqrt{T^2+4\rho w^2EI}-T}{2EI}}x + B_4\sin\sqrt{\frac{\sqrt{T^2+4\rho w^2EI}-T}{2EI}}x\end{aligned} \tag{3.16}$$

Since the displacement of the fixed hinge support point is zero and its moment is also zero, the parameters in formula (3.16) can be solved, namely $B_1 = 0, B_2 = 0, B_3 = 0$. Formula (3.11) can be rewritten as follows.

$$y(x,t) = A\mathrm{e}^{-\xi wt}\cos(w_r t + \theta)\cdot B_4\sin\sqrt{\frac{\sqrt{T^2+4\rho w^2EI}-T}{2EI}}x \tag{3.17}$$

The triangle function transformation is shown below.

$$\sin\alpha\cos\beta = \frac{1}{2}[\sin(\alpha+\beta) + \sin(\alpha-\beta)] \tag{3.18}$$

Let $\alpha = \sqrt{\frac{\sqrt{T^2+4\rho w^2EI}-T}{2EI}}$, then

$$\begin{aligned} y(x,t) &= A\mathrm{e}^{-\xi wt}\cos(w_r t+\theta)\cdot B_4\sin\alpha x \\ &= AB_4\mathrm{e}^{-\xi wt}\cdot\frac{1}{2}\{\sin[\alpha x+(w_r t+\theta)]+\sin[\alpha x-(w_r t+\theta)]\} \end{aligned} \tag{3.19}$$

According to the general description and calculation formula of plane wave [8], $y(x,t) = F(x-vt)+\phi(x+vt)$, and v is the wave motion velocity, the wave motion velocity of contact line with a certain stiffness can be obtained as follows.

$$v = \frac{w_r}{\alpha} = \frac{w_r}{\sqrt{\frac{\sqrt{T^2+4\rho w^2 EI}-T}{2EI}}} = \frac{w_r}{\sqrt{\sqrt{\left(\frac{T}{2EI}\right)^2+\frac{\rho w^2}{EI}}-\frac{T}{2EI}}} \tag{3.20}$$

where $w_r = w\sqrt{1-\xi^2}$, and $w = 2\pi f$. Then

$$v = \frac{w_r}{\sqrt{\sqrt{\left(\frac{T}{2EI}\right)^2+\frac{\rho w^2}{EI}}-\frac{T}{2EI}}} = \frac{2\pi f\sqrt{1-\xi^2}}{\sqrt{\sqrt{\left(\frac{T}{2EI}\right)^2+\frac{\rho(2\pi f)^2}{EI}}-\frac{T}{2EI}}} \tag{3.21}$$

where $\xi = \frac{C}{2\rho w}$.

When $\xi = 0$

$$v = \frac{2\pi f}{\sqrt{\sqrt{\left(\frac{T}{2EI}\right)^2+\frac{\rho(2\pi f)^2}{EI}}-\frac{T}{2EI}}} \tag{3.22}$$

It can be found in formula (3.22) that the tension is the main factor that determines the wave motion velocity. In addition, the bending strength, line density and frequency are also the influence factors on the wave motion velocity of contact line. Given T = 21 kN and EI = 130 Nm^2, the relationship curve between wave motion velocity and line density can be drawn in Fig. 3.2.

3.3 Wave Motion Velocity of Contact Line Considering Air Damping

In general, the galloping of slender body is a kind of pure bending vibration caused by the airflow. Based on the analysis of contact line wind dance phenomena, it can be found that the wind-induced vibration has a great impact on the dynamic characteristic of contact line. Therefore, the wave motion velocity of contact line should be amended considering the air damping. In view of the quasi steady aerodynamic force, the unsteady flow field around the contact line can ignored. Considering the air damping, for the solution of wave motion velocity of contact

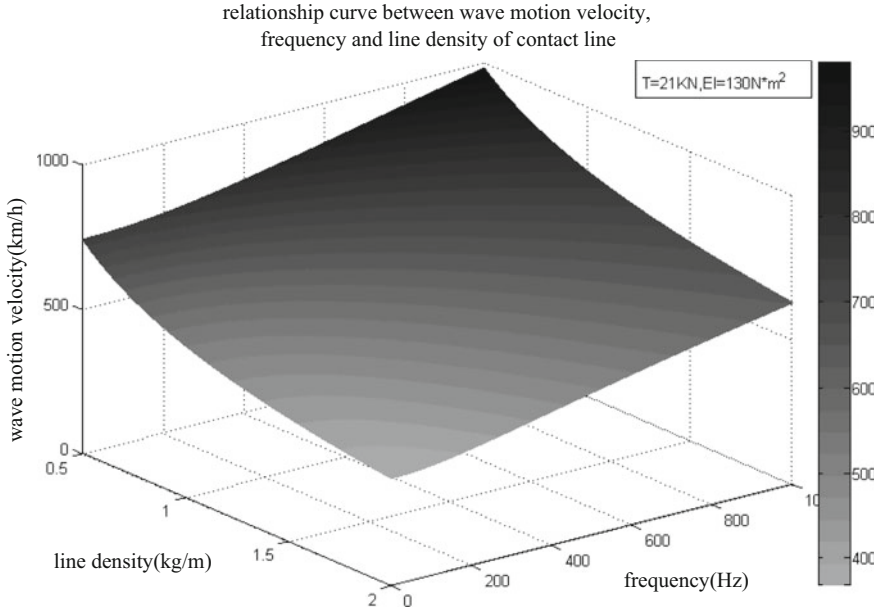

Fig. 3.2 Relationship curve between wave motion velocity, frequency and line density of contact line

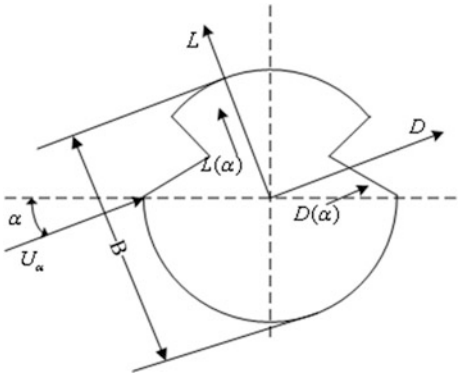

Fig. 3.3 Component diagram of contact line in the wind

line, the effect of wind-induced galloping should be included. The component diagram of contact line in the wind is shown in Fig. 3.3.

Assume that the air uniformly flows through the contact line, the angle of attack is α, speed is U_α, maximum diameter is B, and airflow density is ρ_{air}. In the wind axis coordinate system L–D in Fig. 3.3, the drag $D(\alpha)$ and lift $L(\alpha)$ are respectively computed as follows.

$$\begin{aligned} D(\alpha) &= \frac{1}{2}\rho_{air}U_{\alpha}^2 BC_D(\alpha) \\ L(\alpha) &= \frac{1}{2}\rho_{air}U_{\alpha}^2 BC_L(\alpha) \end{aligned} \tag{3.23}$$

In the vertical direction, their force is shown below.

$$F_y = D(\alpha)\sin\alpha + L(\alpha)\cos\alpha \tag{3.24}$$

Formula (3.24) can be rewritten as follows.

$$F_y = \frac{1}{2}\rho_{air}U^2 BC_{F_y}(\alpha) \tag{3.25}$$

where U is the horizontal component of U_α, and $U = U_\alpha \cos\alpha$. Then,

$$\begin{aligned} F_y &= \frac{1}{2}\rho_{air}U_{\alpha}^2 B(C_D(\alpha)\sin\alpha + C_L\cos\alpha) \\ &= \frac{1}{2}\rho_{air}U^2 B(C_D(\alpha)\sin\alpha + C_L\cos\alpha)\cdot\frac{1}{\cos^2\alpha} = \frac{1}{2}\rho_{air}U^2 B(C_D\tan\alpha + C_L)\sec\alpha \end{aligned} \tag{3.26}$$

Comparing with formula (3.25), it can be obtained as follows.

$$C_{F_y} = (C_L + C_D\tan\alpha)\sec\alpha \tag{3.27}$$

Therefore, when the contact line is stable and the wind speed is U, the angle of attack is zero. When the contact line has a low-amplitude vibration in the direction that is perpendicular to the transverse wind flow, and the vibration velocity is $\dot{y}$, the airflow can be considered to attack the contact line at a relative angle of the wind. The speed and angle of attack of airflow are listed as follows.

$$U_\alpha = \sqrt{U^2 + \dot{y}^2}; \quad \alpha = \arctan\frac{\dot{y}}{U} \tag{3.28}$$

Since the vibration of contact line is very small, $\alpha \approx \frac{\dot{y}}{U} \to 0$.

First order Taylor expansion of F_y at $\alpha = 0$ is shown below.

$$F_y(\alpha) = F_y(0) + \left.\frac{\partial F_y}{\partial\alpha}\right|_{\alpha=0}\cdot\alpha + \Delta(\alpha^2) \tag{3.29}$$

As $F_y(0)$ do not change with time, it can be ignored for the dynamic response analysis. $\Delta(\alpha^2)$ is the remainder of aerodynamic force and its order is the same as that of α^2, so it can also be ignored. Then,

$$F_y(\alpha) \approx \left.\frac{\partial F_y}{\partial \alpha}\right|_{\alpha=0} \cdot \alpha = \frac{1}{2}\rho_{air} U^2 B \cdot \left.\frac{dC_{F_y}}{d\alpha}\right|_{\alpha=0} \cdot \frac{\dot{y}}{U} \tag{3.30}$$

Based on formula (3.27), it can be obtained as follows.

$$\left.\frac{dC_{F_y}}{d\alpha}\right|_{\alpha=0} = \left.\left(\frac{dC_L}{d\alpha} + C_D\right)\right|_{\alpha=0} \tag{3.31}$$

The expression of steady aerodynamic force is obtained as follows.

$$F_y(\alpha) = \frac{1}{2}\rho_{air} U^2 B \left.\left(\frac{dC_L}{d\alpha} + C_D\right)\right|_{\alpha=0} \cdot \frac{\dot{y}}{U} \tag{3.32}$$

Therefore, the vibration differential Eq. (3.9) of contact line with certain stiffness can be amended below.

$$\begin{aligned} &EI\frac{\partial^4 y(x,t)}{\partial x^4} - T\frac{\partial^2 y(x,t)}{\partial x^2} + \rho\frac{\partial^2 y(x,t)}{\partial t^2} + C\frac{\partial y(x,t)}{\partial t} + \rho g \\ &= P_0\delta(x, vt) + \frac{1}{2}\rho_{air} U^2 B \left.\left(\frac{dC_L}{d\alpha} + C_D\right)\right|_{\alpha=0} \cdot \frac{1}{U} \cdot \frac{\partial y(x,t)}{\partial t} \end{aligned} \tag{3.33}$$

It can be found that only the coefficient of first order reciprocal term of y changes in the correction formula. Therefore, the air damping coefficient considering the air damping can be defined as follows.

$$C_{air} = C - \frac{1}{2}\rho_{air} \cdot U \cdot B \left.\left(\frac{dC_L}{d\alpha} + C_D\right)\right|_{\alpha=0} \tag{3.34}$$

Based on the above discussion, it can be found that the air damping mainly influences the system damping in the dynamic equation of contact line. Formula (3.21) can be amended as follows [9].

$$v = \frac{2\pi f\sqrt{1-\xi_{air}^2}}{\sqrt{\sqrt{\left(\frac{T}{2EI}\right)^2 + \frac{\rho(2\pi f)^2}{EI}} - \frac{T}{2EI}}} \tag{3.35}$$

where,

$$\xi_{air} = \frac{C_{air}}{2\rho w} = \frac{C - \frac{1}{2}\rho_{air} \cdot U \cdot B\left(\frac{dC_L}{d\alpha} + C_D\right)\big|_{\alpha=0}}{2\rho w} \tag{3.36}$$

In general, the damping coefficient of contact line itself is very small. Formula (3.36) can be simplified as follows.

$$\xi_{air} = \frac{\rho_{air} \cdot U \cdot B(\frac{dC_L}{d\alpha} + C_D)\big|_{\alpha=0}}{4\rho w} \tag{3.37}$$

It can be found in formula (3.35) that the wave motion velocity of contact line is related to the air damping coefficient besides the tension, bending strength, line density and frequency of contact line. The air damping coefficient is directly related to the galloping force coefficient, namely the airflow density ρ_{air}, the horizontal component of airflow velocity, galloping force coefficient $\left(\frac{dC_L}{d\alpha} + C_D\right)\big|_{\alpha=0}$, maximum diameter B, line density and frequency of contact line. The galloping force coefficient is closely related to the object surface morphology.

If the tension, bending strength, line density, and frequency of contact line in actual high-speed railway are given, the relationship curve between wave motion velocity of contact line and air damping coefficient can be drawn in Fig. 3.4, where T = 21 kN, EI = 130 Nm^2, f = 1 Hz and ρ = 1.082 kg/m.

If the bending strength, line density, and frequency of contact line in actual high-speed railway are given, namely the material parameters of contact line, the relationship curve between wave motion velocity, tension of contact line and air damping coefficient can be drawn in Fig. 3.5, where EI = 130 Nm^2, ρ = 1.082 kg/m, and f = 1 Hz.

From Figs. 3.3 and 3.4, it can be found that if the tension value is given, the wave motion velocity of contact line will become lower with the increasing of air damping coefficient. The higher air damping coefficient means more obviously decreasing of wave motion velocity. If the material parameters of contact line are given, the tension is the main factor that influences the wave motion velocity, and the influence of air damping coefficient is small. With the increase of air damping coefficient, the decreasing trend of wave motion velocity is obvious. Therefore, the requirements of tension and air damping coefficient for a given wave motion

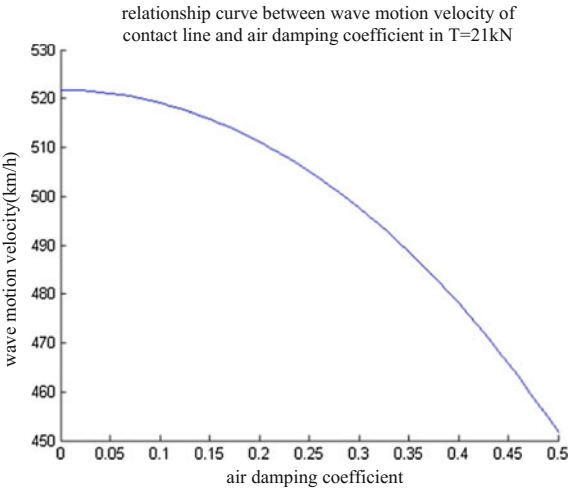

Fig. 3.4 Relationship curve between wave motion velocity of contact line and air damping coefficient

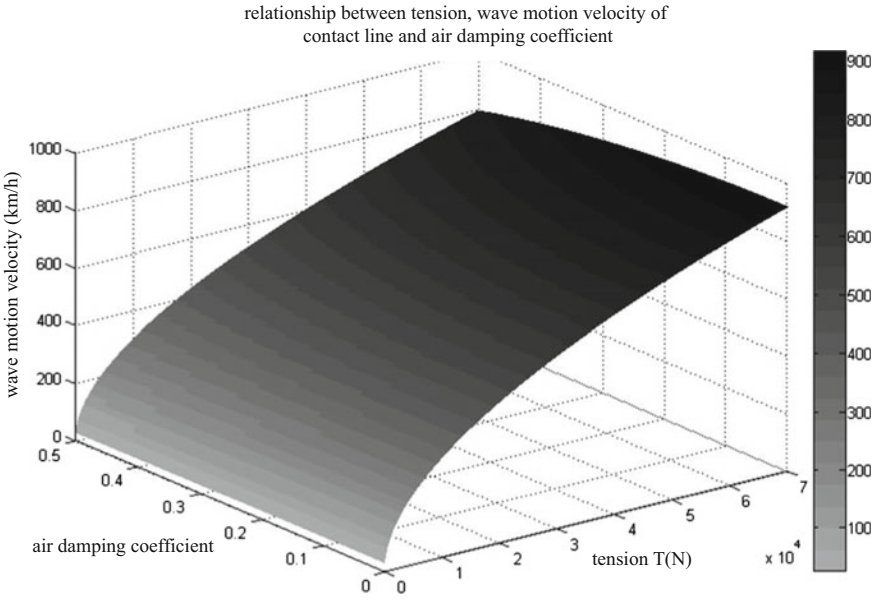

Fig. 3.5 Relationship curve between wave motion velocity, tension of contact line and air damping coefficient

velocity of contact line can be obtained, which is helpful to the catenary design in high-speed railway.

3.4 Static Aerodynamic Parameters of Contact Line

The aerodynamic parameters are the decisive factors that influence Carmen vortex, flutter and galloping of contact line, and they are also the essential parameters to analyze the influence of the aerodynamic force on the dynamic performance of high-speed railway catenary. In order to determine the influence of the wind action on wave motion velocity of contact line, the drag coefficient C_D and the lift coefficient C_L at zero angle of attack must be measured. Therefore, considering the contact line type and shape structural characteristics in China, the static wind tunnel experiment is designed to obtain the precise galloping coefficients.

(1) Wind speed design

In general, the variation law of average wind speed along the height is called the gradient of wind speed. Because of the surface friction of the ground, the closer to the ground, the lower the wind speed will be. Only when the height is beyond 300–500 m, it can be considered that the wind speed is no longer affected by the surface.

According to the common calculation method, the average wind speed along the vertical height can be expressed as follows.

$$U = \left(\frac{Z}{Z_s}\right)^{\alpha} U_s \tag{3.38}$$

where U is the average wind speed, z is the height off ground, z_s is the average wind speed at the standard height (10 m), and U_s is the standard height. α is the roughness coefficient of ground surface, as listed in Table 3.1.

In [7], the standard design of wind speed was suggested to be 26 m/s for the overhead catenary of railway lines with the operation speed above 200 km/h in German. In the experiments, the measurements are carried out when the wind speed is 16, 20 and 26 m/s, respectively.

(2) Wind tunnel test of static force section model

The three component force coefficients of static force are the dimensionless coefficients that can characterize the force of various structure cross sections under average wind. They reflect the steady aerodynamic force of wind acting on the contact line.

The purpose of the experiment is to measure the three component force coefficients at different angles of attack through the wind tunnel test of static force section model of contact line. The experimental results can provide the computational parameters for the static wind response, vibration response, static wind stability and engineering design of contact line. The experiment is mainly for the measurement of static aerodynamic parameters of typical contact line in China high-speed railway.

The contact line type CTMH150 and CTMH120 are selected as the simulation objects according to the China Standard "TB/T2809-2005 Copper and Copper Alloy Contact Wire for Electrified Railway". The cross section of contact line has dovetail groove and multiple fillets, as shown in Fig. 3.6.

The wooden models of the contact line with 5:1 and 10:1 ratio to the actual contact line are made respectively [10], as shown in Fig. 3.7. The two kinds of contact lines are widely adopted in China high-speed railway, such as Hada Line, Jinghu Line, Wuguang Line and so on. In order to control the mass and mass moment of the model, and to ensure that the model itself has enough rigidity, the model adopts high quality wood material. The end of model section is directly mounted on the balance of three component force test. In order to ensure the

Table 3.1 Roughness coefficients of different surroundings

	Sea surface	Open plain	Forest and street	City center
α	0.125–0.100	0.167–0.125	0.250	0.333
$1/\alpha$	8–10	6–8	4	3

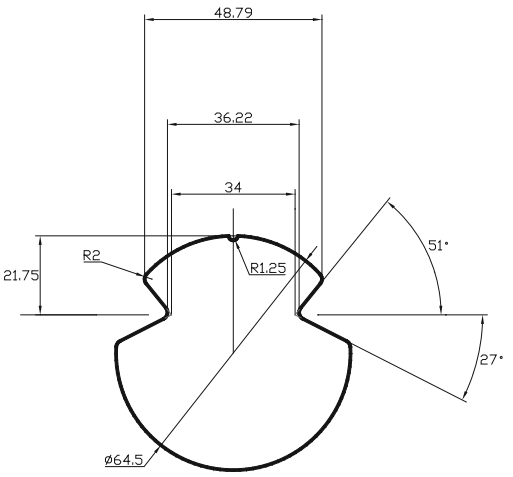

(a) Dimension of CTMH120 type contact line model

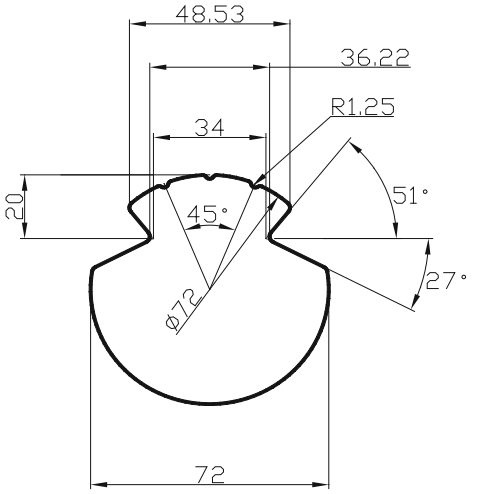

(b) Dimension of CTMH150 type contact line model

Fig. 3.6 Cross section dimensions of the contact lines

two-dimensional flow of airflow, both ends of model are fixed in the end plates, and the test support is laid on the outer wall, for avoiding the interference of airflow field.

The experiment is carried out in the second section of industrial wind tunnel (XNJD-1) with single return pipeline in Southwest Jiaotong University. The cross section area of tunnel is 2.4 m (width) × 2.0 m (height), the maximum speed of airflow is 45 m/s and the minimum speed of airflow is 0.5 m/s.

Fig. 3.7 Contact line model photos

The side support and force balance system for the three component force test of model are provided in the test section. The range of attitude angle α namely the attack angle of airflow is from −20° to +20°, and the minimum rotation interval is 0.1°. The loads of three component force strain gage balance for the static force measurement are the drag force $F_D = 50$ kgf, lift force $F_L = 120$ kgf and pitching moment $M_Z = 12$ kgf m. The test wind speed is from 5 to 30 m/s. The test angle of attack is $\alpha = -12^\circ$ to $+12^\circ$, and $\Delta\alpha = 1^\circ$. The test instrument is shown in Figs. 3.8 and 3.9.

According to the different coordinate system of the static three component force of contact line, there are two kinds of representation methods, namely the body axis coordinate system (coordinates along the centroid coordinates of cross section) and the wind axis system (coordinates along the wind direction). The static wind axis coordinates of three component coefficients are defined as follows.

Drag coefficient: $C_D(\alpha) = \frac{F_D(\alpha)}{\frac{1}{2}\rho U^2 BL}$.

Lift coefficient: $C_L(\alpha) = \frac{F_L(\alpha)}{\frac{1}{2}\rho U^2 BL}$.

Fig. 3.8 Test device for contact line static coefficients measurement

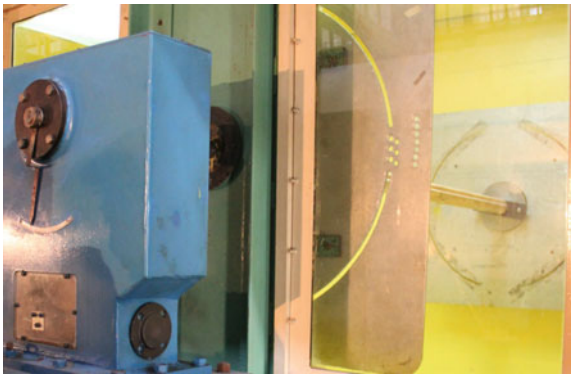

Fig. 3.9 Wind angle of attack regulator for contact line model

Moment coefficient: $C_M(\alpha) = \frac{M_Z(\alpha)}{\frac{1}{2}\rho U^2 B^2 L}$.

where α is the attack angle of airflow, $0.5\beta U^2$ is the airflow dynamic pressure, B is the diameter of model section and L is the model length. $F_D(\alpha)$, $F_L(\alpha)$ and $M_Z(\alpha)$ are the drag, lift and moment in the wind coordinates at attack angle α, respectively.

(3) Test results of wind tunnel

a. Test results of drag coefficient of contact line
The drag coefficient curves of different contact line models at 20 m/s wind speed are shown in Fig. 3.10. It can be found that the drag coefficients range from 1 to 1.2, which are close to the results in [7]. The drag coefficient curves of same contact line models at different wind speeds are shown in Fig. 3.11. It can be found that the drag coefficient decreases slightly with the increase of wind speed. It gradually decreases with the increase of Reynolds

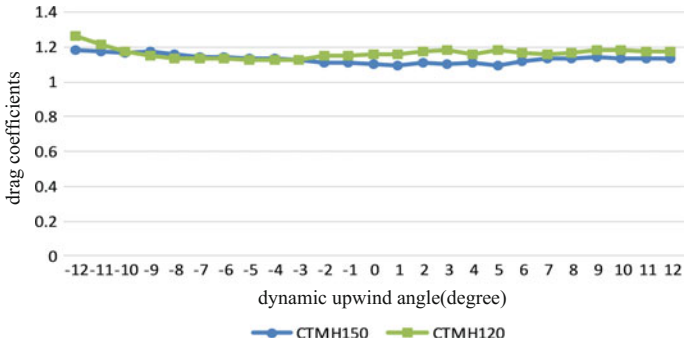

Fig. 3.10 Drag coefficients of different models at the same wind speed

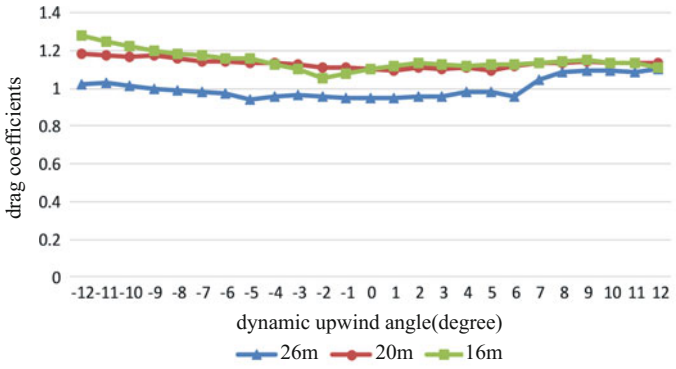

(a) Drag coefficients of CTMH150 at the different wind speeds

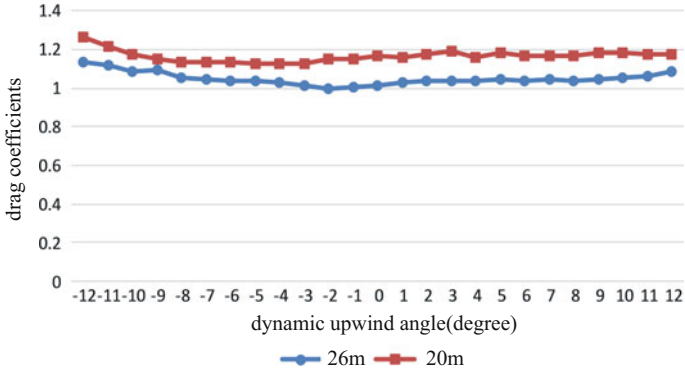

(b) Drag coefficients of CTMH120 at different wind speeds

Fig. 3.11 Drag coefficients of the same model at the different wind speeds

number, which is similar to the drag coefficient of cylinder. The value of drag coefficient is near 1.1–1.2 in general.

b. Test results of lift coefficient of contact line

The lift coefficient curves of different contact line models at 20 m/s wind speed are shown in Fig. 3.12. It can be found that though the lift coefficients are different for different contact line models, their overall trends are consistent. The lift coefficient curves of same contact line models at different wind speeds are shown in Fig. 3.13. It can be found that the lift coefficient decreases with the increase of wind speed, and the trend is consistent when the angle of attack is zero.

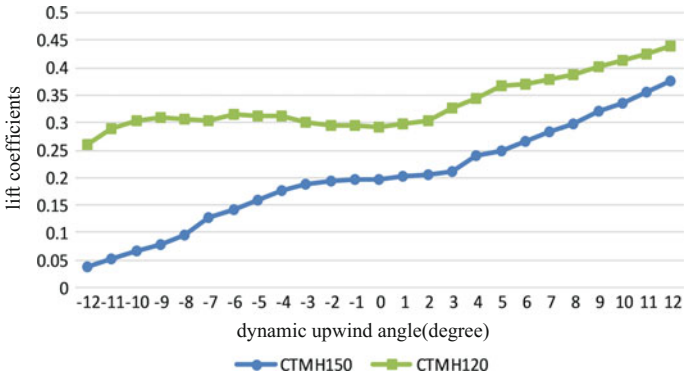

Fig. 3.12 Lift coefficients of different models at the same wind speed

3.5 Modification of Dynamic Equations of Pantograph-Catenary System Considering Air Damping

For the pantograph-catenary interaction analysis, the numerical solution of the coupled dynamic model is a common method, which is constructed based on the second Lagrange equation. In order to improve the simulation accuracy, the equation should be modified considering the air damping.

In general, the displacements of contact line and messenger wire are assumed as follows.

$$\begin{cases} y_A(x,t) = \sum\limits_m A_m(t) \sin\frac{m\pi x}{L} \\ y_B(x,t) = \sum\limits_m B_m(t) \sin\frac{m\pi x}{L} \end{cases} \tag{3.39}$$

where A is the amplitude of messenger wire, B is amplitude of contact line, and L is the length of anchor section. Suppose A and B are the generalized coordinates. When the influence of aerodynamic force is not considered, the kinetic energy T of catenary can be expressed as follows.

$$\begin{aligned} T = {} & \text{Contact line kinetic energy } T_B + \text{Messenger kinetic energy } T_A \\ & + \text{Dropper kinetic energy } T_D + \text{Support bar } T_{S1} + \text{Locator kinetic energy } T_{S2} \end{aligned}$$

The potential energy V of catenary is expressed as follows.

$$\begin{aligned} V = {} & \text{Catenary tensile potential energy } V_{AB} + \text{Catenary bend potential energy } V_W \\ & + \text{Dropper elastic potential energy } V_D + \text{Support bar elastic potential energy} V_{S1} \\ & + \text{Pantograph} - \text{catenary elastic potential energy } V_K \end{aligned}$$

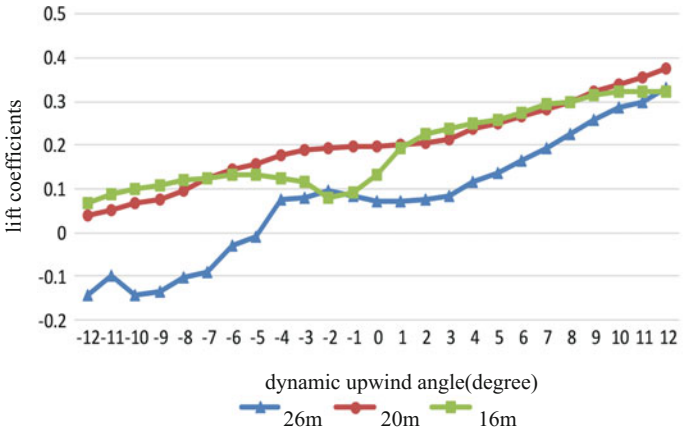

(a) Lift coefficients of CTMH150 at the different wind speeds

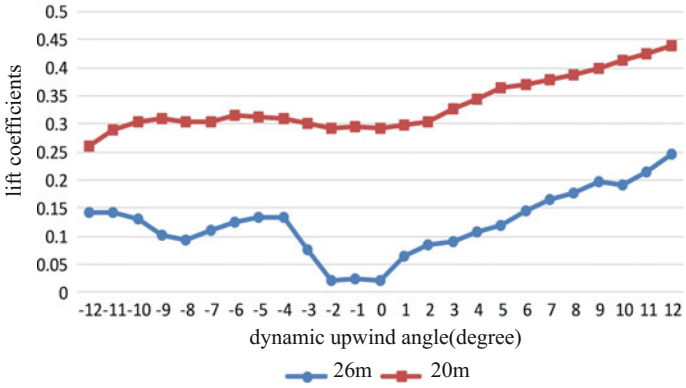

(b) Lift coefficients of CTMH120 at the different wind speeds

Fig. 3.13 Lift coefficients of the same model at different wind speeds

Substitute T and V into the second Lagrange equation, it can be obtained

$$\begin{cases} \frac{d}{dt}\left(\frac{\partial(T-V)}{\partial \dot{A}_m}\right) - \frac{\partial(T-V)}{\partial A_m} = 0 \\ \frac{d}{dt}\left(\frac{\partial(T-V)}{\partial \dot{B}_m}\right) - \frac{\partial(T-V)}{\partial B_m} = 0 \end{cases} \tag{3.40}$$

Then,

$$\begin{cases} \dfrac{\rho_A L}{2}\ddot{A}_n + \sum\limits_{m}^{\infty}\ddot{A}_m\left(\sum\limits_{r=1}^{p}M_{Dr}\sin\dfrac{m\pi x_r}{L}\sin\dfrac{n\pi x_r}{L}+\sum\limits_{r=1}^{q}M_{S1r}\sin\dfrac{m\pi x_r}{L}\sin\dfrac{n\pi x_r}{L}\right) \\ \quad+\left[\dfrac{EI_A}{2L^3}(n\pi)^4+\dfrac{S_A}{2L}(n\pi)^2\right]A_n+\sum\limits_{m}^{\infty}A_m\left(\sum\limits_{r=1}^{p}K_{Dr}\sin\dfrac{m\pi x_r}{L}\sin\dfrac{n\pi x_r}{L}\right. \\ \quad\left.+\sum\limits_{r=1}^{q}K_{S1r}\sin\dfrac{m\pi x_r}{L}\sin\dfrac{n\pi x_r}{L}\right)-\sum\limits_{m=1}^{\infty}B_m\sum\limits_{r=1}^{p}K_{Dr}\sin\dfrac{m\pi x_r}{L}\sin\dfrac{n\pi x_r}{L}=0 \\ \dfrac{\rho_B L}{2}\ddot{B}_n+\sum\limits_{m=1}^{\infty}\ddot{B}_m\left(\sum\limits_{r=1}^{p}M_{Dr}\sin\dfrac{m\pi x_r}{L}\sin\dfrac{n\pi x_r}{L}+\sum\limits_{r=1}^{q}M_{S2r}\sin\dfrac{m\pi x_r}{L}\sin\dfrac{n\pi x_r}{L}\right) \\ \quad+\left[\dfrac{EI_B}{2L^3}(n\pi)^4+\dfrac{S_B}{2L}(n\pi)^2\right]B_n+\sum\limits_{m=1}^{\infty}B_m\sum\limits_{r=1}^{p}K_{Dr}\sin\dfrac{m\pi x_r}{L}\sin\dfrac{n\pi x_r}{L} \\ \quad-\sum\limits_{m=1}^{\infty}A_m\sum\limits_{r=1}^{p}K_{Dr}\sin\dfrac{m\pi x_r}{L}\sin\dfrac{n\pi x_r}{L}+\sum\limits_{m=1}^{\infty}B_m K_S\sin\dfrac{m\pi x_c}{L}\sin\dfrac{n\pi x_c}{L} \\ \quad-y_1 K_S\sin\dfrac{n\pi x_c}{L}=0 \end{cases} \tag{3.41}$$

where ρ_A is the unit length density of messenger wire, ρ_B is the unit length density of contact line, M_D is the mass of dropper, M_{S1} is the mass of support bar, M_{S2} is the mass of locator, E_{IA} is the anti-bending stiffness of messenger wire, E_{IB} is the anti-bending stiffness of contact line, S_B is the tension of contact line, K_D is the stiffness of dropper, K_{S1} is the stiffness of support bar, and K_S is the contact stiffness between pantograph and catenary.

When the influence of aerodynamic force on the catenary is studied, the influence of aerodynamic damping should be considered. Suppose that the damping in a differential section of contact line and messenger wire is C_B and C_A, respectively. Based on the Lagrange equation, the generalized force produced by the damping for the contact line and messenger wire with L length is shown as follows.

$$\begin{cases} Q_A = -\frac{1}{2}\int\limits_0^L c_A\dot{y}_A\,dx = -\frac{1}{2}c_A L\sum\limits_m\dot{A}_m \\ Q_B = -\frac{1}{2}\int\limits_0^L c_B\dot{y}_B\,dx = -\frac{1}{2}c_B L\sum\limits_m\dot{B}_m \end{cases} \tag{3.42}$$

The above formula is substituted into the Lagrange equation, namely

$$\begin{cases} \frac{d}{dt}\left(\frac{\partial(T-V)}{\partial \dot{A}_m}\right) - \frac{\partial(T-V)}{\partial A_m} = Q_A \\ \frac{d}{dt}\left(\frac{\partial(T-V)}{\partial \dot{B}_m}\right) - \frac{\partial(T-V)}{\partial B_m} = Q_B \end{cases} \tag{3.43}$$

The dynamic equation of pantograph-catenary interaction can be rewritten below [11].

$$\begin{cases} \frac{\rho_A L}{2}\ddot{A}_n + \sum_m^{\infty}\ddot{A}_m(\sum_{r=1}^{p} M_{Dr}\sin\frac{m\pi x_r}{L}\sin\frac{n\pi x_r}{L} + \sum_{r=1}^{q} M_{S1r}\sin\frac{m\pi x_r}{L}\sin\frac{n\pi x_r}{L}) \\ + \frac{c_A L}{2}\dot{A}_n + \left[\frac{EI_A}{2L^3}(n\pi)^4 + \frac{S_A}{2L}(n\pi)^2\right]A_n + \sum_m^{\infty}A_m(\sum_{r=1}^{p} K_{Dr}\sin\frac{m\pi x_r}{L}\sin\frac{n\pi x_r}{L} + \\ \sum_{r=1}^{q} K_{S1r}\sin\frac{m\pi x_r}{L}\sin\frac{n\pi x_r}{L}) - \sum_{m=1}^{\infty} B_m\sum_{r=1}^{p} K_{Dr}\sin\frac{m\pi x_r}{L}\sin\frac{n\pi x_r}{L} = 0 \\ \frac{\rho_B L}{2}\ddot{B}_n + \sum_{m=1}^{\infty}\ddot{B}_m(\sum_{r=1}^{p} M_{Dr}\sin\frac{m\pi x_r}{L}\sin\frac{n\pi x_r}{L} + \sum_{r=1}^{q} M_{S2r}\sin\frac{m\pi x_r}{L}\sin\frac{n\pi x_r}{L}) \\ + \frac{c_B L}{2}\dot{B}_n + \left[\frac{EI_B}{2L^3}(n\pi)^4 + \frac{S_B}{2L}(n\pi)^2\right]B_n + \sum_{m=1}^{\infty} B_m\sum_{r=1}^{p} K_{Dr}\sin\frac{m\pi x_r}{L}\sin\frac{n\pi x_r}{L} \\ - \sum_{m=1}^{\infty} A_m\sum_{r=1}^{p} K_{Dr}\sin\frac{m\pi x_r}{L}\sin\frac{n\pi x_r}{L} + \sum_{m=1}^{\infty} B_m K_S\sin\frac{m\pi x_c}{L}\sin\frac{n\pi x_c}{L} - y_1 K_S\sin\frac{n\pi x_c}{L} = 0 \end{cases} \tag{3.44}$$

In general, the coupling dynamic equation can be expressed using the matrix form, namely

$$M\ddot{Y} + C\dot{Y} + KY = F \tag{3.45}$$

Comparing Eqs. (3.41) with (3.44), it can be found that if the aerodynamics is not considered, the terms related to catenary in damping matrix C are all zero. If the aerodynamics is considered, the terms related to catenary in damping matrix C becomes $cL/2$. c is expressed below.

$$c = \frac{1}{2}\rho_{air}\cdot U\cdot B\left(\frac{dC_L}{d\alpha} + C_D\right)\Big|_{\alpha=0} \tag{3.46}$$

3.6 Summary

The wave motion characteristic of contact line is one of most important factors that influence the dynamic characteristics of pantograph-catenary. In the high-speed operation of train, the aerodynamics also directly influences the dynamic characteristics of pantograph-catenary interaction. In this chapter, at first, the wave motion equation of catenary is presented, and the wave motion velocity of contact line is

deduced. Second, the wave motion velocity of contact line considering air damping is deduced in detail and the influence factors are discussed. Third, the static aerodynamic parameters of contact line are analyzed. The test experiment of static aerodynamic parameters of contact line is designed and carried out in the wind tunnel. The drag and lift coefficients of contact line are obtained through the wind tunnel experiment. In the end, the dynamic equations of pantograph-catenary interaction considering air damping are modified and discussed.

References

1. Railway Research Institute (Japan) (2010) Catenary and pantograph characteristics. Railway Science Press, Beijing, China
2. Wang JJ, Tian ZJ, Li HJ, Mei GM (2005) Study of the influence of current-receiving quality between pantograph and O CS from tensile force acting on catenary wire. J China Railway Soc 27(1):114–118
3. Pan Y, Ming Q (2005) The catenary tension plan of high-speed railway. In: The symposium of 20,000 kilometers of electric railway in China
4. Liu CL, Huang H (2009) Force of wires and ropes in curve section. Electr Railway 6:27–29
5. Kim WM, Kim JT, Kim JS, Lee JW (2003) A numerical study on dynamic characteristics of a catenary. J Mech Sci Technol 17(6):860–869
6. Fengliang L, Qian S (1996) The dynamic model and differential equations of the catenary. J Changsha Railway Univ 14(2):90–93
7. Bling K, Schmieder P et al (2004) Electrified railway catenary. China Electric Power Press, Beijing
8. Fang T, Xue P (2010) Vibration theory and application. Northwestern Polytechnical University press, Xi'an
9. Liu ZG, Liu YC, Han ZW et al (2013) Modified formula of wave motion velocity of catenary inclusive of air damping. J China Railway Soc 35(1):41–45
10. Liu YC, Liu ZG, Song Y et al (2014) Simulation calculation and wind tunnel test of static aerodynamic parameters of high-speed railway contact line. J China Railway Soc 36(5):33–38
11. Han ZW (2013) The dynamic characteristics assessment of high speed catenary-pantograph based on modern spectrum analysis and intelligent fault image identification. Southwest Jiaotong University Ph.D Dissertation, Chengdu

Chapter 4
Geometry Parameters Detection of Catenary Based on Image Processing

4.1 Introduction

The dynamic detection of stagger and height of contact line mainly includes contact and non-contact methods. For the contact detection, the sensors of contact pressure and accelerator are mounted in the pantograph. For the non-contact detection, CCD (Charge-coupled Device) camera is mounted on the roof of train, and used to take the dynamic images. By using image processing methods, the stagger and height of contact line can be detected. Comparing with the contact detection, the non-contact detection system that can be away from the electromagnetic interference and have high detection accuracy, simple structure and low cost, is favored by the maintenance and construction company. Because the detection efficiency of traditional non-contact detection methods is low, the target identification is difficult, and the accuracy is relatively low at present, it cannot meet the requirements of high-speed detection in electric railway. In this chapter, some new detection methods of stagger and height of contact line are discussed based on image processing.

4.2 Non-Contact Detection for the Height and Stagger of Contact Line

In this section, a non-contact detection method for the height and stagger of contact line is presented in detail. First, the image of the CCD camera is pre-processed. Second, the center points from the image can be located by the iterative threshold method. Third, the feature points on the 2D plane and the 3D space coordinates of the camera are established. The detection plan for the height and stagger of contact line is shown in Fig. 4.1 [1].

Z. Liu, *Detection and Estimation Research of High-speed Railway Catenary*,
Advances in High-speed Rail Technology, DOI 10.1007/978-981-10-2753-6_4

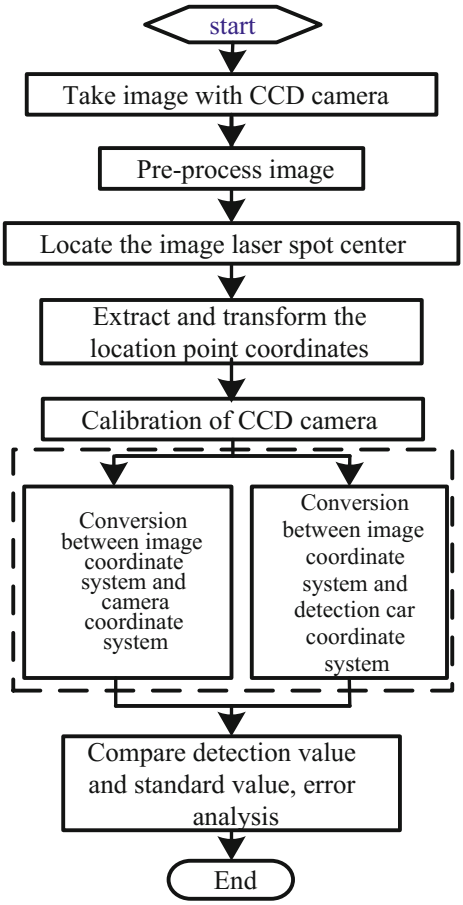

Fig. 4.1 Schematic diagram of non-contact detection for the height and stagger of contact line

4.2.1 Field Image Acquisition of Contact Line

The structure of detection vehicle for geometry parameters of contact line is shown in Fig. 4.2.

In the process of the detection vehicle along the track, the laser beam is illuminated on the contact line and the bright spot is formed. The CCD camera located at the rear of detect vehicle can capture images in a certain time interval. With the change of space locations of contact line, the laser spot in the image will have the corresponding variation. Through locating the laser spot's position, the height and stagger of contact line can be calculated. Regardless of the change of track' surface height, the distance from the spot to the bottom of image can reflect the height of contact line, and the distance deviating from the center of image can reflect the change of contact line stagger.

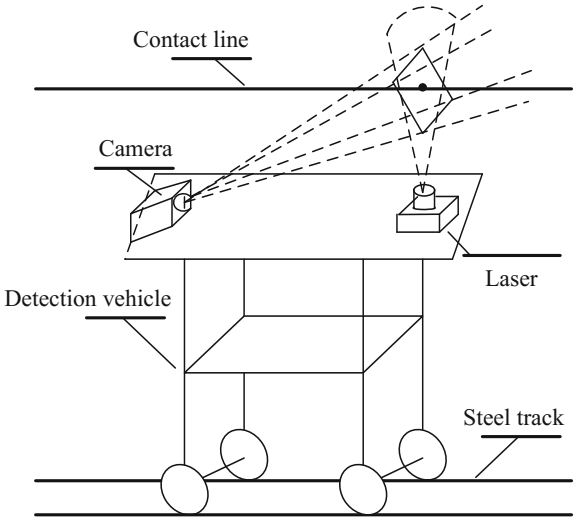

Fig. 4.2 Structure of detection vehicle for geometry parameters of contact line

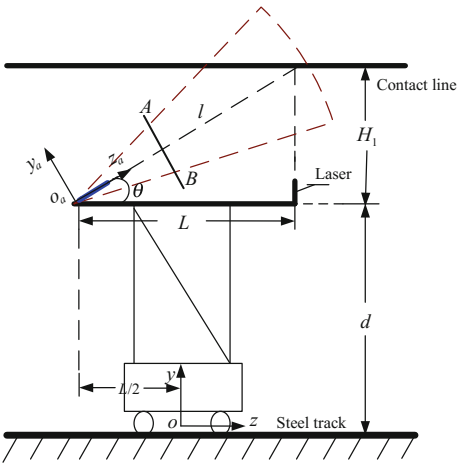

Fig. 4.3 Parameters of detection vehicle

The detection vehicle parameters are marked in Fig. 4.3. The principal optic axis of camera is the straight line l, the horizontal interval distance between laser and camera is L, the plane of image is AB, the interval distance between the beam of

detection vehicle and contact line is H_1, and the vertical distance between the beam of detection vehicle and the center line of steel track is d.

4.2.2 Pinhole Model Calibration of CCD Camera

The models of CCD camera calibration have the linear and non-linear ones [2]. The linear model is the pinhole model. In this section, the pinhole model is adopted. The world coordinate system, camera coordinate system and computer coordinate system are defined in Fig. 4.3. For the world coordinate system, the origin of world coordinates is located in the weight center of detection vehicle. The x axis is perpendicular to the surface of the paper, the y axis is perpendicular to the track plane, and the z axis is along the track. For the camera coordinate system, the origin of camera coordinates is o_a. The direction of z_a is consistent to the camera axis direction. y_a is perpendicular to z_a. x_a is perpendicular to the surface of the paper and is consistent to the coordinates of detect vehicle. In Fig. 4.3, the image plane is AB, which is perpendicular to the optical axis and the length from o_a is f, namely the focal length of camera.

1. Correspondence between world coordinates, camera coordinates and image coordinates [3–5]

If the camera coordinates are rotated clockwise by θ, the y axis of rotated coordinates is moved by $-d$, and z axis is moved by $L/2$, it will become the world coordinates. The rotation transform matrix is shown below.

$$M_1 = Rot(x, \theta) = \begin{bmatrix} 1 & 0 & 0 & 0 \\ 0 & \cos\theta & -\sin\theta & 0 \\ 0 & \sin\theta & \cos\theta & 0 \\ 0 & 0 & 0 & 1 \end{bmatrix} \tag{4.1}$$

The translation transform matrix is shown below.

$$M_2 = Trans(0, -d, d_1) = \begin{bmatrix} 1 & 0 & 0 & 0 \\ 0 & 1 & 0 & -d \\ 0 & 0 & 1 & L/2 \\ 0 & 0 & 0 & 1 \end{bmatrix} \tag{4.2}$$

Therefore, the correspondence between point (x_r, y_r, z_r) in the world coordinates, and point (x_c, y_c, z_c) in the camera coordinates is obtained as follows.

$$\begin{aligned}\begin{bmatrix} x_c \\ y_c \\ z_c \\ 1 \end{bmatrix} &= M_1 \cdot M_2 \begin{bmatrix} x_r \\ y_r \\ z_r \\ 1 \end{bmatrix} = Rot(x,\theta)Trans(0,-d,d_1)\begin{bmatrix} x_r \\ y_r \\ z_r \\ 1 \end{bmatrix} \\ &= \begin{bmatrix} 1 & 0 & 0 & 0 \\ 0 & \cos\theta & -\sin\theta & -d\cos\theta - L\cdot\sin\theta/2 \\ 0 & \sin\theta & \cos\theta & -d\sin\theta + L\cdot\cos\theta/2 \\ 0 & 0 & 0 & 1 \end{bmatrix} \cdot \begin{bmatrix} x_r \\ y_r \\ z_r \\ 1 \end{bmatrix}\end{aligned} \tag{4.3}$$

Because the arrangement of contact line shows the "zigzags" shape, the correspondence between the points in the camera coordinates and the ones in the image physical coordinates is shown in Fig. 4.4. x represents the stagger of laser spot location of contact line. y represents the height of laser spot location of contact line. Point (x, y) in the image physical coordinate system corresponds to point (u, v) in the image coordinate system, as shown in Fig. 4.5.

In this section, the pinhole model is adopted for the coordinate relationship calculation. Based on the correspondences in Figs. 4.4 and 4.5, it can be obtained as follows.

$$Z\begin{bmatrix} x \\ y \\ 1 \end{bmatrix} = \begin{bmatrix} f & 0 & 0 & 0 \\ 0 & f & 0 & 0 \\ 0 & 0 & 1 & 0 \end{bmatrix}\begin{bmatrix} x_c \\ y_c \\ z_c \\ 1 \end{bmatrix} \tag{4.4}$$

$$\begin{bmatrix} u \\ v \\ 1 \end{bmatrix} = \begin{bmatrix} s_x & 0 & x_0 \\ 0 & s_y & y_0 \\ 0 & 0 & 1 \end{bmatrix}\begin{bmatrix} x \\ y \\ 1 \end{bmatrix} = \begin{bmatrix} s_x & 0 & x_0 \\ 0 & s_y & y_0 \\ 0 & 0 & 1 \end{bmatrix} \cdot M_1 \cdot M_2 \begin{bmatrix} x_r \\ y_r \\ z_r \\ 1 \end{bmatrix} \tag{4.5}$$

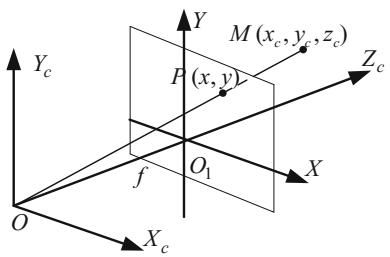

Fig. 4.4 Correspondence between the image physical coordinates and camera coordinates

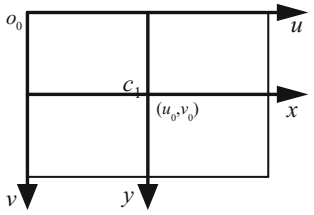

Fig. 4.5 Correspondence between the image physical coordinates and image coordinates

where s_x and s_y respectively mean the physical interval between the image horizontal and vertical adjacent pixel.

Thus, the correspondence between point (u, v) in the image coordinates and point (x_r, y_r, z_r) in the world coordinates can be obtained as follows.

$$\begin{cases} x_r = \sin\theta \cdot (y_r - d + L \cdot \cot\theta) \cdot (u - u_0)/(f_x \cdot s_x) \\ y_r = \frac{(\cot\theta \cdot L - d) \cdot (v - v_0) + (L + d \cdot \cot\theta) \cdot f_x \cdot s_y}{\cot\theta \cdot f_x \cdot s_y - (v - v_0)} \\ z_r = L/2 \end{cases} \tag{4.6}$$

2. Calibration of CCD camera

Given n calibration points, the pixel coordinates of calibration point i are (u_i, v_i), and its world coordinates are (x_{ri}, y_{ri}, z_{ri}). Then

$$z\begin{bmatrix} u_i \\ v_i \\ 1 \end{bmatrix} = M_0 \cdot M_1 \cdot M_2 \begin{bmatrix} x_r \\ y_r \\ z_r \\ 1 \end{bmatrix} = \begin{bmatrix} m_{11} & m_{12} & m_{13} & m_{14} \\ m_{21} & m_{22} & m_{23} & m_{24} \\ m_{31} & m_{32} & m_{33} & 1 \end{bmatrix} \begin{bmatrix} x_{ri} \\ y_{ri} \\ z_{ri} \\ 1 \end{bmatrix} \tag{4.7}$$

Eliminating z_c in formula (4.7), it can be obtained as follows.

$$\begin{cases} m_{11}x_{ri} + m_{12}y_{ri} + m_{13}z_{ri} + m_{14} - m_{31}u_i x_{ri} - m_{32}u_i y_{ri} - m_{33}u_i z_{ri} = u_i \\ m_{21}x_{ri} + m_{22}y_{ri} + m_{23}z_{ri} + m_{24} - m_{31}v_i x_{ri} - m_{32}v_i y_{ri} - m_{33}v_i z_{ri} = u_i \end{cases} \tag{4.8}$$

The linear equation set with $2n$ dimension can be obtained, namely

$$KM_4 = U \tag{4.9}$$

where M_4 is the column vector composed of 11 unknown elements in matrix $\boldsymbol{M}$. $\boldsymbol{U}$ is the column vector with $2n$ dimension composed of horizontal and vertical coordinates of n calibration points. $\boldsymbol{K}$ is the vector composed of $x_{ri}, y_{ri}, z_{ri}, u_i x_{ri}, u_i y_{ri}, u_i z_{ri}, v_i x_{ri}, v_i y_{ri}, v_i z_{ri}$.

When $2n > 11$, the least squares solution of the overdetermined equation can be adopted to obtain its solution as follows.

$$M = (K^T K)^{-1} K^T U \tag{4.10}$$

The parameters of camera F, u_1, v_1, d, L, θ can be solved. This method with simple model can directly realize the linear calibration, and efficiently amend the internal and external parameters of camera.

4.2.3 Center Point Location of Laser Spot

The iterative threshold method is adopted for the center point location of laser spot. The flow chart of the method is drawn in Fig. 4.6.

1. Pre-processing the sampled images

The images from camera that may be influenced by different position, light and shade, should be pre-processed. The image contrast can be adjusted and balanced, which can suppress the lower and higher gray value of image and enhance the gray value in a specific range of pixels for the laser spot.

$$G(m,n) = \begin{cases} 0 & I(m,n) < L_{in} \text{ or } I(m,n) > H_{in} \\ I(m,n) - L_{in}) \cdot \frac{H_{out} - L_{out}}{H_{in} - L_{in}} + L_{out} & L_{in} < I(m,n) < H_{in} \end{cases} \tag{4.11}$$

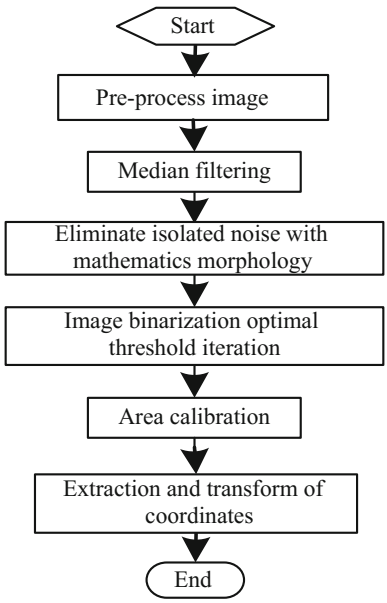

Fig. 4.6 Flow chart of center point location of laser spot

where I and G represent the original image and enhanced image respectively. $G(m,n)$ and $I(m,n)$ are the grey value at column row mth and column nth in image G and I, respectively. $[L_{in}, H_{in}]$ is the grey value range of original image. $[L_{out}, H_{out}]$ is the grey value range of enhanced image.

2. Eliminating isolated noise with mathematics morphology

In mathematics morphology, the expansion is defined as a set operation. R expanded by S is defined as follows.

$$R \oplus S = \left\{ z | (\widehat{S})_z \cap R = \varnothing \right\} \tag{4.12}$$

R corroded by S is defined as follows.

$$R \Theta S = \left\{ z | (\widehat{S})_z \cap R^c = \varnothing \right\} \tag{4.13}$$

where R is the binary image, S is the structural element, and z_{RS} is the pixel coordinates.

The open operation of mathematics morphology is a process of first corrosion and then expansion, whose purpose is to eliminate the noise of isolated point beyond the object and smooth the object' edge [6]. The S open operation for R is defined below.

$$R \circ S = (R \Theta S) \oplus S \tag{4.14}$$

Because of the influence of image quality, quality of pre-processing and small laser spot area, the multiple targets will be detected in many cases, which may lead to a large location deviation of the center point. Therefore, the open operation of mathematics morphology is adopted.

The rectangle template is used to realize the corrosion operation. In order to make the laser spot area more obvious, the method of large expansion and small corrosion is used to realize the close operation. The expansion template is 7×9 and the corrosion template is 2×9, which can eliminate the isolated noise points and make the object area more obvious.

3. Obtaining the center point of laser spot

In order to obtain the center point of laser spot, the best threshold iteration method is adopted. First, an approximate threshold is set as the initiate value. Then, the sampled image is segmented to produce the sub-images. Based on the characteristics of images, the new threshold can be selected, which will be used to segment the image. After several loops, the pixels of error segmentation can be reduced to the least [7]. The computation steps of iteration algorithm are listed below.

(1) If there is no exact location information for the object, the average gray value can be set as the initial threshold value.
(2) Through the threshold, the image can be divided into two segmentations Q_1 and Q_2.
(3) Calculate the grey mean value of Q_1 and Q_2, namely U_1 and U_2.
(4) Obtain the new threshold $T_n = (U_1 + U_2)/2$.
(5) If $T_n = T_{n+1}$, the iteration ends, otherwise, the iteration continues to carry out step (2).

In the end, the T_{n+1} will be set as the best segmentation threshold. The optimal threshold can be obtained when the iteration number is about 5. The method has a certain adaptivity.

4.2.4 Results Analysis of Experiments

1. Locating the center point of laser spot

In order to verify the location correctness of laser spot, the location experiments of actual images under the different shooting conditions and the different contact line locations are carried out. Figure 4.7a is the image that captured by CCD camera during the day. It can be found that it is very difficult to identify the weak laser spot because of the interference of support components in catenary image during the day. Therefore, it is suggested to capture the image during the night. Figure 4.7b is the image that captured by CCD camera during the night, whose contrast has been adjusted. In order to make the image more obvious, the image in Fig. 4.7b is only the left upper frame of Fig. 4.7a. It can be found that the laser spot is more obvious, but there is the interference of isolated noise. Figure 4.7c is the de-noised image by using mathematics morphology. It can be found that the mathematics morphology has good de-noising performance.

The calibration results are listed in Table 4.1. It can be found in Table 4.1 that the location algorithm can accurately locate the center point of laser spot. Because the laser point perhaps locates on the clips of contact line, the laser spot will become bigger and have the serious distortion in the image, which results in the bigger error for the coordinate's computation of iteration algorithm. In the analysis process, the threshold for the number of pixels in the laser spot can be set. If the pixels' number is higher than the threshold, the location can be justified as the clip's location. Thus, some compensation measures can be adopted to compute the location's coordinates.

2. Calibration result analysis

The internal and external parameters of CCD camera are listed in Table 4.2.

It can be found in Table 4.2 that the parameters of the camera are different from those of the factory. Because of the tilt of detection vehicle platform, the angle of the camera and the height of the camera are changed. Therefore, the calibration of

(a) Image captured by CCD camera during the day

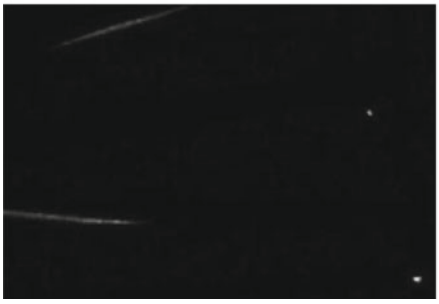

(b) Image after adjusting contrast;

(c) Center point image of laser spot after de-noising with mathematics morphology

Fig. 4.7 Location of the center point of laser spot

Table 4.1 Calibration result comparison with actual coordinates of image

Image No.	Actual coordinates		Calibration coordinates	
	x	y	x	y
1	838	718	838	704
2	1371	671	1372	665
3	1409	690	1433	683
4	1775	680	1785	675
5	1343	636	1341	628
6	1003	684	1000	683

Table 4.2 Internal and external parameters of CCD camera

Parameters	F	(u_1, v_2)	d(m)	L(m)	θ (°)
Ex-factory	1.1×10^{-8}	(1295, 971)	4.50	1	51
Calibration	1.9×10^{-8}	(1297, 975)	4.57	1	51.6

Table 4.3 Calibration result comparison with actual coordinates of image

Image No.	Coordinate transform method		Optical measurement method		Error (%)	
	x	y	x	y	Δx	Δy
1	838	718	838	704	2.6	6.0
2	1371	671	1372	665	2.5	9.8
3	1409	690	1433	683	10.3	8.9
4	1775	680	1785	675	1.0	2.2
5	1343	636	1341	628	7.2	7.3
6	1003	684	1000	683	10.4	7.7

geometry parameters for the contact line in detection vehicle can improve the experimental accuracy.

3. Transformation result analysis from image coordinates to detect vehicle coordinates

At present, the optical measurement instrument with the characteristics of high precision and high accuracy is widely used in actual engineering. In order to verify the validity of the proposed method, the decentralized points in contact line from 3 adjacent spans in a certain anchoring section of actual railway are selected for stagger and height detection. These points are detected with the optical measurement instrument. The detection results are listed in Table 4.3. x means the stagger and y means the height of contact line.

In Table 4.3, 6 groups of data are listed. Because the stagger value of contact line is corresponding to the decentralized points, the comparison results can guarantee the credibility of proposed method. If the coordinates are computed based on the optical measurement instrument, the error of stagger computed with the coordinate transform method is less than 11 mm, and the error of height is less than 10 mm. It can be found that non-contact detection method based on image processing has higher detection accuracy and can replace the traditional manual measurement method for the geometric parameter detection of the contact line.

4.3 Detection Value Correction of Catenary Geometric Parameters Based on Kalman Filtering

4.3.1 Vibration Influence of Detection System and Compensation Method

1. Influence of vibration on the detection system

In the operation process of detection vehicle, many kinds of vibration are produced. These vibrations will make the train body produce horizontal displacement

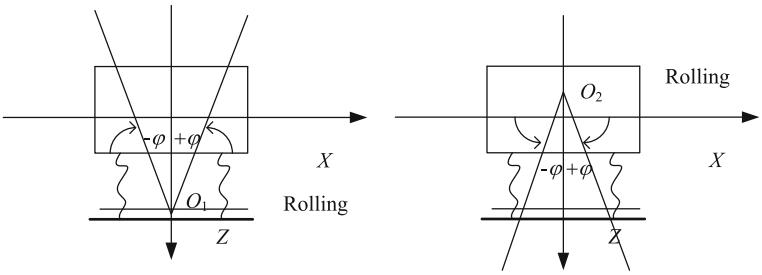

Fig. 4.8 Diagram of the rolling vibration of detection vehicle body

relative to the line center and the vertical displacement relative to the track surface. The train is a multi-freedom vibration system with spring suspension device, which can produce complex vibration phenomenon. This kind of complex vibration is the result of a combination of several basic forms of vibration [8–10]. Some compensation methods were presented in [11–13]. The experiments show that the rolling vibration of detection vehicle body has a decisive influence on the stagger, as shown in Fig. 4.8. φ is the rolling angle from the center line of detection vehicle body.

The influence of detection vehicle vibration on the detection performance is shown in Fig. 4.9.

It can be found in Fig. 4.9 that the vibration of detection vehicle will directly influence the relative location of laser spot in the image and increase the computation error of stagger and height of contact line.

2. Compensation of detection vehicle vibration

When the vibration of detection vehicle occurs, the captured image will have a certain deflection. The detection vehicle has the rotation to the track edge point C by the angle φ, which will make the coordinates of image produce the deflection, as shown in Fig. 4.10.

Therefore, the coordinates of laser spot J in the world coordinates based on Formula (4.6) is the coordinates (X'_{w1}, Y'_{w1}) in the coordinate system $Y'_w O'_w X'_w$ after the deflection of laser spot J. In order to obtain the coordinates (X_w, Y_w) of laser spot J in the world coordinate system, the correspondence between the coordinates (X'_{w1}, Y'_{w1}) of laser spot deflection and the world coordinates (X_w, Y_w) should be constructed based on the rotation relationship in Fig. 4.10.

Suppose that the horizontal vibration of detection vehicle body attaches at X_{w0}, vertical vibration attaches at Y_{w0}, the rolling angle is φ, and the track's width is W, then the correspondence can be obtained as follows.

$$X_w = X_{w0} + X'_{w1} \cos\varphi + Y'_{w1} \sin\varphi \tag{4.15}$$

(a) Detection effect without vibration

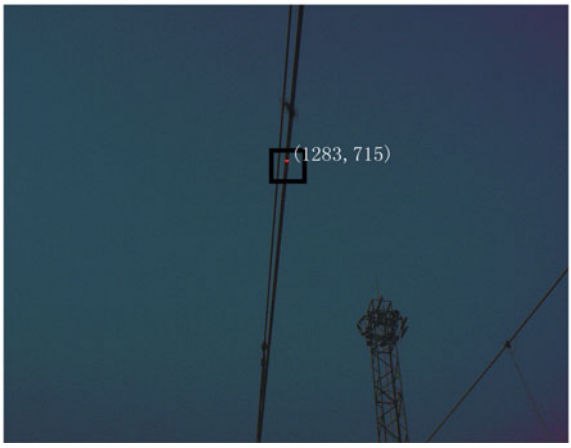

(b) Detection effect with vibration

Fig. 4.9 Detection result comparison with and without vibration

$$Y_w = Y_{w0} - X'_{w1}\sin\varphi + Y'_{w1}\cos\varphi \tag{4.16}$$

$$X_{w0} = W/2(1-\cos\varphi) \tag{4.17}$$

$$Y_{w0} = W/2\sin\varphi \tag{4.18}$$

Based on Formulas (4.15)–(4.18), it can be obtained below.

$$\begin{bmatrix} X_w \\ Y_w \end{bmatrix} = \begin{bmatrix} \cos\varphi & \sin\varphi \\ -\sin\varphi & \cos\varphi \end{bmatrix} \begin{bmatrix} X'_{w1} \\ Y'_{w1} \end{bmatrix} + \begin{bmatrix} W/2(1-cos\varphi) \\ W/2\sin\varphi) \end{bmatrix} \tag{4.19}$$

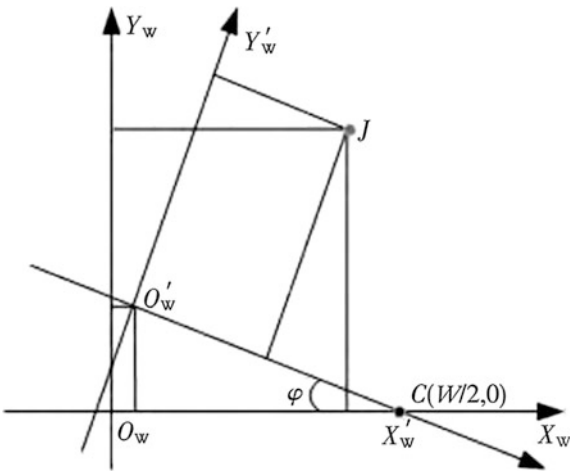

Fig. 4.10 Coordinate deflection of detection vibration

Substitute Formula (4.19) into Formula (4.6), the computation formula of contact line's geometry parameters after compensation can be obtained below.

$$\begin{cases} X_w = X_{w0} + \dfrac{(L + L\cot^2\theta)(U - U_0)\sin\theta}{(f/\Delta Y)\cot\theta + (V - V_0)}\cos\varphi \\ \qquad + \dfrac{-(L\cot\theta - d)(V - V_0) + (L + d\cot\theta)(f/\Delta Y)}{(f/\Delta Y)\cot\theta + (V - V_0)}\sin\varphi \\ Y_w = Y_{w0} - \dfrac{(L + L\cot^2\theta)(U - U_0)\sin\theta}{(f/\Delta Y)\cot\theta + (V - V_0)}\sin\varphi \\ \qquad + \dfrac{-(L\cot\theta - d)(V - V_0) + (L + d\cot\theta)(f/\Delta Y)}{(f/\Delta Y)\cot\theta + (V - V_0)}\cos\varphi \\ Z_w = L/2 \end{cases} \tag{4.20}$$

4.3.2 Correction Method of Contact Line Height

1. Influence factors on the height of contact line

The suspension methods of contact line are mainly divided into two categories with equal and unequal height of two ends. The suspension sketch map of contact line is shown in Fig. 4.11. The different suspension methods correspond to the different equations. For the height detection of contact line, because there are some interference, such as the coordinate deflection caused by the rolling vibration of vehicle body, the random vibration caused by the mechanical close connected components enough, and the low detection accuracy caused by the vibration sensor, it is very difficult to obtain the accurate the suspension curve.

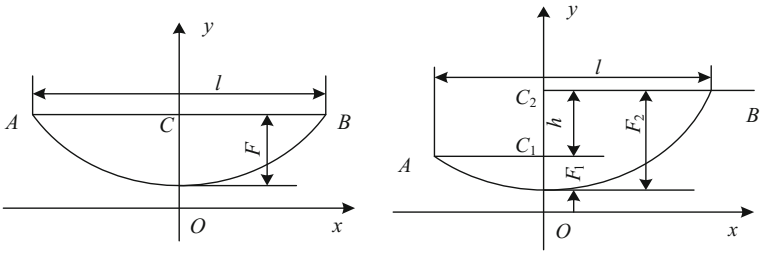

(a) Equal height of two ends; (b) Unequal height of two ends

Fig. 4.11 Suspension sketch map of contact line

Suppose that A and B are two suspension points. If their heights are equal, the suspension is shown in Fig. 4.11a, where l is the horizontal distance of two suspension points, and F is the vertical distance between the lowest point of contact line curve and the straight line of two suspension points, namely the sag. When the two suspension points are not in the same horizontal plane, the suspension is shown in Fig. 4.11b, where F_1 and F_2 are respectively the height difference between the lowest points of contact line curve and two suspension points, and h is the height difference between the two suspension points.

2. Correction equations of contact line height

In order to improve the detection accuracy of contact line height, considering the possible curve forms of adjacent suspension points, the correction model based on Kalman filtering for the unequal height of two ends is deduced as follows.

The mathematical curve equation of the unequal height of two ends of contact line is listed below [14].

$$y = D - \frac{h}{l}x - \frac{4F \cdot x(l-x)}{l^2} \tag{4.21}$$

where D is the basic height from the track surface to the suspension point of contact line, x is the horizontal distance from the laser of detection vehicle along the train operation direction, and y is the height of contact line. The coordinate system xoy coincides with coordinate system $Z_wO_wY_w$, and the original point o is the projecting point of suspension point from the start location of detection vehicle at the track plane.

After discretization of Formula (4.21), it can be obtained as follows.

$$\begin{cases} x_k = D - \frac{h}{l}x - \frac{4F \cdot k \cdot (l-x)}{l^2} \\ x_{k-1} = D - \frac{h}{l}(k-1) - \frac{4F \cdot (k-1) \cdot (l-(k-1))}{l^2} \end{cases} \tag{4.22}$$

where $k = 1, 2, \ldots, \infty$, k is the horizontal distance from the laser of detection vehicle along the train operation direction, x_k is the corresponding height to the point k, and x_{k-1} is the corresponding height to the point $k - 1$.

Based on Formula (4.22), the state equation can be obtained as follows.

$$x_k = x_{k-1} + \frac{4F \cdot (2k - l - 1)}{l^2} - \frac{h}{l} \tag{4.23}$$

Suppose u_k is the control variable, let

$$u_k = \frac{4F \cdot (2k - l - 1)}{l^2} - \frac{h}{l} \tag{4.24}$$

Then

$$x_k = x_{k-1} + u_k \tag{4.25}$$

Let $\mathbf{X}_k = x_k, \mathbf{U}_k = u_k, \mathbf{A} = 1, \mathbf{B} = 1$, then Formula (4.25) can be rewritten with matrix form.

$$\mathbf{X}_k = \mathbf{A}\mathbf{X}_{k-1} + \mathbf{B}\mathbf{U}_k \tag{4.26}$$

Suppose the observed value is z_k and the observed noise is Δx_k, then the observed equation can be written as follows.

$$z_k = x_k + \Delta x_k \tag{4.27}$$

Let $\mathbf{Z}_k = z_k, \mathbf{H} = 1$, then Formula (4.27) can be rewritten with matrix form.

$$\mathbf{Z}_k = \mathbf{H}\mathbf{X}_k + \Delta x_k \tag{4.28}$$

Considering the random error caused by the height detection of contact line and the independence of adjacent detection points, if the observed noise and process noise are supposed as the Gaussian white noise, Kalman equation can be written as follows.

Time renewal equation:

$$\begin{cases} \bar{\mathbf{X}}_k = \mathbf{A}\mathbf{X}_{k-1} + \mathbf{B}\mathbf{U}_{k-1} \\ \bar{\mathbf{P}}_k = \mathbf{A}\mathbf{P}_{k-1}\mathbf{A}^T + \mathbf{Q} \end{cases} \tag{4.29}$$

State renewal equation:

$$\begin{cases} \mathbf{K}_k = \bar{\mathbf{P}}_k\mathbf{H}^T / (\mathbf{H}\bar{\mathbf{P}}_k\mathbf{H}^T + \mathbf{R}) \\ \mathbf{X}_k = \bar{\mathbf{X}}_k - \mathbf{K}_k(\mathbf{Z}_k - \mathbf{H}\bar{\mathbf{X}}_k) \\ \mathbf{P}_k = (1 - \mathbf{K}_k\mathbf{H})\bar{\mathbf{P}}_k \end{cases} \tag{4.30}$$

where $\mathbf{X}_k$ is the estimation value of posteriori state at time k, $\bar{\mathbf{X}}_k$ is the estimation value of priori state at time k, $\mathbf{P}_k$ is the covariance of posteriori estimation error at time k, $\bar{\mathbf{P}}_k$ is the covariance of priori estimation error at time k, $\mathbf{Q}$ is the process the covariance, $\mathbf{K}_k$ is the Kalman gain, and $\mathbf{Z}_k$ is the observed value at time k.

It can be found that if substitute $\bar{\mathbf{X}}_k$ and $\bar{\mathbf{P}}_k$ into the state renewal equation, the posteriori data can be obtained, namely the best estimation value $\mathbf{X}_k$.

Because of the long-term usage of suspension device, the deformation of suspension device and the settlement of pillar, the positions of suspension points may change, which results in the change of the variable h and H in the model. In order to ensure the model correctness, the parameters often need to be modified. Thus, the correction equation of Formula (4.21) is rewritten as follows.

$$F = \frac{l^2}{4}\left(\frac{x_k - D}{k} - \frac{x_{k-1} - D}{k-1}\right) \tag{4.31}$$

$$h = \frac{l(k-l-1)(x_k - D)}{k} - \frac{l(k-l)(x_{k-1} - D)}{k-1} \tag{4.32}$$

In order to correctly modify h and F with the substituted coordinate parameters, each point data is obtained by the weighted average of 3 group data.

4.3.3 Result Analysis of Experiments

1. Result analysis after the compensation

Suppose that the coordinates of stagger and height of contact line obtained by the optical measure instrument at the static state are considered as the standard value. The standard value, the compensated value and non-compensation value for the stagger and height of contact line are listed in Tables 4.4 and 4.5. It can be found that the compensated value and non-compensation value can satisfy the technology index of catenary detection. But, the accuracy of compensated value for the stagger

Table 4.4 Non-compensation value for the stagger and height

Image No.	Non-calibration coordinates (mm)		Standard value (mm)		Error of stagger/height (mm)	
	x	y	x	y	Δx	Δy
1	301.5	5890.8	304.1	5884.8	2.6	6.0
2	173.2	5925.2	177.3	5917.5	4.1	7.7
3	−75.8	5900.0	−78.2	5906.2	2.4	6.2
4	−98.5	5926.4	−101.0	5936.2	2.5	9.8
5	−142.1	5921.2	−131.8	5913.3	10.3	8.9
6	−410.5	5931.6	−411.5	5929.4	1.0	2.2

Table 4.5 Compensated value for the stagger and height

Image No.	Non-calibration coordinates (mm)		Standard value (mm)		Error of stagger/height (mm)	
	x	y	x	y	Δx	Δy
1	297.8	5886.7	304.1	5884.8	6.3	1.9
2	181.2	5915.1	177.3	5917.5	3.9	2.4
3	−74.5	5909.8	−78.2	5906.2	3.7	3.6
4	−98.5	5940.0	−101.0	5936.2	2.5	3.8
5	−140.2	5908.5	−131.8	5913.3	8.4	4.8
6	−409.9	5928.3	−411.5	5929.4	1.6	1.1

and height of contact line are respectively 9 and 5 mm, while the non-compensation value for the stagger and height of contact line are respectively 11 and 10 mm [15].

2. Result analysis of Kalman filtering

In order to verify the modified results with Kalman filtering for the compensated height observed value, 60 height data after the compensation are selected in the same interval between the two suspension points. After Kalman filtering, these data are compared with the standard value, and the different value curves are shown in Figs. 4.12 and 4.13.

It can be found in Figs. 4.12 and 4.13 that the absolute error of height observed value after compensation is in the range of 1.0–2.0 m. Based on the observed value of height, the Kalman filtering is adopted, and the absolute error of height is in the range of 0.5–1.0 m. Therefore, the modification with Kalman filtering can efficiently improve the accuracy of observed value.

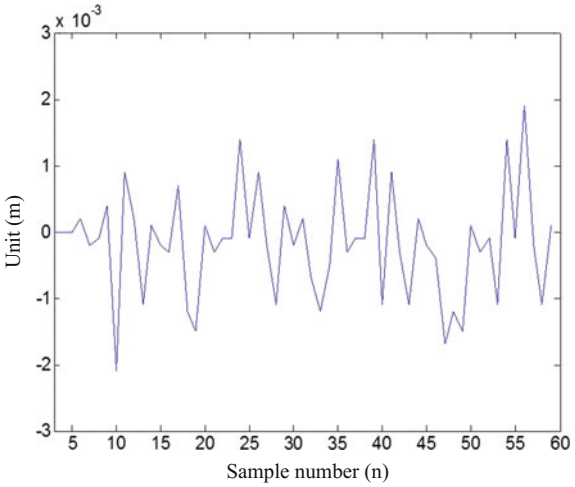

Fig. 4.12 Different value curves between the standard value and the observed value (after compensation)

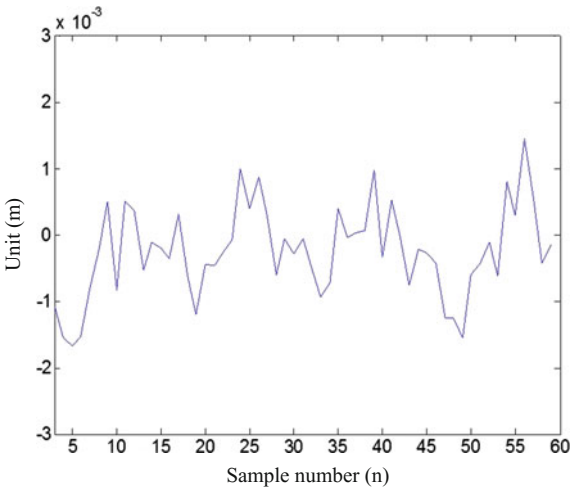

Fig. 4.13 Different value curves between the standard value and the Kalman filtered value (after compensation)

3. System time consuming

In order to verify the real-time performance of the plan, 1000 images captured by the camera are selected randomly, and the time consuming computation is carried out by using this method. Computer configuration: Windows 7 operation system (32 bits), CPU frequency of 2.4 GHz, RAM memory capacity of 4.0 0 GB, card type, GT4 25M1G the independent video card.

Through the test and calculation, it is concluded that the expected value of time consumption is 35 ms, and the variance is 1 ms. Considering the operation speed of the detection vehicle and the consumption time for drawing the height curve of contact line, 70–100 detection points can be sampled and processed in 50 m. According to the speed formula, the speed of detection vehicle can reach 51.248–73.469 km/h, which can meet the requirements of real-time operation.

4.4 Detection Method of Catenary Geometric Parameters Based on Mean Shift and Particle Filter Algorithm

Based on the images of contact line, which are captured by the single camera on the roof of detection vehicle, the stagger and height of contact line can be computed by the image processing. However, with the increase of train' speed and operation density, the detection accuracy and real time of this method hardly meet the actual detection demands.

The target detection and tracking algorithm based on vision technology is one of the hot research topics in computer vision field. The main current target tracking algorithm is divided into two categories, namely deterministic and random tracking algorithms [16]. The mean shift algorithm is a deterministic tracking algorithm, and it needs no parameters and does not require exhaustive search features. It has been

successfully applied in the target tracking with high real-time requirements. But when the image background is complex, it easily falls into the local minimum value, and the tracking effect is not ideal. Particle Filter (PF) is a representative of random tracking algorithm, which can avoid the local optimum trap. But it has to set up a large number of particles to improve the accuracy of sample estimation at the cost of algorithm time. Recently, the combination algorithm of mean shift and PF was proposed in [17], namely MSPF (Mean Shift Particle Filter) algorithm. MSPF algorithm can have the advantages of the two methods, and its performance is better than that of any one of the two algorithms alone [18].

In this section, the detection method of catenary geometric parameters based on mean shift and PF algorithm is presented. First, according to the Gray histogram feature distribution and the "zigzags" structure of catenary, the object model of laser spot is constructed. Second, the particles are clustered with the clustering method, and the iteration that starts from the clustering center is carried out with the mean shift algorithm. Third, the coordinates of object image are obtained through the PF of the iteration results. Lastly, the stagger and height of contact line can be obtained through the space coordinate transformation of image coordinates of laser spot. The detection plan of stagger and height of contact line based on MSPF is shown in Fig. 4.14 [19].

4.4.1 Data Model of Laser Spot

1. Observed model of laser spot object

The laser spot object is located by using the particle filter algorithm based on gray histogram feature distribution. First, the object area is initialized. Taking the center point of the object area as the standard point, the rectangle window including all the laser spot's pixels and some background pixels is obtained, as shown in Fig. 4.15. Second, the two-dimension coordinates in the window of laser spot are projected to the index m in the histogram section divided by the pixel value level u. Then, the density estimation of probability density function of laser spot area can be computed based on the below formula.

$$q_u = C\sum_{i=1}^{n} k\left(\left\|\frac{x_0 - x_i}{h}\right\|\right)^2 \delta[b(x_i) - u] \tag{4.33}$$

where x_0 is the coordinate of center pixel in the initial search window (n pixels), $k(\cdot)$ is the Epanechnikov kernel function, $\delta(\cdot)$ is the Delta function, $b(x_i)$ is the level index image at x_i, C is the standardized constant coefficient, and $\sum_u^m q_u = 1$.

The Bhattacharyya distance is selected to measure the similarity between the candidate object color distribution $p_u(x)$ and the object template color distribution q_u. The coefficient of Bhattacharyya can be obtained as follows.

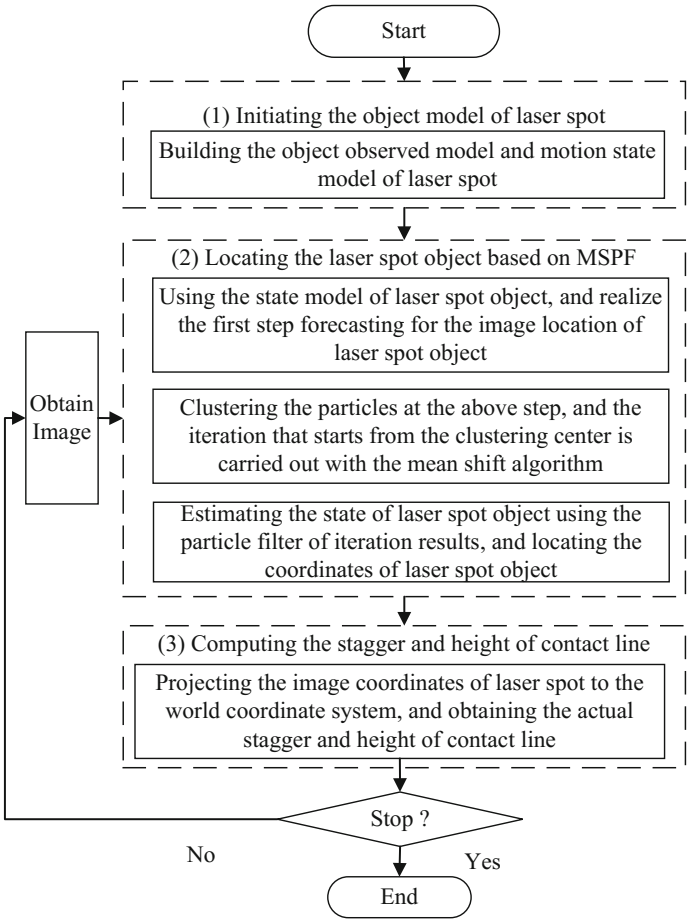

Fig. 4.14 Detection plan of stagger and height of contact line based on MSPF

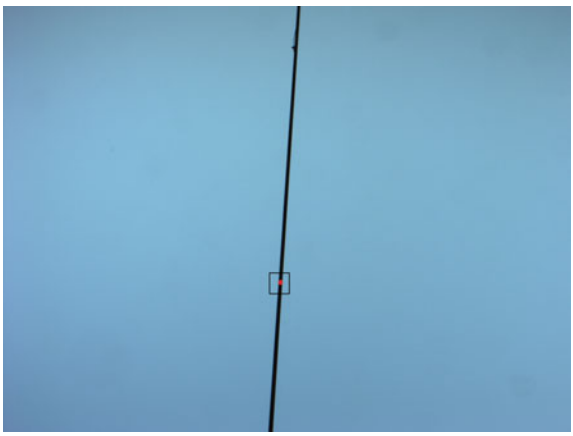

Fig. 4.15 Detection plan of stagger and height of contact line based on MSPF

$$\rho[p_u(x), q_u] = \sum_{u=1}^{m} \sqrt{p_u(x) q_u} \tag{4.34}$$

The Bhattacharyya distance between q_u and $p_u(x)$ is shown below.

$$d = \sqrt{1 - \rho[p_u(x), q_u]}; i = 1, 2 \tag{4.35}$$

The observed probability based on Bhattacharyya distance d can be obtained below.

$$p(\boldsymbol{Z}_k | \boldsymbol{X}_k) = \frac{1}{\sqrt{2\pi}\sigma} \exp\left(-\frac{d^2}{2\sigma^2}\right) \tag{4.36}$$

2. Motion state model of laser spot

With the moving of detection vehicle, the trial of laser spot on the contact line will regularly move along the contact line. Therefore, in order to reflect the variation rule of laser spot with the location of detection vehicle and quickly locate the laser spot, the motion state model of laser spot is built according to the "zigzags" structure of catenary, as shown in Fig. 4.16.

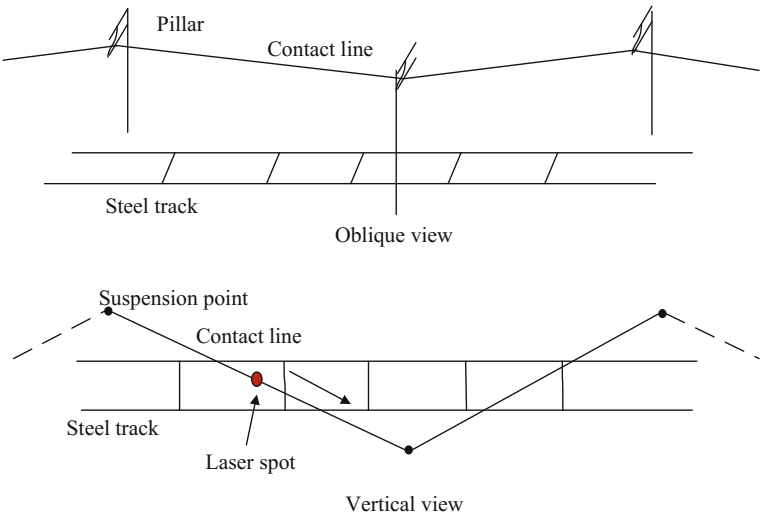

Fig. 4.16 Oblique view and vertical view of catenary

The curve equation of unequal height suspension of two ends for contact line [14] is shows as follows.

$$\begin{cases} x_r = K_r \cdot z_r + C \\ y_r = H - \left(\frac{h}{l} z_r + \frac{4F \cdot z_r (l - z_r)}{l^2} \right) \end{cases} \tag{4.37}$$

where K_r is the straight line slope of horizontal projecting plane of contact line between the two adjacent suspension points, C is the initial value of stagger, H is the basic height between the adjacent two suspension points of contact line, h is the vertical height difference between two adjacent suspension points of contact line, z_r is the horizontal location along the train's operation direction, and y_r is the height of contact line.

After the discretization of formula (4.37), it can be obtained as follows.

$$\begin{cases} x_k = x_{k-1} + K_{k-1} \\ y_k = y_{k-1} - \left(\frac{h}{l} + \frac{4F \cdot (l - 2(k-1) - 1)}{l^2} \right) \end{cases} \tag{4.38}$$

Because the height change of the adjacent two frame images is not obvious, the height of former frame is used to estimate the height of current frame for the simplification of the model construction.

$$\begin{cases} x_k = x_{k-1} + K_{k-1} \\ y_k = y_{k-1} \end{cases} \tag{4.39}$$

The state of laser spot object based on the coordinates transform can be obtained as follows.

$$\mathbf{X}_k = \mathbf{A}\mathbf{X}_{k-1} + \mathbf{B}\xi_{k-1} \tag{4.40}$$

where $\mathbf{X} = [x \quad y]^T$, $\mathbf{A}$ is the state transition matrix, $\mathbf{B}$ is the covariance matrix of process noise, and ξ is the process noise at $k - 1$.

4.4.2 *Tracking and Positioning of Laser Spot Based on MSPF*

In [20], the clustering algorithm was introduced to improve the MSPF algorithm, which can optimize the highly representative particles through observing the particles' probability and their distances between each other. Compared with the classical MSPF method, the proposed algorithm reduces the computation rate. In this section, the algorithm is adopted to realize the tracking and positioning of laser spot. The steps of tracking and positioning of laser spot are listed below.

1. Initiation

In the selected region of laser spot, N particles are randomly sampled to construct the particle set $\{\boldsymbol{X}_k^j\}_{j=1}^N$, and the weight of each particle is $1/N$.

2. Updating set

Each particle of particle set is substituted into the object dynamic equation and new particle set is obtained.

3. Clustering

(1) The updated particles are substituted into Formula (4.36), the observation probability of particle.
(2) The biggest particle is selected to be as the clustering center of grouping, the distances between the other particles and the clustering center are computed. These distances are compared with the given distance threshold R. If they are smaller than R, they are classified as a class.
(3) The particle, whose probability is biggest in the remaining particles that are bigger that the threshold R, is selected to be as the clustering center, and step (1) is executed.
(4) After the clustering of all particles are completed, the class number is smaller than the preset number C, the clustering end; otherwise, the threshold R is adjusted and the step (2) is executed again until the condition is meet.

4. Mean shift

(1) Suppose that $c_0(x_0, y_0)$ is the location c of the given clustering center.
(2) Compute the weight value of particle c.

$$w(x_i) = \sum_{u=1}^{m} \sqrt{q_u / p_u(y_0)}\,\delta[b(x_i) - u] \tag{4.41}$$

(3) Compute the new location of particle c.

$$c_1 = \frac{\sum_{i=1}^{M} x_i w(x_i) k\left\|\frac{c_0 - x_i}{h}\right\|}{\sum_{i=1}^{M} w(x_i) k\left\|\frac{c_0 - x_i}{h}\right\|} \tag{4.42}$$

(4) If the particle c_1 satisfies the two stop conditions below, the process ends, otherwise, return to step (2) to continue the loop.

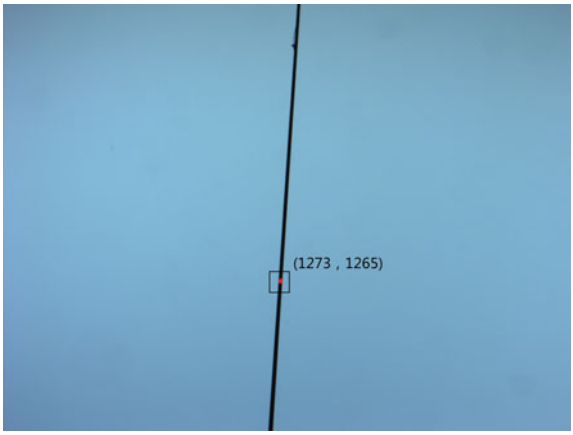

Fig. 4.17 Schematic figure of laser spot object positioning

$$\rho[p_{\mathrm{u}}(C_1), q_{\mathrm{u}}] < \rho[p_{\mathrm{u}}(C_0), q_{\mathrm{u}}] \tag{4.43}$$

or

$$\|y_1 - y_0\| < \varepsilon \tag{4.44}$$

5. Update the particle and compute the weight

The particles of laser spot object $\{\boldsymbol{X}_k^j\}_{j=1}^c$ can be obtained through the clustering and mean shift algorithms. The states of all particles in the same clustering are replaced with those after the optimization, namely from $\{\boldsymbol{X}_k^j\}_{j=1}^c$ to $\{\hat{\boldsymbol{X}}_k^j\}_{j=1}^N$. The weight of the updated the particle is computed.

6. State estimation of laser spot object

With the updated particle state $\{\hat{\boldsymbol{X}}_k^j\}_{j=1}^N$ and the weight $\{w_k^j\}_{j=1}^N$, the final estimation $\tilde{\boldsymbol{X}}_k$ can be obtained, as shown in Fig. 4.17.

$$\tilde{\boldsymbol{X}}_k = \sum_{i=1}^{N} w_k^j \hat{\boldsymbol{X}}_k^j \tag{4.45}$$

7. Repeated sampling

The random sampling method is adopted [21] in this section. Through decreasing the particles with less weight and copying the particles with bigger weight, the particles are repeatedly sampled.

4.4.3 Computing Height and Stagger of Contact Line

Through the coordinate transformation, the object image of laser spot is projected to the world coordinates, and the height and stagger of contact line can be computed and obtained based on Fig. 4.18.

In order to verify the accuracy of the location method and the real-time of detection algorithm, the sampled field images (captured one every 0.5 m) are used and compared with the standard detection value.

1. Positioning of laser spot object

In order to verify the location method's accuracy for the laser spot object, the method in this section is used to compute the location of laser spot object in the catenary image. The coordinates in the image is considered as the standard value. The absolute error and its mean value between the standard value and the detection value are considered as the performance indexes of the proposed method. The results are shown in Figs. 4.19 and 4.20.

The results show that the positioning algorithm can make the absolute error of laser spot less than 8 pixels, the mean error about 3.87 pixels along x axis direction, as well as the absolute error less than 7 pixels, the mean error about 3.33 pixels along y axis direction.

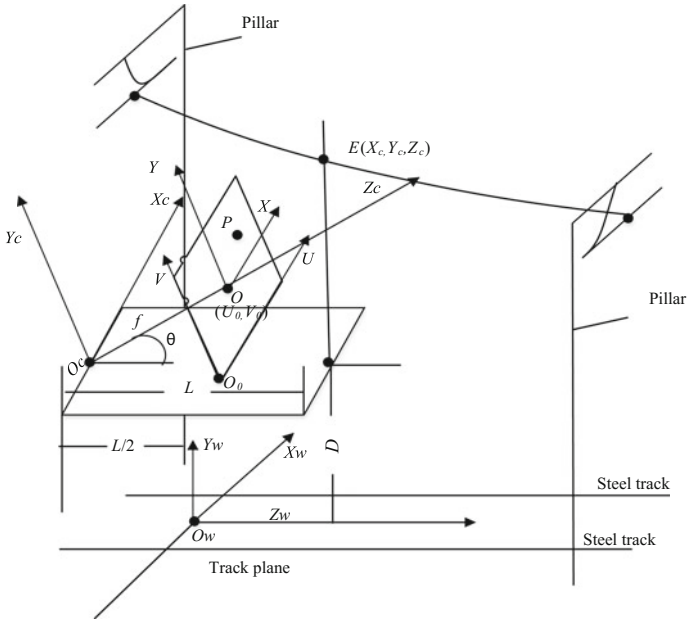

Fig. 4.18 Schematic diagram of detection vehicle parameter

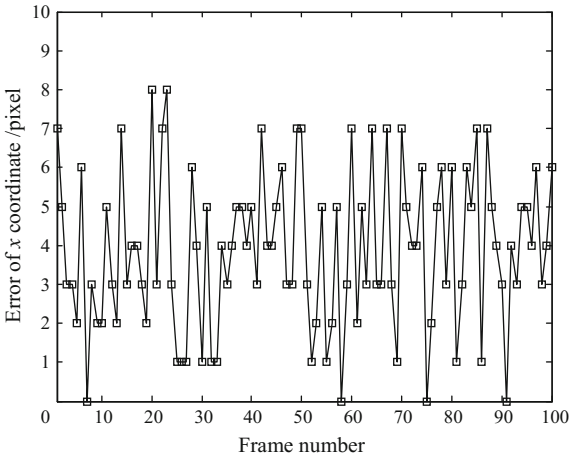

Fig. 4.19 Error of x coordinate with the proposed algorithm

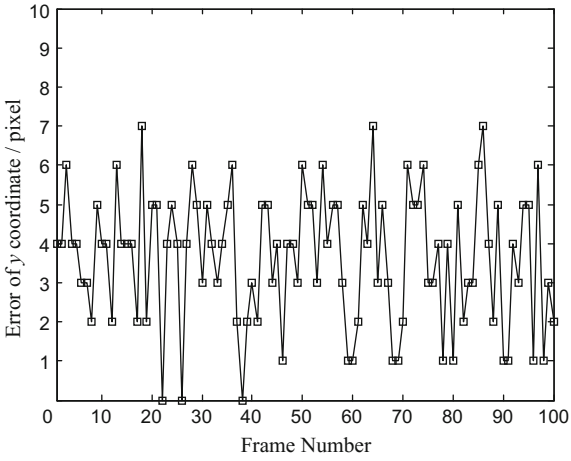

Fig. 4.20 Error of y coordinate with the proposed algorithm

2. Computing height and stagger of contact line

The height and stagger of contact line can be computed based on the proposed algorithm, and the results are shown in Figs. 4.21 and 4.22.

In order to verify the measurement accuracy of height and stagger of contact line, the measurement value by using the optical instrument is considered as the standard value. The absolute difference between the standard value and the computed value, and its mean value are considered as the performance evaluation indexes, as shown in Figs. 4.23 and 4.24.

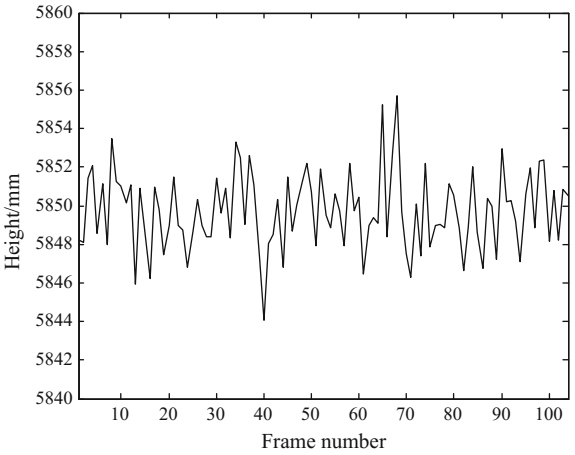

Fig. 4.21 Height curve of contact line

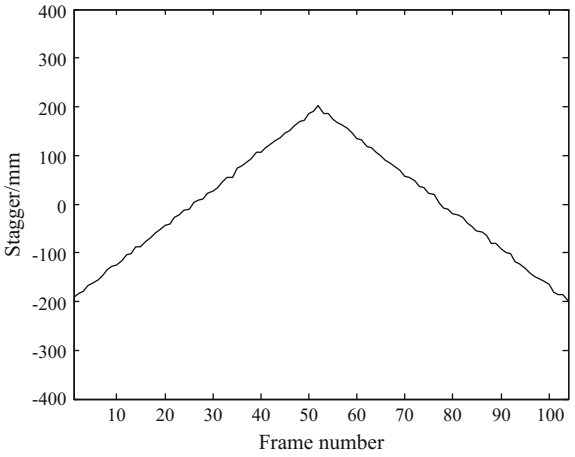

Fig. 4.22 Stagger curve of contact line

The detection results show that the detection absolute error of stagger is less than 7 mm and the mean error is 2.21 mm, and the detection absolute error of height is less than 6 mm and the mean error is 1.61 mm.

3. System time consumption

In order to verify the real-time performance of the plan, 100 images captured by the camera are selected randomly, and the time consumption computation is carried out by using this method. Computer configuration: Windows 7 operation system (32 bits), CPU frequency of 2.4 GHz, and RAM memory capacity of 4.0 0 GB. The experimental results are shown in Fig. 4.25.

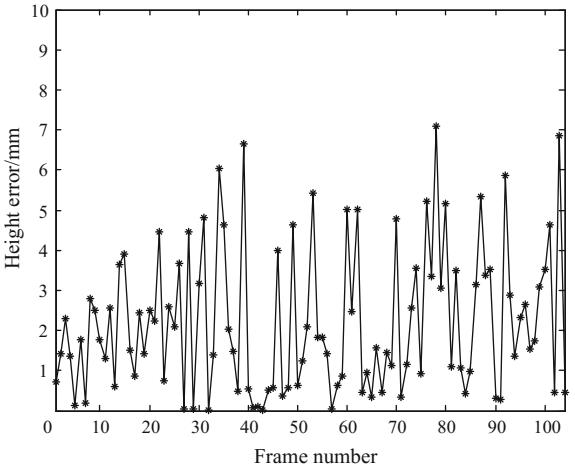

Fig. 4.23 Absolute error curve of stagger

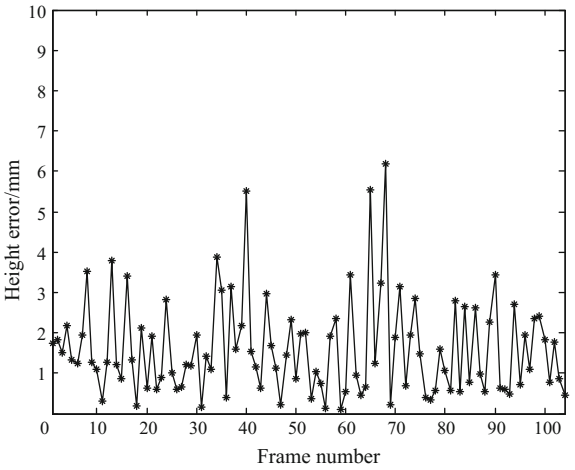

Fig. 4.24 Absolute error curve of height

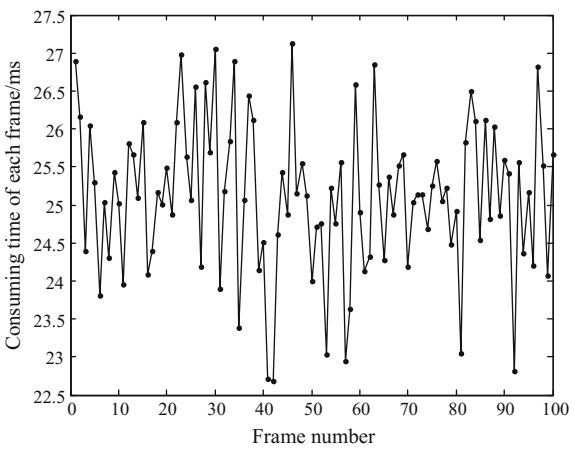

Fig. 4.25 Consuming time curve of each frame

The test results show that if the operation speed of the detection vehicle and the consumption time for drawing the height curve of contact line are considered, the time consumption of processing the single frame image is about 22.5–27.5 ms, and the mean time is about 25.035 ms.

4.5 Summary

The geometry parameter detection of catenary is one of most important tools that ensure the train's operation safety. The traditional detection methods for the stagger detection of contact line are generally based on the contact methods, which are influenced by the electromagnetic interference, mounted device and so on. In this chapter, the non-contact detection methods for the stagger detection of contact line are presented and discussed in detail, which are based on the coordinates transform and image processing. First, a non-contact detection for the height and stagger of contact line is presented in detail. The main content includes the field image acquisition of contact line, the pinhole model calibration of CCD camera, the center point location of laser spot and the results analysis of experiments. Second, the detection value correction of catenary geometric parameters based on Kalman filtering is presented, which mainly includes the influence of vibration on the detection system and its compensation method, the detection correction method of height of contact line and the results analysis of experiments. In the end, the detection method of catenary geometric parameters based on mean shift and particle filter algorithm is presented, which mainly includes the data model of laser spot, tracking and positioning of laser spot based on MSPF and computing the height and stagger of contact line. The experimental results show that the presented methods can efficiently detect the stagger and height of contact line based on the coordinates transform and image processing.

References

1. Zhang G, Liu Z, Liu W et al (2014) Non-contact detection of conductor height & stagger of contact line based on camera calibration. J China Railway Soc 36(3):25–30
2. Wang J, Feng F, Liang W et al (2012) Non-linear model based calibration. Optoelectron Technol 32(1):33–38
3. Kunfeng S, Qiulei D, Fuchao W (2012) Weighted similarity-invariant linear algorithm for camera calibration with rotating objects. IEEE Trans Image Process 21(8):3806–3812
4. Zhang W, Chen J (2009) CCD camera calibration. Transducer Microsys Technol 28(2):107–109
5. Li X, Li F (2009) Camera calibration for monocular vision. Comput Eng Appl 22(1):229–232
6. Wang W, Yan C, Zhang T et al (2004) Application of mathematical morphology image processing. Comput Eng Appl 32:89–92
7. Chen J, Zhu H (2011) A method of image segmentation based on mutual information and threshold iteration. J Wuhan Univ Technol Transp Sci Eng 35(3):641–644

8. Zhu C, Ni S, Gao H (1990) Capacitor type car body compensation device and its application to the contact network of test coach. J China Railway Soc 12(1):21–26
9. Zhang X, Wanju Y (1994) The vibration measuring and compensation calculation method of the overhead contact system test coach. J Southwest Jiaotong Univ 29(6):633–639
10. Chen T, Di Y, Chen Y (1999) Study on vibration compensation of measuring cars for overhead contact line equipment. J Southwest Jiaotong Univ 34(4):461–465
11. Zhan D, Long Y, Xiao J et al (2013) Computer vision approach to conductor rail detecting vehicle vibration compensation method and its application. J China Railway Soc 35(1):25–30
12. Aydin I, Karakose M, Akin E (2012) A new contactless fault diagnosis approach for pantograph-catenary system. In: MECHATRONIKA, 15th International Symposium. IEEE, pp 1–6
13. Luna Vázquez CA, Mazo Quintas M, Marrón Romera M (2010) Non-contact sensor for monitoring catenary-pantograph interaction. In: IEEE International symposium on industrial electronics (ISIE), pp 482–487
14. Wanju Y (2003) High-speed electric railway catenary. Southwest Jiaotong University Press, Chengdu
15. Liu W, Liu Z, Zhang G et al (2014) Correction of detected value of catenary geometric parameters based on camera calibration and Kalman filtering. J China Railway Soc 36(9):28–33
16. Jiang M, Qin X, Shang T et al (2010) Tracking algorithm based on particle filtering and mean-shift. Comput Eng 36(5):21–25
17. Shan C, Tan T, Wei Y (2007) Real-time hand tracking using a mean-shift embedded particle filter. Pattern Recogn 110(7):175–197
18. Li K, Kehu X, Huang D (2012) Improved object tracking method based on mean shift and particle filter. J Comput Appl 32(2):504–506
19. Liu W, Liu Z, Gen X et al (2015) Research on detection method for geometrical parameter of catenary system based on mean shift and particle filter algorithm. J China Railway Soc 37 (11):30–36
20. Shiqiang, Zhongliang J (2010). The theory and application of particle filtering. Science Press, Beijing
21. Liu JS, Chen R (1995) Sequential Monte Carlo methods for dynamical systems. J Am Stat Assoc 90:567–576

Chapter 5
Slide Plate Fault Detection of Pantograph Based on Image Processing

5.1 Introduction

The pantograph faults mainly include four types.

(1) Pantograph component damage

The structure of pantograph is complex. During the train's operation, the pantograph is influenced by the contact pressure, friction, temperature and so on, which can result in some faults of the pantograph's components.

(2) Slide plate loss of pantograph

Because the powder metallurgy slide plate is fixed by screw, the collision and vibration can easily cause the screw loosening during the train's operation, and result in the slide plate loss.

(3) Slide plate wear of pantograph

There are mainly mechanical wear and electrical wear for the pantograph slide plate. Since the train power is supplied through the contact between the pantograph and the catenary, it is difficult to avoid the wear of pantograph slide plate. In addition, because the new contact line surface has some hard burrs, and the used contact line surface has some dirt, the poor contact will form the electric spark and cause serious electrical wear.

(4) Slide plate crack of pantograph

Because the arc burning or oxidation can reduce the strength of pantograph slide plate, when the pantograph passes some irregular points of contact line, the slide plate of pantograph may be broken. The slide plate cracks often result in serious accidents, such as scraping pantograph, and these accidents directly influence the train' safe operation.

Z. Liu, *Detection and Estimation Research of High-speed Railway Catenary*,
Advances in High-speed Rail Technology, DOI 10.1007/978-981-10-2753-6_5

In [1], the online monitoring method was proposed through mounting detection device in the pantograph, which could influence the pantograph performance. In [2], the optical measurement method was proposed to detect the pantograph's wear. The ultrasonic detection method was adopted to detect the pantograph's wear in [3]. The image processing and pattern recognition technologies have high degree of freedom and the modification of pantograph is unnecessary for the online monitoring method of pantograph. Therefore, some researches based on image processing and pattern recognition technologies have been carried out. In [4], the detection method based on image processing was adopted in the detection system of pantograph-catenary system. The slide plate wear detection of pantograph used the methods based on image processing in [5, 6]. At present, the researches on the slide plate faults were focused on the detection of slide plate wear [6, 7], and the researches on the bad state detection of the slide plate surface, such as crack, are less seen. In addition, since the fault characteristic of slide plate loss is very obvious and the term of slide plate wear is very long, the research in this chapter mainly focuses on the slide plate crack of pantograph.

5.2 Features of Pantograph Slide Plate Image

5.2.1 Pantograph Structure

The pantograph is composed of the bow head, rod and hinge devices. The bow head is composed of the supporting device, guiding device, contact plate, bracket and bow angle. The contact plate is also called slide plate, and its surface is directly contacted with the contact line, whose main function is to collect the current. The bow angle is formed at the end of bow head, which can ensure the close contact with the contact line. The general structure of pantograph is shown in Fig. 5.1.

According to the different materials, the pantograph slide plate can be classified into two types, namely powder metallurgy slide plate and carbon slide plate. The applications of powder metallurgy slide plate are more common. There are two rows, each row has 5 slide plate bars, and 5 slide plate bars are arranged into a line.

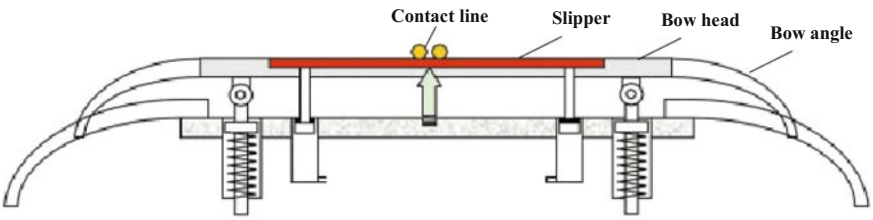

Fig. 5.1 Sketch figure of pantograph general structure

Each slide plate bar is fixed with two screws from its back. Carbon slide plate is mainly used for the new pantograph, each pantograph requires two carbon slide plates, and the length of a slipper is equivalent to the sum of the length of 5 powder metallurgy slide plates. Because the carbon slide plate is soft, its wear is more severe and it needs to be replaced frequently.

5.2.2 Pantograph Slide Plate Type

According to the different materials of pantograph slide plate, there are pure carbon, powder metallurgy and impregnated metal carbon pantograph slide plates.

(1) At present, pure carbon slide plate is one of the most mainly used slide plates in electrical railway in China. The mechanical strength of pure carbon slide plate is relatively low, the bending strength is 30–40 MPa and the compressive strength is 60–80 MPa. Because the impact resistance is poor, it sometimes breaks during operation and can easily cause pantograph scraping accident. In addition, due to the fluctuation of various factors during the production, the performance of pure carbon slide plate is uneven. The wear is frequently occurred, and the service life is relatively short.
(2) Powder metallurgy slide plate belongs to the metal base slide plate. According to the different sintering material, it includes copper base and iron base. The iron base is suitable for steel and aluminum wire, and the copper base is suitable for copper wire. Powder metallurgy slide plate has high mechanical strength, good toughness, good abrasion resistance, and strong impact resistance performance. In addition, the phenomenon of fracture is relatively less, and the resistance is very small, which is favorable to the current collection of electric locomotive. In this chapter, the slide plate means the powder metallurgy one.
(3) The material of impregnated metal carbon slide plate has both the self-lubrication property of pure carbon slide plate, and the high mechanical strength and impact resistance property of powder metallurgy slide plate. In addition, it has high arc resistance, low contact resistance with contact wires, low self-resistance, good thermal conductivity and good thermal dissipation. But, its price is high and the maintenance costs are also relatively high.

5.2.3 Image Features of Pantograph Slide Plate

In this chapter, the powder metallurgy slide plate is as the experimental object. Each pantograph head is equipped with two mutually parallel slide plates, and each slide plate is respectively connected with five short slide bars through the fixed screws.

In order to correctly extract the crack characteristic in pantograph slide plate, above all, the image elements in the slide plate should be analyzed. The main image elements in the slide plate are shown in Fig. 5.2.

In order to more clearly demonstrate the image elements in pantograph slide plate image, the binarization processing of Fig. 5.2 is performed, and the threshold of binarization processing for the gray histogram of slide plate is obtained by using OTSU algorithm. The gray histogram of slide plate is shown in Fig. 5.3.

It can be found that there are two obvious peaks, the right side peak involves a large gray range, and the gray value is also higher, which is corresponding to the normal work surface of pantograph slide plate image. The left side peak involves a small gray range, and the gray value range is narrow, which is corresponding to the edges, parallel seams, screws and cracks in slide plate image. Because the gray value of the scratch in slide plate image is similar to that of image background, their gray value is located in the right side of gray histogram.

The valley between the two peaks is the threshold value of the binarization processing, which can be obtained by OTSU algorithm. The image can be divided into two classes. One is corresponding to the image background, and the other is corresponding to the parallel seams, screws and cracks in slide plate image. Therefore, the variance in the two kinds of gray values is the smallest, and the variance between the two classes is the largest.

If the gray scale in an image is $1 \sim m$, suppose that the image is divided into $C_1 = \{1, 2, \ldots, k\}$ and $C_2 = \{k+1, k+2, \ldots, m\}$, their production probabilities ω_1 and ω_2 can be calculated, as well as the mean value μ_1 and μ_2. The gray mean value μ of whole image can be also obtained.

$$\sigma^2(k) = \omega_1(\mu_1 - \mu)^2 + \omega_2(\mu_2 - \mu)^2 = \omega_1\omega_2(\mu_1 - \mu_2)^2 = \frac{[\mu\omega(k) - \mu(k)]^2}{\omega(k)[1 - \omega(k)]} \tag{5.1}$$

If k changes in $1 \sim m$, when the variance $\sigma^2(k)$ between the classes is maximum, the k is the threshold of binarization processing. After the threshold is obtained, the binarization processing of image is performed as follows.

$$g(x, y) = \begin{cases} 1 & f(x, y) \le T \\ 0 & f(x, y) > T \end{cases} \tag{5.2}$$

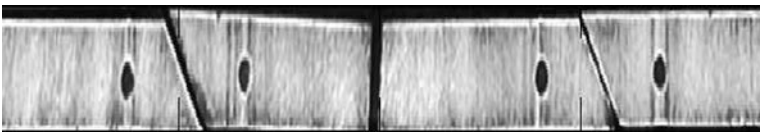

Fig. 5.2 Pantograph slide plate image

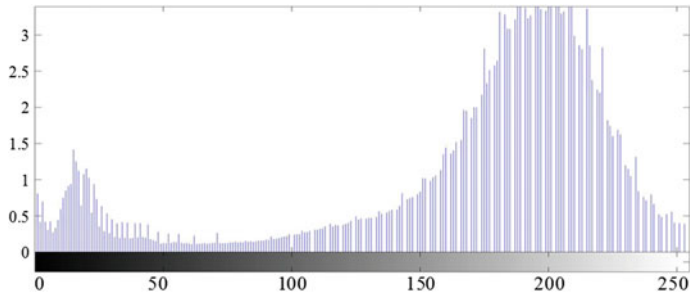

Fig. 5.3 Gray histogram of slide plate

Thus the binarization image can be obtained in Fig. 5.4. The image features, such as slide plate edges, parallel seams, screws and cracks, can be clearly found.

The description of main image features of pantograph slide plate is listed as follows:

(1) When the pantograph slide plate image is extracted, because the slide plate image is not in accordance with the standard linear horizontal direction of the pantograph, considering the precision of algorithm, it is very difficult to strictly extract the edge along the actual edge line, which results in that some parts of background image are extracted. As shown in Fig. 5.4, the background image is included in the slide plate image.

(2) The powder metallurgy slide plate consists of 5 short slide bars with the same size that are linked the front and back. The shape of short slide bar is a parallel quadrilateral with 135° angle hypotenuse. Thus, in the slide plate image, there are some seams with 135° angle direction, and they are parallel to each other, and have the same size. In addition, the distance between two adjacent seams is also equal.

(3) The powder metallurgy slide plate is fixed in the pantograph by screws. There are two screws on each short slide. The size of the screw is the same. The position and the distance have the obvious regularity.

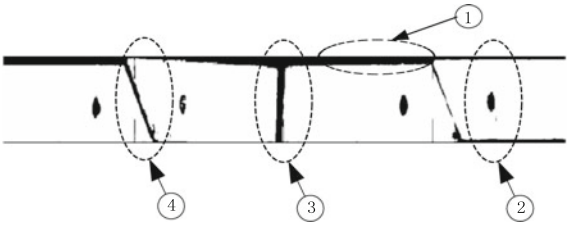

Fig. 5.4 Binarization image of pantograph slide plate. ① Slide plate edge; ② screw; ③ crack; ④ parallel seam

① slide plate edge; ② screw; ③crack; ④parallel seam

(4) The tight contact between catenary and pantograph ensures the current collection for train operation. Because the layout of contact line is "zigzags", it can result in the scratches in pantograph during the train operation. The scratches are generally zonal distribution, and their directions are basically same in a certain area. In the whole area, the scratches direction is within 45–135°.
(5) Although the mechanical strength of powder metallurgy slide plate is high and the toughness is good, it may lead to the fracture of slide plate and form a crack during the train's high-speed operation, when the impact of the hard point happens. Due to the occasional failure of pantograph, the position, length and shape of cracks in the slide plate are random and there is no regularity.

In Fig. 5.3, the crack is in the middle position of slide plate, the length is equal to the width of slide plate, and the direction is vertical.

Based on the analysis of pantograph image characteristics, the inherent image elements in pantograph have obvious regularity. Although the location and shape of crack are not fixed, they can be distinguished by using other characteristics of image element.

5.3 Characteristics of Pantograph Slide Plate Image Based on Curvelet Transform

For the two-dimensional image of pantograph in electrical railway, the image features are in different scales and different directions. Therefore, the traditional Fourier transform and wavelet transform cannot meet the requirements of the characteristics analysis. In this chapter, Curvelet transform is adopted as the main processing method for pantograph image.

It is known that the wavelet transform has some limitations for image processing, which can only be used to better represent one-dimensional function with singular point, but it is not the optimal representation for the high dimensional function with the singular line or singular surface. In 1998, Candès proposed the two-dimensional continuous Ridgelet transform in his dissertation [8]. The idea of this transform is that the one-dimensional singular features (line singular) are mapped into the zero dimensional (point singular) features by using the Radon transform, and then the wavelet transform is performed. Then, the construction algorithm of orthogonal Ridgelet transform was proposed by Donoho [9]. In 1999, Candès proposed the single scale Ridgelet transform, which can realize the construction of multi-variable function with curve singularity [10]. Ridgelet transform is considered as the best base that represents multi-variable function with line singularity in general. But for the curve edge description of image, the approximation performance is only equivalent to the wavelet transform. In 1999, Candès and Donoho put forward the theory of Curvelet transform [11]. Curvelet transform

can better realize the sparse representation for two-dimensional signal with multi-scale, multi direction and anisotropy. Curvelet transform was originally for the ridge wave block localized processing, and its mathematical theory is not perfect enough. In 2002, Candès put forward the new curvelet transform [12], which was called the second generation curvelet transform. In 2005, the discrete algorithm of second generation Curvelet transform was proposed in [13]. Compared with the first generation of curvelet transform, the parameter number of second generation curvelet transform is reduced from 7 to 3, which makes the realization greatly simplified, and easier to understand. The computation speed of second generation curvelet transform is only 6–10 times as that of Fast Fourier Transform (FFT) [13]. In addition, there is also a great improvement on redundancy for second generation curvelet transform.

5.3.1 Curvelet Transform

1. Radon transform

The ridgelet transform is the basis of the first generation curvelet, and the Radon transform is the important connection of continuous wavelet transform and ridgelet transform. In fact, the coefficients of ridgelet transform are the wavelet decomposition results of image in Radon domain.

If function $f(x, y) \in L^2(D)$ is square integrable in domain D of plane, the Radon transform of $f(x, y)$ is represented as follows.

$$Rf(\theta, t) = \iint_D f(x, y)\delta[t - (x\cos\theta + y\sin\theta)]dxdy \tag{5.3}$$

where δ is the unit pulse function, $t - x\cos\theta - y\sin\theta = 0$ is an arbitrary straight line in polar coordinates. The process is shown in Fig. 5.5.

The essence of Radon transform of image is the projection of image in each direction. The project in any angle θ direction of image $f(x, y)$ is defined as follows.

$$R_\theta(x') = \int_{-\infty}^{+\infty} f(x'\cos\theta - y'\sin\theta, x'\sin\theta - y'\cos\theta)dy' \tag{5.4}$$

where $\begin{pmatrix} x' \\ y' \end{pmatrix} = \begin{pmatrix} \cos\theta & \sin\theta \\ -\sin\theta & \cos\theta \end{pmatrix} \begin{pmatrix} x \\ y \end{pmatrix}$.

2. Ridgelet transform

In two-dimensional space, Radon transform is connected with the line. The straight line, plane or hyper plane are mapped into a point in the two-dimensional

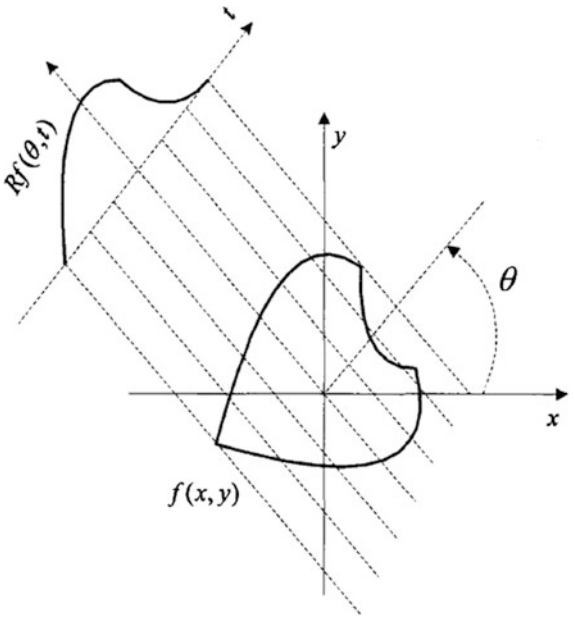

Fig. 5.5 Diagram of Radon transform

space. Wavelet transform can optimize sparse representation of signal singularity. Therefore, the ridgelet transform can be considered as the one-dimension wavelet transform in Radon domain [8], which is represented below.

$$RFT_f(a,b,\theta) = \int_{R^2} \psi_{a,b}(x) R_f(\theta,t)dt \tag{5.5}$$

where $\psi_{a,b}(x) = a^{-1/2}\psi\left(\frac{x-b}{a}\right)$. As seen from the above, the ridgelet transform is the one-dimensional wavelet transform in Radon domain.

The reconstruction formula is shown as follows.

$$f(x) = C_\psi \int RFT_f(a,b,\theta)\,\psi_{a,b,\theta}(x)\frac{da\,db\,d\theta}{a^3} \tag{5.6}$$

where $C_\psi = (2\pi)^{-2}K_\psi^{-1}$.

The ridgelet transform process is shown in Fig. 5.6 [8].

3. The first generation curvelet transform

The ridgelet transform can overcome the shortcoming of wavelet transform that can only effectively express the point singularity. It is a kind of analysis tool that can solve the line singularity or plane singularity. Compared with wavelet transform, the ridgelet transform has certain advantages for linear edge detection of image. But in the image, the number of straight lines is little, and the curve is in the

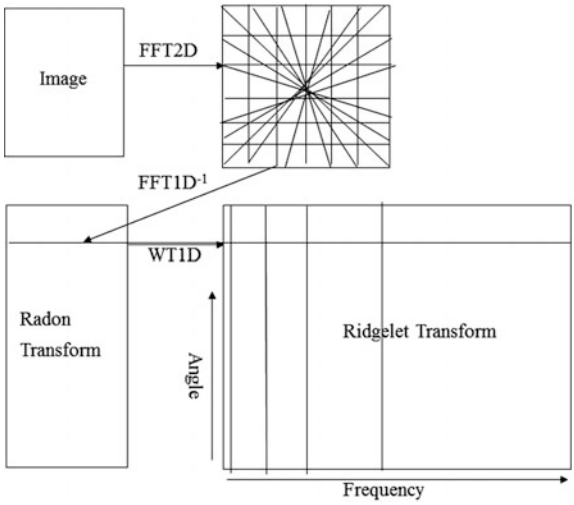

Fig. 5.6 Diagram of ridgelet transform

majority. Therefore, the image is divided into some small block areas, so that each area of the curve can be approximated as a straight line. Then, if the ridgelet transform is performed for each area, the favorable results can be achieved.

The first generation curvelet transform is essentially the ridgelet transform in multiple scales. First, the image is filtered through subband decomposition. The image is divided into the subband in different scales. Then, the images in each subband are performed with ridgelet transform.

The curvelet base satisfies the anisotropic relationship, namely:

$$width \approx length^2 \tag{5.7}$$

This relationship shows that curvelet is a kind of directional base. In the scale relationship of curvelet, from one scale to the next, the spatial resolution and the angular resolution are double times higher than those of previous scale. The process of first generation curvelet transform is shown in Fig. 5.7 [11].

4. The second generation curvelet transform

Some parameters are introduced first.

- Scale parameter: j
- Rotation angles: $\theta_l = 2\pi \cdot 2^{-\lfloor j/2 \rfloor} \cdot l$, $l = 0,1, \ldots, 0 \le \theta_l \le 2\pi$
- Translation parameters: $k = (k_1, k_2) \in Z^2$

So, the second generation curvelet transform can be defined by:

$$C(j,l,k) = \frac{1}{(2\pi)^2} \int \hat{f}(\omega) U_j(R_{\theta_l}\omega) e^{i\left\langle x_k^{(j,l)}, \omega \right\rangle} d\omega \tag{5.8}$$

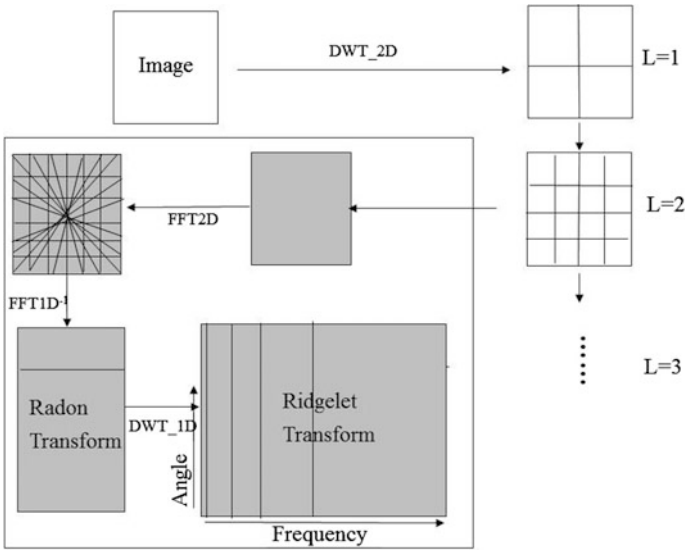

Fig. 5.7 Diagram of first generation curvelet transform

where $\hat{f}(\omega)$ is the signal in the frequency-domain, r and θ are the polar coordinates in the frequency-domain. $U_j(r,\theta) = 2^{-3j/4} W(2^{-j}r) V(\frac{2^{\lfloor j/2 \rfloor}\theta}{2\pi})$ is the frequency window. W is the radial window and V is the angular window. From the formula (5.8), it can be concluded that the curvelet transform has explicit directivity besides the multiscale property.

Another advantage of the curvelet is the approximation performance. The best m-term curvelet approximation obeys

$$\|f - f_m\|_{L_2}^2 \leq C \cdot (\log\, m)^3 \cdot m^{-2} \tag{5.9}$$

Compared with the Fourier approximation and the wavelet approximation, the curvelet approximation has better performance. More information can be represented with less data and more concentrative energy. For all these reasons, the curvelet transform is suitable for the image processing.

Although the curvelet transform has been wide adopted in the image processing, it has also some demerits as follows, which influence the usage of curvelet transform in the image recognition fields.

- There are too many data in the curvelet transform result.
- The coefficients of curvelet transform are distributed in the decomposition matrices with different angle. It is difficult to analyze the whole image's characteristic through the relationship between them.
- There are massive coefficients of type A and B [12] for the characteristics of the curvelet transform. They are useless in analyzing the image.

5.3.2 Curvelet Coefficient Directional Projection Transform

To make full use of the curvelet transform to recognize the images, the useful information from the curvelet transform matrices is very necessary for the analysis. Therefore, a new transformation called curvelet coefficients directional projection (CCDP) is presented in this section [14]. The key point of the CCDP transform is the explicit usage of the curvelet's directivity. Through the CCDP transform, the high dimension information in the curvelet transform matrices at a fixed scale j is projected to the 2-dimension θ–D (decomposition angle–location point) coordinates, so that the whole characteristics of the image represented by the curvelet decomposition coefficients at the scale j can be analyzed in a single matrix. In this way, the characteristics of the image distributed in the decomposition matrices with different angle can be concatenated and be obtained more easily.

(1) CCDP transform principle

From the definition of curvelet transform, it can be found that through the expansion, rotation, and translation of the curvelet elements shown in Fig. 5.8, the local linear characteristics of the image can be obtained with the multi-scale and multi-angle decomposition.

Therefore, the decomposition matrix M_{j,θ_l}, actually uses a curvelet of $scale = j$ and $angle = \theta_l$ to decompose the image. This means only the information along the θ_l direction in an image, and the local linear singularity along the θ_l direction can be detected by some curvelets in the matrix M_{j,θ_l}, shown in Fig. 5.9 (each ellipse stands for a curvelet).

Thus, the distribution of curvelet decomposition coefficients is also along with θ_l' for the edge with the local linear singularity along θ_l, where θ_l' is the corresponding angle of θ_l in the matrix M_{j,θ_l} (for the different size between the original image and

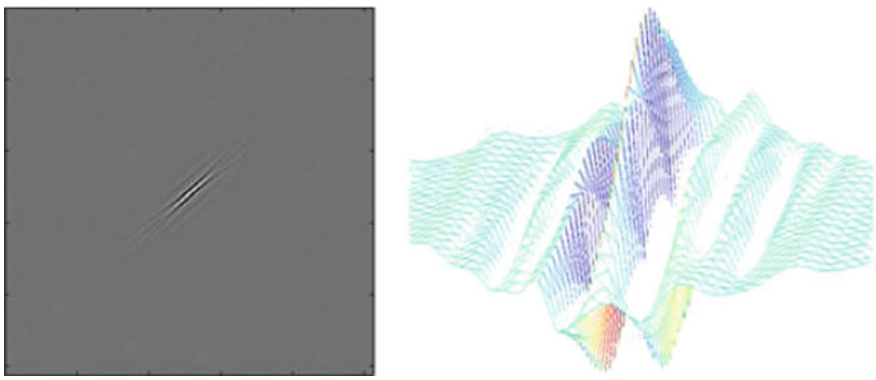

Fig. 5.8 Curvelet elements figures (the *left* figure represents the curvelet in the plane and the *right* figure represents the curvelet in the tridimensional space)

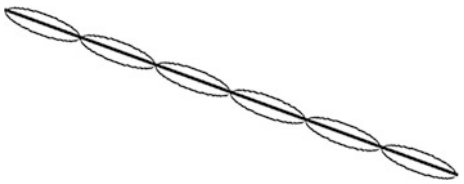

Fig. 5.9 Curvelet decomposition along a line

the matrix M_{j,θ_l}. The line with angle θ_l in the original image will be θ_l' direction in the matrix M_{j,θ_l}, correspondingly). θ_l' is called the coefficient distribution angle (CDA). Therefore, it is enough to study the coefficients along θ_l', and all information of the local linear edge along angle θ_l in the image can be obtained. The CCDP transform is a kind of linear transform for the coefficients in the matrix M_{j,θ_l} essentially.

2. Calculation of CDA-θ_l'

In order to get the information along θ_l, the CDA-θ_l' in the matrix M_{j,θ_l} should be calculated first. Suppose that the size of original image $I(x, y)$ is $X \times Y$, where X is the row and Y is the column of image respectively. The size of matrix M_{j,θ_l} is $a \times b$ ($row \times column$). The angle θ_l' in the matrix M_{j,θ_l} corresponding to the angle θ_l in the original image can be calculated by:

$$\theta_l' = \arctan\left(\frac{aY}{bX} \times \tan\ \theta_l\right) \tag{5.10}$$

(3) CCDP transform

a. Implementation of CCDP transform
The CCDP transform is illustrated in Fig. 5.10. The transformation can be defined by

$$f_j(\theta, D) = CCDP(M_{j,\theta_l}(x, y)) = C(M_{j,\theta_l}(x, y) \cdot \delta(Line_{(\theta_l', D)})) \tag{5.11}$$

where $l = 0, 1, \ldots, 0 \le \theta_l \le 2\pi$. $C(M_{j,\theta_l}(x, y) \cdot \delta(Line_{(\theta_l', D)}))$ is the linear function along θ_l' direction, and D is a fixed point in the *Line*. The CCDP transform's projective value is a complex number $G + jL$, so that more information can be reserved during the CCDP transform.
Through CCDP transform, a curvelet angle decomposition matrix M_{j,θ_l} can be projected to a line that is perpendicular to θ axis. And all curvelet transform angle decomposition matrix at a fixed scale j is projected to the 2-dimension θ–D (decomposition angle–location point) coordinates. The

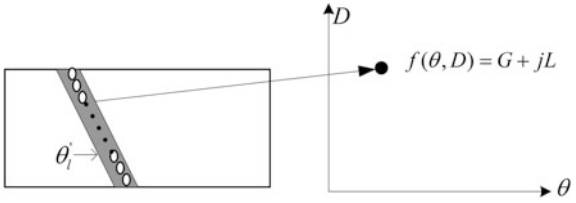

Fig. 5.10 CCDP transform principle figure

whole characteristics of the image represented by the curvelet decomposition coefficients at the scale j can be obtained in a single matrix $f_j(\theta, D)$. In this way, the dimension of the data can be reduced, and the characteristics of different direction in the image can be explicit. In all, the CCDP transform can make the analysis and the recognition of image easier than those in the original curvelet decomposition matrices.

b. Choices of location point—D

From Fig. 5.11, it is clear that for the different slopes of θ_l', the choices of location point—D are also different.

Now, k stands for the diagonal's slope and $k_{\theta_l'}$ stands for the line's slope along θ_l' in M_{j,θ_l}. If the situation is like L_1, the locating point—D must use the row coordinate value. If the situation is like L_2, the locating point—D must use the column coordinate value. The choices of the coordinate value depend on the magnitude of $k_{\theta_l'}$ compared with k.

$$O_D = \begin{cases} 0 & \left|k_{\theta_l'}\right| < |k| \\ 1 & \left|k_{\theta_l'}\right| \geq |k| \end{cases} \tag{5.12}$$

where O_D represents the choices of location point. Zero means that D is the row coordinate value (just like L_1) and one means that D is the column coordinate value (just like L_2).

c. Angle θ_l

According to the definition of curvelet transform, $1 \leq \theta_l \leq 2\pi$ is clear. Based on the symmetry of curvelet, a curvelet of θ_l and a curvelet of $\theta_l + \pi$ can detect the same characteristics of the image. It means that all

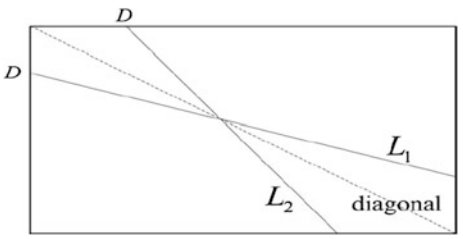

Fig. 5.11 Choice of location point

information by using a series of curvelets in the angle $1 \leq \theta_l \leq \pi$ can be obtained. Therefore, in the CCDP transform, only a half of the decomposition matrices will be projected to the θ–D coordinates, which will speed up the computation and reduce the redundancy of information.

4. Projective value in $f_j(\theta, D)$

Until now, the calculation of projective value in $f_j(\theta, D)$ has not been discussed. The reason is that for the different purposes, the projective values $G + jL$ have the different choices. By doing this, more useful information can be preserved appropriately during the CCDP transform for a particular application. Generally speaking, G includes the global information and L includes the local information along θ_l'. The choice of $G + jL$ called the "line integral (G) + coefficients locating encoding (L)" will be mainly discussed.

a. Choice of G—line integral

For the projective value of "line integral (G) + coefficients locating encoding (L)", G includes the global information that is represented with the line integral along θ_l', defined as follows.

$$G_j(\theta, D) = \sum_{\substack{1 \leq x \leq a \\ 1 \leq y \leq b}} \left| M_{j,\theta_l}(x, y) \cdot \delta(Line_{(\theta_l', D)}) \right| \tag{5.13}$$

Therefore, if there is a linear edge along θ_l direction in the image, the projective value G will be a local maximum value in the CCDP transform matrix.

b. The parameter L includes the local information along θ_l of image. The coefficient locating encoding is a kind of binary encoding. It is used to represent the location of coefficients that are higher than the threshold T in the $Line(\theta_l', D)$. The threshold T that determines the kind of linear edge is needed for the image processing.

As shown in Fig. 5.9, each coefficient point along θ_l' corresponds to a binary bit. If the coefficient is higher than the threshold T, it means this coefficient point is a desirable local linear edge and the corresponding point of L is to be 1. For representing the numbers of coefficients N in $Line(\theta_l', D)$, the location $N + 1$ of L is to be 1. The coefficient locating encoding is represented by

$$L = 2^N + \sum_{k=0}^{N-1} 2^k \cdot sig(coefficient) \tag{5.14}$$

where

$$sig(coefficient) = \begin{cases} 0 & if\ coefficient < T \\ 1 & if\ coefficient \geq T \end{cases} \tag{5.15}$$

c. Extracting the information from L

In general, there are two methods for extracting the information from L.

The first step is to use log operator to get all bits' location of 1. For each loop, k can detect a bit of 1.

$$\begin{aligned} &While \quad L \neq 0 \\ &\quad k = \lfloor \log_2 L \rfloor \\ &\quad L = L - 2^k \\ &End \quad loop \end{aligned}$$

The second step is to use a template to detect whether a fixed bit is 1. In order to know whether the kth bit is 1, a "bitwise AND" operation of L with 2^{k-1} can be calculated. If the answer is 0, the kth bit is 0. Otherwise, the kth bit is 1.

d. Other possible choice of projective value

Besides the projective value of "line integral (G) + coefficients locating encoding (L)", some other possible choices of the projective value can also be obtained.

G is the coefficients' mean in the $Line(\theta_l', D)$, and L is the coefficient's number that is higher than the threshold T. If we need not to know the location details of the coefficients, this scheme is fast and easy to use.

5.3.3 Characteristics of Pantograph Slide Plate Image

In order to distinguish the different elements in the slide plate image, it is necessary to study the slide plate image's composition and obtain the curvelet decomposition coefficients' distribution characteristics. The main elements in the pantograph slide plate's image are shown in Fig. 5.12.

The main elements include:

- Some backgrounds are included in the slide plate image and become the interference. It is called the slide plate edge extract defects.
- In the powder metallurgical slide plate, there are slide plate joints and rivets.
- There are slide plate scratches because of the friction between the slide plate and the catenary.
- The slide plate cracks maybe exist.

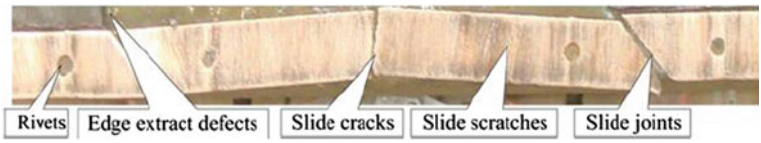

Fig. 5.12 Pantograph slide plate image

(1) The coefficients' distribution of the slide plate edge extraction defects

It is difficult to partition the slide plate's image along the slide plate edge strictly because of the algorithm's precision when the pantograph slide plate's image is partitioned from the image originated from the cameras. Some backgrounds are included and become the interference. In the edge of the partitioned image, the explicit boundaries exist. There are high and horizontal coefficients in the edge of curvelet decomposition matrix $M_{j,0}$. The typical figure of coefficients' distribution is shown in Fig. 5.13.

(2) The coefficients' distribution of slide plate joints and rivets

The powder metallurgical slide plate is composed of some small parallelogram blocks. The edge of the parallelogram block is about $3\pi/4$. The adjacent joints are parallel and equidistant. The coefficients' distribution in curvelet decomposition matrix $M_{j,3\pi/4}$ is shown in Fig. 5.14.

The rivets are small and circular, and the coefficients of rivets are small and are distributed into all of the curvelet decomposition matrices. The influence of the rivets is negligible when the slide plate cracks are detected. Therefore, the rivets' coefficients need not to be processed specially.

(3) Coefficients' distribution of slide plate scratches

The electric locomotives obtain power via catenary pantograph coupling. There is the mechanical friction between the pantograph slide plate and the catenary. The scratches are shaped in the pantograph slide plate's surface gradually. The slide plate scratches are zonal with the similar angles in the adjacent domain. The slide plate scratches' edge is a gradually vibrational one compared with the slide plate joints' sharp edge. Therefore, the curvelet coefficients are lower than the slide plate joints' coefficients. The typical figure of coefficients' distribution is shown in Fig. 5.15.

Fig. 5.13 Coefficients' distribution of slide plate edge extraction defects

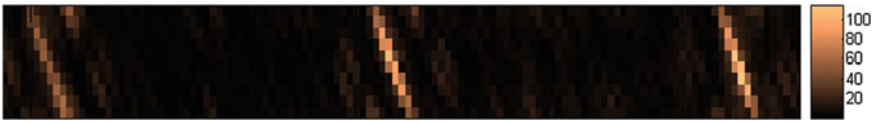

Fig. 5.14 Coefficients' distribution of slide plate joints

Fig. 5.15 Coefficients' distribution of slide plate scratches

(4) Coefficients' distribution of slide plate cracks

Because of the external force and other reasons, the pantograph slide plate may produce the cracks. It is the momentous safety hazard to the train operation. The slide plate crack is a kind of sharp edge just as the slide plate joints. Although the shapes are irregular, the slide plate cracks can be obtained after eliminating other coefficients analyzed above. The typical figure of coefficients' distribution is shown in Fig. 5.16.

Based on the analysis of decomposition results for pantograph slide plate with curvelet transform, the coefficient statistics characteristics of different pantograph slide plate images are listed in Table 5.1 [15].

In Table 5.1, it can be found that the curvelet decomposition coefficients of scratches are located in the matrix with $\pi/4-3\pi/4$ direction. Since the shape of screw is circle, its curvelet decomposition coefficients are located in the matrix with all directions. Though the curvelet decomposition coefficients of background, screw and scratch are located in the wide range, the coefficient range is very different from that of joints. The classification can be performed by using the global threshold. The curvelet decomposition coefficients' distributions of joints and cracks are similar, namely, the coefficients of 4 joints are located in the matrix with same angle, and the area interval of high coefficients is approximately equal. Thus, the special classification should be performed.

Fig. 5.16 Coefficients' distribution of slide plate cracks

Table 5.1 Coefficient characteristics of pantograph slide plate image

	Direction angle	Coefficient value	Coefficient number	Coefficient ratio (%)
Parallel joints	$3\pi/4$	[36, 63]	416/129,544	0.32
Cracks	–	[35, 76]	156/129,544	0.12
Scratches	$[\pi/4, 3\pi/4]$	[5, 15]	7958/129,544	6.14
Screws	$[0, 2\pi]$	[10, 15]	1080/129,544	0.83
Background	$[0, 2\pi]$	[0, 5]	119,934/129,544	92.59

5.4 Pantograph Slide Plate Crack Extraction Based on Translational Parallel Window in Curvelet Transform Domain

5.4.1 Extraction Algorithm of Cracks

Through the global threshold of coefficients, the pseudo fault features in the pantograph slide plate can be filtered, and the features of cracks and parallel joint are remained. Therefore, the fault features in the slide plate image can be divided into three types, namely crack, parallel joint and other pseudo fault features. For the parallel joint, the direction is $3\pi/4$ and the interval is same in the location. In this section, the algorithm based on translation parallel window is presented to extract the crack features through processing the parallel joint in the slide plate image.

Suppose that the size of slide plate image is $M \times N$. The image is decomposed with curvelet transform, the decomposition level number is n, the $n-1$th level is composed of the matrix with l directions. $l = (l_1, \ldots, l_l)$ represents the different decomposition directions. If the parallel joint at $3\pi/4$ direction is corresponding to the l_kth direction matrix in the curvelet decomposition matrix, the matrix can be represented with $C\{n-1\}\{k\}$, and its size is $M' \times N'$.

In Fig. 5.17, the direction of parallel joint is $3\pi/4$ and relatively regular, and its coefficients of curvelet decomposition are higher than those of background and other regular elements, which show obvious line singularity features. Therefore, after the curvelet decomposition, in the matrix $C\{n-1\}\{k\}$, the parallel joint is

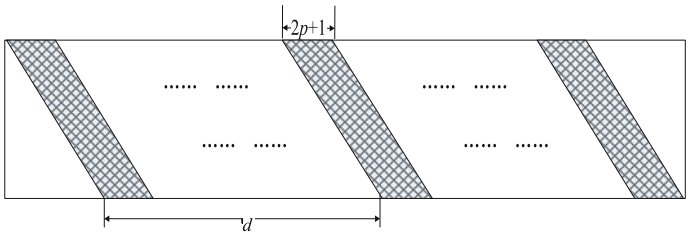

Fig. 5.17 Schematic diagram of parallel moving window

corresponding to the zonal parallel region with higher coefficients, and the width of zonal parallel region and their intervals are roughly equal. Correspondingly, in the curvelet decomposition matrix, the direction of crack's zonal parallel region is approximately is $3\pi/4$. Since the direction of zonal region is parallel and their intervals are the same, the moving parallel window can be adopted to extract the features of parallel joint [16].

As shown in Fig. 5.17, three rectangular windows composed of parallel quadrilateral with $3\pi/4$ direction are constructed. The parallel quadrilateral's horizontal width is $(2p+1)$, the vertical height is the column number of matrix N', and the interval between the adjacent parallel quadrilateral windows is d. The matrix elements corresponding to the shadow part in the rectangle window are set to be 0 and other is set to be 1, as shown below.

$$A_{ij} = \begin{cases} 1 & \begin{pmatrix} 1 \le i \le M' \\ i + kd \le j \le i + (2p+1) + kd \\ k = 0, 1, 2 \end{pmatrix} \\ 0 & else \end{cases} \tag{5.16}$$

where $(2p+1)$ is the horizontal side length, and d is the distance between the adjacent parallel quadrilateral windows.

The rectangle window is adopted to process the direction matrix of curvelet decomposition coefficients, as shown below.

$$C'\{n-1\}\{k\} = A_{ij} \cdot |C\{n-1\}\{k\}| \tag{5.17}$$

where $C'\{n-1\}\{k\}$ is the curvelet decomposition coefficient matrix after window filtering. The element value in the three zonal regions is corresponding to the absolute value of curvelet decomposition coefficient, and the element value out of the regions is 0.

Based on the features of parallel joint coefficients, since there are four parallel joints with the same size and shape in the slide plate, there will be four parallel zonal regions with large numbers of numerical values in the matrix $C'\{n-1\}\{k\}$. Since the element' absolute value in the zonal regions is higher and the distance between the adjacent parallel quadrilateral windows is equal, the accurate locations of the zonal regions can be obtained, which can efficiently distinguish the parallel joint and the crack in the slide plate.

From the first column in the curvelet decomposition direction matrix, the rectangle windows are translated to the right in turn by $step = 1$, and the energy sum SPW of each translated rectangle window is calculated. The one-dimension vector for each translated rectangle window energy sum can be obtained.

$$SPW(t) = \sum_{i=1}^{M'} \sum_{j=t}^{t+\{N'-[(2p+1)+d]\}} [C\{n-1\}\{k\}(i,j)]^2 \tag{5.18}$$

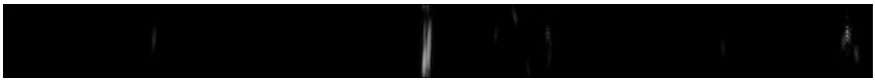

Fig. 5.18 Extraction result of cracks in pantograph slide plate image

It can be found that when three zonal parallel regions in the translated rectangle window match the parallel joint, the energy value is obviously larger than the energy value in other cases, and is the element's maximum value of one-dimension vector. Because there are four parallel joints in powder metallurgy slide plate in general, the maximum value of window energy will occur two times, namely $SPW(t_1)$ and $SPW(t_2)$. Therefore, according to the locations of maximum value, the accurate locations of parallel joints in the slide plate image can be quickly obtained, and then the parallel joints of slide plate are filtered.

The cracks and parallel joints can be distinguished based on the crack extraction algorithm based on the translation window. The regions of parallel joints corresponding to the direction matrix can be processed with the threshold. Thus, after the coefficients of scratches, screws, parallel joints and edges are processed, if the line or approximate line singularities still exist, they are considered as the crack fault.

The algorithm is used to extract the crack in pantograph slide plate image, as shown in Fig. 5.12, the extraction result is shown in Fig. 5.18. It can be found that the crack faults can be accurately extracted and their locations can also be efficiently positioned.

If there are some cracks that are parallel to the joint direction, the situation that the cracks have equal interval and are parallel to three parallel joints at the same time will never occur. Even if there are the cracks with the $3\pi/4$ direction, the general maximum is only one. In addition, the SPW value of single crack in the rectangle window is much lower than that in the three parallel joints situation. It cannot be misjudged as the joint. Therefore, whether the crack direction is parallel to the direction of the joint, it can be recognized.

The slide plate image including the crack that is parallel to the parallel joint is chosen to verity the algorithm, as shown in Fig. 5.19. The slide plate image includes two cracks, one is in vertical direction and in the center of slide plate, and the other is in the parallel joint direction and in the slide plate's left. The extraction result is shown in Fig. 5.20.

Based on the results in Fig. 5.20, it can be found even if there are the cracks that are parallel to the joints in pantograph slide plate images, the cracks can be accurately detected and located.

Fig. 5.19 Slide plate image with two cracks

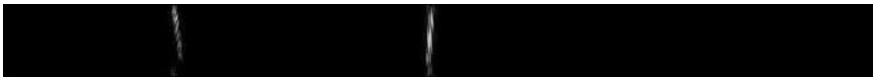

Fig. 5.20 Extraction result of slide plate cracks

5.4.2 *Experiment Verification*

The RGB (1536 × 2048 × 3) slide plate image is shown in Fig. 5.21. In the front slide plate of pantograph, the scratches are heavy, and there is a vertical crack in the rear slide plate center.

Based on the Sobel operator and Radon transform, the outline of rear slide plate can be obtained, as shown in Fig. 5.22.

Because there are cracks in the slide plate and the installation is not accurate for the slide plate, the deformation and displacement of slide plate may happen, which makes the slide plate outline image include some background images and the upper and lower edges be not strictly in accordance with the horizontal direction.

In order to facilitate the realization of the crack extraction algorithm, Fig. 5.22 is converted to gray scale image, as shown in Fig. 5.23.

The extraction result of slide plate cracks is shown in Fig. 5.24.

Fig. 5.21 Slide plate image

Fig. 5.22 Outline of rear slide plate

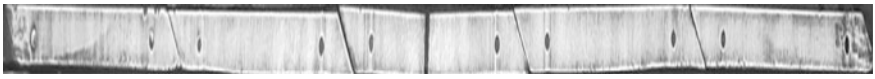

Fig. 5.23 Grayscale image of slide plate

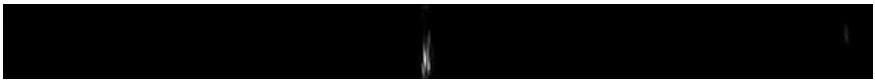

Fig. 5.24 Extraction result of slide plate cracks

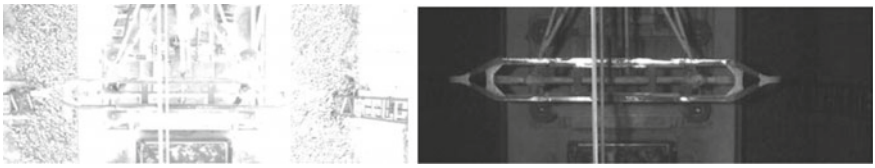

(a) Over exposure image (b) Insufficient exposure image

Fig. 5.25 Exposure defect image

In addition, due to the influence of natural factors such as weather and light intensity, the images collected in the field have the problems of fuzzy and poor exposure. For the situation of poor exposure, if the exposure is a serious problem (as shown in Fig. 5.25), the crack feature will be very difficult to extract from the original extraction slide plate, and when the exposure is light, it does not affect the algorithm on the crack extraction.

Two images with the light exposure problem are chosen to verify the algorithm, as shown in Fig. 5.26. In Fig. 5.26a, there is a vertical crack. In Fig. 5.26b, there is a vertical crack and a parallel crack to the joint between two joints on the left.

The extraction result of slide plate cracks is shown in Fig. 5.27.

In the experiments, 17 images are chosen. There are 8 normal exposure images, where there are 6 images with cracks. The false detection rate of all normal exposure images containing cracks is 0 and that of insufficient exposure and over exposure images is 11.1 %.

The experiment results show that the algorithm can accurately extract the crack fault in the pantograph slide plate image. Even for the cracks that are parallel to the joint direction, the cracks and parallel joints can be efficiently distinguished. In addition, the algorithm is still efficient for the over exposure images. But when the quality of the image is poor, it will affect the recognition of the crack due to the loss

Fig. 5.26 Over exposure slide plate images

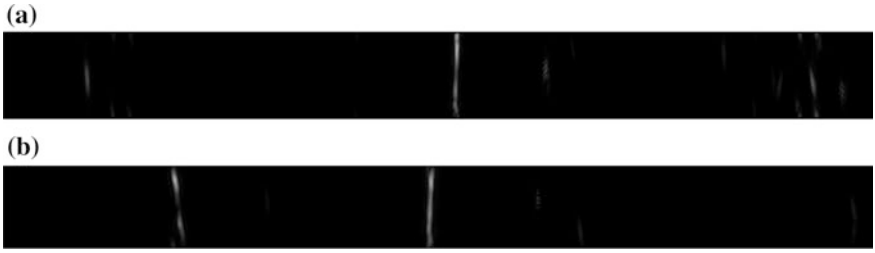

Fig. 5.27 Extraction result of slide plate cracks

of the image information. In order to improve the accuracy of crack identification, the image quality can be improved by improving the shooting condition or image denoising, image enhancement and so on.

5.5 Detection of Slide Plate Cracks Based on CCDP Transform

It can be found in Sect. 5.3 that the different elements in the slide plate image have different coefficients' distribution characteristics. It is possible to distinguish the different elements according to the curvelet decomposition coefficients. The coefficients distribution has explicit linear characteristics. The elements' characteristics can be analyzed easily and the different types of the edge can be distinguished directly in a single matrix by using CCDP transform. The edge information of image is concentrated in the high frequency domain, and the penultimate scale level of curvelet decomposition matrix can be used. A slide plate image is shown in Fig. 5.28 [15]. There are two cracks in the image marked with ellipse in the experiment here.

For the different choices of location point, the CCDP transform matrix will be displayed in two figures. The data are in the same matrix actually, but for the simplicity of the analysis, they are displayed separately here. The CCDP transform figure with the row locating point is shown in Fig. 5.29. The CCDP transform figure with the column locating point is shown in Fig. 5.30.

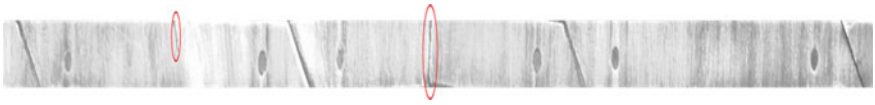

Fig. 5.28 Slide plate image with two cracks

Fig. 5.29 Row locating point with CCDP transform

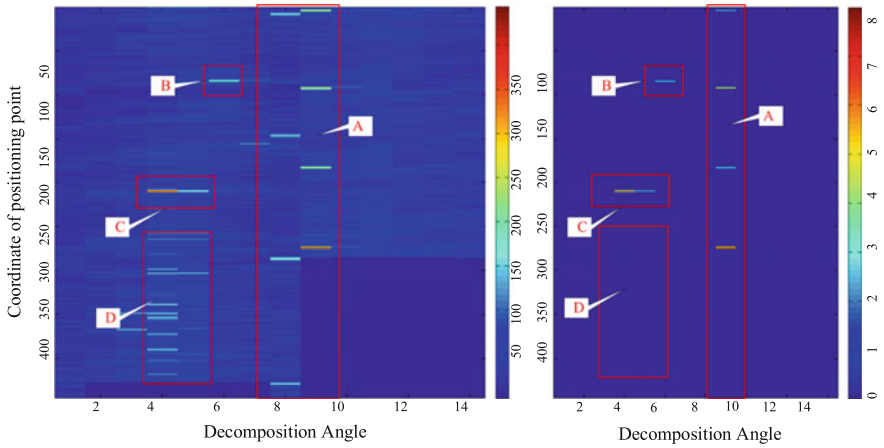

Fig. 5.30 CCDP transform of column location point. The real part G is displayed in the *left* and the number of coefficients obtained from the imaginary part L, which is higher than the threshold T, is displayed in the *right*

5.5.1 Distinguishing Slide Plate Edge

As has been analyzed in Sect. 4.1, the slide plate edge extraction defect coefficients can be obtained in the horizontal direction in the matrix $M_{j,0}$. Therefore, in the CCDP transform matrix, they are concentrated in the adjacent domain of $\theta_l = 0$ as is shown in Fig. 5.29.

From Fig. 5.29, it can be found that there are high coefficients in the edge, and they are the edge extraction defects in the CCDP transform matrix. There is nothing except for them. This means there is no other image elements in the horizontal direction and the slide plate edge extraction defects have be distinguished from the CCDP matrix.

5.5.2 Distinguishing Slide Plate Joints

In Fig. 5.30, the coefficients are distributed mainly in four regions “A”–“D”.

Region "A" corresponds to the $\theta = 3\pi/4$ direction. According to the analysis in Sect. 5.3, the slide plate joints coefficients are distributed in this domain. In Region "A" domain, there are some high coefficients with the equal distance. They coincide with the characteristics of slide plate joints. The reason why there are two columns with the similar coefficients is that the curvelet with the adjacent angles will detect the same image characteristics twice. It is enough to keep a single column with higher coefficients than the other. Now, the slide plate joints have been distinguished from the CCDP matrix.

5.5.3 *Distinguishing Slide Plate Scratches*

As known in Sect. 5.3, the slide plate scratches' coefficients are lower than those of slide plate joints. Through the CCDP transform, the coefficients concentrate on the small points compared with the slide plate joints'. Of course, these coefficients are higher than those produced by the type "A" and "B" coefficients. It is shown in Region "D".

However, the slide plate cracks can also obtain the similar coefficients just as the Region "B" sometimes. For example, there is a small crack in the slide plate. The single coefficient is high, but the quantity is small. Therefore, this crack's coefficients are similar to those of scratches through the line integral of CCDP transform. In order to separate them from each other, the key point is in the right figure. For the scratch's low coefficients, there are no coefficients higher than the threshold T in Fig. 5.30. The L will not include the information of the scratches' coefficients and the corresponding location is zero just as Region "D" shown in the right figure. And now, the slide plate scratches can be distinguished.

For convenience, the left and right figures of Fig. 5.30 can be combined together by multiplying the corresponding points of the two figures. The combined figure is shown in Fig. 5.31. In this figure, the slide plate scratches' coefficients can be eliminated automatically. It is more convenient for distinguishing the slide plate cracks.

5.5.4 *Analysis of Slide Plate Cracks*

The slide plate edge extraction defects, the slide plate joints and the slide plate scratches in the CCDP transform matrix can be distinguished. There are only slide plate cracks left in the CCDP transform matrix to be detected if it exists. In the experiment, the residual regions are "B" and "C". It means that there are two cracks in the slide plate.

Now, the location and the size of the cracks should be analyzed. The coordinate of "B" and "C" are $(15\pi/32, 85)$ and $(19\pi/32, 210)$. The coefficients locating encoding of "B" and "C" are 100000110 and 111111110 respectively. Therefore,

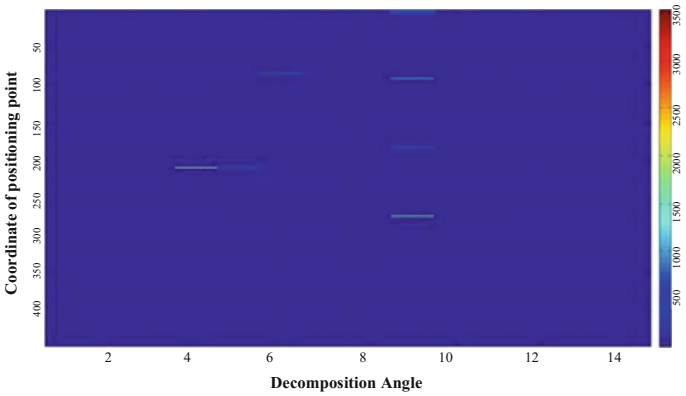

Fig. 5.31 Combined figure of CCDP transform

Fig. 5.32 Detection result of slide plate crack based on CCDP transform

from the coefficients encoding of "B", it can be found that this crack is a short one in the upper half plane. It is in the line of $angle = 15\pi/32$ and the beginning point in the original image is about 409 (This point is obtained from locating point "D"). Correspondingly, "C" is a long crack about full length of the slide plate's width. It is in the line of $angle = 19\pi/32$ and the beginning point in the original image is about 1009.

Finally, the detection of pantograph slide plate cracks based on the CCDP transform is shown in Fig. 5.32.

5.5.5 *Detection Experiments*

In order to verify the validity of the algorithm, this algorithm is used to identify a set of pantograph slide plate images. The experiments are carried out with a camera which is perpendicular to the plane of pantograph slide plate. Test images are from the shooting pantograph slide plate. The images include the normal exposure, insufficient exposure and over exposure images, as shown in Table 5.2.

Figure 5.33 shows the experimental results of some typical crack detections. Figure 5.33b, d are the results of crack identification using the presented algorithm.

Through the crack recognition experiments, it can be found that when the image quality is higher, the algorithm can better identify the slide plate's crack. When the

Table 5.2 Crack detection experiments of pantograph slide plate

	Normal exposure	Over exposure	Insufficient exposure
Total number of images	21	14	13
Image number including cracks	4	3	4
Correct recognition number with cracks	4	2	2
False recognition number without cracks	1	0	2

(a) Slide plate image with big crack

(b) Extraction result of (a)

(c) Slide plate image of over exposure

(d) Extraction result of (c)

Fig. 5.33 Crack detection diagram of pantograph slide plate

image appears over exposure or insufficient exposure, it will cause the image information loss and influence the crack identification. It has shown that non-crack image false detection is mainly caused by the certain region on a slide plate, where there are particularly obvious wear marks or light effects. It will result in the local edge gradient, make the corresponding position of curvelet coefficients be very large, and produce the misjudgment. Therefore, in order to improve the recognition effect, on the one hand, it is needed to improve the imaging quality of image acquisition equipment, especially the quality of light source, as far as possible to use the surface light source to prevent the local reflection of light source. In addition, the image enhancement technology is used to process the collected images to enhance the contrast between different image features and improve the recognition rate.

A computer with CPU (E2140) and Memory (2G) is used, and the crack extraction experiments for the slide plate images with 1700×43 pixels are performed. The time consumption is listed in Table 5.3. It can be seen that the crack

Table 5.3 Time consumption of pantograph slide plate crack detection experiments

	Total time	Curvelet decomposition	Cracks extraction	Inverse transform of curvelet
Time-consuming	1.85	0.37	1.05	0.43
Percentage	–	20 %	56.7 %	23.3 %

extraction part takes much time, but the total time can meet the requirements of the monitoring system.

To implement the automatic detection of the pantograph slide plate cracks, in this section, the curvelet's directional characteristics and the ability of the curvilinear edge detection are made full use of. Then the CCDP transform is adopted to analyze the curvelet decomposition matrix. Through the CCDP transform, all information at a fixed scale can be studied in a single matrix and it is convenient to recognize the image's characteristics.

By using the CCDP transform, the slide plate cracks' coefficients can be distinguished from other elements' coefficients easily. The slide plate cracks can be detected accurately and quickly. It has shown that the automatic detection technique of pantograph slide plate cracks based on the CCDP transform has the high practical value.

5.6 Summary

The pantograph is one of most important devices that take charge of collecting current in electrical railway. Its normal operation directly influences the train's operation safety. The fault detection of slide plate is very important for pantograph normal operation. In this chapter, the image processing of slide plate faults are introduced. First, the features of pantograph slide plate image including pantograph structure, slide plate type and image features of slide plate are given and discussed in detail. Second, the characteristics of pantograph slide plate image based on curvelet transform are presented. In this section, the curvelet transform is introduced and the curvelet coefficient directional project (CCDP) transform is presented in detail. Then, the characteristics of pantograph slide plate image based on curvelet transform are analyzed. Third, the pantograph slide plate crack extraction based on translational parallel window in curvelet transform domain is given. The extraction algorithm of cracks and experiment verification are performed. In the end, the detection of slide plate cracks based on CCDP transform is presented in detail. The detection steps, including the identifications of slide plate edge, joints, scratches and cracks, are given. In addition, the detection experiments are carried out. The experiments show that the slide plate fault detection of pantograph based on curvelet transform is efficient and feasible.

References

1. Ren S (2000) New device of abrasion detection of pantograph slipper and automatic pantograph descent. Railway Oper Technol 6(4):139–141
2. Lou P, Wang Z, Gao X et al (2004) Abrasion detection of pantographic slipper when locomotive entering warehouse. Opto-Electron Eng 31(12):88–90
3. Baolai Y, Boming W (2008) Application of ultrasonic ranging principle in monitoring abrasion of pantograph slider. Electr Drive Locomotives 5:57–59
4. Hamey LGC, Watkins T et al (2007) Pancam: in-service inspection of locomotive pantographs. In: Digital image computing techniques and applications: 9th Biennial conference of the Australian pattern recognition society, Glenelg, pp 493–499
5. Yang K, Wang L, Gao X et al (2009) Application of CCD measurement technique for wear on pantograph sliding plates. In: 4th International symposium on advanced optical manufacturing and testing technologies: optical test and measurement technology and equipment, vol. 7283, Chengdu, pp 34–37
6. Huang Y, Gao X, Wang L et al (2009) Research and realization of image processing algorithm in pantograph slide abrasion detection. Modern Electron Tech 11:191–194
7. Donnel Co, Palacinr R (2006) Pantograph damage and wear monitoring system. In: The institution of engineering and technology international conference on railway condition monitoring, pp 178–181
8. Candès EJ (1998) Ridgelets: theory and applications. Ph.D. Dissertation, Department of Statistics, Stanford University, Stanford, CA
9. Donoho D (1998) Orthonormal Ridgelets and linear singularities Technical Report. Department of Statistics
10. Candes EJ (1999) Monoscale Ridgelets for the representation of images with edges. Department of Statistics, Stanford University, USA
11. Candes EJ, Donoho D (1999). Curvelets—A surprisingly effective non-adaptive representation for objects with edges, curves an surfaces. In: Schumaker L et al. (ed.) Vanderbilt University Press, Nashville, TN
12. Candès E (2002) New tight frames of Curvelets and optimal representations of objects with piecewise-C2 singularities. Comm Pure Appl Math 57:219–266
13. Candès E, Demanet L, Donoho D et al (2005) Fast discrete curvelet transforms. Multiscale Model Simul 5(3):861–899
14. Han ZW, Liu ZG, Zhao F (2011) Directional reconstruction of super resolution Image by magnifying curvelet basis. J Southwest Jiaotong Univ 46(4):620–625
15. Han ZW, Liu ZG, Chen KF, You Z (2011) Pantograph slide cracks detection technology based on curvelet coefficients directional projection (CCDP). J China Railway Soc 33(11): 63–69
16. Chen KF, Liu ZG, Han ZW et al (2012) Pantograph slipper cracks identification based on translational parallel window in curvelet transform domain. J China Railway Soc 34(10): 43–47

Chapter 6
Detection of Catenary Support System

6.1 Introduction

In 2012, "Technical requirements of high-speed railway power supply safety detection and monitor system" is published by the Railway Ministry of China [1]. The key idea of this system is to achieve the non-contact detection of the safety-threatening working state of catenary system and its fittings based on the images and videos captured by inspection vehicles or devices. The non-contact detection methods have been proved to have the following advantages, such as high detection efficiency, small interference to train operation, low cost and high flexibility. However, currently, the detection of catenary fittings and the diagnosis of faults are heavily dependent on human observation. The automation degree and processing speed of detection systems cannot meet the requirement of improving the maintenance efficiency and reducing the labor cost. In this chapter, some automatic detection methods of safety-threatening working state of different catenary fittings are presented based on image processing and computer vision techniques. Typically, the detection of safety-threatening working state can be divided into two steps, namely fault positioning and fault detection.

6.2 Image Acquisition

The images of catenary are taken by HD (High Definition) cameras mounted on the top of inspection vehicle. As the vehicle runs along the railway line at night, the camera automatically shoots when it encounters a catenary pillar. The shooting angle and the shooting range are shown in Fig. 6.1a, as the dotted line indicates. In order to make sure the parts in the images enough clear for fault detection, pictures

Z. Liu, *Detection and Estimation Research of High-speed Railway Catenary*,
Advances in High-speed Rail Technology, DOI 10.1007/978-981-10-2753-6_6

of different portions of the catenary system are shot by different cameras, shown in Fig. 6.1b. In general, the resolution of images is 2448 × 2048 pixels. In addition, to eliminate the interference of the background scenery, the catenary images are taken at night. LED (Light Emitting Diode) spotlights are utilized for illumination.

6.3 Insulator Fault Detection

Compared with other fittings in the catenary system, the features of insulators are easy to capture, so the recognition and fault detection of insulators are easier than those of other fittings. Several different methods are presented to detect the breakage and other safety-threatening working state of insulators.

6.3.1 Insulator Positioning Based on Affine Invariant Moments

In this section, the insulator detection method based on affine invariant moments is adopted, and the graphic elements in the image are classified into two classes, namely the rod-shaped objects and the joint devices. The graphic elements that belong to the rod-shaped object class, which usually corresponds to the poles in the image, are ignored so that the recognition of insulators can be less interfered by the background [2].

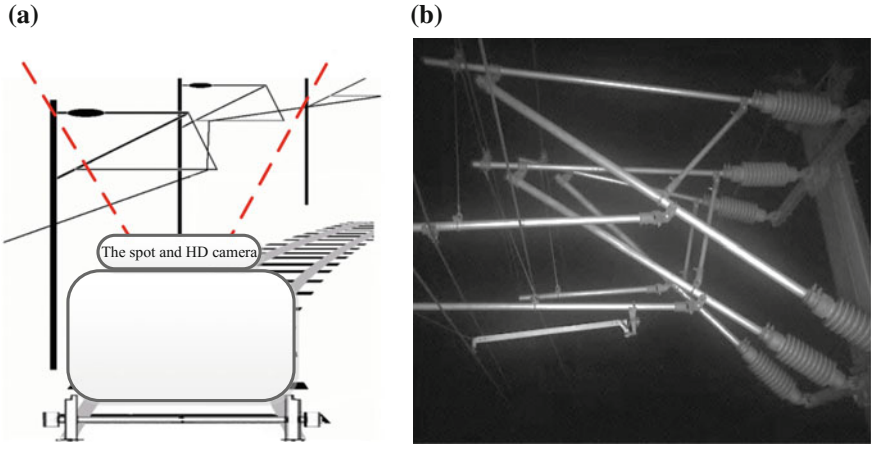

Fig. 6.1 **a** Sketch of image acquisition, **b** catenary suspension system image

1. Algorithm process

The rod-shaped objects are recognized in the process of line detection, which is achieved by Hough transform. The line detection process includes five main steps.

(1) Image enhancement, to sharpen the edges of rod-shaped objects so that they are easier to be detected.
(2) Apply Hough transform to the enhanced images and locate the segments detected by Hough transform.
(3) Connect the short segments whose endpoints are close to long segments by clustering methods. Thus, the edges of rod-shaped objects can be formed.
(4) Determine the correspondence between the long segments and the rod-shaped objects by further clustering, and judge which edges are correspondent to the same object. Then, the rod-shaped objects can be localized.
(5) The rest of graphic elements can be classified as the joint device class.

The result of graphic element classification is shown in Fig. 6.2.

As can be seen in Fig. 6.2c, the joint devices are separately distributed in the image. By analyzing the affine invariant moments of these graphic elements, the insulators can be finally recognized.

The affine invariant moments are derived from the origin moments and the central moments [3]. If the pixel value of image f is defined as $f(x, y)$, in which (x, y) is the pixel's coordinate, the origin moments of a certain region are defined as follows.

$$m_{pq} = \int_{-\infty}^{+\infty} \int_{-\infty}^{+\infty} x^p y^q f(x, y) dx dy, \quad p, q = 0, 1, 2, \ldots \tag{6.1}$$

And the central moments are defined as

$$\mu_{pq} = \int_{-\infty}^{+\infty} \int_{-\infty}^{+\infty} (x - \overline{x})^p (y - \overline{y})^q f(x, y) dx dy, \quad p, q = 0, 1, 2, \ldots \tag{6.2}$$

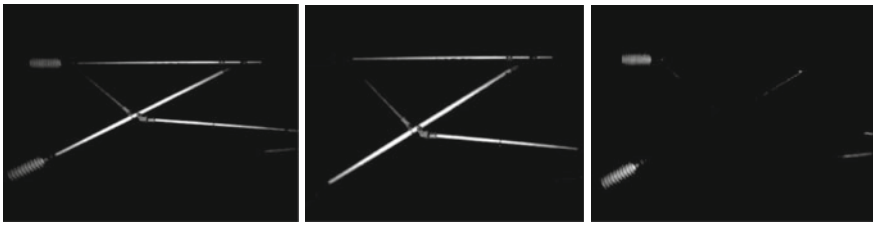

(a) Original image (b) Rod-shaped class (c) Joint device class

Fig. 6.2 Graphic element classification results

in which $(\overline{x}, \overline{y})$ is the centroid of the image grayscale, defined as

$$\overline{x} = \frac{m_{10}}{m_{00}}, \overline{y} = \frac{m_{01}}{m_{00}} \tag{6.3}$$

The affine invariant moment [4, 5] is evolved from the central moment [3]. The affine invariant feature extraction of target area can be realized by moving the coordinate origin to the center of target contour region.

Affine invariant moment is a transformation from a two-dimensional coordinate transformation to another two-dimensional coordinate, all of which can constitute a group as follows.

$$① \begin{cases} x' = x + \alpha \\ y' = y \end{cases} \quad ② \begin{cases} x' = x \\ y' = y + \beta' \end{cases} \quad ③ \begin{cases} x' = \omega x \\ y' = \omega y \end{cases}$$

$$④ \begin{cases} x' = \delta x \\ y' = y \end{cases} \quad ⑤ \begin{cases} x' = x + ty \\ y' = y \end{cases} \quad ⑥ \begin{cases} x' = x \\ y' = t'x + y \end{cases}$$

where ① and ② are the translation transforms, ③ and ④ are the scale zoom transforms, and ⑤ and ⑥ are oblique transforms.

By solving the partial differential equations coefficient method [6] to obtain the affine invariant moments, using the first three affine moment invariants to participate in the identification of insulator image, the affine invariant polynomial is defined as follows.

$$F = \frac{\sum_i k_i \mu_{p_1(i)q_1(i)} \cdots \mu_{p_n(i)q_n(i)}}{\mu_{00}^{z(i)}} \tag{6.4}$$

The first three affine invariant moments are listed below.

$$I_1 = (\mu_{20}\mu_{02} - \mu_{11}^2)/\mu_{00}^4 \tag{6.5}$$

$$I_2 = \frac{\mu_{30}^2\mu_{03}^2 - 6\mu_{30}\mu_{03}\mu_{21}\mu_{12} + 4\mu_{03}\mu_{21}^3 + 4\mu_{30}\mu_{12}^3 - 3\mu_{21}^2\mu_{12}^2}{\mu_{00}^{10}} \tag{6.6}$$

$$I_3 = \frac{\mu_{20}\mu_{21}\mu_{03} - \mu_{20}\mu_{12}^2 - \mu_{11}\mu_{30}\mu_{03} + \mu_{11}\mu_{21}\mu_{12} + \mu_{02}\mu_{30}\mu_{12} - \mu_{02}\mu_{21}^2}{\mu_{00}^7} \tag{6.7}$$

2. Experiment verification

The affine invariant moments of graphic elements that belong to the joint device class are computed and compared with the samples of the insulator. The samples of insulators vary in the orientation, scale and brightness (as seen in Fig. 6.3), however, their affine invariant moments are almost the same (as is shown in Table 6.1). The difference between the graphic element and the insulator sample is evaluated below.

$$D = \sqrt{(P_{(I_1)} - Q_{(I_1)})^2 + (P_{(I_2)} - Q_{(I_2)})^2 + (P_{(I_3)} - Q_{(I_3)})^2} \tag{6.8}$$

where D is defined as the distance between the graphic element and the insulator example, P means the affine invariant moments of graphic element, and Q means the affine invariant moments of insulator samples. The graphic element is recognized as an insulator if its distances to the insulator samples are smaller than a certain threshold, which is empirically set to $0.1 \times \sum D$.

6.3.2 *Insulator Positioning Based on Fast Fuzzy Matching*

Some methods can directly extract the insulators from the original images. For example, the image pyramid offers a flexible and convenient multi-resolution presentation of image. The neighborhood average pyramid algorithm can greatly reduce the computation load and increase the processing speed [7].

1. Algorithm process

The ground layer of the pyramid is the original image. The $(i + 1)$th layer of the pyramid is generated by down-sampling the ith layer of the pyramid. The down-sampling is accomplished in four different ways.

(1) Reserve all the pixels whose horizontal coordinates and vertical coordinates are both odd numbers
(2) Reserve all the pixels whose horizontal coordinates and vertical coordinates are both even numbers
(3) Reserve all the pixels whose horizontal coordinates are odd numbers and vertical coordinates are even numbers
(4) Reserve all the pixels whose horizontal coordinates are even numbers and vertical coordinates are odd numbers.

The four down-sampled matrixes with the same size are resized, and then the average value of four matrixes is taken. The schematic of neighborhood average pyramid algorithm is shown in Fig. 6.4 [8].

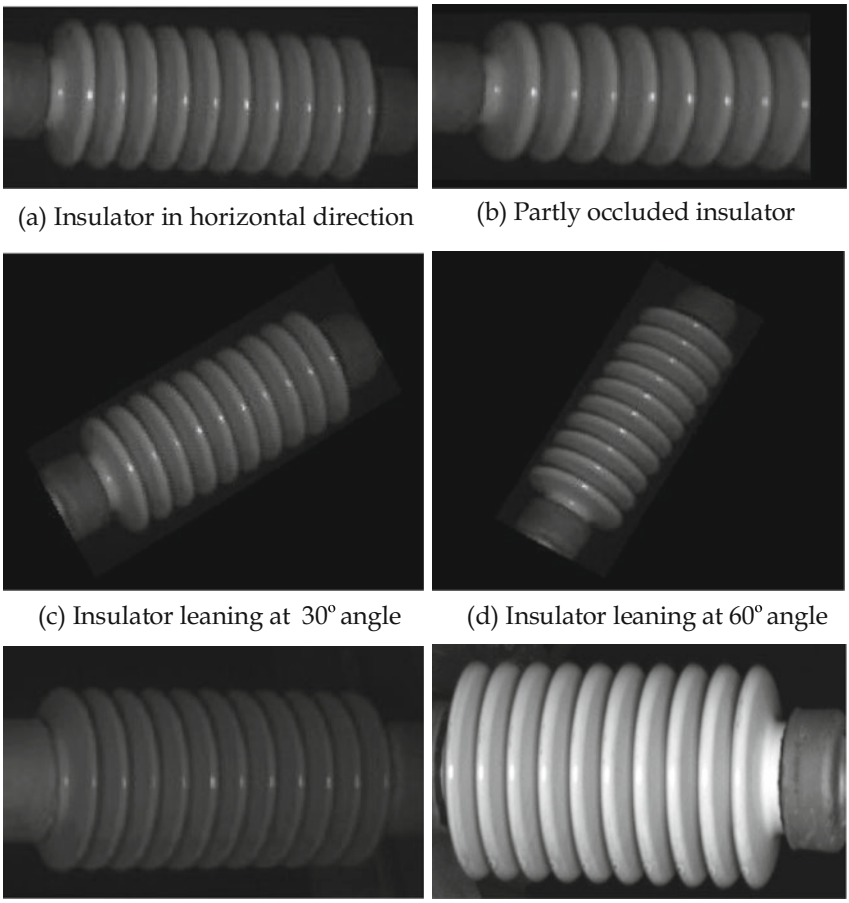

(a) Insulator in horizontal direction (b) Partly occluded insulator

(c) Insulator leaning at 30° angle (d) Insulator leaning at 60° angle

(e) Insulator with more ceramic chips (f) Insulator with high grayscale values

Fig. 6.3 Insulator samples

Table 6.1 Affine invariant moments of different insulator samples

Affine invariant moments	I_1	I_2	I_3
Figure 6.3a	13.0490	50.8542	35.2271
Figure 6.3b	13.1004	50.0375	32.3050
Figure 6.3c	13.0484	50.8460	35.1213
Figure 6.3d	13.0488	50.8446	35.1394
Figure 6.3e	12.1726	44.0774	30.5523
Figure 6.3f	14.8884	54.5518	34.4479

The fuzzy matching is achieved by using NCC (Normalized Cross Correlation) [9]. The insulators' images, whose inclination angles are different, are used as the templates. Assume that the size of global image I is $M \times N$, and the size of insulator

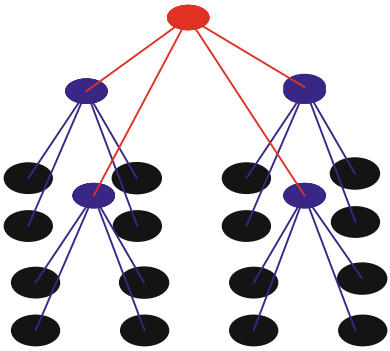

Fig. 6.4 Schematic of neighborhood average pyramid algorithm

template T is $m \times n$. Choose a sub-image $I_{x,y}$ randomly from the global image I, and the size of $I_{x,y}$ is also $m \times n$. Set the coordinate of the top left corner of sub-image in the global image as (x, y), then, $0 \leq x \leq M - m$, $0 \leq y \leq N - n$. The normalized cross-correlation value of $I_{x,y}$ and T is

$$R_{(x,y)} = \frac{\sum_{i=0}^{m-1} \sum_{j=0}^{n-1} \left[I_{(x+i,y+j)} - \overline{I}_{x,y}\right] \left[T_{(i,j)} - \overline{T}\right]}{\sqrt{\sum_{i=0}^{m-1} \sum_{j=0}^{n-1} \left[I_{(x+i,y+j)} - \overline{I}_{x,y}\right]^2 \sum_{i=0}^{m-1} \sum_{j=0}^{n-1} \left[T_{(i,j)} - \overline{T}\right]^2}} \tag{6.9}$$

where $T_{(i,j)}$ is the pixel grayscale value of the ith row and the jth column, and $\overline{I}_{(x,y)}$ is the average grayscale value of $I_{x,y}$. The definition of $\overline{I}_{(x,y)}$ is described below.

$$\overline{I}_{x,y} = \frac{1}{mn} \sum_{i=0}^{m-1} \sum_{j=0}^{n-1} \left[I_{(x+i,y+j)}\right] \tag{6.10}$$

$\overline{T}$ is the average grayscale value of template T. The definition of $\overline{T}$ is shown below.

$$\overline{T} = \frac{1}{mn} \sum_{i=0}^{m-1} \sum_{j=0}^{n-1} T_{(i,j)} \tag{6.11}$$

All the normalized cross-correlation values $R(x, y)$ form the normalized cross correlation matrix R. In the normalized cross correlation matrix R, for arbitrary x and y that satisfy $0 \leq x \leq M - m$, $0 \leq y \leq N - n$, if $R^*_{(x,y)} = \max\left\{R_{(x,y)}\right\}$, then $R^*_{(x,y)}$ is the optimal solution. The corresponding sub-image $I_{x,y}$ is the best matching of the template T.

Simplify Eq. (6.8), and set $T'_{(i,j)} = T_{(i,j)} - \bar{T}$. The simplified normalized cross correlation value $R'_{(x,y)}$ is expressed below [10].

$$R'_{(x,y)} = \frac{\sum_{i=0}^{m-1}\sum_{j=0}^{n-1} I_{(x+i,y+j)} T'_{(i,j)}}{\sqrt{\sum_{i=0}^{m-1}\sum_{j=0}^{n-1}\left[I_{(x+i,y+j)} - \overline{I}_{x,y}\right]^2}} \tag{6.12}$$

In order to reduce the computational cost, Fourier transform is adopted. When the image is transformed to the frequency domain, the cross-correlation operation becomes the multiply operation. The cross correlation matrix R' can be obtained as follows.

$$R' = F^{-1}[F(I)F^*(T')] \tag{6.13}$$

where $F(I)$ is the Fourier transform result of I, $F^*(T')$ is the complex conjugate of $F(T')$, and $F^{-1}(\cdot)$ is the inverse transformation of Fourier transform. T' should be padded with zero to reach the size of $M \times N$.

Set a threshold for the normalized cross correlation values in matrix R'. If the normalized cross correlation value of the sub-image $I_{x,y}$ and T is higher than the threshold, this sub-image will be recognized as containing an insulator.

Insulator templates of three different inclination angles are prepared, as can be seen in Fig. 6.5.

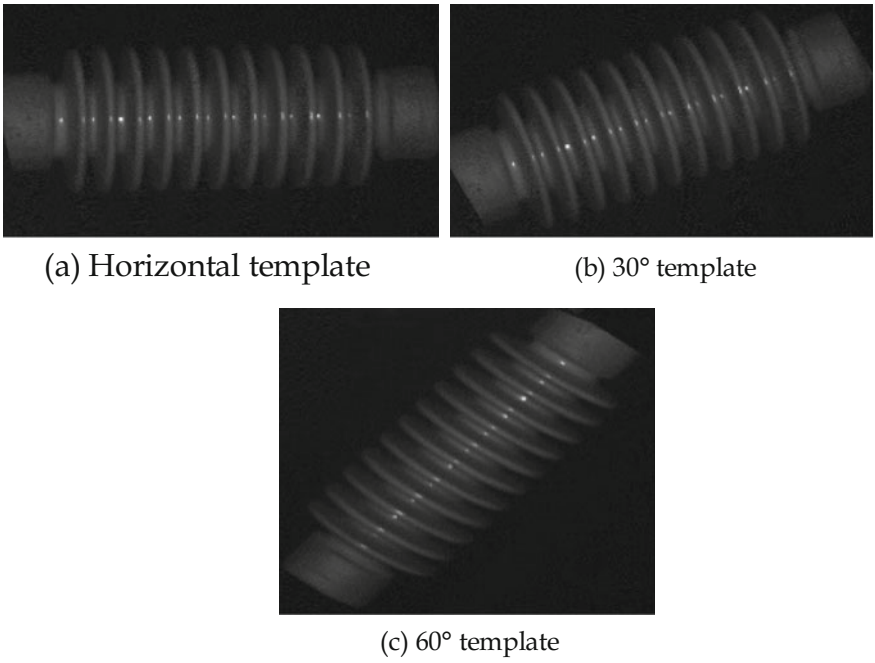

(a) Horizontal template

(b) 30° template

(c) 60° template

Fig. 6.5 Insulator templates

Matching the global image with the horizontal template is able to detect the insulators whose inclination angles are between −15° and 15°. Matching the global image with the 30° template is able to detect the insulators whose inclination angles are between 15° and 45°. Matching the global image with the 60° template is able to detect the insulators whose inclination angles are between 45° and 75°. Considering the installation angles of insulators, the inclination angles of insulators in the image will not be below −15° or above 75°, and using these three templates can detect all the insulators installed in the catenary system.

The images in the up line library are respectively matched with the above templates, and the insulators from the various directions are extracted. Because the calculation results in the process of cross correlation of normalized function have a fixed range of [−1, 1], it is easy to set the detection threshold. After the images are matched with the horizontal template, the insulator in [−15°, 15°] can be detected. After the images are matched with the template of 30°, the insulator in [15°, 45°] can be detected. After the images are matched with the template of 60°, the insulator in [45°, 75°] can be detected. Based on the matching of three templates, all the rod insulators in the image can be detected. Therefore, when the images in the down line library are processed, the horizontal insulator template is chosen and rotated at 30° and 60° directions. Similarly, when the images in the down line library are processed, the horizontal insulator template is chosen and rotated at −30° and −60° directions. In Fig. 6.6, the left is the range of up line images and the right is that of down line images.

2. Experiments

To verify the performance of the presented algorithm based on the normalized cross correlation matching and Pyramid nearest neighbor algorithm, some images from different conditions and locations in the image database are chosen for the positioning experiments. The normal rod insulator is shown in Fig. 6.7. Figure 6.7a shows the matching of image and horizontal template. Figure 6.7b shows the matching of image and −30° template. Figure 6.7c shows the matching of image and −60° template. It can be seen that the matching effect is good. The damaged rod insulator is shown in Fig. 6.8. Figure 6.7a is the positioning image of damaged

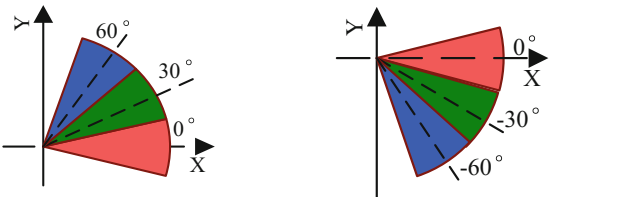

(a) Matching range of up line images (b) Matching range of down line images

Fig. 6.6 Matching range

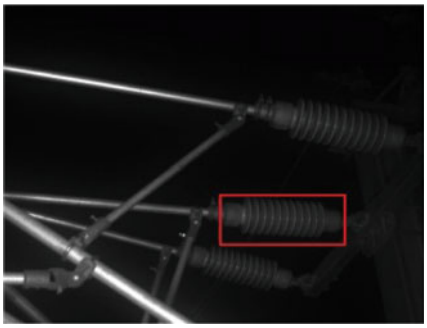

(a) Horizontal template matching

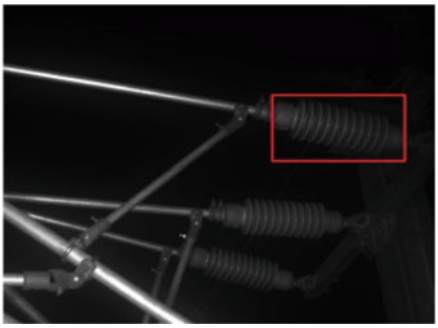

(b) -30° template matching

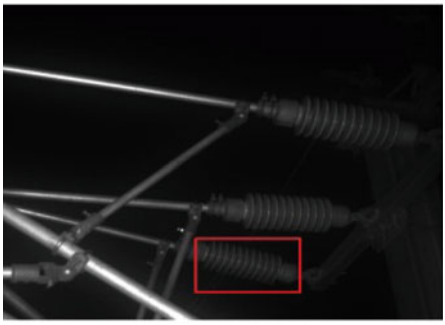

(c) -60° template matching

Fig. 6.7 Matching of normal rod insulator

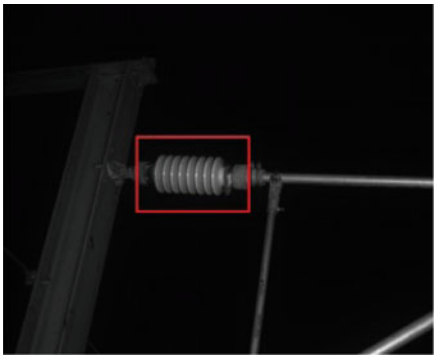

(a) Positioning of damaged insulator

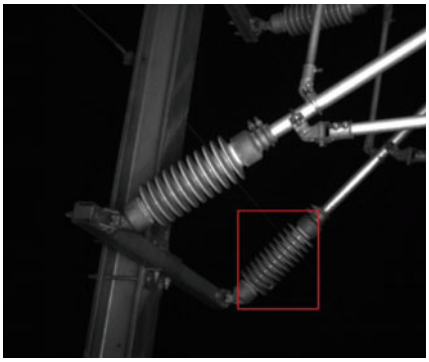

(b) Positioning with inclusion foreign body

Fig. 6.8 Matching of faulty rod insulator

Table 6.2 Matching time statistics for Fig. 6.7

Template	0°	−30°	−60°
Time	2.404231	2.100431	2.303324

Table 6.3 Statistics data of insulator positioning experiments

Image number		Correct number	Wrong number	Recognition ratio
Total number	30	27	3	90 %
With insulator	28	25	3	–
Without insulator	2	2	0	–
Fault number	2	2	0	–

insulator. Figure 6.7b shows the positioning image of insulator with inclusion foreign body. It can be seen that the matching effect is good. The matching time statistics for Fig. 6.7 are listed in Table 6.2, where the detection threshold is $\tau = 0.68$.

The results of image recognition in the gallery are shown in Table 6.3. It can be seen that the matching algorithm can quickly realize the accurate positioning of rod insulator. The reason of false positioning is that when the distance of the shooting range becomes longer, the image object will be more blurred. In the shooting process, through setting the appropriate interval, the influence of shooting distance and target objects can be effectively improved.

6.3.3 Insulator Positioning Based on Harris Corner Points

1. Algorithm process

There are two advantages of detecting with Harris corner points [11].

(1) Only the computation of first order derivatives is needed, thus the cost of computational is reduced. Besides, this computation is insensitive to the variance of the brightness and the contrast of images. The variance of brightness and the contrast does not change the extreme point of the Harris response.
(2) The Harris corner detector adopts the secondary moment matrix of a pixel's adjacent area. The matrix corresponds to an ellipse. The major and minor axes of ellipse are the square roots of matrix's eigenvalues. These eigenvalues do not change with the rotation of ellipse and the response of corner point is also invariant, which means that the stability is high.

Let I_x and I_y denote the gradient of image $I(x, y)$ in horizontal and vertical direction, and compute the product of the gradients $I_x^2 = I_x \cdot I_x$, $I_y^2 = I_y \cdot I_y$, $I_{xy} = I_{yx} = I_x \cdot I_y$. Use Gaussian function to generate the weights of gradients' products, then Matrix M is obtained as follows.

$$M = \sum_{u,v} w(u,v) \begin{bmatrix} I_x^2 & I_{xy} \\ I_{yx} & I_y^2 \end{bmatrix} = \exp\left(-\frac{u^2+v^2}{2\sigma^2}\right) \begin{bmatrix} I_x^2 & I_{xy} \\ I_{yx} & I_y^2 \end{bmatrix} \tag{6.14}$$

where $w(u,v)$ are the coefficients of the Gaussian window at (u,v).

Set the threshold for Harris response R as follows.

$$R = \{R : \det M - \alpha(traceM)^2 < t\} \tag{6.15}$$

Then Non-maximum suppression is performed in the $n \times n$ neighborhood of pixels. The local maximum value points are regarded as the corner points.

In order to enhance the efficiency of corner point matching, the SSDA (Sequential Similarity Detection Algorithm) is adopted. The main process of SSDA is described as follows in [12, 13].

Suppose that the size of template T is $N \times N$ and its center is the ith corner point of image. The size of searching sub-image $S^{i,j}$ to be matched is also $N \times N$, and its center is the some corner point of image. The coordinate of the top right corner of $S^{i,j}$ is defined as (i,j). Then the absolute error is defined as follows.

$$\varepsilon(i,j,m_k,n_k) = \left|S^{i,j}(m_k,n_k) - \hat{S}(i,j) - T(m_k,n_k) + \hat{T}\right| \tag{6.16}$$

in which,

$$\begin{aligned} \hat{S}(i,j) &= \frac{1}{N^2}\sum_{m=1}^{N}\sum_{n=1}^{N} S^{i,j}(m,n) \\ \hat{T} &= \frac{1}{N^2}\sum_{m=1}^{N}\sum_{n=1}^{N} T(m,n) \end{aligned} \tag{6.17}$$

Randomly select the pixels in $S^{i,j}$, compute the difference value between the selected pixel and its corresponding point in template T, and repeat this process and accumulate the difference values. When the sum of the difference values exceeds the threshold T_k, stop accumulating. Record the number of times of accumulation (represented as r), then define the SSDA surface as $I(i,j) = r$. The maximum of $I(i,j)$ is regarded as the matching point.

In this section, Fuzzy C-means clustering [14] is utilized to distinguish the Harris corner points corresponding to different insulators.

If the data set is $X = \{x_1, \cdots, x_N\}$, its fuzzy C partition can be represented by $U = [U_{ij}] \in R^{CN}$. U_{ij} means the membership degree of the ith class for the jth point. $\sum_i^c u_{ij} = 1$, $u_{ij} \in [0,1]$, $i \in [1,c]$ and $j \in [1,N]$. The fuzzy C-mean clustering means the solution of minimum value as follows.

$$J = \min\{\sum_{j=1}^{N}\sum_{i=1}^{c} u_{ij}^{m}\left\|x_j - v_i\right\|^2\} \tag{6.18}$$

where v_i is the clustering center of the ith class, $\left\|x_j - v_i\right\|$ is the Euclidean distance of the ith class for the jth sequence, and m is the weighted index.

The steps of fuzzy C-means clustering are listed below.

(1) Determine the number of clusters c and m, as well as the iterative stopping threshold ε. Initialize the membership degree matrix U^0 and the iterative number l.

(2) Update the clustering center V^l, namely

$$v_i^l = \left[\sum_{j=1}^{n}(u_{ij}^l)^m x_j\right] / \left[\sum_{j=1}^{n}(u_{ij}^l)^m\right], \quad i \in [1, c] \tag{6.19}$$

(3) Update the membership degree matrix U^{l+1}, namely

$$u_{ij}^{l+1} = \left\{\left[\sum_{k=1}^{c}\frac{\left\|x_j - v_i\right\|^2}{\left\|x_k - v_j\right\|^2}\right]^{2/(m-1)}\right\}^{-1}, \quad (i, j \in R^+) \tag{6.20}$$

(4) If $\max\left\{\left|u_{ij}^l - u_{ij}^{l-1}\right|\right\} < \varepsilon$, stop the calculation, and output the clustering center V^l and membership degree matrix U^l, otherwise continue to perform the iteration.

The accurate positioning of insulator axis can be realized by using SSDA matching corner. Because the similarity degree is set by the threshold in the matching process, some corners in the center axis will lose. In order to fully reflect the length of center axis, corners in the region near the clustering centers are recovered, and the restored corners can be fit with straight line by using the least square method. Suppose that the coordinate (x_i, y_i) of ith corner satisfies

$$y_i = \eta_1 x_i + \eta_0 \quad i \in [1, N] \tag{6.21}$$

where η_1 is the slope of straight line and η_0 is the intercept.

In order to ensure the minimum of deviation weighted square sum, the parameters of straight line are estimated by using the least square method, namely

$$\begin{aligned}
\frac{\partial}{\partial\eta_1}\sum_{i=1}^{N}\left[y_i - (\eta_1 x_i + \eta_0)\right]^2\Big|_{\eta=\hat{\eta}} &= -2\sum_{i=1}^{N}\left[y_i - (\hat{\eta}_1 x_i + \hat{\eta}_0)\right] = 0 \\
\frac{\partial}{\partial\eta_0}\sum_{i=1}^{N}\left[y_i - (\eta_1 x_i + \eta_0)\right]^2\Big|_{\eta=\hat{\eta}} &= -2\sum_{i=1}^{N}\left[y_i - (\hat{\eta}_1 x_1 + \hat{\eta}_0)\right] = 0
\end{aligned} \tag{6.22}$$

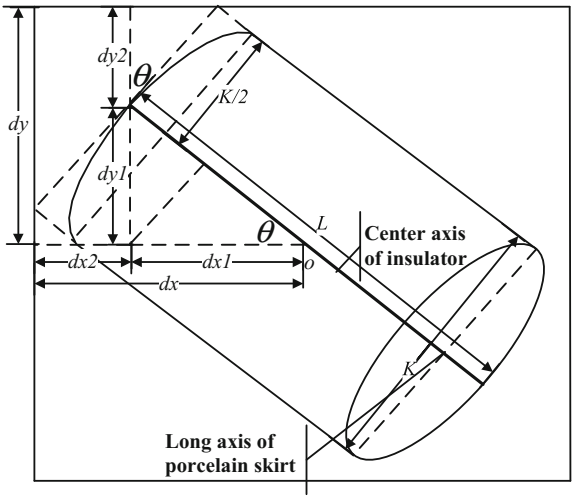

Fig. 6.9 Object region location sketch of insulator

The best estimation $\hat{\eta}_1, \hat{\eta}_0$ of η_1, η_0 can be obtained as follows.

$$\begin{aligned}\hat{\eta}_1 &= \left(N \cdot \sum_{i=1}^{N} x_i y_i - \sum_{i=1}^{N} x_i \cdot \sum_{i=1}^{N} y_i\right) / \left(N \cdot \sum_{i=1}^{N} x_i^2 - \left(\sum_{i=1}^{N} x_i\right)^2\right) \\ \hat{\eta}_0 &= \left(\sum_{i=1}^{N} x_i^2 \cdot \sum_{i=1}^{N} y_i - \sum_{i=1}^{N} x_i \cdot \sum_{i=1}^{N} x_i y_i\right) / \left(N \cdot \sum_{i=1}^{N} x_i^2 - \left(\sum_{i=1}^{N} x_i\right)^2\right)\end{aligned} \tag{6.23}$$

Combining the coordinate of clustering center and the fitting line, the location situation of rod insulator is supposed in Fig. 6.9 [15]. The center coordinate of insulator is O, the axis length is L, the long axis of porcelain skirt is K, and the slope angle is θ.

No matter how the scale and the angle of inclination of the insulator change in the image, the ratio between the symmetry axis length and the section width of insulator remains consistent. Therefore, the bounding rectangle of the insulator (denoted as $M \times N$) can be determined by using the trigonometric transform.

$$\begin{cases} \gamma = L/K \approx 2.3 \\ M = 2d_x = L \cdot \cos\theta + K \cdot \sin\theta \\ M = 2d_y = L \cdot \sin\theta + K \cdot \cos\theta \end{cases} \tag{6.24}$$

where L is the central axis length of insulator, K is the section width of the insulator, and θ is the angle of inclination of the insulator.

2. Experiments

In order to verify the accuracy of Harris corner detection, SSDA matching algorithm and target area positioning, the experiments are carried out. The images are from the image database of Wuhan-Guangzhou high speed railway. The positioning results of image with a normal insulator are shown in Fig. 6.10.

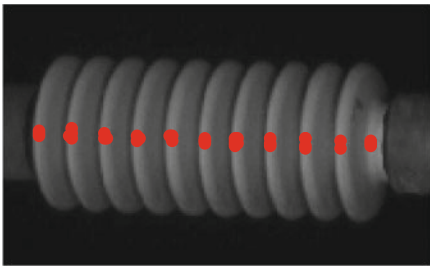

(a) Corner detection image of insulator template

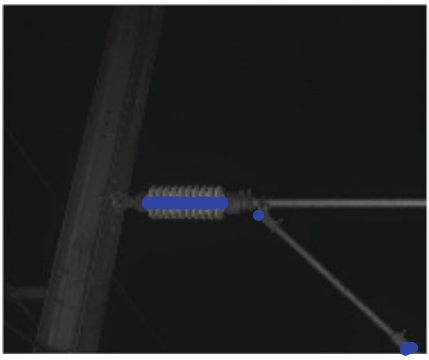

(b) Corner detection image of being detected

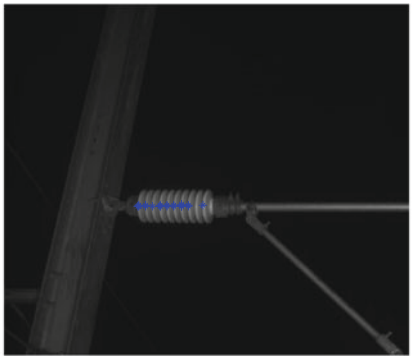

(c) Corner matching result

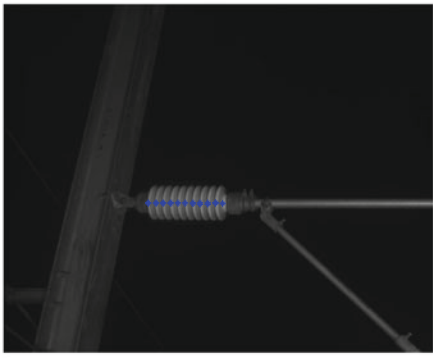

(d) Corners recovery of insulator center axis

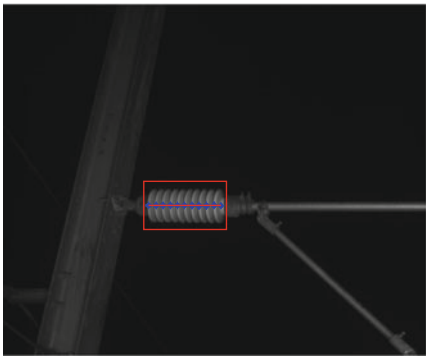

(e) Fitting line image of corner recovery

Fig. 6.10 Positioning result of image with only one normal insulator

Figure 6.10a is the corner detection image of insulator template. Figure 6.10b is the corner detection image of being detected. Figure 6.10c is the corner matching result image. Figure 6.10d is the result image of corners recovery of insulator central axis. Figure 6.10e is the fitting line image of corners recovery. If multiple normal

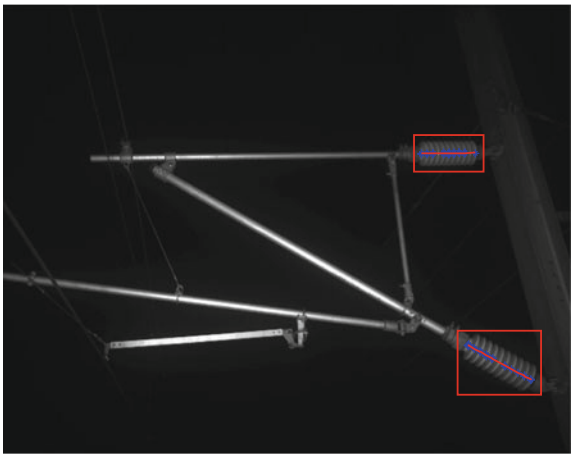

Fig. 6.11 Positioning result of multiple insulators

insulators exist in the image, the insulator positioning image is shown in Fig. 6.11. The fault insulator positioning is shown in Fig. 6.12. Their statistics of straight line tilt angle are listed in Table 6.4.

Based on Figs. 6.10 and 6.11, it can be clearly seen that the positioning region includes all information of insulator. The method can effectively identify the tilting insulator, and has good resistance to rotation. In addition, the fitting line can reflect the inclination degree of insulator. In Table 6.4, the slight tilt angle of insulator can be given quantitatively. In Fig. 6.12, whether the insulator has the fracture or inclusion foreign body, the complete positioning of insulator can be realized. Furthermore, if the boundary of Fig. 6.12b includes the incomplete insulator, the corresponding threshold can be set to eliminate the center point near the image boundary.

There are some failures of image positioning. The main reason is that the improper setting of exposure time leads to the blurring of image. In addition, due to the large area shedding of insulator porcelain, the insulator corners are lost.

6.3.4 Fault Detection Based on Grayscale Statistic

Based on the periodic grayscale distribution of insulator surface, grayscale statistic is one of the easiest features used to detect the safety-threatening working state of insulator. The fracture of ceramic chips or foreign bodies clamped between the ceramic chips will destroy the periodicity of grayscale distribution. Therefore, the detection of foreign bodies clamped between the ceramic chips is used as an example to introduce the process of fault diagnosis based on grayscale statistic.

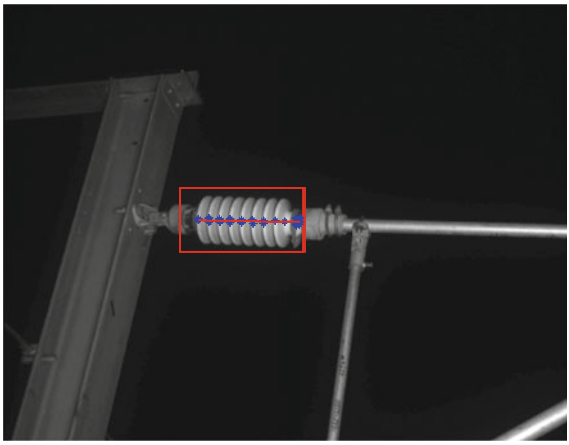

(a) Positioning of fractured insulator

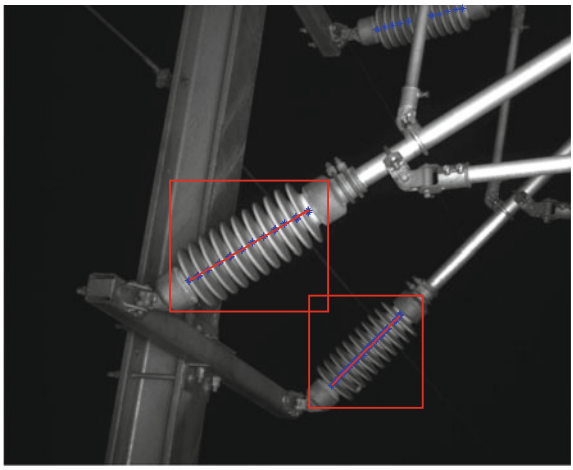

(b) Positioning of insulator with foreign body

Fig. 6.12 Positioning of fault insulators

Table 6.4 Statistics data of insulator tilt angle

Insulator location	Figure 6.10	Figure 6.11	
Deflection angle (°)	−0.1971	−0.8837	29.267

1. Detection Process

The detection of foreign bodies clamped between the ceramic chips can be achieved in four steps, namely angle adjustment, image dilation, image enhancement and grayscale statistic curve analysis [2].

(1) Angle adjustment

The purpose of angle adjustment is to rotate the image of insulator to make sure that the insulator stays horizontally in the image. This can be achieved based on the least square fitting. Firstly, the contour of insulator is detected. Then the insulator's axis of symmetry can be obtained by least square fitting. Basically, it is to fit the contour of insulator with a line. Because the insulator is axisymmetric, the optimal result is the axis of symmetry of insulator. Denote the axis of insulator symmetry by l and the angle between l and the horizontal line by θ. Then the angle that the image needs to be rotated is $180^\circ - \theta$.

(2) Image dilation

Because the sizes of foreign bodies clamped between the ceramic chips are usually small, in order to make sure that the foreign bodies can be successfully detected, the image is dilated first. Then, the features of foreign bodies can be enhanced.

The structuring element used in the dilation is a 4×8 rectangle. This is determined empirically. If the size of the structuring element is too small, the effect of the dilation will be limited. If the size of the structuring element is too big, the contour of the insulator will be blurred.

The results of angle adjustment and image dilation are shown in Fig. 6.13. Figure 6.13a is the original image of insulator. Figure 6.13b is the image of the same insulator after angle adjustment and image dilation. The feature of the grayscale distribution of the insulator, namely the periodically altering brightness and darkness in Fig. 6.13b is more obvious after image dilation.

(3) Image enhancement

The grayscale statistic curve of insulator in the dilated image is shown in Fig. 6.14a. The grayscale statistic curve is obtained by counting the number of non-zero points in each column of image. Although the existence of foreign bodies increases the value of the minimum points, the inherent differences among the values of the minimum points usually make it difficult to recognize this increase.

To solve this problem, the insulator image is divided into several chunks at the minimum of grayscale statistic curve. The image enhancement is accomplished locally in each and every chunk. The image enhancement is accomplished below.

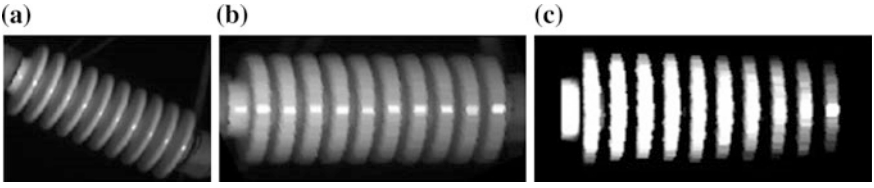

Fig. 6.13 Results of angle adjustment and image dilation

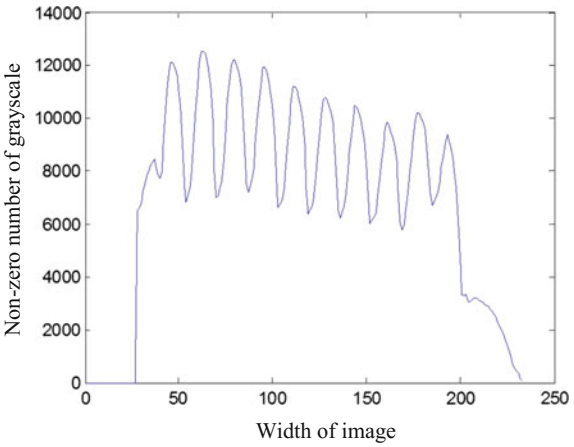

(a) Grayscale statistic curve of original image

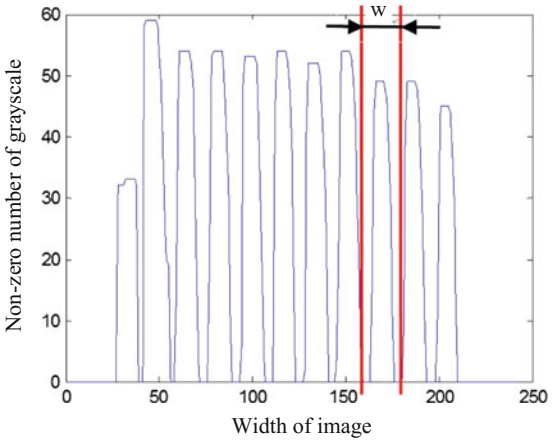

(b) Grayscale statistic curve of enhanced image

Fig. 6.14 Grayscale statistic curve of insulator

$$M(m,n) = \begin{cases} 0 & I(m,n) < I_{in} \\ (I(m,n) - L_{in}) \frac{H_{out} - L_{out}}{H_{in} - L_{in}} + L_{out} & L_{in} < I(m,n) < H_{in} \\ 0 & I(m,n) > H_{in} \end{cases} \tag{6.25}$$

where I is the original image, M is the enhanced image, L_{in} and H_{in} are used to define the grayscale range that needs to be enhanced. L_{out} and H_{out} are the output range of the enhanced grayscale range. The result of image enhancement is shown in Fig. 6.13c. The grayscale statistic curve of insulator in the enhanced image is shown in Fig. 6.14b.

(4) Foreign body detection based on grayscale statistic curve analysis

As shown in Fig. 6.14b, the peaks of grayscale statistic curve correspond to the ceramic chips. The zero points of grayscale statistic curve correspond to the joints between two ceramic chips.

The interval between the central points of adjacent intervals whose the values are consistently zero is defined as the width of ceramic chip, as shown in Fig. 6.14b, denoted by *W*. If no foreign bodies are clamped between the ceramic chips, the value of *W* will remain consistent.

When a foreign body is clamped between the ceramic chips, the value of *W* will rise, because the two ceramic chips are connected by the foreign body and the zero-valued interval between the ceramic chips disappears, as seen in Fig. 6.15. Figure 6.15a is the original image of insulator (with a pebble clamped between the ceramic chips). Figure 6.15b is the result of image enhancement. Figure 6.15c is the grayscale statistic curve of the enhanced insulator image. The criterion for

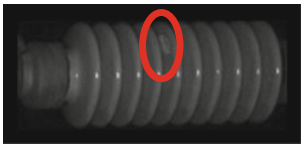

(a) The original image

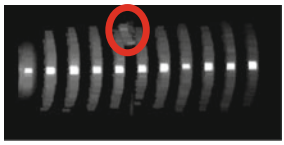

(b) The enhanced image

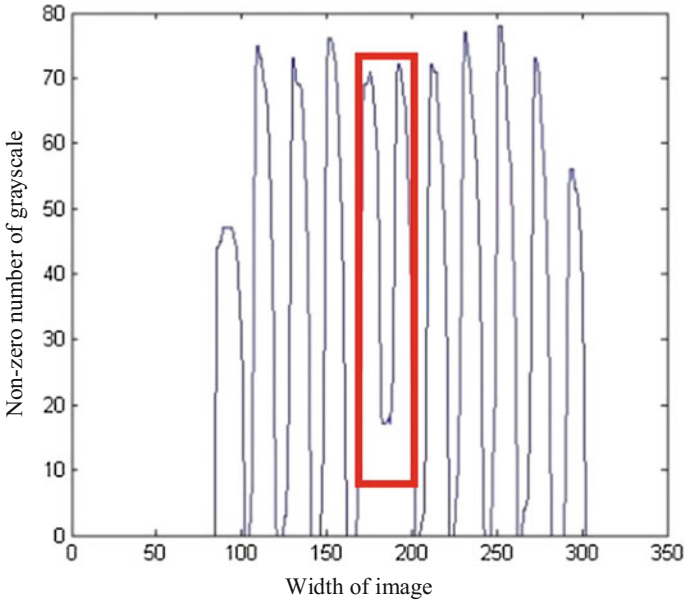

(c) Grayscale statistic curve of the enhanced image

Fig. 6.15 Detection of foreign body

judging whether there is a foreign body clamped between the ceramic chips is determined through a large number of experiments based on W, as listed below.

$$\begin{cases} W \geq 1.5W_m & \text{Foreign body detected} \\ W < 1.5W_m & \text{Normal} \end{cases} \tag{6.26}$$

where W_m is the mean value of W in the experiment.

2. Experiments

In order to verify the validity of the presented method, the experiments are carried out on the normal and faulty images taken under different conditions in the gallery. First, the image elements are pre-classified. Then the affine invariant moment is used to identify and locate the insulator. Finally, the extracted insulator is processed, and the fault condition is identified. The detection process and results are described as follows.

(1) Pre-classification of basic image elements

The results of pre-classification for the basic image elements by using Hough transform are shown in Fig. 6.16. Figure 6.16a is the original image, Fig. 6.16b corresponds to rod objects, and Fig. 6.16c corresponds to the insulator class.

(2) Recognition and positioning of insulator

Through calculating the affine invariant moments of the connected regions in Fig. 6.16c insulator class (shown in the circle), the results are listed in Table 6.5. The affine invariant moment distances between the connected regions and the templates in Fig. 6.3a–f are shown in Table 6.6.

Based on the experiments, if any template in the six insulator templates is used to match the image, it can be obviously found that the distance between the 3th and 4th connected regions and template is the minimum, and the different between other regions is also very distinguishable. Therefore, it can be concluded that the 3th and 4th connected regions are insulator images.

It can be shown that the insulator identification method based on affine invariant moment is not sensitive to the template selection, and the recognition performance is good. At the same time, after classification, because the image elements in insulator class only include the insulator and a small amount of the rod connecting objects, the calculation cost of recognition and positioning is less, fast and accurate.

(3) Fault detection of foreign bodies among insulator pieces

a. Insulator A

The detection process of Insulator A is shown in Fig. 6.17. The extraction of Insulator A in Fig. 6.16c based on affine invariant moment is shown in Fig. 6.17a. The result through eliminating the two ends of insulator based on dilation operation

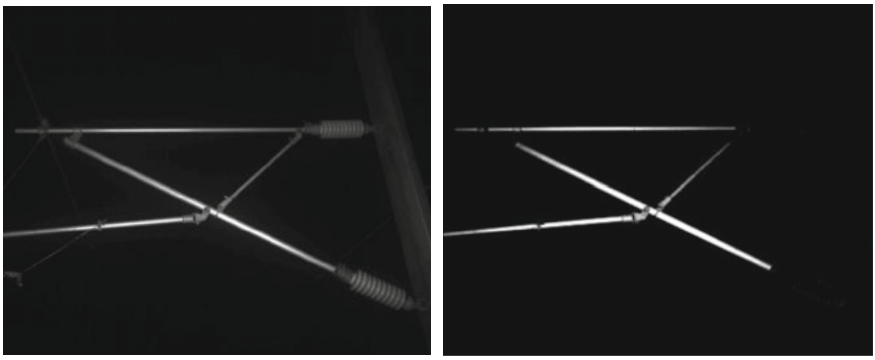

(a) Original image

(b) Rod objects

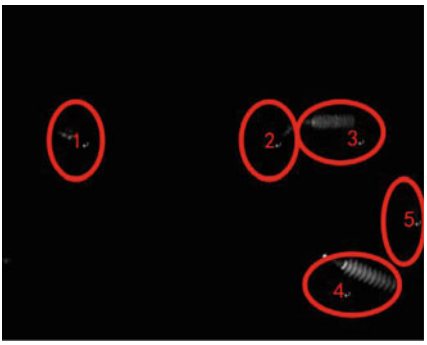

(c) Insulator class

Fig. 6.16 Results of pre-classification for basic image elements

Table 6.5 Affine invariant moments of connected regions

Number	I_1	I_2	I_3
1	9.0215	32.5390	19.3610
2	8.3074	24.0612	18.2413
3	12.6210	47.5519	30.2366
4	12.9254	46.8893	30.5618
5	8.9019	31.6642	20.1935

is shown in Fig. 6.17b. The effect of local region contrast adjustment is shown in Fig. 6.17c. The gray level statistical graph of Insulator A is shown in Fig. 6.17d.

In Table 6.7, the 5th stripe width is two times than that of other interval, so it can be judged that Insulator A is here, and there is a foreign body between the 4th and the 4th porcelain.

b. Insulator B

The detection process of Insulator B is shown in Fig. 6.18. The extraction of Insulator B in Fig. 6.18c based on affine invariant moment is shown in Fig. 6.18a.

Table 6.6 Affine invariant moments between the connected regions and templates

Distance from template	1	2	3	4	5
Figure 6.3a	24.5642	32.0759	5.9995	6.1238	24.7278
Figure 6.3b	22.1446	29.9254	3.2690	3.6029	22.4030
Figure 6.3c	24.4898	32.0131	5.9071	6.0382	24.6571
Figure 6.3d	24.5004	32.0215	5.9213	6.0510	24.6671
Figure 6.3e	16.3800	23.8147	3.5176	2.9112	16.4949
Figure 6.3f	27.3240	35.1517	8.4779	8.8130	27.6201

The result through eliminating the two ends of insulator based on dilation operation is shown in Fig. 6.18b. The effect of local region contrast adjustment is shown in Fig. 6.18c. The gray level statistical graph of Insulator B is shown in Fig. 6.18d.

In Table 6.8, the 4th stripe width is two times than that of other interval, so it can be judged that Insulator B is here, and there is a foreign body between the 4th and the 4th porcelain.

In Table 6.8, the width of this test group has no mutation. Therefore, it can be concluded that the Insulator B is normal. The real-life images are used to verify the detection method, their detection results are listed below.

The experimental picture number is 38, in which there are 33 images with insulator and 3 images including with fault. There are 32 images with insulator and 3 images with fault are correctly recognized, and the recognition rate is 96.97 %. The error recognition is that the large area of insulator is blocked because of the shooting angle, which leads to the affine invariant moment distance over the threshold. The problem can be improved through adjusting the shooting angle.

6.3.5 Fault Detection Based on Wavelet Singular Value

Wavelet transform has been proved to be effective in detecting the spatial singularity of the signal. Because of the periodic grayscale distribution on the surface of insulator, the safety-threatening working state (such as the breakage of ceramic chips) can be regarded as the singularity of grayscale distribution. The detection method based on wavelet singular value detection is presented in this chapter.

1. Detection Process

The process of detecting safety-threatening states of insulators based on wavelet singular value detection is achieved in three steps, namely angle adjustment, image average filtering and singular value detection [7].

(1) Angle adjustment

The purpose of angle adjustment is to rotate the image of insulator to make sure that the insulator stays horizontal in the image. Due to the material (ceramic) and the shape (approximately cylindrical) of the insulators, the line, where the light

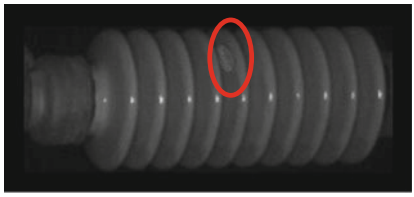

(a) Extraction of Insulator A based on affine invariant moment

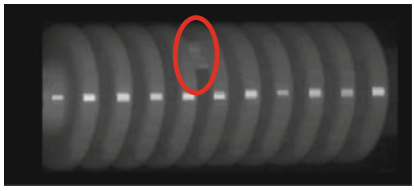

(b) Eliminating the two ends of insulator based on dilation operation

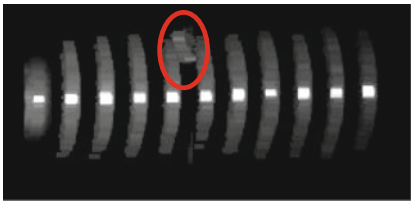

(c) Local region contrast adjustment of Insulator A

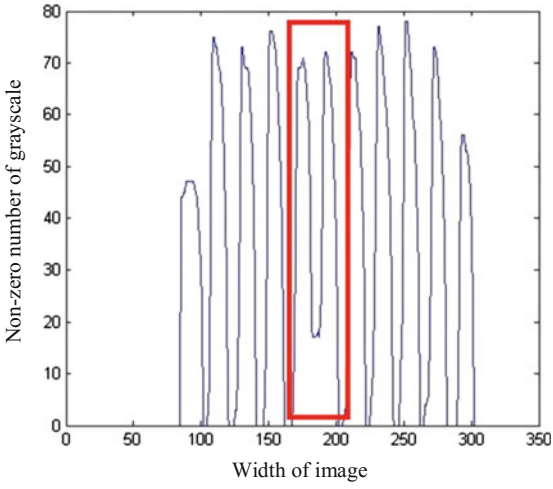

(d) Gray level statistical graph of Insulator A

Fig. 6.17 Detection process of insulator A

Table 6.7 Stripe widths of insulator A

No	1	2	3	4	5	6	7	8	9
Stripe width	20	21	21	40	20	21	20	21	20

Fig. 6.18 Detection process of insulator B

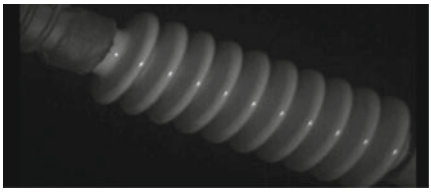

(a) Extraction of Insulator B based on affine invariant moment

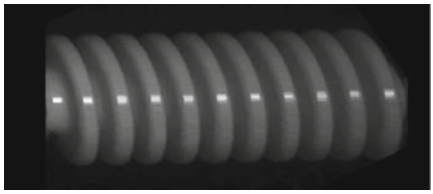

(b) Eliminating the two ends of insulator based on dilation operation

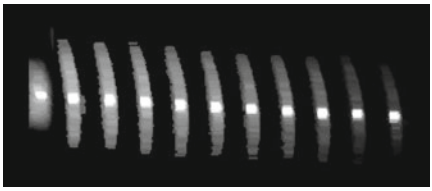

(c) Local region contrast adjustment of Insulator B

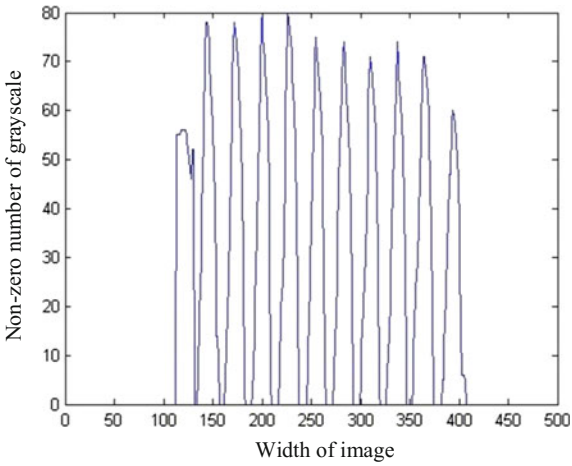

(d) Gray level statistical graph of Insulator B

Table 6.8 Stripe widths of insulator B

No	1	2	3	4	5	6	7	8	9
Stripe width	28	26	28	27	28	27	27	27	28

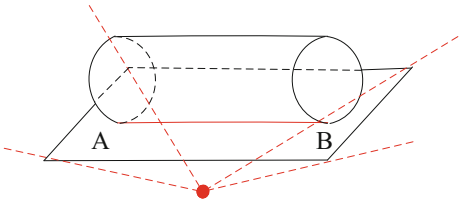

Fig. 6.19 Sketch map of the insulator illumination

plane is tangent to the surface of insulator, is the brightest area on the surface of insulator. In Fig. 6.19, the cylinder represents the insulator, and line *AB* is the strongest reflection location on the surface of insulator.

A high-pass filter is applied to the image of insulator, and then the edges of image are detected by using Canny operator. Some light spots emerge in the edge map, as shown in Fig. 6.20b. Extract the geometric center of light spots and compute the fitting line of e light spots (as shown in Fig. 6.20c), and then the angle that the image needs to be rotated can be determined according to the fitting line's slope.

(2) Image average filtering

For the periodicity of insulator, if the insulator is in good condition, its horizontal gray value change mode is basically the same. The fracture of porcelain skirt and the inclusion of foreign body will damage the regularity of its spatial arrangement.

In general, the piece number of rod insulator porcelain skirt in high speed railway is 10 or 11, namely the number of insulator characteristic regions. Based on the periodicity of characteristic regions, the fracture of porcelain skirt and the inclusion of foreign body can be justified, and the fault can be obtained.

$$T_{m\_x}(y) = T(x = m, y) \tag{6.27}$$

(a) Original insulator Image (b) Edge map extracted by Canny operator (c) Fitting line of light spots

Fig. 6.20 Angle adjustment of insulator

where T_{m_x} is the horizontal gray value corresponding to the mth row. In order to decrease the influence of gray value inequality, the average filtering is utilized to smooth the image [16].

$$T_{m\_x}(y) = \frac{T_{m\_x}(y) - mean(T_{m\_x}(y))}{std(T_{m\_x}(y))} \tag{6.28}$$

In order to make the judgment more intuitive, the wavelet transform is used to calculate the modulus maxima of the horizontal gray value curve.

(3) Singular value detection

The space-frequency localization characteristic of wavelet analysis can make the detection of signal singular values very easy. The problem of localizing the signal singular value can be converted to localizing the maximum values of wavelet coefficients. The exact relationship between the modulus maxima of wavelet transform and the signal singularity can be determined according to the Lipschitz exponent γ. The Lipschitz exponent γ of a function at a certain point represents the singularity of the point. The greater γ means the higher smoothness degree, and on the contrary, the greater singularity.

If the function $f(t)$ in $[t_1, t_2]$ satisfies $\left|W_f(a,t)\right| \leq ka^{\gamma}$, where k is the constant, γ will keep unchanged. The γ value of singularity point t_0 is less than that of other points in (t_0, ε). When $a \to 0$, the wavelet transform coefficient at t_0 has the slowest decay, the wavelet transform coefficients at other points in (t_0, ε) will have constantly convergence, and the wavelet transform coefficient at t_0 become the modulus maxima. Thus, the signal singularity detection can be transformed to the detection of wavelet transform modulus maxima [17, 18].

2. Experiments

The grayscale distribution of 'normal' insulators is cyclical. The breakage of the ceramic chips and the foreign body clamped between the ceramic chips will cause local singularity in the grayscale distribution, which can be detected from the local maximum values of wavelet coefficients on the specific scale. The detection of local maximum values includes the following steps. The image is normalized before singular value detection.

(1) Define the baselines in the insulator image. Perform the convolution between the sub-windows on the baselines and the Gaussian wavelet kernel. Thus the wavelet transform on the baselines is completed.
(2) Compute the magnitude of wavelet coefficients. Detect the local maximum values of the wavelet coefficients.
(3) Normalize the local maximum values of wavelet coefficients.
(4) Set the threshold of local maximum value. Remove the local maximum values that are below the threshold.

(5) Compute the intervals between the indexes of local maximum values. Analyze the regions with abnormalities. Detect the safety-threatening conditions of insulators.

Figure 6.21 shows the detection result of insulator breakage fault. The left image of Fig. 6.21b corresponds to the grayscale distribution on the baseline of which the

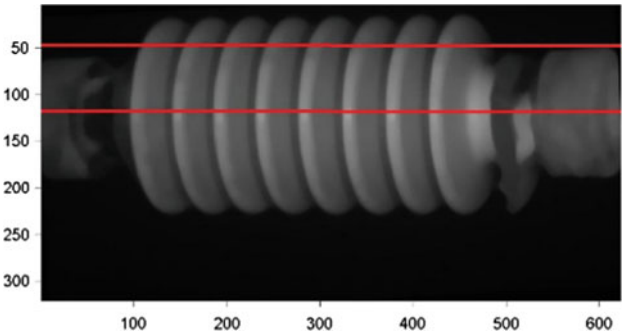

(a) Image of the baselines

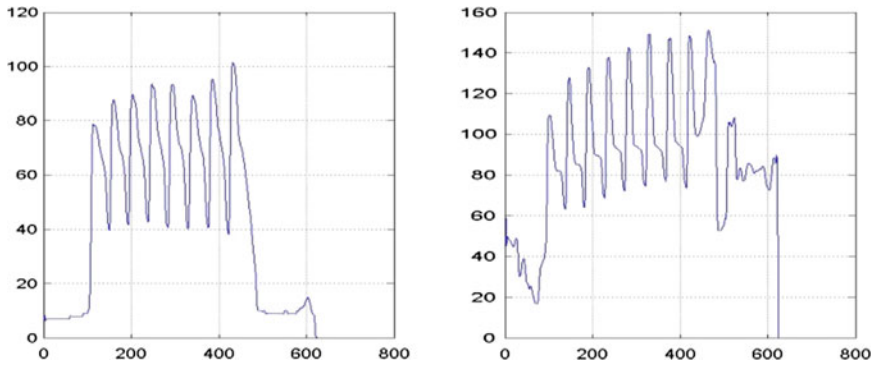

(b) Grayscale distribution on the two baselines

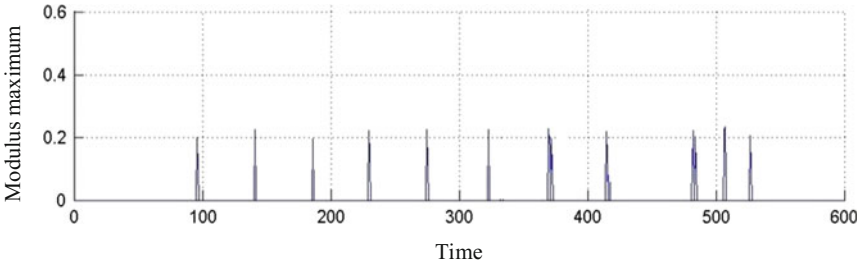

(c) Local maximum values of wavelet coefficients on the baseline

Fig. 6.21 Detection of insulator fracture fault

vertical coordinate is 50. Eight peaks can be found on the curve. However, the normal number of peaks is 10–11 because the insulator usually includes 10–11 ceramic chips. The image of local maximum values of wavelet coefficients on the baseline of which the vertical coordinate is 120 is shown in Fig. 6.21c. The right image of Fig. 6.21b shows the grayscale distribution on this baseline. It can be seen from Fig. 6.21c that the normal interval between two local maximum values is 48. The interval increases to 81 where the ceramic chip is broken. Based on this, the abnormality of this insulator can be detected.

Figure 6.22 shows the result of foreign body detection. Normally, the intervals between the local maximum values are 11 and 18 alternately. However, the interval between the eighteenth and nineteenth local maximum values is 33 (as shown in Fig. 6.22c). Based on this, the foreign body between the ceramic chips of the insulator can be detected.

6.3.6 *Fault Detection Based on Chan-Vese Model*

The insulator's edge information is also helpful for the detection of insulator abnormality. In this section, in order to efficiently extract the contour of the insulator, Chan-Vese model (known as CV model) [11] is adopted.

1. Detection Process

The basic idea of CV model is to use a level set function ϕ to segment an image into two regions, target and background, which are respectively denoted by $\{c_1(x,y) : \phi(x,y) > 0\}$ and $\{c_2(x,y) : \phi(x,y)\}$ [19]. In order to upgrade the convergence speed, Yang et al. proposed an improved CV model [20]. The model can be formulized as follows.

$$F(\phi, C_1, C_2) = u \int_{\Omega} \delta(\phi)|\nabla\phi| dxdy + v \int_{\Omega} H(\phi) dxdy + \lambda_1 \int_{\Omega} |I - C_1|^2 H(\phi) dxdy + \lambda_2 \int_{\Omega} |I - C_2|^2 |1 - H(\phi)| dxdy \tag{6.29}$$

Set I as the original image, u, v, λ_1 and λ_2 as the weight parameters. $\delta(x)$ is the Dirac function and $H(\phi)$ is the Heaviside function. To ensure the smoothness of the contour in the evolution, the front two portions in this formula are used to calculate the length of active contour and the internal area of contour line, respectively. The back two portions are used to calculate the mean density of the regions inside and outside of contour line. And the constant C_1 and C_2 represent the mean intensity value of the region inside or outside the level set ϕ, defined by

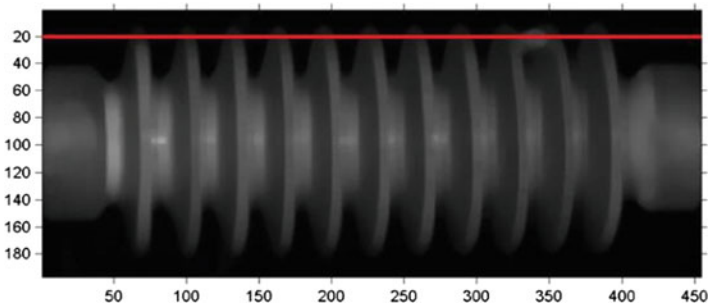

(a) Image of the baselines

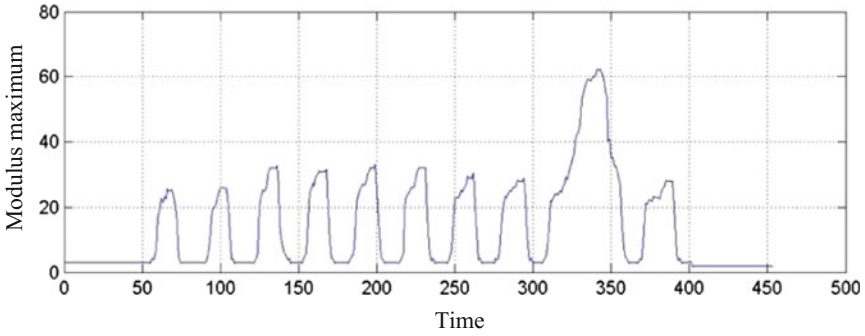

(b) Grayscale distribution on the baselines

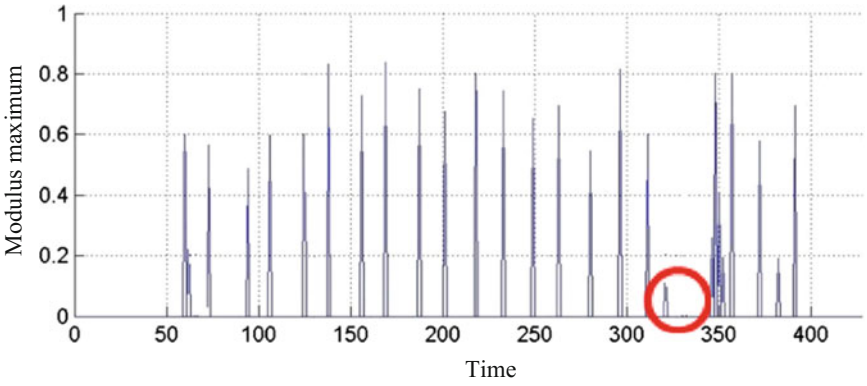

(c) Local maximum values of the wavelet coefficients on the baseline

Fig. 6.22 Detection of the foreign body

$$C_1(\phi) = \int_{\Omega} I(x,y) H_\varepsilon(\phi) dxdy \Big/ \int_{\Omega} H_\varepsilon(\phi) dxdy \tag{6.30}$$

$$C_2(\phi) = \int_{\Omega} I(x,y)[1 - H_\varepsilon(\phi)] dxdy \Big/ \int_{\Omega} [1 - H_\varepsilon(\phi)] dxdy \tag{6.31}$$

$$H_\varepsilon(z) = \frac{1}{2}\left(1 + \frac{2}{\pi}\arctan\left(\frac{z}{\varepsilon}\right)\right), \quad \delta_\varepsilon(z) = \frac{1}{\pi}\frac{\varepsilon}{\varepsilon^2 + z^2} \tag{6.32}$$

where ε is defined as a selected minimum for the numerical calculation.

The equations above are solved as follows.

$$\partial\phi/\partial t = \delta_\varepsilon(\phi)\left[u\nabla \cdot \frac{\nabla\phi}{|\nabla\phi|} v - \lambda_1[I(x,y) - C_1]^2 + \lambda_2[I(x,y) - C_2]^2\right] \tag{6.33}$$

$$\phi(0,x,y) = \phi_0(x,y) \tag{6.34}$$

where $\phi_0(x,y)$ is the constructed signed distance function according to initial contours.

In the formula (6.35), the CV method utilizes the local gradient information to control the curve deformation movement and the evolution of the contour curve.

It can be seen from the above equations that CV model controls the deformation of curve and the evolution of contour curve based on local gradient information. Even the center of contour curve is not in the center of the area, the contour curve of the object can still be extracted.

The contours of insulators extracted by CV model are shown in Fig. 6.23 [21].

Discrete cosine transform is used to design the filters that can eliminate the frequency information corresponding to the background while enhancing the frequency information corresponding to the insulator fault.

The two-dimensional discrete cosine transform for image $f(x,y)$ is defined as

$$C(0,0) = \frac{1}{N}\sum_{x=0}^{M-1}\sum_{y=0}^{N-1} f(x,y) \tag{6.35}$$

$$C(u,v) = \frac{2}{N}\sum_{x=0}^{M-1}\sum_{y=0}^{N-1} f(x,y)\left[\cos\frac{(2x+1)u\pi}{2M}\right]\left[\cos\frac{(2y+1)v\pi}{2N}\right] \tag{6.36}$$

And its inverse transformation is

$$f(x,y) = \frac{1}{N}C(0,0) + \frac{2}{N}\sum_{x=0}^{M-1}\sum_{y=0}^{N-1} C(u \cdot v)\left[\cos\frac{(2x+1)u\pi}{2M}\right]\left[\cos\frac{(2y+1)v\pi}{2N}\right] \tag{6.37}$$

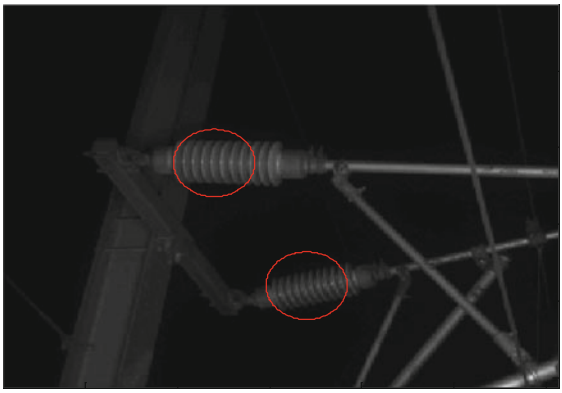

(a) Initial contour

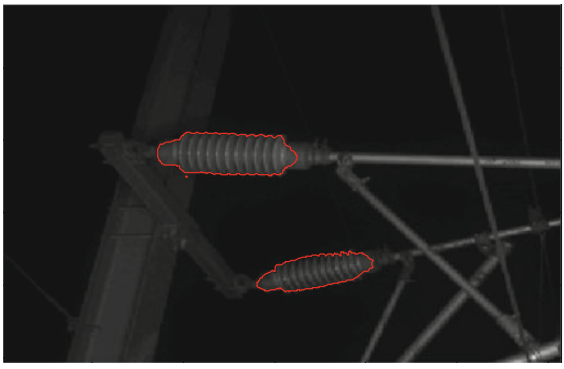

(b) Contour extraction of multiple insulators

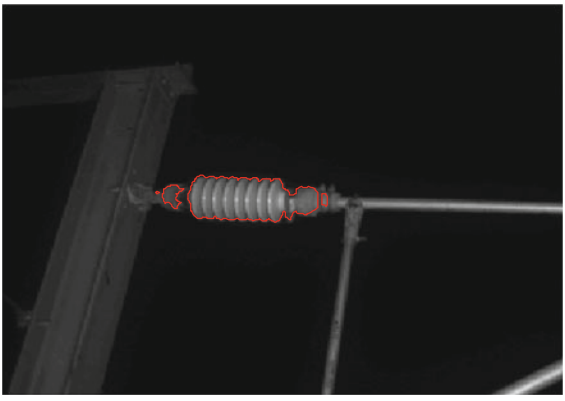

(c) Contour extraction of fault insulator

Fig. 6.23 Insulator contour extraction results

where $C(u, v)$ represents the two-dimensional energy function in the frequency domain after discrete cosine transform.

After discrete cosine transform, the power spectrum of the image is

$$P(u, v) = |C(u, v)|^2 \tag{6.38}$$

As the frequency increases, the power spectrum of image decays rapidly. The feature of the high frequency area is not obvious. Thus the function below is often utilized.

$$P(u, v) = \lg(1 + |C(u, v)|^2) \tag{6.39}$$

Spectral Clustering [22] is used to achieve the edge point clustering after the enhancement of insulator sub-image. Spectral clustering is able to find the globally optimal solutions in sample spaces of any shape. It evaluates not only the intra-class similarity level, but also the inter-class unlikeness level, so the optimization division of the sample space is obtained.

Suppose V vertexes, E edges are included in graph G. By removing certain edges, the graph can be divided into two disjoints vertex sets, A and B. That is, $A \cup B = V$ and $A \cap B = \phi$. Shi and Malik proposed the measurement method of non-correlation degree between the two sets. The formulation of non-correlation degree is shown as follows.

$$Ncut(A, B) = \frac{cut(A, B)}{assoc(A, V)} + \frac{cut(A, B)}{assoc(B, V)} \tag{6.40}$$

where $assoc(A, V) = \sum_{i \in A, j \in V} w_{ij}$ and $assoc(B, V) = \sum_{i \in B, j \in V} w_{ij}$ represent the connection sum between the nodes in the two sets and all nodes in the whole graph, respectively. $cut(A, B) = \sum_{i \in A, j \in B} w_{ij}$, w_{ij} is the weight of connection side between the two vertexes i and j.

To determinate the criterion of the cut set is to find the minimum of function *Ncut*. The *Ncut* method converts the process of optimal value calculation of *Ncut* to the process of solving the matrix eigenvalues and the eigenvectors. Suppose $n = |V|$ and x is an n order direction vector. $x_i = 1$ means that vertex i is in set A, and $x_i = -1$ means that vertex i is in set B. $W_{n \times n}$ is an symmetric matrix. $W(i, j) = w_{ij}$, and $d_i = \sum_j W(i, j)$. D is a diagonal matrix. $D(i, j) = d_i$. Suppose $k = \sum_{x_i > 0} d_i / \sum_i d_i$ then

$$\min Ncut(A, B) = \min_y \frac{y^T (D - W) y}{y^T D y} \tag{6.41}$$

where y is defined in a continuous interval $[-1, 1]$. In order to seek the $\min Ncut(A, B)$, solve

$$\arg \min_{x^T D|=0} \frac{y^T (D - W)y}{y^T Dy} \tag{6.42}$$

According to Rayleigh quotient principle [23], the optimization of (6.34) means finding the second smallest eigenvalue of (6.35).

$$(D - W)x = KDx \tag{6.43}$$

The eigenvector corresponding to the second smallest eigenvalue contains the partition information of graph. The undirected weighted graph G is set up based on the sample set, and matrixes W and D are set up according to G. Then the Fiedler vector corresponding to the second smallest eigenvalue is obtained. The divide-point i, which minimizes $Ncut$ is set in the Fiedler vector based on heuristics rules. The points in the Fiedler vector, whose values are larger than i, are divided into one group. The points, whose values are smaller than i, are divided into the other group.

2. Experiments

In order to verify the effectiveness of the discrete cosine transform and spectral clustering method on fault enhancement and feature extraction of insulators, the insulators with inclusion foreign body, fracture and combination fault, are detected in this section. The detection result of insulator with inclusion foreign body is shown in Fig. 6.24. Figure 6.24a is the insulator with inclusion foreign body. Figure 6.24b is the edge detection result of fault insulator. Figure 6.24c is the edge detection result using Canny edge operator. It can be seen from the comparison analysis that the fault information of image after the cosine transform is more obvious. Figure 6.24d is the result using edge spectral clustering. It can be seen that the clustering method can be used to distinguish the fault area.

The initial two classes are set as x_0 and x_1. After calculation, the ratio of edge points of first class to the whole edge points is 9.1 %. Based on many experiments, the ratio is in the range of 47–53 %, so the fault judgement can be obtained.

The detection results of insulator's other faults by using edge spectral clustering are shown in Figs. 6.25, 6.26 and 6.27. In Fig. 6.25, the ratio of edge points of first class to the whole edge points is 11.2 %. In Fig. 6.26, the ratio of edge points of first class to the whole edge points is 26.2 %. In Fig. 6.27, the ratio of edge points of first class to the whole edge points is 7.6 %. Although the clustering method is not able to classify the faults, it can be used to determine the fault of insulator.

From Table 6.9, it can be seen that the wavelet transform modulus maxima can detect the insulator gray singularity of insulator for judging its state, and the recognition ratio is 89.7 %. For the discrete cosine transform and spectral clustering method to 68 insulator state detection, there are only four failures, and the recognition ratio is 94.1 %. The main reason is that the insulator is in the image boundary, the threshold of clustering center is too small, and the center point is not eliminated, which leads to the incomplete information of the extracted insulator.

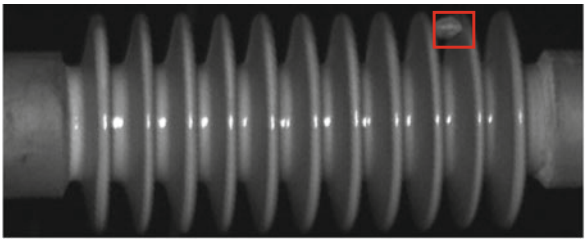

(a) Insulator with foreign body

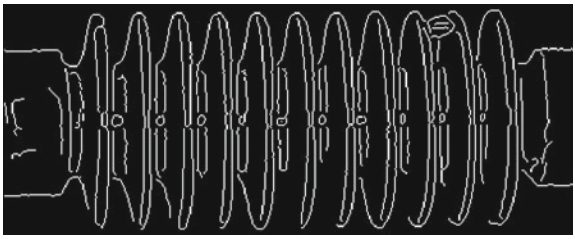

(b) Edge detection of fault insulator

(c) Edge detectionof enhanced fault insulator

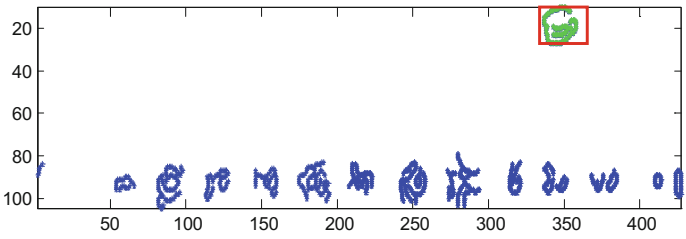

(d) Edge detection of spectral clustering

Fig. 6.24 Detection of insulator with the foreign body

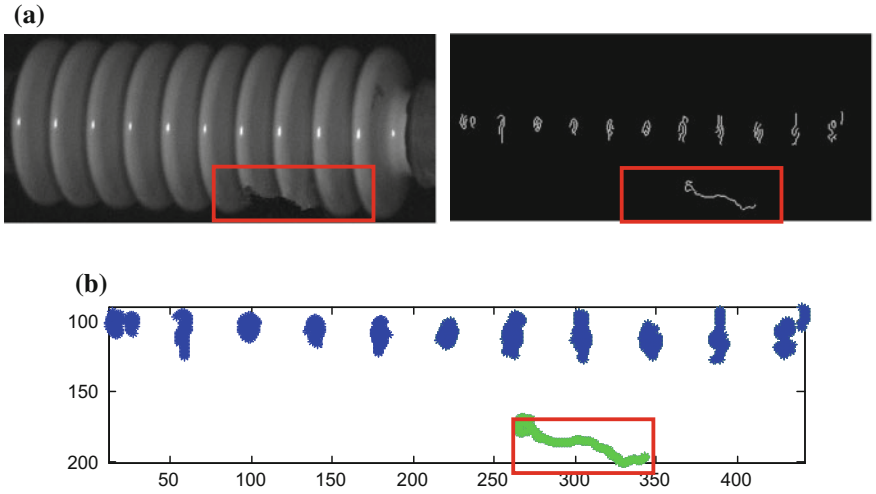

Fig. 6.25 **a** Fault insulator and its edge detection. **b** Detection of edge spectral clustering

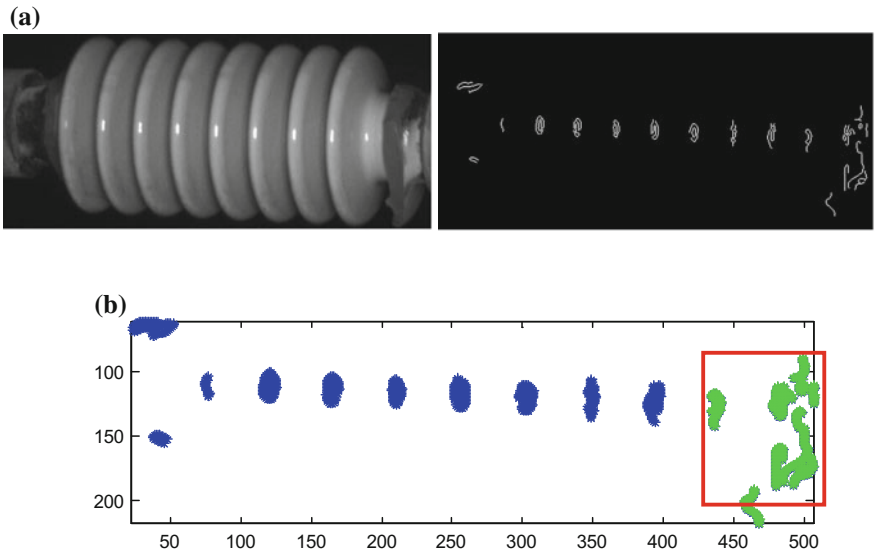

Fig. 6.26 **a** Fault insulator and its edge detection. **b** Detection of edge spectral clustering

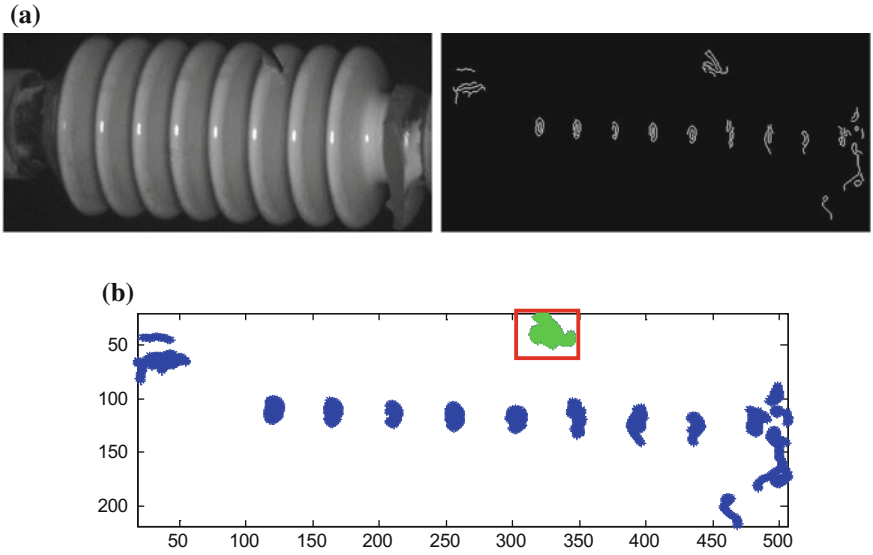

Fig. 6.27 **a** Fault insulator and its edge detection. **b** Detection of edge spectral clustering

Table 6.9 Insulator fault detection comparison with other methods

Fault detection method	Normal	Fault	Correct detection	Recognition ratio (%)
Wavelet transform modulus maxima	60	8	61	89.7
Method used in this section	60	8	64	94.1

6.3.7 *Fault Detection Based on Curvelet Coefficients Morphology*

As the discussion in Chapter 5, the second generation curvelet transform has the characteristics of multiple scales, a number of decomposition directions in each scale, and the characteristics of anisotropy. Therefore, curvelet transform is very suitable for image analysis with the regularity of consistency.

In the catenary suspension system, the insulator porcelains are laid by juxtaposition and superimposition. The captured images show a very regular direction and interval consistency. Other fittings in catenary suspension system have no the similar characteristics, thus the second generation curvelet transform is very suitable for the fault detection of insulators.

1. Detection Process

(1) Pre-processing image

In order to improve the accuracy of image recognition algorithm and reduce the influence of uneven brightness in the insulator image, the pre-processing must be performed to suppress the pixel parts with lower and high gray value and enhance the pixels in the special gray value range of image. The principle of gray balance is shown as follows.

$$M(m,n) = \begin{cases} 0 & I(m,n) < L_{in} \\ (I(m,n) - L_{in}) \cdot \frac{H_{out} - L_{out}}{H_{in} - L_{in}} + L_{out} & L_{in} < I(m,n) < H_{in} \\ 0 & I(m,n) > H_{in} \end{cases} \tag{6.44}$$

where I is the original image, and M is the enhances image. L_{in} and H_{in} are the ranges to enhance pixels in the original image. L_{out} and H_{out} are the pixels range after enhancement.

The pre-processing of image mainly plays two roles. The first is to make the edge of single insulator edge clearer, and the second is suppress the connection parts of pull rod, arm joints and insulator, where their pixel gray value is low.

(2) Insulator positioning based on curvelet transform

From Fig. 6.1b, the image of catenary suspension system is very complicated, including insulator, arm, positioner, contact line, bearing cable and so on, which adds the difficulty of insulator detection.

The statistics of a number of image acquisition and catenary design data show that the insulators that connect pillar and horizontal rod are arranged horizontally and the insulator porcelains are perpendicular to the ground. The angle of insulator that connects arm and pillar is 135°, and the angle between their porcelains and the ground is 45°. Due to the different lines and regions, the number of insulator pieces may be different, but the insulator pieces should be uniform and parallel. This directional distribution can provide the convenient to use curvelet transform to locate the insulator.

In order to ensure the accuracy of analysis, the curvelet decomposition is carried out in 64 directions. Because of the curvelet's directional filtering characteristic, the single direction coefficient matrix can only detect the image elements in a certain direction, so it can eliminate the influence of other hanging devices on the insulator detection.

In Fig. 6.28, the circle marks the location of large curvelet coefficient aggregation, which indicates at the location of image there are singularity characteristics that consistent with the decomposition direction. The vertical image elements (horizontal rod insulator) are in 24th characteristic matrix, as shown in the left of Fig. 6.29. The image elements whose angle is 45° (inclined arm insulator) are in 28th characteristic matrix, as shown in the right of Fig. 6.29.

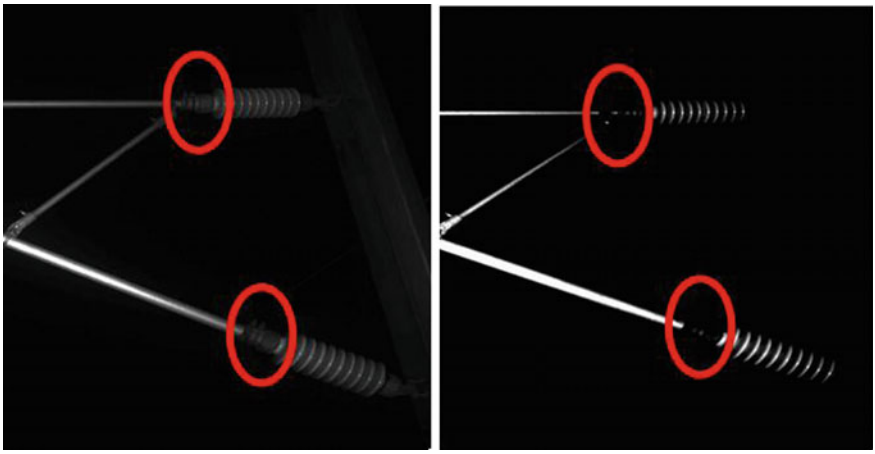

Fig. 6.28 Results after pre-processing

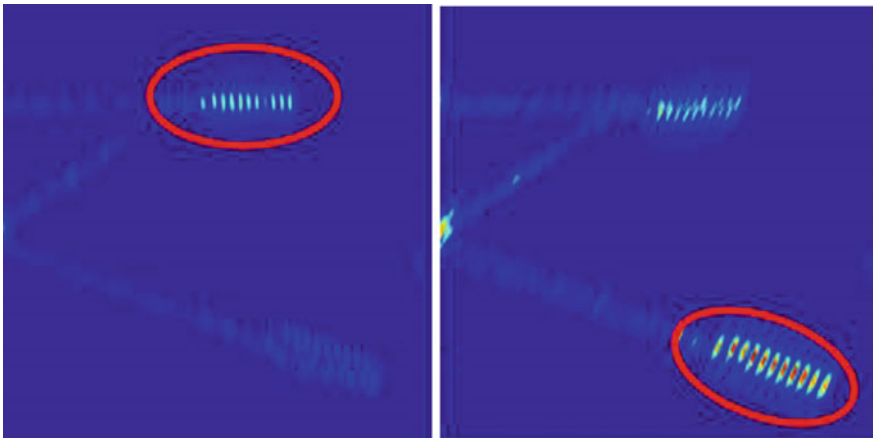

Fig. 6.29 Analysis results of insulator curvelet coefficients

(3) Curvelet coefficients energy consistency correction based on morphological closing operation

For two images A and B, the expansion operation is defined as follows [24, 25].

$$dilation(A, B) = \{a + b | a \in A, b \in B\} \tag{6.45}$$

The corrosion operation is defined as follows.

$$erosion(A, B) = \{a|(a + b) \in A, a \in A, b \in B\} \tag{6.46}$$

Morphological closing operation is a corrosion process after expansion. Its purpose is to fill the objects inside the small holes, and connect the adjacent objects.

When the insulator is positioned based on curvelet decomposition, because of the influence of image shooting and pre-processing, the coefficients of detection region may be not clear, irregular or have big difference between different insulator test results, which will lead the heavy influence on the later fault detection. Therefore, in this section, morphological closing operation is adopted to correct the coefficient matrix, which can make the coefficient distribution of different insulators more regular and the consistency better.

In order to make the coefficient distribution more regular, the method of large expansion and small corrosion can be used to the close the operation. The corrosion operation is used to a rectangular template, the expansion template is 20×2 and the corrosion template is 4×1. The distributions of curvelet coefficient matrix before and after correction are shown in Fig. 6.30. It can be found that the distributions of curvelet coefficients of different insulators are more regular and the edges are clearer.

(4) Zonal energy analysis of curvelet coefficients

In order to automatically determine the coefficient distributions of insulator by computer, it is necessary to reduce the dimension of coefficient matrix to the one dimension. The decomposition matrix of curvelet coefficients can be divided by using the zonal band whose angle is consistent to that of curvelet decomposition. The energy of each zonal band is computed, shown in Fig. 6.31.

In order to solve the analysis difficulty that the difference of curvelet coefficients between different insulator porcelain locations is large, the zonal energy is defined as the number of curvelet coefficients that are bigger than the given threshold, shown below.

$$f(x) = C_j(x, y) \cdot \delta(Line_j|C_j(x, y) > k) \tag{6.47}$$

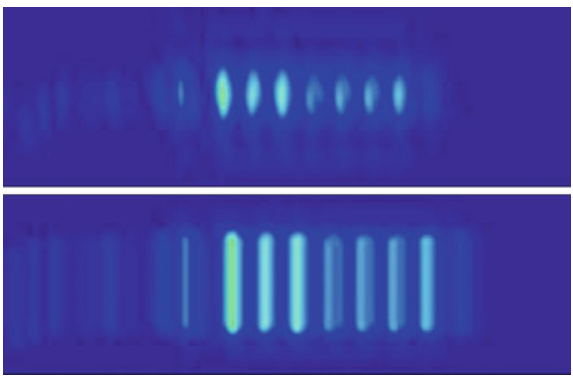

Fig. 6.30 Curvelet coefficient consistency correction using morphological closing operation

where $f(x)$ is the zonal energy distribution function, C_j is the curvelet coefficient matrix at angle j, δ is the zonal choosing function of corresponding angle, and k is the given threshold.

The energy band distributions of insulator porcelain are shown in Fig. 6.32. It can be seen that the energy band with uniform distribution corresponding to insulator porcelain has unique characteristic. The energy band of other fittings in catenary system has no such regularity. Therefore, the energy band distributions can be used to judge the locations of insulator, and their intervals can be adopted to identify whether there is insulator porcelain fracture or lack.

2. Experiment verification [26]

Fault 1: as shown in Fig. 6.33, the left edge of insulator is missing. Figure 6.34 shows the closed operation results, and Fig. 6.35 is the band energy distribution. It can be seen that there is an abnormal location in the uniform distributions of curvelet coefficients, which can be used to judge that there is a fracture of insulator in this location.

Fault 2: as shown in Fig. 6.36, there is a missing piece in the middle of the insulator. Test results are shown in Fig. 6.37. There is a location lack in the uniform

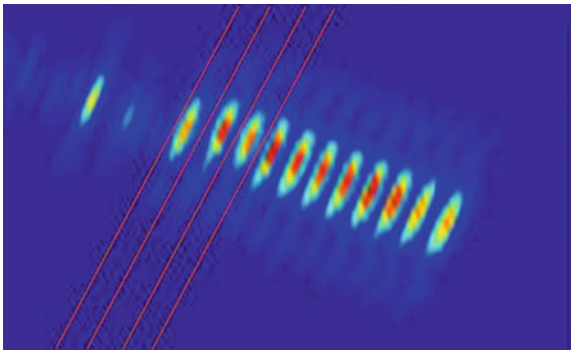

Fig. 6.31 Band calculation principle of curvelet coefficients

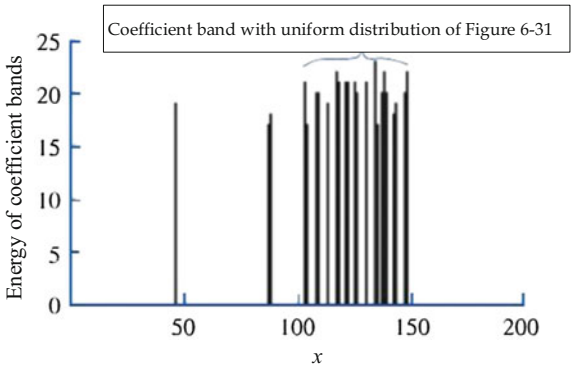

Fig. 6.32 Energy distributions of curvelet coefficient bands

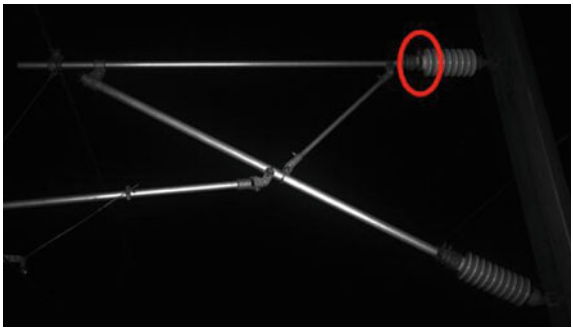

Fig. 6.33 Missing left edge of insulator

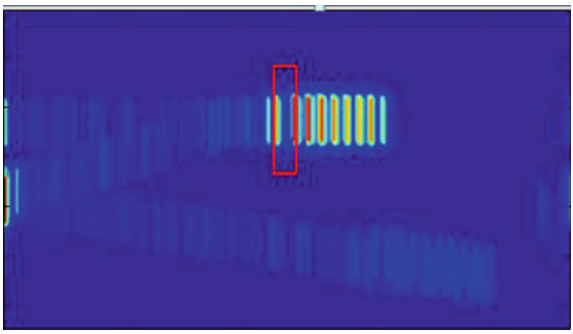

Fig. 6.34 Closed operation results

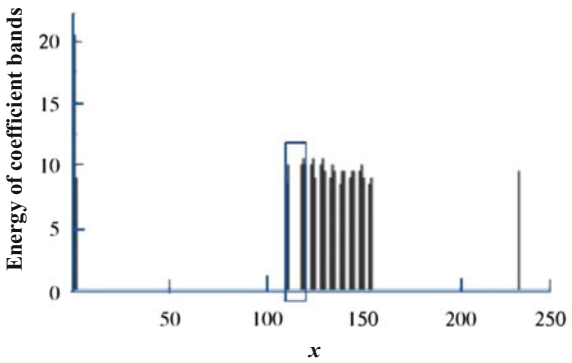

Fig. 6.35 Band energy distribution

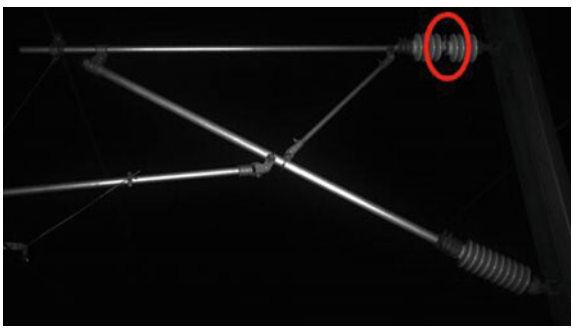

Fig. 6.36 Missing middle piece of insulator

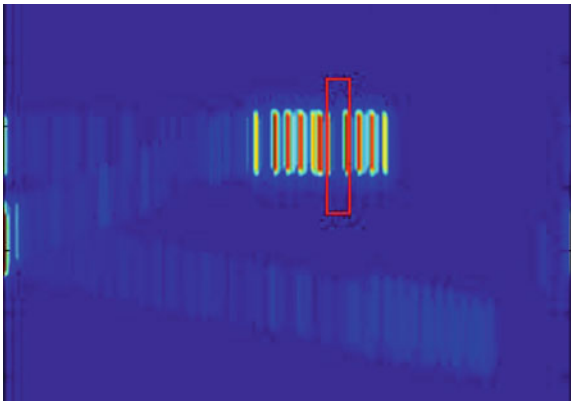

Fig. 6.37 Closed operation results

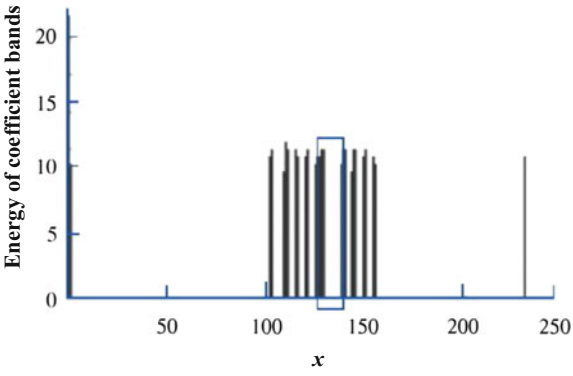

Fig. 6.38 Band energy distribution

distributions of curvelet coefficients, namely the fracture location of insulator (Fig. 6.38).

6.4 Clevis Fault Detection

The clevis is an important load-bearing component in the support structure of high speed railway catenary. In order to ensure the safe operation of train, the construction quality of clevis must be ensured to satisfy the strict requirements [27]. Due to the influence of train vibration in the operation, the fracture of clevis may occur, which will directly reduce the strength of catenary suspension system. Therefore, the fault clevis must be replaced in time. The traditional fault detection method mainly depends on the maintenance staff. This method is less efficient and cannot find the clevis fault in time, so it is necessary to study the automatic detection method.

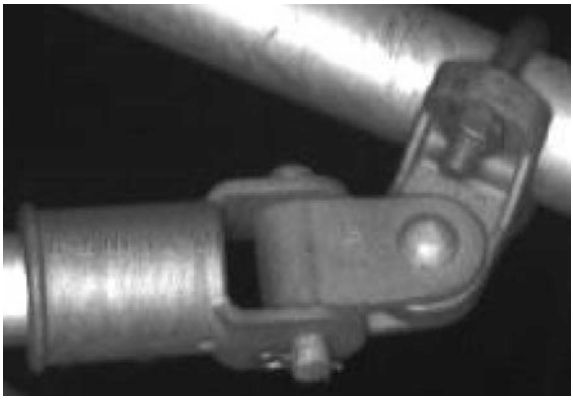

Fig. 6.39 Normal clevis image

In general, the image of catenary suspension system is complex, as shown in Fig. 6.1b, so it is also very difficult to detect the single component fault in the suspension system by using the image processing, especially for the fault detection of the clevis located at the junction of positioner. The normal clevis image is shown in Fig. 6.39.

In this chapter, the matching, positioning and detection methods based on local features and transforms, such as SIFT (Scale-invariant Feature Transform), SUFT (Speed-up Robust Features), HOG(Histogram of Oriented Gradient) features, Hough transform, Gabor wavelet transform and so on, are introduced and applied.

6.4.1 Clevis Matching Based on SIFT

SIFT descriptor was first proposed by Lowe in 1999 [28], and was improved in 2004 [29]. This method can achieve the local feature point matching between images, and it is invariant to rotation, scale variation and grayscale change. In addition, it is able to eliminate the impact of affine transformation, perspective change and noise to a certain extent. The SIFT descriptor is widely adopted in image mosaic, pattern recognition and many other image processing fields [30–32].

1. Algorithm Process

The main steps based on SIFT feature points are shown as follows.

(1) Extrema detection of scale space

The scale space of two dimensional image $I(x, y)$ is defined as the convolution of the image and the Gaussian kernel $G(x, y, \sigma) = \frac{1}{2\pi\sigma^2} e^{-(x^2+y^2)/2\sigma^2}$, namely $L(x, y, \sigma) = G(x, y, \sigma) * I(x, y)$. DOG (Difference-of-Gaussian) pyramid is defined as the difference between the adjacent layers of scale space, denoted as $D(x, y, \sigma)$ below.

$$\begin{aligned} D(x,y,\sigma) &= (G(x,y,k\sigma) - G(x,y,\sigma)) * I(x,y) \\ &= L(x,y,k\sigma) - L(x,y,\sigma) \end{aligned} \tag{6.48}$$

After each detection point (except top or bottom point) of DOG scale space is compared with the 8 adjacent points of the same layer, the 18 adjacent points of the adjacent upper and lower two layers in the pyramid, and the local extrema can be judged. Because the value of DOG scale space is sensitive to the noise and edge, the scale and location of local extrema can be obtained through the fitting of three-dimension two-order function. At the same time, through eliminating the low contrast points and unstable edge response points, the feature points of image in this scale can be determined.

(2) Feature vector

Based on the gradient direction distribution of pixels in the feature point neighborhood, the direction parameter of each feature point can be appointed to ensure the rotation invariance of descriptor. Let

$$m(x,y) = ((L(x+1,y) - L(x-1,y))^2 + (L(x,y+1) - L(x,y-1))^2)^{\frac{1}{2}} \tag{6.49}$$

$$\theta(x,y) = \arctan\left[\frac{L(x,y+1) - L(x,y-1)}{L(x+1,y) - L(x-1,y)}\right] \tag{6.50}$$

where $m(x,y)$ and $\theta(x,y)$ are the gradient amplitude and direction of point (x,y), respectively.

The histogram is adopted to represent the gradient direction of feature point neighborhood pixels. The peak location means the main direction of neighborhood gradient at the key point. In order to ensure the rotation invariance of descriptor, the coordinate of feature point neighborhood is rotated to the main direction of feature points. The 8×8 window centered at the feature point is chosen and segmented into four 4×4 regions, as shown in the left of Fig. 6.40. Each grid represents a pixel in the scale space of feature point neighborhood. The arrow direction

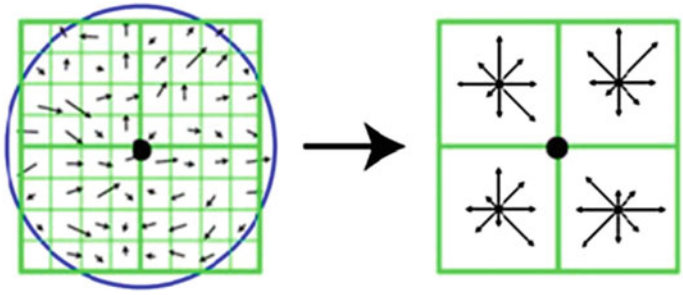

Fig. 6.40 Feature vector generated in feature point neighborhood

represents the orientation of the gradient of the pixel, and the arrow length represents the modulus of gradient. The circle represents the weighting range of Gaussian window. The closer the point is to the feature point, the more it contributes to the statistics of the gradient.

The gradient histograms of 8 directions in each 4 × 4 region are computed, and the accumulated value of each gradient direction is drawn, which can form a seed point, as shown in the right of Fig. 6.40. In this figure, there are 2 × 2 = 4 seed points, and each seed point includes the vector information of 8 directions. Thus, each feature vector can generate 4 × 8 = 32 dimensional data, namely a 32 dimension SIFT feature vector.

(3) Matching of feature vector

In order to localize the clevises in the catenary images, clear clevis images are chosen as standard images for feature point matching, as is shown in Fig. 6.39. The SIFT feature points of catenary images and the standard clevis images are extracted and the feature vectors are generated. The Euclidean distance between the feature vectors is used as the similarity measure.

When the feature points to be matched are less than a certain threshold value d, the matching point is accepted. When the ratio of the nearest and next feather points is smaller than a threshold d, the matching point is accepted. If d is bigger, the matched points will be more, but the mismatching will easily occur and the distribution will be more dispersed. If d is smaller, the matched points will be less, but the matching accuracy is high and the distribution is more concentrated.

2. Matching process

The clevis in the global detecting image can be regarded as the affine transformation of the standard image. The coordinate transformation of two images can be expressed as follows.

$$\begin{pmatrix} x' \\ y' \\ 1 \end{pmatrix} = H_1 \begin{pmatrix} x \\ y \\ 1 \end{pmatrix} = \begin{pmatrix} h_{11} & h_{12} & h_{13} \\ h_{21} & h_{22} & h_{23} \\ 0 & 0 & 1 \end{pmatrix} \begin{pmatrix} x \\ y \\ 1 \end{pmatrix} \tag{6.51}$$

where H_1 is the affine transform matrix, (x, y) and (x', y') are the coordinates of the standard image and the global image. Denote the coordinates of a pair of successfully matched feature points as (x_i, y_i) and (x_i', y_i'), $i \in [1, N]$, N is the number of the successfully matched feature points, then

$$H_1 = BA^T(AA^T)^{-1} \tag{6.52}$$

where $A = \begin{pmatrix} x_1 & x_2 & \dots & x_N \\ y_1 & y_2 & \dots & y_N \\ 1 & 1 & \dots & 1 \end{pmatrix}$, $B = \begin{pmatrix} x_1' & x_2' & \dots & x_N' \\ y_1' & y_2' & \dots & y_N' \\ 1 & 1 & \dots & 1 \end{pmatrix}$.

Because the freedom degree of the affine transform matrix is 6, $N \geq 3$ must be ensured. In order to eliminate the mismatched feature point pairs. The following algorithm is adopted.

All the feature points whose spatial distances are smaller than a certain value are clustered into one cluster, corresponding to a candidate area of the clevis. Each cluster represents an image region that has similar local features to the clevis.

The image of catenary suspension system including clevises is shown in Fig. 6.41. After successful matching with the standard clevis image, the feature points form four clusters, shown in Fig. 6.42.

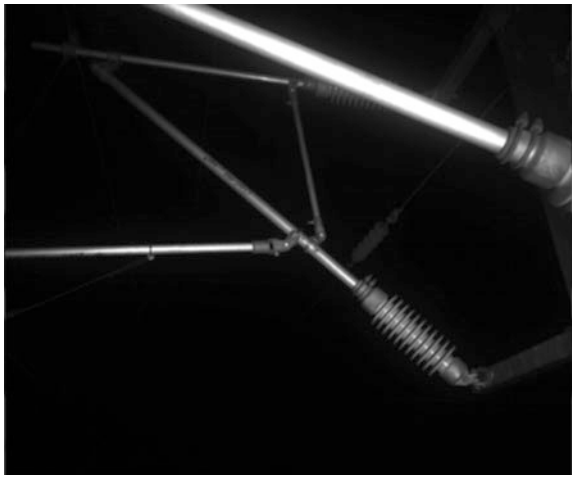

Fig. 6.41 Catenary suspension system including clevises

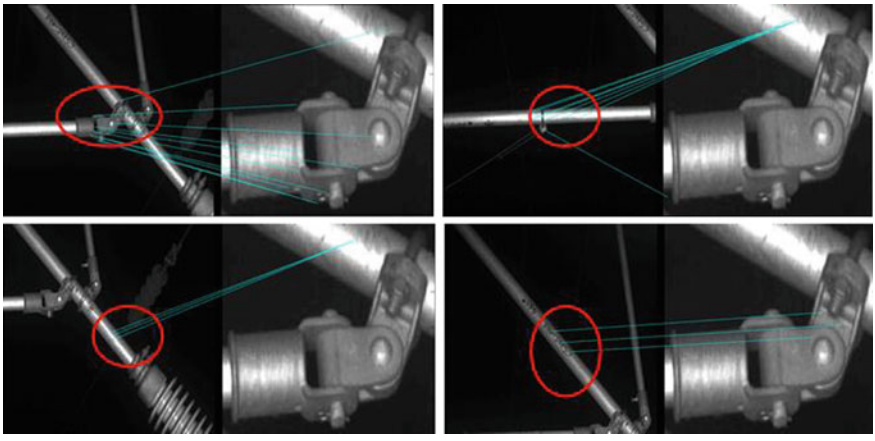

Fig. 6.42 Cluster results of clevis feature points

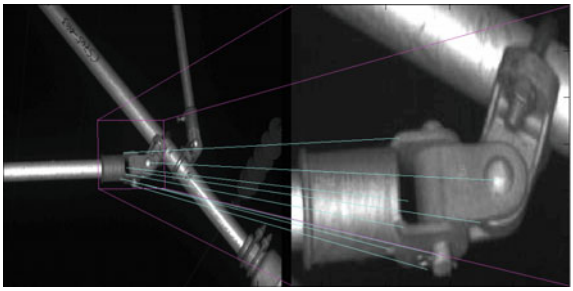

Fig. 6.43 Matching result of clevis

For each candidate area, RANSAC (Random Sample Consensus) [33] algorithm is adopted to eliminate the mismatched points. When judging whether a point pair is an 'outlier' during the calculation of the affine transform matrix (considered as the matching model), the relative position of feature point is also considered. This is because the installation angles of all the clevises are similar.

After computing the affine transform matrix, the clevis in the global image can be located by matching the standard image with the global image. The matching result is shown in Fig. 6.43 [34].

6.4.2 Clevis Matching Based on SURF

SURF (Speeded-up Robust Features) is a local feature detector and descriptor proposed in 2006 [35]. Compared with SIFT, the processing speed of SURF is much faster [36]. The main steps of generating SURF descriptor are described as follows.

1. Algorithm process

(1) Feature point detection

Square-shaped filters are used as the approximation of Gaussian smoothing used in SIFT descriptor. Filtering the image with a square is much faster if the integral image is used, which is defined as follows.

$$I_{\sum}(P) = \sum_{i=0}^{i \le x} \sum_{j=0}^{j \le y} I(i,j) \tag{6.53}$$

where $I(i,j)$ denotes the pixel value of the original image at (i,j), and $I_{\sum}(P)$ denotes the value of the integral image.

The sum of the original image within a rectangle can be evaluated quickly using the integral image, which requires four evaluations at the corners of the rectangle.

Through locating the feature points based on the local maximum of determinant in Hessian matrix, the feature point detection of SURF is realized. For a certain point $X = (x, y)$, its Hessian matrix $H(X, \sigma)$ at the scale σ is defined as

$$H(X,\sigma) = \begin{bmatrix} L_{xx}(X,\sigma) & L_{xy}(X,\sigma) \\ L_{xy}(X,\sigma) & L_{yy}(X,\sigma) \end{bmatrix} \tag{6.54}$$

where $L_{xx}(X, \sigma)$ is the convolutions of the image I and the second-order derivatives of Gaussian function at X, $L_{xy}(X, \sigma)$ and $L_{yy}(X, \sigma)$ have similar meanings as $L_{xx}(X, \sigma)$.

(2) Feature point description

The circular region whose center is the feature point and radius is $6 \times s$ (s is the scale value of feature points) is taken, and then the Haar wavelet responses d_x and d_y of the pixels at the direction x and y are computed. The dominant orientation of the feature points is estimated by calculating the sum of all responses within a sliding orientation window of angle 60°. The entire circular area is traversed through computing the vector at every 5°. Therefore, 72 vectors are generated when the orientation window turns a circle. The orientation of the longest value is determined as the dominant orientation. Then, the rectangle with $20 \times s$ is chosen as the feature extraction region. This region is divided into 4×4 sub-regions. For each sub-region, horizontal and vertical wavelet responses are taken and a feature vector is formed as follows.

$$V = \left(\sum d_x, \sum d_y, \sum |d_x|, \sum |d_y|\right) \tag{6.55}$$

The SURF feature descriptor is generated by combining the feature vectors in the 16 sub-regions, so the total dimension of SURF descriptor is 64.

2. Positioning Process

After extracting the feature points and generating the SURF descriptor in both the global image and the standard clevis image, the clevises can be localized by matching the interesting points between the two images. The matching is also based on Euclidean distance [37].

Euclidean distance is adopted to calculate the similarity of two descriptor metrics, as shown below.

$$Dis_{ij} = \left[\sum_{k=0}^{k=n} (X_{ik} - X_{jk})^2\right]^{1/2} \tag{6.56}$$

where X_{ik} is the kth element in the ith feature descriptor in the matching image, X_{jk} is the kth element in the jth feature descriptor in the template image, and n is the dimension of feature vectors.

For the matching feature points, their Euclidean distances to the template image are computed, and then the distance set can be obtained. The minimum and the second minimum Euclidean distances are obtained through the comparison operation. If the ratio of minimum and the second minimum Euclidean distances is less than the threshold, the two feature points are considered as the matching.

Based on SURF, the local invariant feature points of the original and template images are extracted and described, respectively. The clevis template image is shown in Fig. 6.44, and the original image is shown in Fig. 6.45. The matching results are shown in Fig. 6.46. In order to reduce the error matching points, considering the difficulty of image matching of the catenary suspension system, the error matching elimination method is presented as follows.

(1) The extraction feature points from the original image are clustered through the space distance threshold, which can quickly eliminate the discrete error matching points.

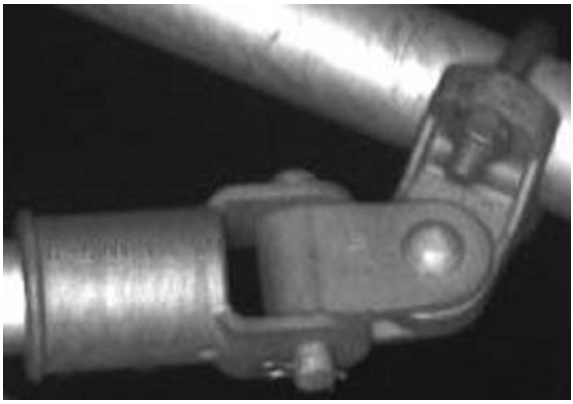

Fig. 6.44 Clevis template image

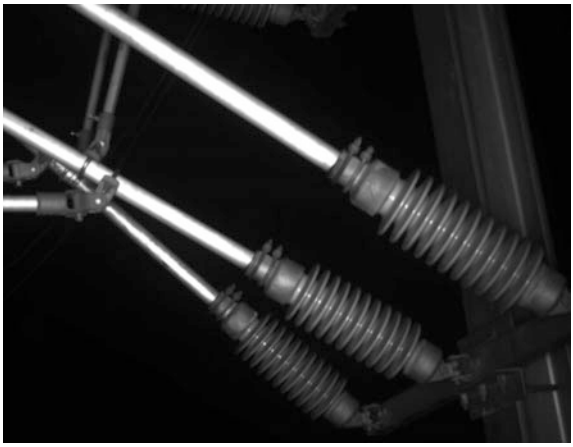

Fig. 6.45 Original image

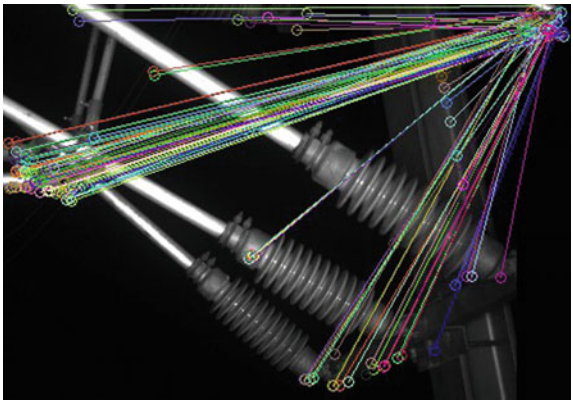

Fig. 6.46 Matching results

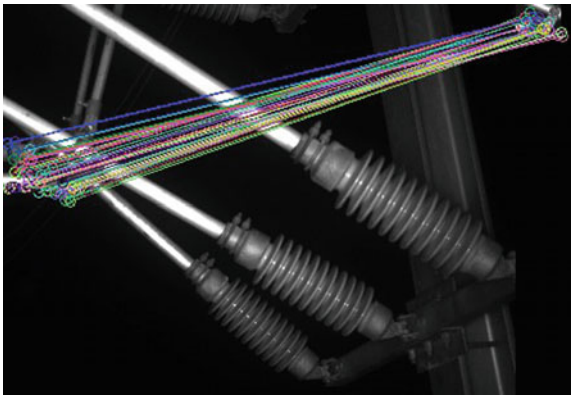

Fig. 6.47 Results after eliminating error matching

(2) The number N_i of matching points in each class is solved, as well as the feature points N in the clevis template image. If N_i is less than 0.6 times of N, the class is considered as the error matching. If N_i is bigger than 0.6 times of N, the class is considered as the correct matching.

The results after eliminating error matching are shown in Fig. 6.47.

6.4.3 Clevis Positioning Based on HOG

Although the detection based on SIFT and SURF can obtain good results, sometimes it is difficult to acquire the feature points. In addition, the results of feature point matching can be affected by the variance of grayscale distributions on the surface of clevises. This problem can be avoided by using a detector based on a sliding window that scans over the global image. The Histograms of Orientated Gradients (HOG) descriptor is widely used in frontal face detection, pedestrian

detection, and vehicle detection. Based on HOG features, an SVM classifier is trained and applied subsequently to all the sub-windows within the image and the presence of clevises by its output is judged in this section.

1. Algorithm process

The basic hypothesis is that the local object appearance and the shape of the object can often be characterized rather well by the distribution of local intensity gradient or edge directions, even without precise knowledge of the corresponding gradient or edge positions [38].

At first, the image is divided into a number of square cells with the same size, and then the four adjacent cells are merged into a square block. They can overlap with each other for the blocks, as shown in Fig. 6.48.

The gradient amplitude $m(x, y)$ and direction $\theta(x, y)$ of each pixel can be computed and the gradient histogram of each cell can be obtained, as shown below.

$$dx = I(x+1, y) - I(x-1, y) \tag{6.57}$$

$$dy = I(x, y+1) - I(x, y-1) \tag{6.58}$$

$$m(x, y) = \sqrt{dx^2 + dy^2} \tag{6.59}$$

$$\theta(x, y) = \tan^{-1}\left(\frac{dy}{dx}\right) \tag{6.60}$$

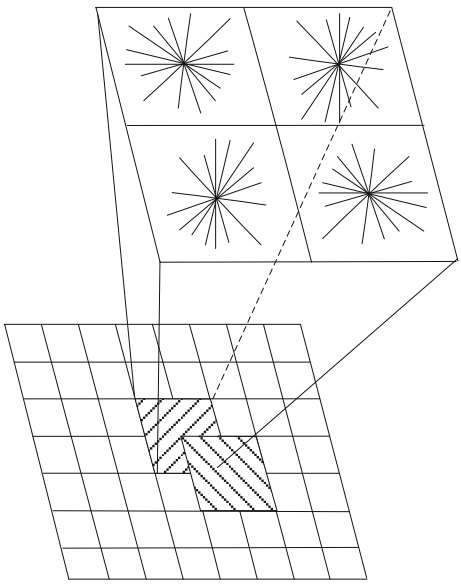

Fig. 6.48 Generation of HOG features

According the Dalal's suggest, each gradient histogram includes 9 column direction histograms, thus a feature vector with $4 \times 9 = 36$ dimensions can be produced through connecting the 4 histograms. In order to eliminate the influence of light and background, the feature vector is normalized in the sense of L_2 as follows.

$$v \leftarrow v / \sqrt{\|v\|_2^2 + \varepsilon^2} \tag{6.61}$$

where v is the feature vector without normalization, $\|v\|_2$ is the 2-norm, and ε is adopted to avoid that the denominator is 0.

HOG feature vector can be obtained by connecting all block feature vectors in the image. A pictorial rendition of the HOG features of a clevis (shown in Fig. 6.49) is shown in Fig. 6.50.

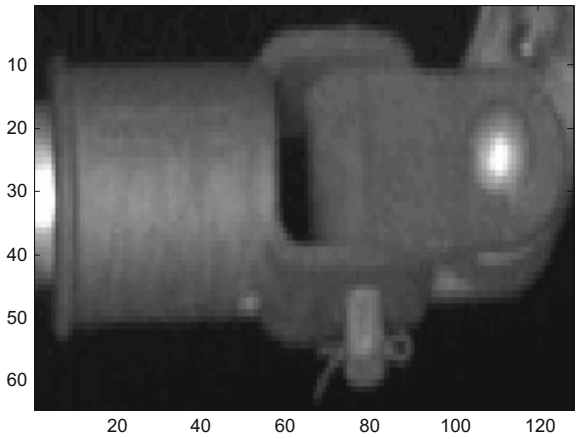

Fig. 6.49 Original image of a clevis

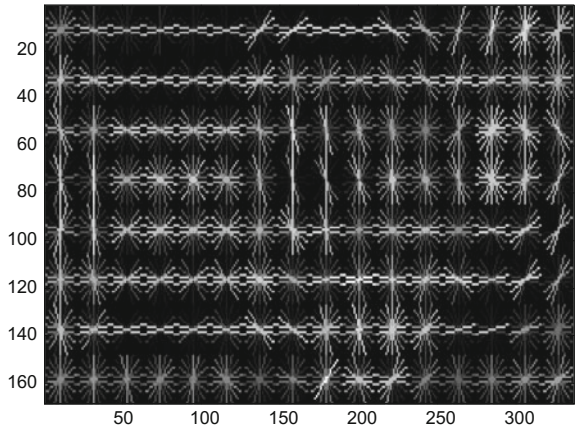

Fig. 6.50 A pictorial rendition of the HOG features

In addition, in order to improve the computation speed of gradient histogram, the integral graph method [39] is adopted. The value of any point in the integral image is defined as the sum of gray values of all the pixels in the rectangular region between the original image coordinates and the coordinate origin, namely

$$ii(x,y) = \sum_{x' \le x, y' \le y} i(x',y') \tag{6.62}$$

where $ii(x,y)$ is the coordinate point (x,y) in the integral graph, and $i(x',y')$ is the pixel gray value of coordinate point (x',y'). A traversal calculation of original image in integral graph can be completed as follows.

$$s(x,y) = s(x,y-1) + i(x,y) \tag{6.63}$$

$$ii(x,y) = ii(x-1,y) + s(x,y) \tag{6.64}$$

where $s(x,y)$ is the pixel accumulated value of same row at the left. Let $s(x,-1) = 0$ and $s(-1,y) = 0$.

HOG features of arbitrary rectangular area can be calculated by using the integral graph, as shown in Fig. 6.51. The computation formula is expressed below.

$$\sum_{i(x',y') \in D} i(x',y') = ii(4) + ii(1) - (ii(2) + ii(3)) \tag{6.65}$$

2. Positioning process

The positive and negative samples for training are from all artificial interception of catenary suspension system images. In the positive samples, the clevis is located in the middle of the image and occupies the main position of image. The HOG features of positive and negative samples are calculated respectively, and the linear support vector machine (SVM) is trained through the description of samples. SVM is used to determine the maximum interval of two kinds of samples.

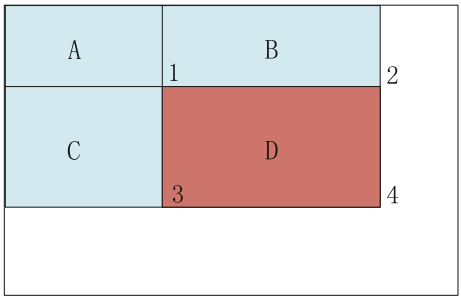

Fig. 6.51 Integral graph principle

Suppose that the training sample set is (x_i, y_i), $i = 1, \ldots, l$, $x_i \in R^n$ and $y_i \in \{1, -1\}$. l is the sample number and n is the feature dimension. The classification-plane for all samples should satisfies

$$\{y_i(w^T \phi(x_i) + b) + C \sum_{i=1}^{l} \xi_i\} \geq 1 - \xi_i \tag{6.66}$$

where the classification-plane is determined by parameter w and b, w is the weight vector, and b is the threshold. ξ_i is the relaxation term in the case of linear non-separable cases. C is the punishment coefficient that is used to realize the balance between the error classification ratio of samples and the algorithm complexity. The minimum value of $\phi(w, \xi)$ can be solved by using the iterative method, namely the optimal classification plane $[w^*, b^*]$ and optimal decision function, as shown below.

$$\phi(w, \xi) = \min\{\frac{1}{2} w^T w\} + C \sum_{i=1}^{l} \xi_i \tag{6.67}$$

$$f(x) = \text{sgn}(w^* \cdot x + b^*) \tag{6.68}$$

For the training of the SVM classifier, a dataset of the clevis is generated. The training dataset includes the positive and negative samples of the clevis. Both the positive and negative samples are cropped from the images captured by the inspection vehicle. Each positive sample contains an instance of the clevis. The clevis is placed in the center of the sample image and takes up most part of it. Clevis in all possible lighting conditions should be included. Each negative sample contains an object that is irrelevant to clevises. The ratio of the length and the width of positive samples are fixed to 2:1, which can ensure that all positive samples have the same (or almost the same) gradient distribution. The samples are normalized to the fixed resolution (64 × 32). Some of the positive and negative samples are demonstrated in Fig. 6.52a, b [40].

Whether does the test window contain the clevis can be judged based on the SVM in the sample training phase. The location results are shown in Fig. 6.53. Figure 6.53a, c and e are the images of catenary suspension system, and their shooting range, shooting angle and exposure intensity are different. Figure 6.53a, e are from the tunnel outside, and Fig. 6.53c is in the tunnel. The different shooting environments result in the large difference of surface and texture of clevis. Figure 6.53b, d and f are the positioning results of clevis in Fig. 6.53a, c and e, respectively.

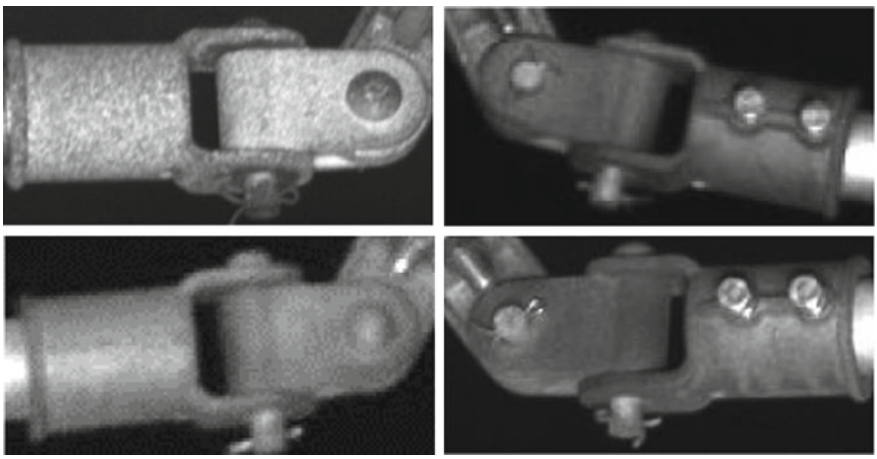

(a) Positive samples

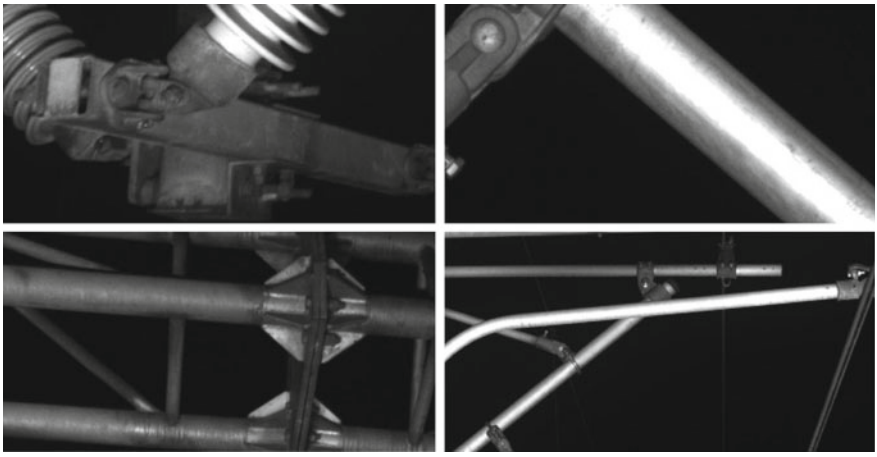

(b) Negative samples

Fig. 6.52 Positive and negative samples of clevises

6.4.4 Clevis Positioning Based on Hough Transform

When the fractures and cracks occur in a certain range of clevis, shown in Figs. 6.54 and 6.55, the extraction local image based on above matching methods is still big for the abnormal features of clevis. In addition, the inherent features of clevis, such as the bilateral screws and "R" bolt, will heavily influence the detection results. Therefore, it is very necessary to exclude the inherent features of clevis before the detection.

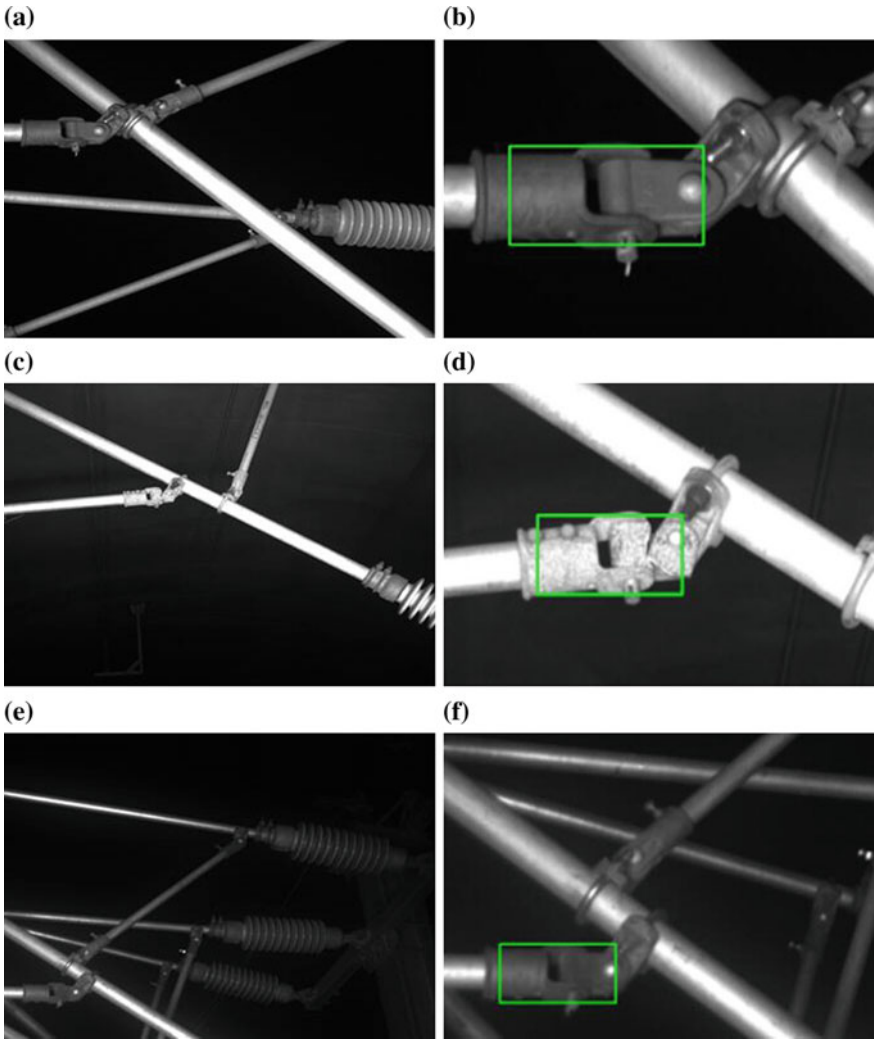

Fig. 6.53 Clevis images and their positioning results

Fig. 6.54 Fracture of clevis

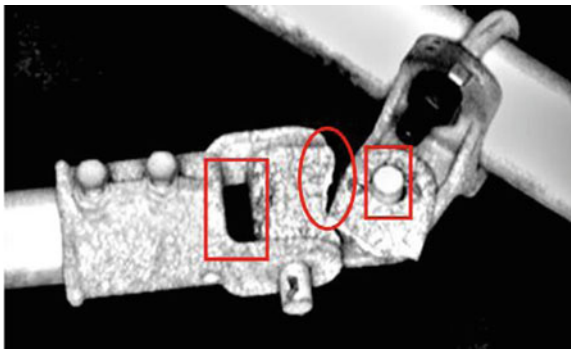

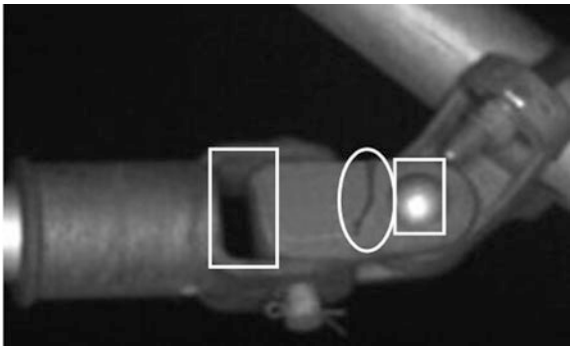

Fig. 6.55 Crack of clevis

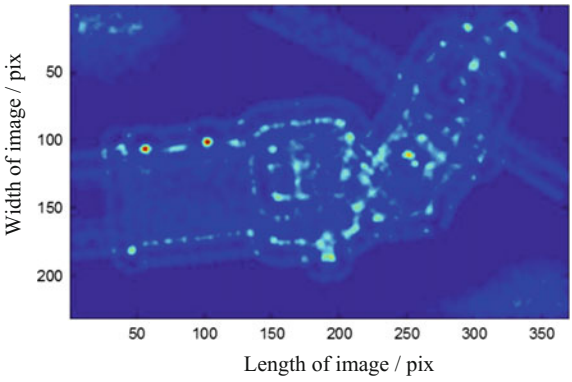

Fig. 6.56 Circle energy of clevis fracture

In general, the inherent features of clevis can be considered as the rectangle and circle, as shown in Figs. 6.54 and 6.55. Hough transform [41] is adopted to detect the features of rectangle and circle, the centers and radius of rectangle and circle can be obtained.

1. Screw positioning

The detected close contour line is scanned along the horizontal and vertical directions. Based on Hough transform, two diameters L_v and L_h of circle can be obtained. Their cross point is the center of circle (x_c, y_c). The radius of contour line is estimated through the pixels' coordinates as follows.

$$r = \max((x_{\max} - x_{\min})/2, (y_{\max} - y_{\min})/2) \tag{6.69}$$

where $x_{\max}$ and $x_{\min}$ are the max and min x coordinates of contour line, $y_{\max}$ and $y_{\min}$ are the max and min y coordinates of contour line. If the radius of circle is set as the radius range of screw, the center coordinates and radius of screw in the clevis image can be detected, as shown in Figs. 6.56 and 6.57.

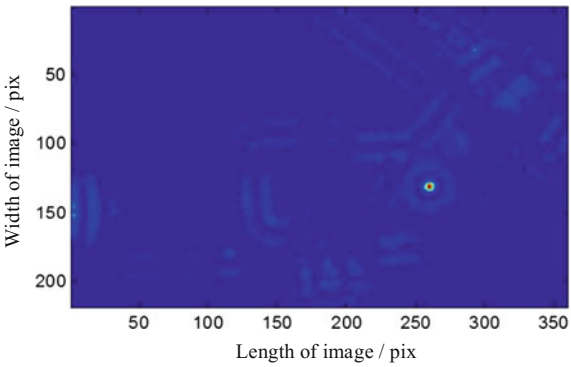

Fig. 6.57 Circle energy of clevis crack

Fig. 6.58 Rectangle positioning of clevis fracture

2. Rectangle positioning

After the edge detection of clevis local image using Canny operator, the rectangle positioning can be realized using Hough transform. Through the Hough transform of the rectangle contour line, there will be 4 peak values $H_1 = (P_1, \theta_1)$, $H_2 = (P_2, \theta_2)$, $H_3 = (P_3, \theta_3)$ and $H_4 = (P_4, \theta_4)$, which are corresponding to the 4 edges of rectangle P_1P_2, P_2P_3, P_3P_4 and P_4P_1. Based on the angle θ_i when the peak value occurs, the pair edges of rectangle can be judged by the paired peak values. The positioning results of rectangle are shown in Figs. 6.58 and 6.59.

3. Local image positioning

Based on the information of circle and rectangle, such as center point, radius, length and width, the clevis region, where the probability of fractures or cracks is maximal, can be obtained. For the different type of clevis, the number of screw is different, which can be determined according to the measured center relative distance. In order to exclude the influence of rectangle and circle edges and keep more local image information, the horizontal coordinates of the rectangular edge to the screw side of the translation of 5 pixels are taken, and at the edge of the rectangle side of the screw they stop. The vertical coordinates of the upper and lower edges of

Fig. 6.59 Rectangle positioning of clevis crack

the rectangle are taken and then move out of the 5 pixels. The vertex coordinates are listed below [42].

$$x_1 = (o_1 + b/2 + 5, o_1 + a/2 + 5) \tag{6.70}$$

$$x_2 = (o_1 + b/2 + 5, o_1 - a/2 - 5) \tag{6.71}$$

$$x_3 = (o_2 - r, o_1 + a/2 + 5) \tag{6.72}$$

$$x_4 = (o_2 - r, o_1 - a/2 - 5) \tag{6.73}$$

where o_1 and o_2 are the center of rectangle and circle, respectively, a and b are the length and width of rectangle, respectively, and r is the radius of screw. Therefore, the positioning results of local image are shown in Fig. 6.60.

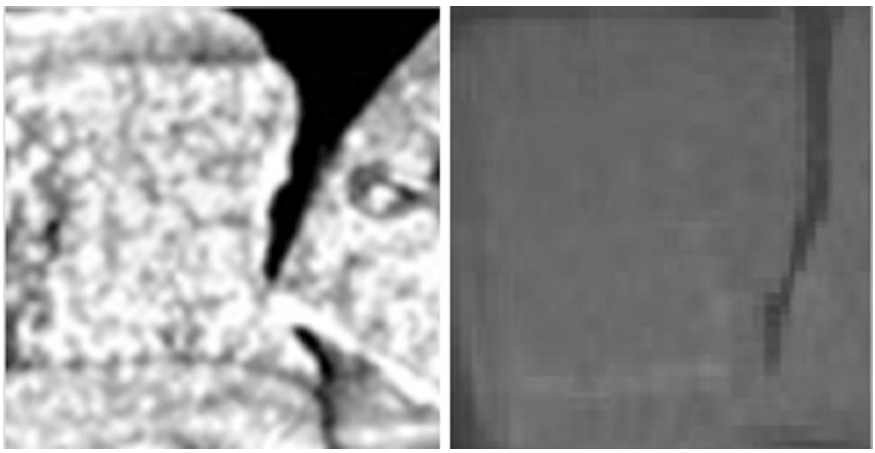

Fig. 6.60 Positioning results of local image with fracture and crack

6.4.5 *Fault Detection Based on Curvature*

1. Detection Process

When the fracture of clevis occurs, the shapes of clevis's top and bottom boundary will change. The method based on the boundary curvature is presented to judge the fracture of clevis in this section. Because the difference of R type bolt installation angle may have heavy disturbance to the fracture judgement, the upper boundary curve is adopted.

After the clevis in the catenary suspension system image is located, the clevis image can be extracted, as shown in Fig. 6.61. The upper boundary curve can be obtained.

After the clevis image binarization, the biggest connected area is identified as the clevis area, which can exclude the influence from the objects whose distance is very near to the clevis. Since the installation angle of clevis in high speed railway is the same, the highest point in the left edge of clevis area is chosen as the tracking start point. From the tracking start point, the boundary point of image is tracked in turn, until the upper edge of the mage is reached. The coordinate series of the upper boundary curve of clevis can be obtained. Considering the calculation speed and the detection accuracy, the inclination angle of connection line between the kth point and the k + 50th point in the coordinate series is defined as the curvature of the kth point, as shown below.

$$c_k = \begin{cases} \arctan\left[\frac{y_{k+50}-y_k}{x_{k+50}-x_k}\right] & (\text{atrcan}\left[\frac{y_{k+50}-y_k}{x_{k+50}-x_k}\right] > 0) \\ \arctan\left[\frac{y_{k+50}-y_k}{x_{k+50}-x_k}\right] + \pi & (\text{atrcan}\left[\frac{y_{k+50}-y_k}{x_{k+50}-x_k}\right] < 0) \end{cases} \tag{6.74}$$

where x_k, y_k are the coordinate of the kth point in the upper boundary curve, x_{k+50}, y_{k+50} are the coordinate of the k + 50th point in the upper boundary curve, and c_k is curvature of the kth point in the upper boundary curve, whose unit is radian and the range is $0 \sim \pi$.

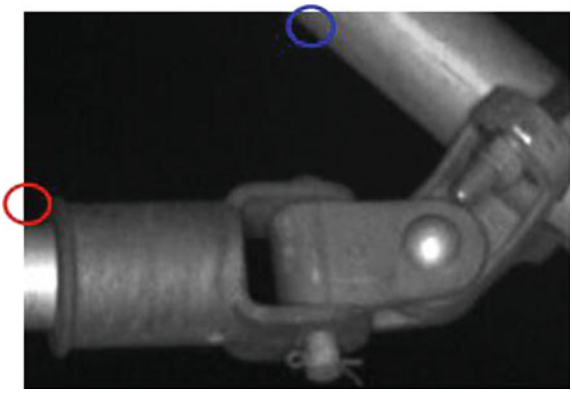

Fig. 6.61 Clevis image

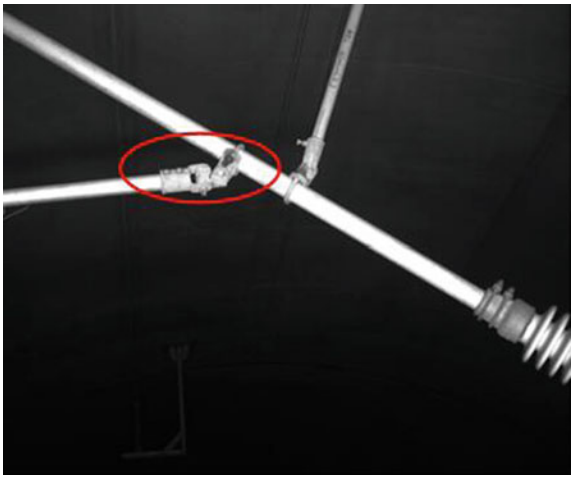

Fig. 6.62 Catenary suspension system image containing the clevis fracture

Through the curvature curve of all points in the upper boundary curve, the difference between the normal and fault curvature curves is compared. If the point in the difference curve is bigger than a certain threshold, the fracture will exist in the image.

2. Experiments

The catenary suspension system image containing the clevis fracture is shown in Fig. 6.62. The image resolution is 2048 × 2048 pixels. Based on SIFT algorithm, the local feature point matching of catenary suspension system image with the standard clevis image is performed. The feature points that are successfully matched can form 3 clusters, as shown in Fig. 6.63 [34].

The matching error is eliminated by using RANSAC algorithm, as shown in Fig. 6.64. After the location of clevis, the clevis image is extracted, as shown in Fig. 6.65, and the results of boundary tracking is shown in Fig. 6.66.

The point-to-point difference between the curvature of the upper boundary curve in Fig. 6.65 and that of normal boundary curve are calculated and drawn in Fig. 6.67. There are two peak values that are bigger than 0.5 in Fig. 6.67, so the fracture of clevis occurs. In addition, the peak value points are corresponding to the deformation positions of boundary curves. For the comparison, the point-to-point difference for normal clevis is drawn in Fig. 6.68, where the value of all points are less than 0.5, so there is no fracture of clevis.

In order to verify the validity of the presented method, the 30 images of catenary suspension system are tested. The test results are listed in Table 6.10. If the clevis is obscured by other objects, when the boundary is tracked, the error of boundary curve occur, which result in the wrong identification.

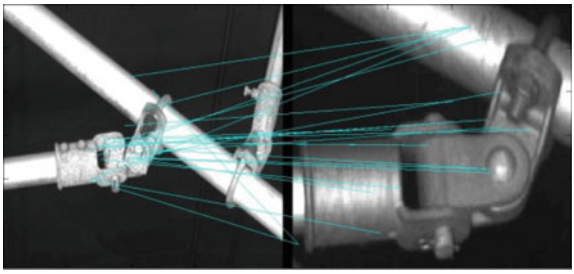

(a) Cluster 1

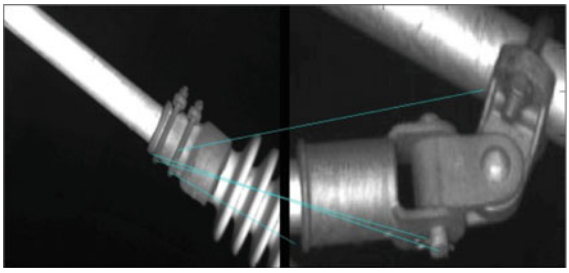

(b) Cluster 2

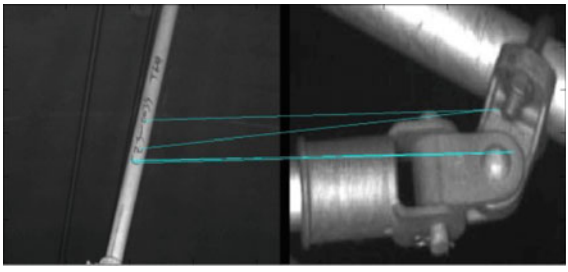

(c) Cluster 3

Fig. 6.63 Clustering results of feature points

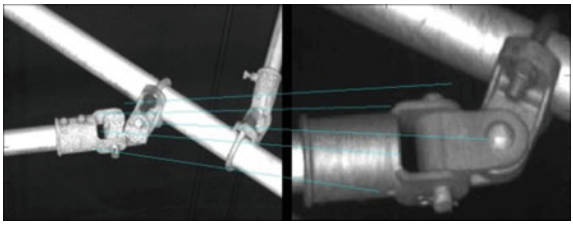

Fig. 6.64 Matching results after eliminating the matching error

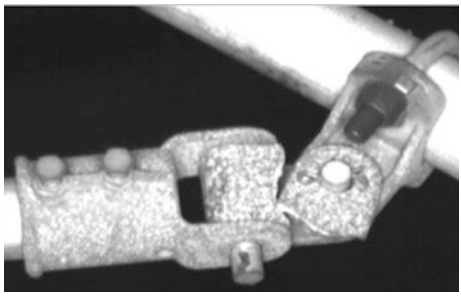

Fig. 6.65 Clevis image

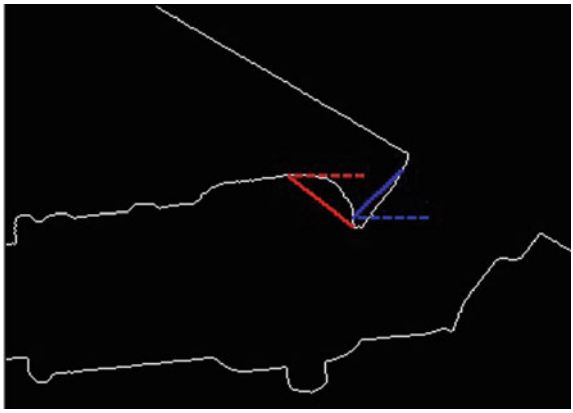

Fig. 6.66 Boundary curve of clevis image

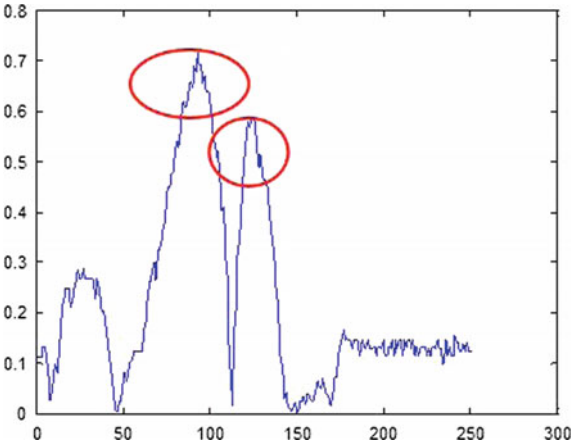

Fig. 6.67 Difference curve of curvature for fault clevis

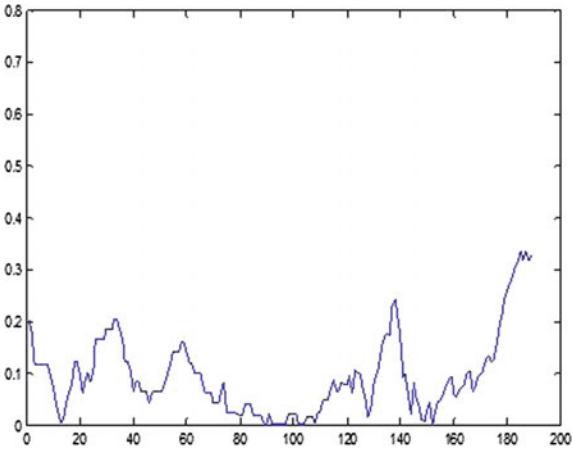

Fig. 6.68 Difference curve of curvature for normal clevis

Table 6.10 Test results of clevis fault

	Total number	Correct identification	Wrong identification
Total number of images	30	29	1
Images with clevis	20	19	1
Images without clevis	10	10	0
Fault image	2	2	0

6.4.6 Fault Detection Based on Gabor Wavelet Transform

1. Detection Process

Because the crack of clevis fault is narrow, it should be extracted in the small scale, which is easily influenced by the surface texture in the clevis, as shown in Fig. 6.69. In this section, the energy of two-dimension Gabor wavelet transform is adopted to filter the edge information after Canny operator extraction. It can filter the pseudo edges that are produced by the surface texture of clevis.

Two dimensional Gabor wavelet transform has a high similarity with the biological vision system, and it can be used in the process of visual perception of the

Fig. 6.69 Edge extraction of clevis

brain cortex [42, 43]. The mother wavelet and its frequency form are listed below, respectively.

$$g(x,y) = \frac{1}{2\pi\sigma_x\sigma_y}\exp\left[-\frac{1}{2}\left(\frac{x^2}{\sigma_x} + \frac{y^2}{\sigma_y}\right)\right] \cdot \exp[2\pi jWx] \tag{6.75}$$

$$G(u,v) = \exp\left\{-\frac{1}{2}\left[\frac{(u-W)^2}{\sigma_u^2} + \frac{v^2}{\sigma_v^2}\right]\right\} \tag{6.76}$$

where $W = U_H$, $\sigma_u = 1/2\pi\sigma_x$, $\sigma_v = 1/2\pi\sigma_y$, U_L and U_H mean the minimal and maximal center frequency. Through the dilation and rotation of mother wavelet, a series of wavelet functions with different dilation and direction can be obtained.

$$g_{mn}(x,y) = a^{-m}G(x',y'), \quad a > 1, m, n \in Z \tag{6.77}$$

where $x' = a^{-m}(x\cos\theta + y\sin\theta)$, $y' = a^{-m}(-x\sin\theta + y\cos\theta)$, $\theta = n\pi/K$, $m = 0, 1, \ldots S-1$, $n = 1, \ldots, K$, S and K are the numbers of dilations and directions of Gabor wavelet, respectively. $a = (U_H/U_L)^{-\frac{1}{S-1}}$.

In the frequency domain, the half peak support interval of the two dimensional Gabor wavelet functions with different scales and directions should be connected to each other, namely the determination criterion of σ_u and σ_v (σ_x and σ_y) [44].

$$\begin{cases} \sigma_u = \frac{(a-1)U_H}{(a+1)\sqrt{2\ln 2}} \\ \sigma_v = \tan\left(\frac{\pi}{2K}\right)\left[U_H - 2\ln\left(\frac{\sigma_u^2}{U_H}\right)\right] \cdot \left[2\ln 2 - \frac{(2\ln 2)^2\sigma_u^2}{U_H^2}\right]^{-1/2} \end{cases} \tag{6.78}$$

Since the images are similar for all clevises, their frequency distributions U_L and U_H are relatively fixed. The energy $E(x,y)$ of each pixel in two dimensional Gabor wavelet transform is defined as follows.

$$E(x,y) = \sum_{m=0}^{S-1}\sum_{n=1}^{K}\left|I(x,y) * g_{m,n}(x,y)\right| \tag{6.79}$$

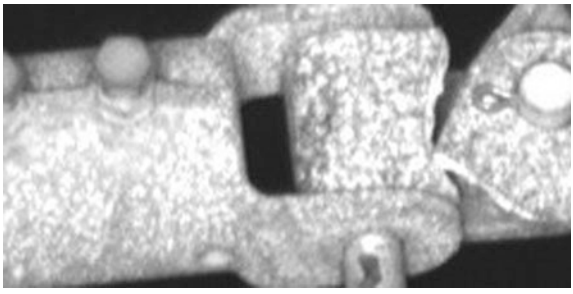

Fig. 6.70 Clevis image

The clevis image extracted from the original image and its energy distribution after two dimensional Gabor wavelet transform are shown in Figs. 6.70 and 6.71, respectively.

It can be found that the energy distributions near the boundaries of cracks and clevis are large, and the energy distribution of center region with much texture is small. The multiplication of Figs. 6.69 and 6.71 binarization is performed, which can realize the filtering of Pseudo edges produced by the surface texture of clevis, as shown in Fig. 6.72.

For the features of clevis crack, one side should be near the boundary of clevis, and the boundary of clevis crack has a larger longitudinal span. After the binarization of clevis image, its upper and lower boundary curves can be extracted easily. The upper and lower boundary curves are expanded, and the image edge which is intersection with the expansion area is identified as the boundary curve, as shown in Fig. 6.73. The edge information retained in Fig. 6.73 can be used as a candidate edge of the fault.

The longitudinal span of each edge can be computed as follows.

$$\Delta Y = |y_{\max} - y_{\min}| \tag{6.80}$$

where $y_{\max}$ and $y_{\min}$ are the maximal and minimal value of vertical coordinate.

The longitudinal span histogram of each edge in Fig. 6.73 is drawn in Fig. 6.74, as well as the normal histogram in Fig. 6.75.

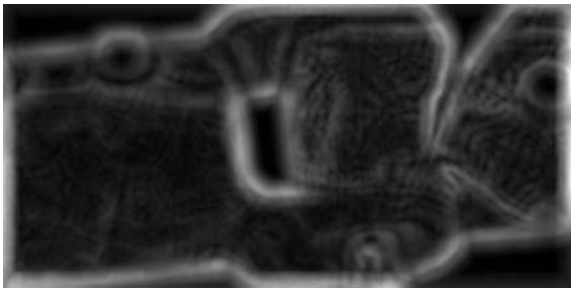

Fig. 6.71 Energy distribution after two dimensional Gabor wavelet transform

Fig. 6.72 Filtering result of the pseudo edges

Fig. 6.73 Image edge connected with boundary curve

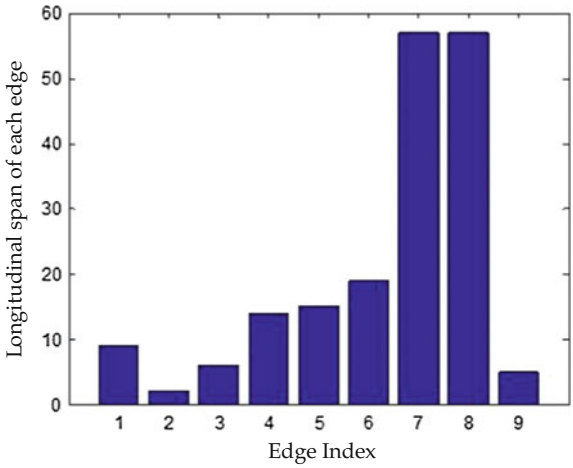

Fig. 6.74 Longitudinal span histogram of each edge with crack

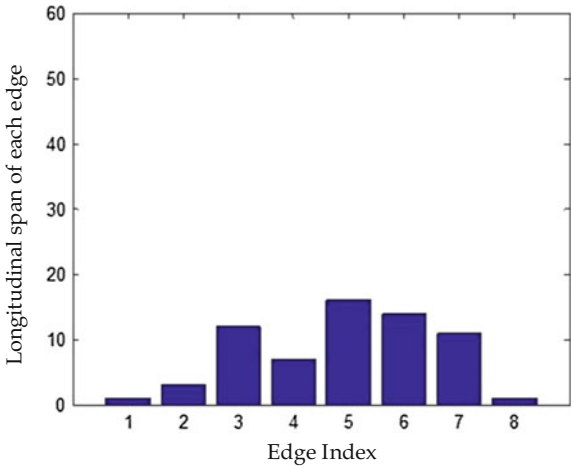

Fig. 6.75 Longitudinal span histogram of each edge without crack

Table 6.11 Test results of clevis fault

	Total	Number of correctly positioning	Number of error
Image number	50	49	1
Images with clevis	40	39	1
Images without clevis	10	10	0
Fault images	2	2	0

It can be found that when there is a fault in the clevis, the longitudinal span histogram shows the specific distribution law, and the image edge corresponding to the fault will produce a significant peak in the histogram, as shown in Fig. 6.73. The longitudinal span of crack's edges is far greater than the other edges, so it can be determined that these edges are corresponding to the crack, as shown in Fig. 6.73.

2. Experiments

In order to verify the presented method, 50 images of the catenary suspension system from the field are tested, in which there are 40 clevis images, and 2 fault clevis images. The detection results are listed in Table 6.11 [40]. It can be seen that there is one positioning error due to the occlusion between the clevis and other object, which results in the false judgment of SVM.

6.4.7 Fault Detection Based on Second Generation Curvelet

1. Algorithm process

If the clevis is fractured or there are cracks on the surface of clevis, the fracture sites and the cracks will present the linear singularity of edge feature. The curvelet transform is able to achieve the multi-scale and multi-direction image decomposition and has a strong ability in sparse representation, which is suitable to detect the clevis fault. The second generation curvelet transform not only has the multi-scale property, but also achieves multi-directional decomposition in every scale. Besides, the curvelet base is anisotropy. Therefore, the second generation curvelet transform is ideal to analyze the high-dimensional singularity features in the images.

The magnitude of the second generation curvelet decomposition coefficients of 'normal' clevises is small and evenly distributed. If the clevis is fractured or there are cracks on the surface of clevis, the fracture sites and the cracks will present linear singularity edge feature and the coefficients of curvelet decomposition will suddenly change. Therefore, a threshold can be set to detect the linear coefficient group with large values in the curvelet decomposition coefficient matrix. These coefficient groups can be regarded as the feature of fracture failure. The concrete steps are described as follows.

(1) Perform second generation curvelet transform to the accurately localized local image of the clevis.
(2) Compute the mean value of the curvelet decomposition coefficient matrix M_{mean}.
(3) Determine the numbers of pixels of which the curvelet decomposition coefficients are larger than $5 \times M_{mean}$ along the horizontal and vertical direction respectively N_{X5Mean} and N_{Y5Mean}. After many experiments, $5 \times M_{mean}$ is chosen as the threshold. It is found that the threshold $5 \times M_{mean}$ is able to distinguish the suddenly changed coefficients from the 'normal' coefficients with a large value. Because the cracks that are rather short or approximately horizontal direction may not be detected if they are not done separately, the statistics of coefficients are separately along the two directions.
(4) Analyze the regularities of the distribution of N_{X5Mean} and N_{Y5Mean}. If the centralized distributed areas of N_{X5Mean} and N_{Y5Mean} (which are defined as L_{N_X} and L_{N_Y}) are over 30, then these areas are regarded as the regions of cracks. It is defined that in the centralized distributed areas, the interval between every two N_{X5Mean} and N_{Y5Mean} that are over the threshold is below 5. It is found that by setting the interval threshold to be 5 and the distribution threshold to be 30, the false alarms caused by the clustering of the discrete points can be eliminated.

The final criterion of cracks and the fracture is shown as follows.

$$\begin{cases} L_{N_X} \geq 30 \quad \text{or} \quad L_{N_Y} \geq 30 & \text{Fracture} \\ \text{else} & \text{Normal} \end{cases} \tag{6.81}$$

2. Experiments

(1) Detection of 'normal' clevises

Apply the method presented above to the local images of 'normal' clevises, the detection result is shown in Fig. 6.76b–e.

It can be seen from Fig. 6.76d, e, there are no coefficient groups with large values according to the definition in Formula (6.72). So this clevis is judged as a 'normal' clevis.

(2) Detection of fractured clevises

The same method is applied to the local images of the fractured clevises, as shown in Fig. 6.77a. The detection result is shown in Fig. 6.77b–e [40].

It can be seen from Fig. 6.77c, d, the coefficient groups with large values exist in the curvelet distribution image. So this clevis is judged as a fractured clevis.

(a) Local image of 'normal' clevis

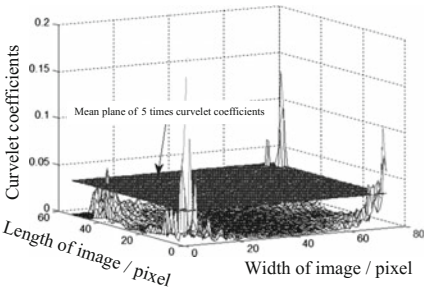

(c) 3D distribution of curvelet coefficients

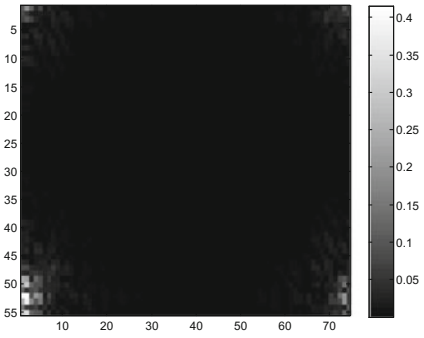

(b) Distribution of curvelet coefficients of 'normal' clevis

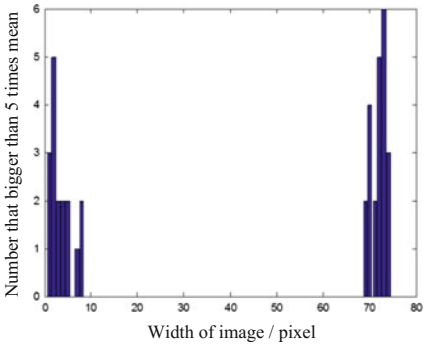

(d) Distribution of N_{X5Mean}

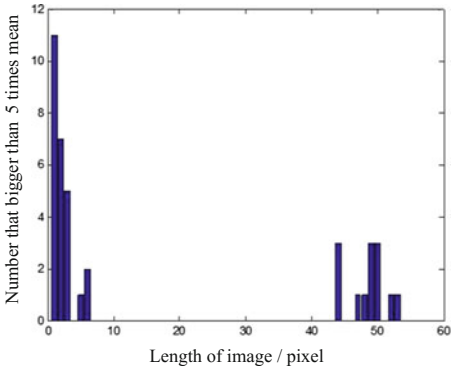

(e) Distribution of N_{Y5Mean}

Fig. 6.76 Detection result of the 'normal' clevis

(3) The detection of cracks on the surfaces of clevises

Apply the proposed method to the local images of the clevises with cracks on the surface, as shown in Fig. 6.78a. The detection result is shown in Fig. 6.78b–e

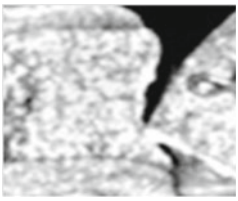

(a) Local image of fractured clevis

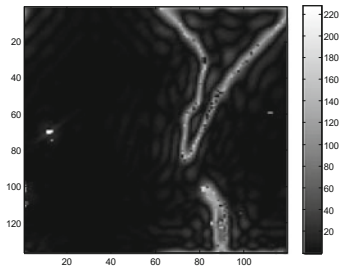

(b) Distribution of curvelet coefficients of fractured clevis

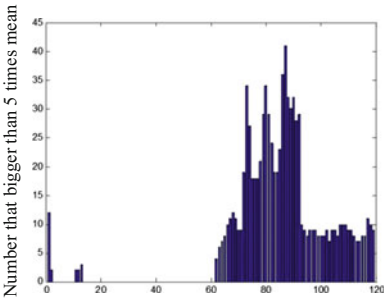

(d) Distribution of N_{X5Mean}

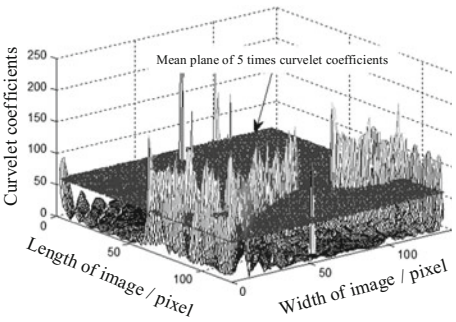

(c) 3D distribution of the curvelet coefficients

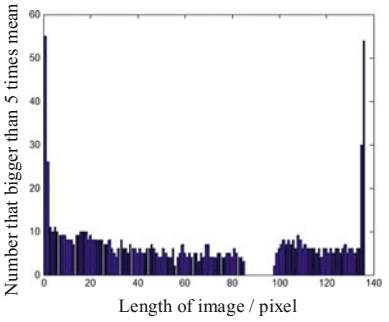

(e) Distribution of N_{Y5Mean}

Fig. 6.77 Detection result of the fractured clevis

It can be seen from Fig. 6.78, the coefficient groups with large values exist in the curvelet distribution image. So the crack can be detected.

6.4.8 Detection of Clevis Pins

Because the loosening and falling off of clevis pins can directly influence the normal operation of catenary suspension system, as shown in Fig. 6.79, it is very

(a) Local image of clevis with a crack

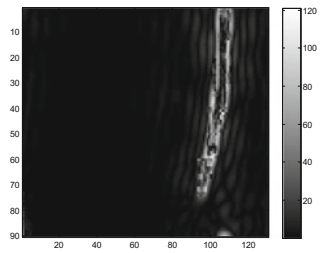

(b) Distribution of curvelet coefficients of the clevis with cracks

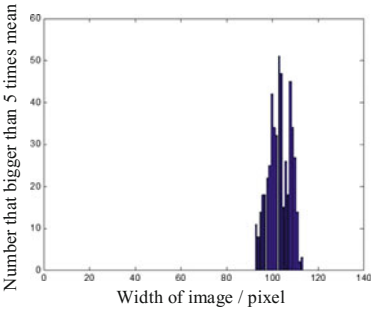

(d) Distribution of N_{X5Mean}

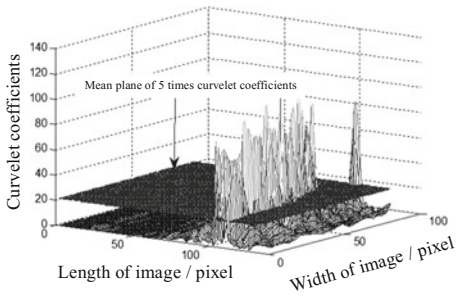

(c) 3D distribution of curvelet coefficients

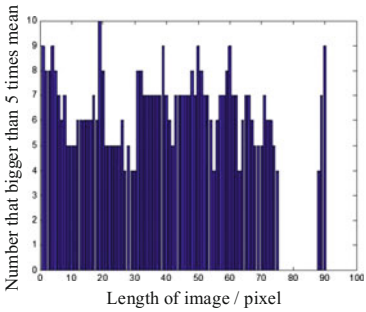

(e) Distribution of N_{Y5Mean}

Fig. 6.78 Detection result of the clevis with a crack

important to detect their state in time. For the clevis pin detection, there are two main steps. First, the pin is isolated from the clevis, and then, the working state of the pin is determined by analyzing the sub-image of the pin.

1. Pin extraction

In order to find the line to separate the pins in the clevis image, the edges of clevis are processed. In order to make the two sides of clevis close to straight lines, the Gaussian filter and contrast enhancement methods are adopted, as shown in Fig. 6.80.

Hough Transform is used to detect the straight lines which will be connected to get the inclined angles. Figure 6.81 shows the first three gray scale peaks

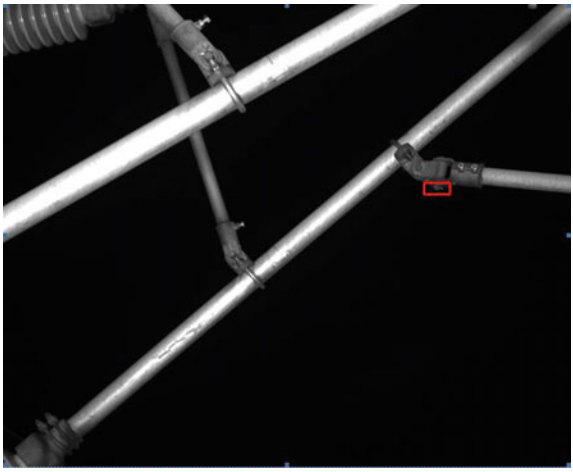

Fig. 6.79 Clevis pin image

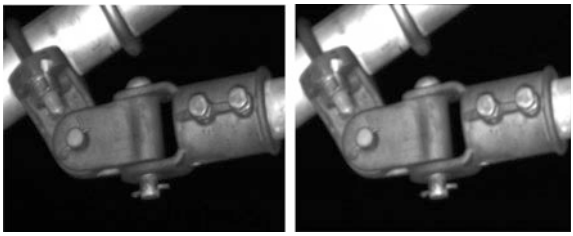

Fig. 6.80 Comparison of original image and the enhanced image

corresponding to the three longest lines in the clevis image. The green lines show the detection result.

According to the clevis structure, the long straight lines in the image above are mainly distributed in the oblique cantilevers and clevis tubes. A set of approximate parallel lines can be detected from the first three peak points of the Hough matrix, as shown in Fig. 6.81a. Set the two inclined angles as θ_1 and θ_2, corresponding to the parallel edges of the tube. θ_3 has a big difference with θ_1 and θ_2, and the detection angles of the oblique cantilevers are usually less than 75°.

$$\begin{cases} \theta_1\theta_2 \geq 0 \\ \theta_3 < 75^\circ \\ \forall\{|\theta_1|, |\theta_2|\} > 75^\circ \end{cases} \tag{6.82}$$

Thus, θ can be solved according to θ_1 and θ_2 by $\theta = 90^\circ - \frac{\theta_1+\theta_2}{2}$. The image of clevis is rotated by θ so that the upper and the lower edge of the tube can be in a horizontal direction.

Canny operator is used to find the split line. Take the longitudinal midpoint of the image as the origin, upward direction as the positive direction of y-axis. Firstly, the image edge after rotation is detected by using Canny operator, and the pixel

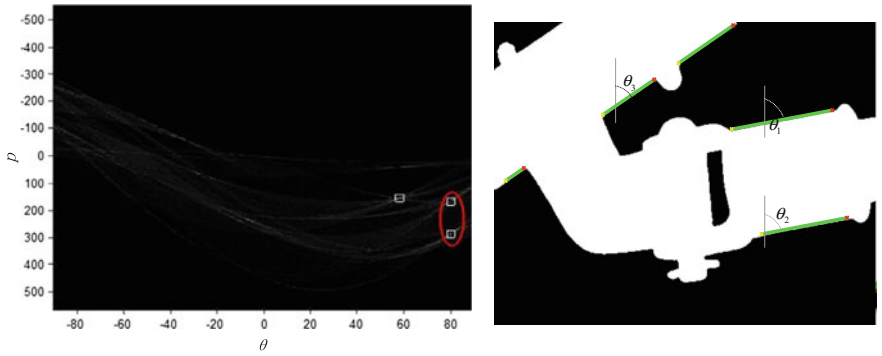

(a) Matrix of Hough transform and three peak points

(b) Corresponding lines of the peaks

Fig. 6.81 Computation of the inclined angle using Hough transform

gray values are accumulated in horizontal direction to get the statistical curve, as shown in Fig. 6.82a. The straight line, which the horizontal line segment of the maximum length below the clevis tubes is located, is determined as the segmentation straight line of the pin portion. The segmentation results are shown in Fig. 6.82b.

2. Pin detection

Three typical installation situations of the pins are shown in Fig. 6.83. By analyzing the installation situations of the pins, it can be concluded that the direction and the shape of the pin in the image is inconsistent.

Analyzing the images in Fig. 6.83, the following conclusions can be given.

(a) The directions of each pin are not uniform. Both ends of each pin are not uniform.
(b) The R-shaped pins are considered as acceptable as long as both ends of the pin shaft exist, as shown in Fig. 6.83a. Pins in Fig. 6.83b are considered as loosened. Pins in Fig. 6.83c are considered as safety-threatening.

Because of the complexity of the pins' condition, the defective condition detection is based on the pins' grayscale distribution feature extraction. The detection steps are listed as follows.

(a) Accumulate pixel gray values in the vertical direction of the pin component image after segmentation.
(b) Analyze the grayscale value curve to get the four horizontal coordinates that are on both sides of the pin and the pin shaft at both ends, as shown in Figs. 6.84c, 6.85c, and 6.86c by red circle.
(c) Determine the length of the 'middle part' d of the pin and the length of both the two 'ends', d_1 and d_2, of the pin.

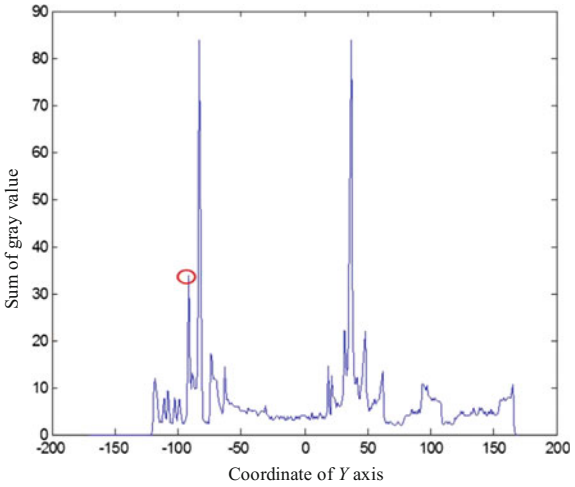

(a) Statistical curve of grayscale sum on the horizontal direction

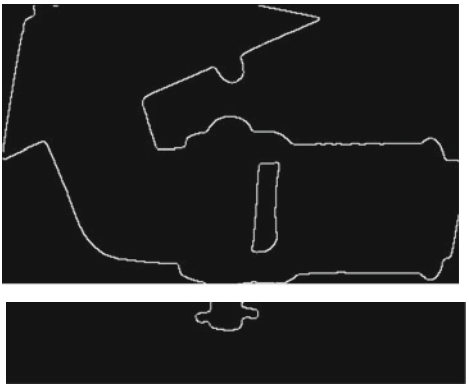

(b) Segmentation result of the pin and main part of the clevis

Fig. 6.82 Segmentation of the pin

The detection process and the detection results of the pin loosening (shedding) fault and the normal state are shown in Figs. 6.84, 6.85 and 6.86, respectively.

The determination process of horizontal coordinate for each point is described below [45].

First, search the smallest and largest non-zero points' coordinates x_1 and x_4. Second, search two end points x_2, x_3, whose vertical coordinate value is 1 and have the absolute maximum of horizontal coordinate difference. Because the sum of pixel gray value of pin head or end in some instances is large, directly searching the two peaks is not accurate. The lengths of the non-stressed and stressed are calculated as d_1, d_2 and d. Because of the disturbance of the photograph, the pin shafts

(a) Normal condition

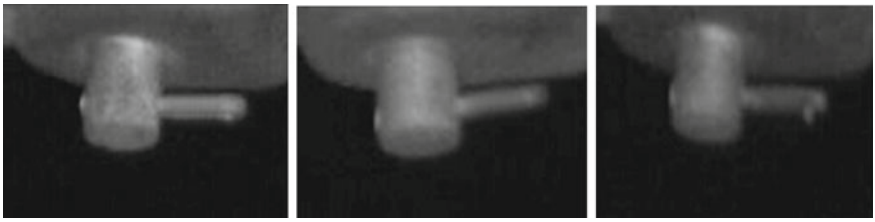

(b) Loosening condition

(c) Missing condition

Fig. 6.83 Three typical installation situations of clevis pins

are not in the vertical plane ideally. Thus d_1 and d_2's values are very small but not zero. By observing pins' d_1 and d_2 in the three conditions, the detection rules are made. The width of the pin is placed in the denominator in order to eliminate the influence of different angles and scales of the image. By a series of experiment analysis, T_1 in the formula above takes 0.1, T_2 takes 0.3.

3. Experiments

In order to verify the presented method, 60 images of the catenary suspension system from the field are tested, in which the number of images including normal, loosening and missing pins are each 20, respectively. The detection results are listed in Table 6.12.

Through the grayscale distribution feature extraction of a pin, most of the pin states can be judged, but there are still a few ones unable to analyze. The possible reason is that there is a big block overlap between pin and axis due to the shooting angle and pin installation angle, as shown in Fig. 6.87.

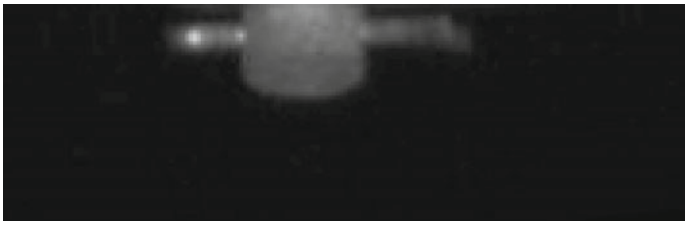

(a) Original image of the pin

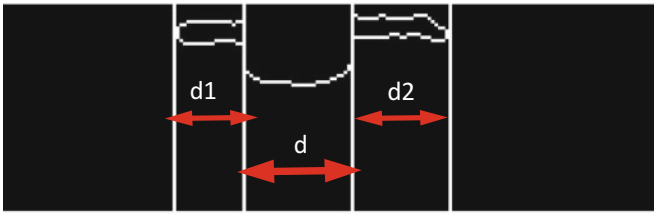

(b) The 'middle part' and the 'ends' of the pin

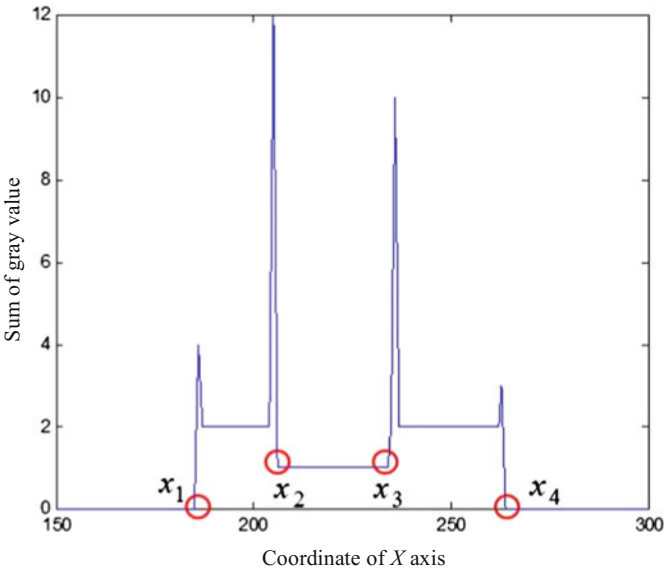

(c) Grayscale value curve of the pin image

Fig. 6.84 Normal condition detection

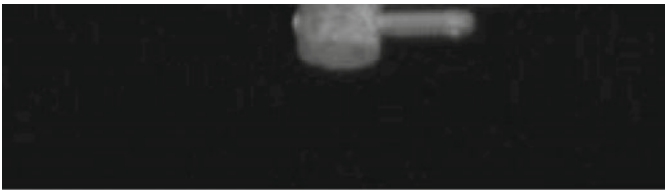

(a) Original image of the pin

(b) The 'middle part' and the 'ends' of the pin

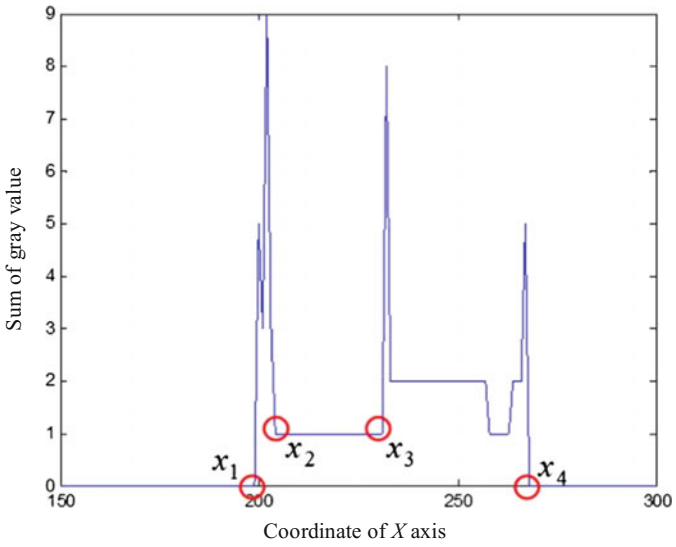

(c) Grayscale value curve of the pin image

Fig. 6.85 Loosening condition detection

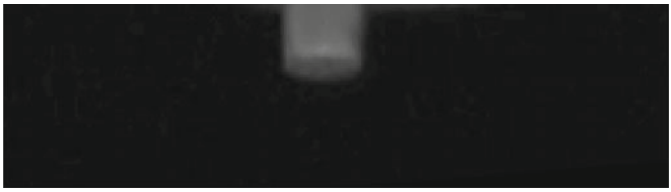

(a) Original image of the pin

(b) The 'middle part' and the 'ends' of the pin

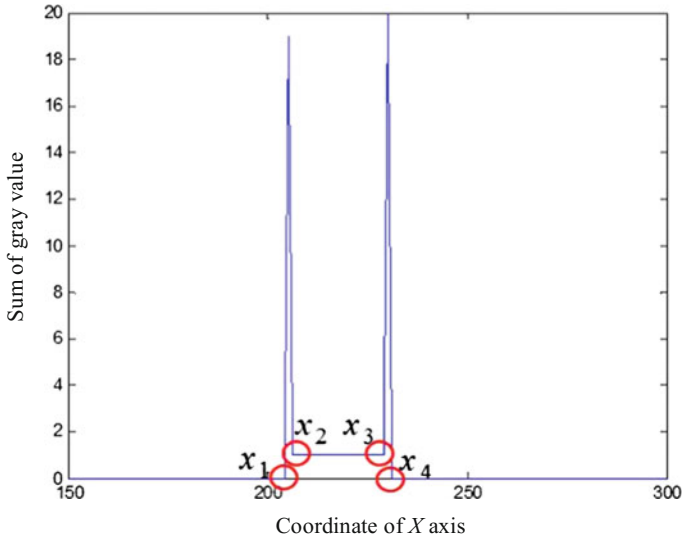

(c) Grayscale value curve of the pin image

Fig. 6.86 Missing condition detection

Table 6.12 Detection results of pin state

Pin state	Image number	Successful positioning	Correct detection	Correct detection ratio (%)
Normal	20	18	16	80
Loosening	20	19	17	85
Missing	20	19	19	95

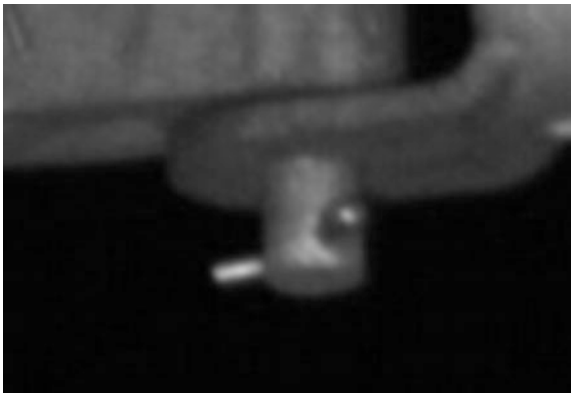

Fig. 6.87 Overlap between pin and axis

6.5 Fault Detection of Diagonal Tube

The diagonal tube is an important load-bearing component in the "L" arm support structure of high speed railway catenary. As introduced above, the performance of HOG features in detecting the fittings of which the lighting condition and the grayscale distribution on the surface are different is satisfying. In this section, HOG features are used to detect the diagonal tubes from the global image, and the cascaded AdaBoost classifier is adopted to increase the detection speed.

6.5.1 Diagonal Tube Detection Based on Cascaded AdaBoost Classifier

The cascade classifier is used to accelerate the process of clevis detection, and remove most non-clevis areas with small computational cost. Each layer of the cascade classifier is trained using Gentle AdaBoost algorithm, which combines the output of a set of "weak classifiers" into a weighted sum to form a "strong classifier", and uses Newton steps to minimize the training error. Each weak classifier focuses on the classification of one dimension of the input feature vector. In summary, AdaBoost classifier is a strong classifier which is obtained by the linear superposition of several weak classifiers and these weak classifiers are trained on different training sets [46].

In AdaBoost algorithm, the weight of the error sample is increased by a factor, and the effect of the sample on the next weak classifier becomes larger. AdaBoost algorithm uses the weighted majority voting principle, which is to give higher weight to the classifier with lower error rate, which can make them play a greater role in decision-making. Therefore, the error rate of the classifier will be reduced with the increase of the number of weak classifier. The detailed training procedure of Gentle AdaBoost algorithm is described in Fig. 6.88 [47].

1. Start with weights $w_{i,1} = 1/N$, where $i = 1, 2, ..., N$ (N is the number of training samples).
2. Repeat for $t = 1, 2, ..., T$ times,
   (a) Train a stump decision tree to divide the training set into two classes, S_1 and S_2 (positive and negative classes). Then calculate W_{t+}^1 (true positive), W_{t-}^1 (false positive), W_{t-}^2 (true negative) and W_{t+}^2 (false negative) by

$$W_{t+}^1 = \sum_{i:x_i \in S_1 \& y_i = 1} w_{i,t},$$

$$W_{t-}^1 = \sum_{i:x_i \in S_1 \& y_i = -1} w_{i,t},$$

$$W_{t-}^2 = \sum_{i:x_i \in S_2 \& y_i = -1} w_{i,t}, \text{ and}$$

$$W_{t+}^2 = \sum_{i:x_i \in S_2 \& y_i = 1} w_{i,t}.$$

   (b) Set the weak hypothesis

$$f_t^j(x) = (W_{t+}^j - W_{t-}^j) / (W_{t+}^j + W_{t-}^j),$$ where j=1 means hypotheses for samples in S_1 and j=2 means hypotheses for samples in S_2.

   (c) Update sample weights by $w_{i,t+1} = w_{i,t} \, exp[-y_i f_t(x_i)] / Z_t$ where $Z_t = \sum_i w_{i,t} \, exp[-y_i f_t(x_i)]$
3. Output the strong hypothesis $F(x_i) = \sum_{t=1}^{T} f_t(x_i)$

Fig. 6.88 Training procedure of Gentle AdaBoost algorithm

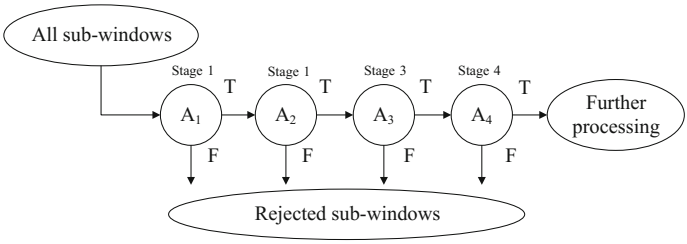

Fig. 6.89 Structure of the cascade classification system

However, too many weak classifier combinations will affect the detection speed and the classification accuracy cannot be guaranteed in AdaBoost algorithm. Therefore, the cascade structure proposed by Viola and Jones is utilized [39]. Its structure is shown in Fig. 6.89, where A_i is the AdaBoost strong classifier in the ith stage.

In the process of diagonal tube detection, the detection window slides on the image in order to calculate the HOG features in the window. When the feature

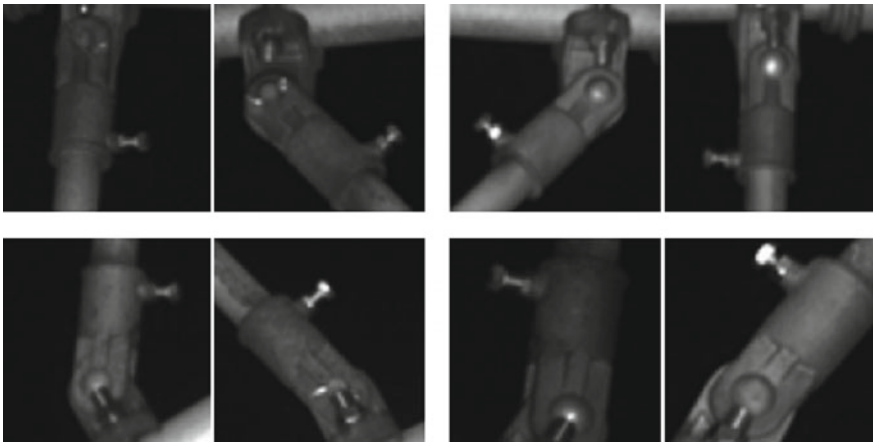

(a) Positive samples

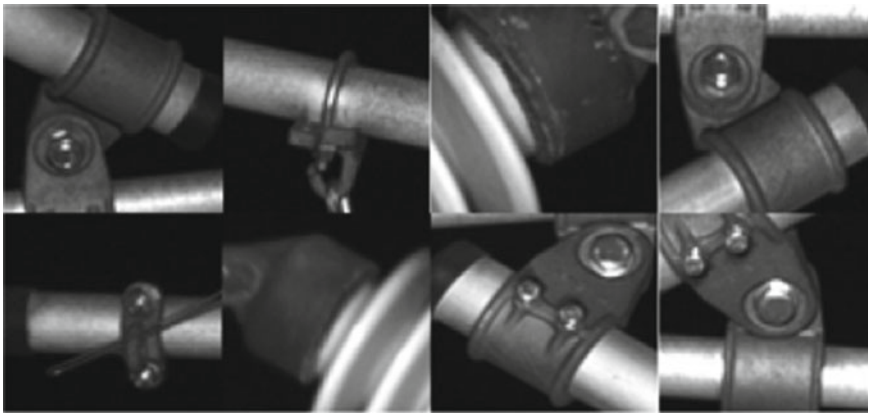

(b) Negative samples

Fig. 6.90 Positive and negative samples of diagonal tubes

vector passes through the cascade classifier, if one of the sub-classifiers judges it as the non-target, the window will be rejected. It will not enter the next classifier. If the window contains detection targets, it will go through all the AdaBoost classifiers to the last stage. Because most of the non-target windows are rejected by the AdaBoost classifiers in the previous layers, and the AdaBoost classifier in the previous layers is usually composed of a few simple linear combination of weak classifiers. So the cascade classifier with veto mechanism will reduce the computational complexity greatly, and improve the detection speed at the same time.

The generation of the training dataset is similar to the one described in 6.4.3. The size of positive and negative samples is normalized to 64×64 pixels. In order to improve the accuracy of localization, the uplink and downlink diagonal tubes are divided into four groups to train four different cascade classifiers (Fig. 6.90).

Most possible sub-windows can be detected by the cascaded AdaBoost classifier, as seen in Fig. 6.91a, b. However, false positives still exist. To eliminate the false positives, all the outputs of the cascade classifier are inputted to an SVM classifier, which is more accurate than the cascade classifier. SVM classifier is trained using the same positive samples as the cascade classifier, but the negative samples are the false alarms of the cascaded AdaBoost classifier. Because the dimension of HOG features is high, the processing speed of SVM is slower than that of the cascaded AdaBoost classifier. That's why the utilization of cascaded AdaBoost classifier is able to increase the detection speed. The final detection result is shown in Fig. 6.91c, d labeled with red rectangles.

6.5.2 *Detection of Loosening and Missing of Screws*

In order to analyze the working state of the screw, the screw on the diagonal tube is firstly separated. The vertical edges of diagonal tube are extracted to determine the separation line. Before dividing the screws, smooth filtering and contrast enhancement are made in the diagonal tube image in order to make the tube's edge close to the straight line to determine the separating point, as shown in Fig. 6.92.

Hough transform is used to detect straight lines in order to get the inclined angles of the tube. Figure 6.93a, b show the matrix of Hough transform. Figure 6.93c, d corresponds to two diagonal tubes towards two different directions. The first three grayscale peaks correspond to the three longest straight lines. According to the diagonal tube's image, the long and straight lines are distributed in the cantilevers and tubes. Since the installation angle of cantilever fits in a specific rule, the long straight lines distributed in the cantilevers can be eliminated based on the inclination angle of the line. Hough transform is used to detect a pair of parallel lines corresponding to the tube's edges.

The origin is set to the horizontal middle point in the diagonal tube's edge and the statistical curve is obtained by accumulating the grayscale value of the edge pixels along the horizontal direction. For the tubes whose screw is towards left, the separating line is on the origin's left. On the contrary, for the tubes that the screw is towards right, the same method is used to find the separating line on the origin's right, as shown in Fig. 6.94.

After getting the screw image segmented, we distinguish the three states of screw and detect the loosening and missing states of the screws, as shown in Fig. 6.95.

Although the screws' orientations of uplink and downlink diagonal tubes are different, after separated from the tube, due to the screw's axial symmetry, the head of the screw can be no longer distinguished, according to the relevant fault criterions.

Screw is the small target. It is difficult to obtain the accurate information on thread or other parts. So the detection is based on pixel grayscale distribution characteristics of two kinds of fault conditions.

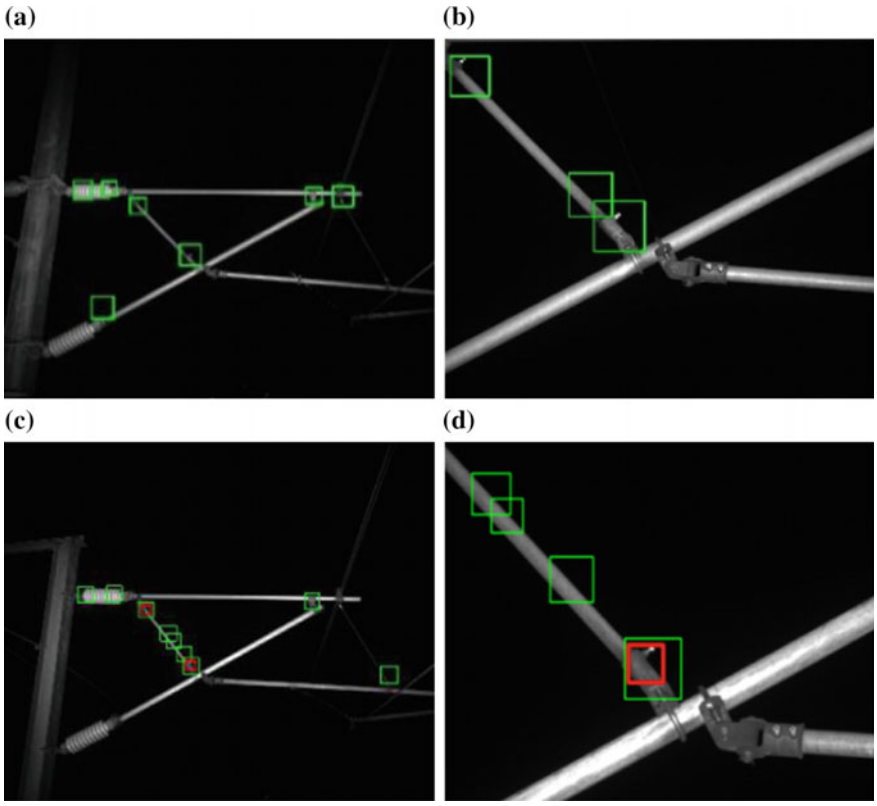

Fig. 6.91 Detection results of diagonal tubes. **a**, **b** Detection results of cascaded Adaboost classifier; **c**, **d** detection results of the cascaded AdaBoost classifier and the SVM classifier

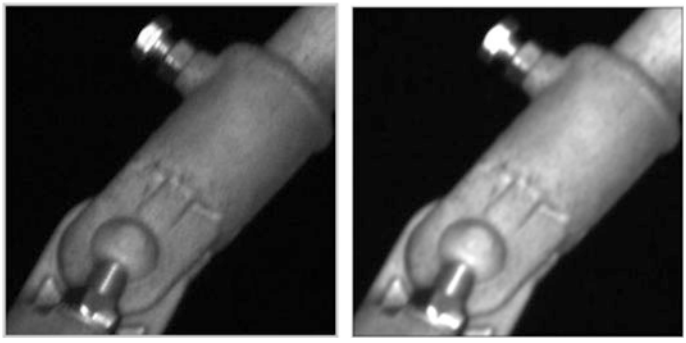

Fig. 6.92 Comparison of original image and preprocessed image

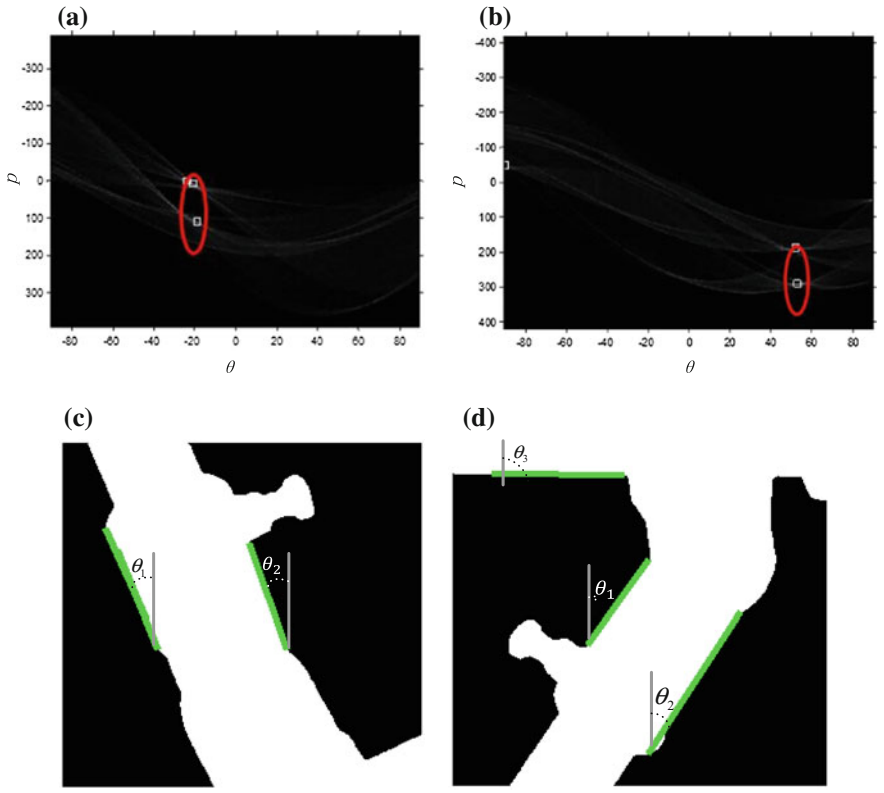

Fig. 6.93 Computing the inclination angle using Hough transform: **a**, **b** matrix of Hough transform and the first three peak points; **c**, **d** diagonal tubes that towards to different directions

When the screws fall down, both bolts and nuts will be missing. Therefore, the falling fault can be judged by the length of the screws and their sockets, while loosening of the screws can be judged by the position of nuts since the nuts will move by the thread.

(1) Detection of falling

Different screen angles and locations will influence the pixels of the bolts. According to TB/T 2075.1-2010, the bolts on the diagonal tube clevises should fit in DIN43165 and the thin nuts should fit in GB/T 6172.1-2000. Therefore, the diameter of the bolts is a constant. In order to eliminate the influence of the shooting angle, the ratio of bolt length to its diameter is set as the criterion of the falling of the bolts, as shown in Fig. 6.96.

(1) Firstly, after the binary processing and the edge detection of screw image, pixels of the screw's binary image are accumulated in the horizontal direction,

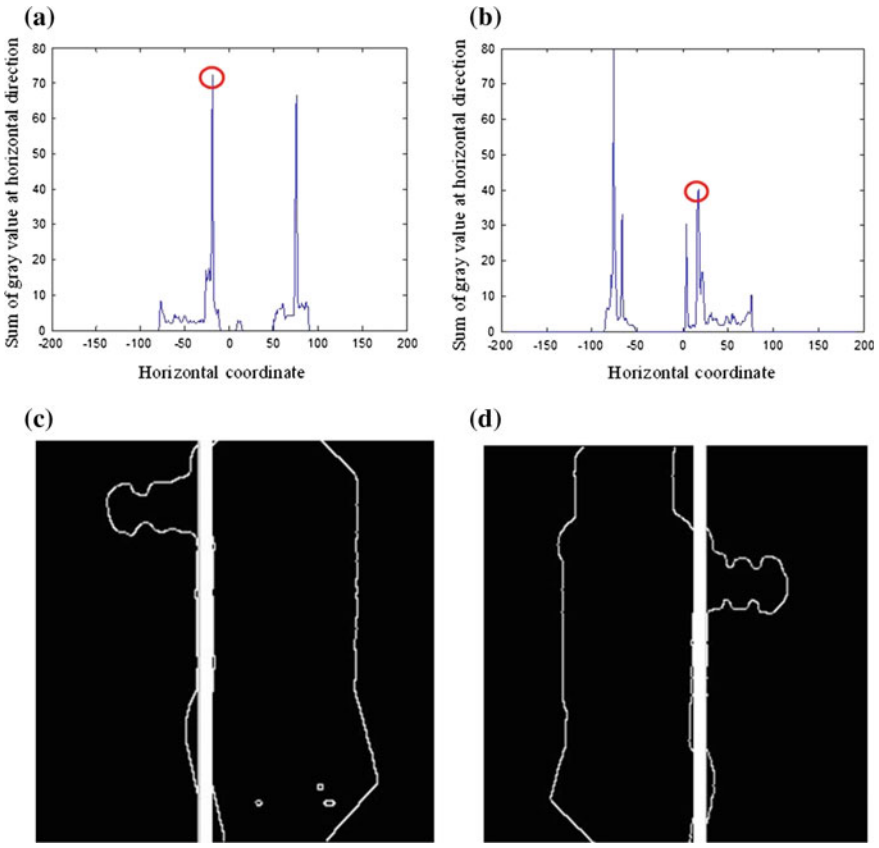

Fig. 6.94 Segmentation of the screw: **a**, **b** statistical curve of the grayscale sum on the horizontal direction; **c**, **d** segmentation result of the screw and the main part of the diagonal tubes

as shown in Fig. 6.97a. Meanwhile, the vertical edge pixel accumulation distributions are shown in Fig. 6.97b by the same way.

(2) In horizontal direction, the two biggest points correspond to the two edges of the screws. Thus the diameter of the screws can be calculated by the two largest edge pixel accumulation values. The fault of screw falling off can be judged by the ratio of the length to the diameter.

It can be found that the ratio of screw length to diameter in falling condition is $c \approx 0.5$, while the normal or loosening condition's is $c \geq 1.2$. Thus set $c \geq 1$ as the judgment of the normal-state screw, on the contrary, $c < 1$ as the judgment of the falling-state.

(2) Detection of loosening

Because of the movement of the thin nut, a new peak will occur in the horizontal pixel distribution in the loosening state. Then the difference curves of horizontal

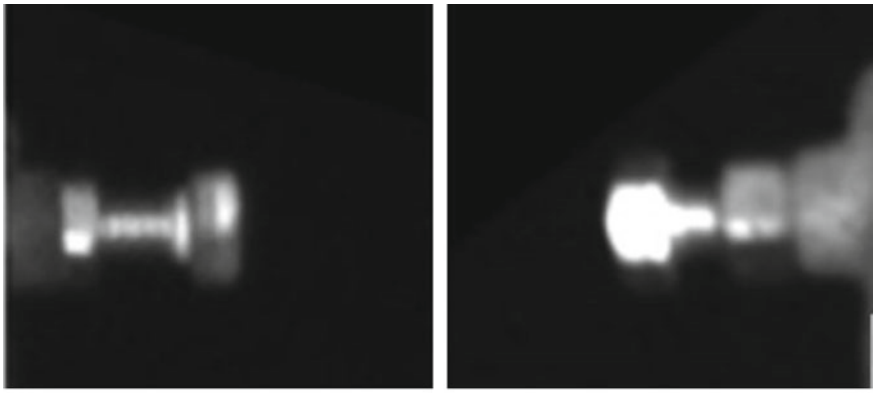

(a) Normal condition

(b) Missing condition

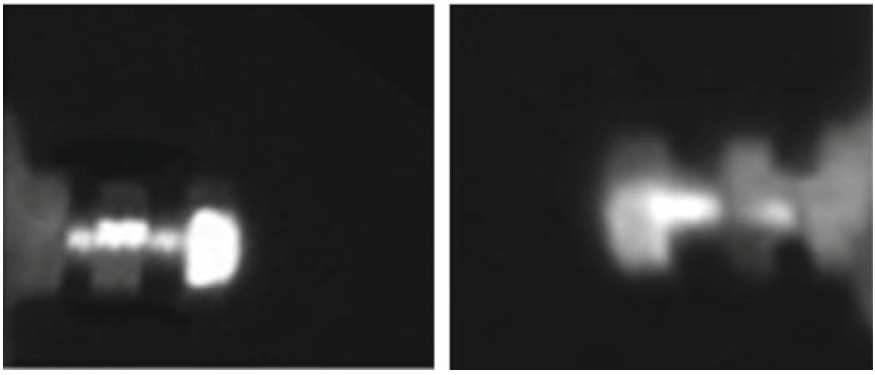

(c) Loosening condition

Fig. 6.95 Three typical states of the screws

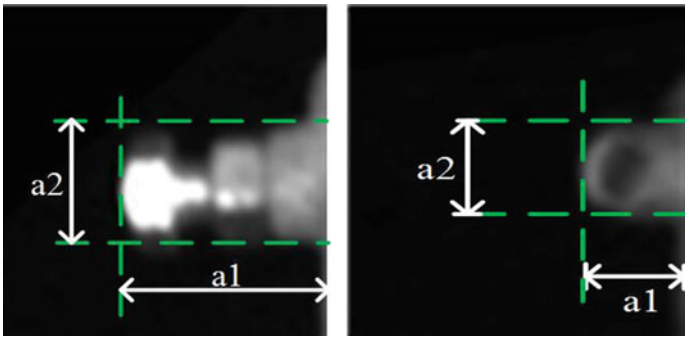

Fig. 6.96 Ratio of bolt length to its diameter

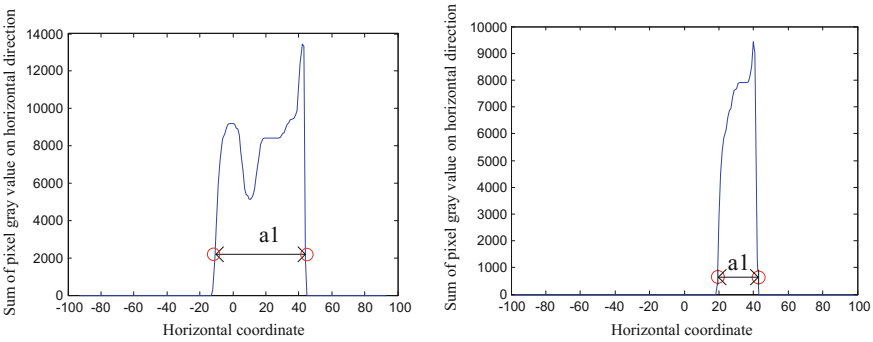

(a) Cumulative grayvalue distribution on the horizontal direction

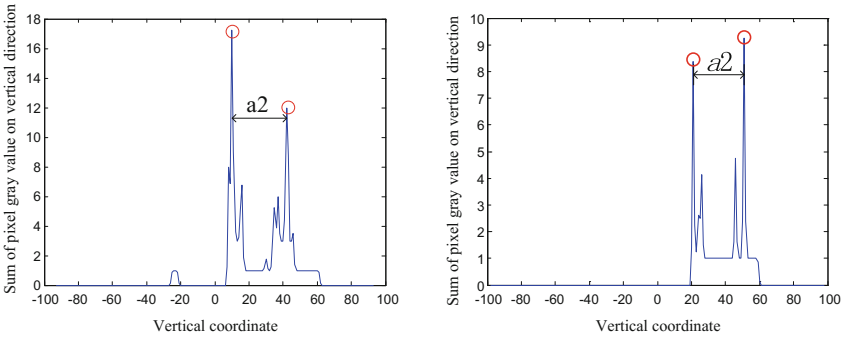

(b) Cumulative grayvalue distribution on the verticle direction

Fig. 6.97 Detection of the falling fault of screw

pixel accumulation distribution can be calculated and the loosening fault can be judged by the times of the zero-crossing (Fig. 6.98).

In order to verify the presented method, based on OpenCV and Matlab, 60 images of the catenary suspension system from the field are tested. 50 images contain diagonal tube, and 10 images do not contain diagonal tube. The number of loosening and missing screws in the images is each 5, respectively. The detection results are listed in Table 6.13.

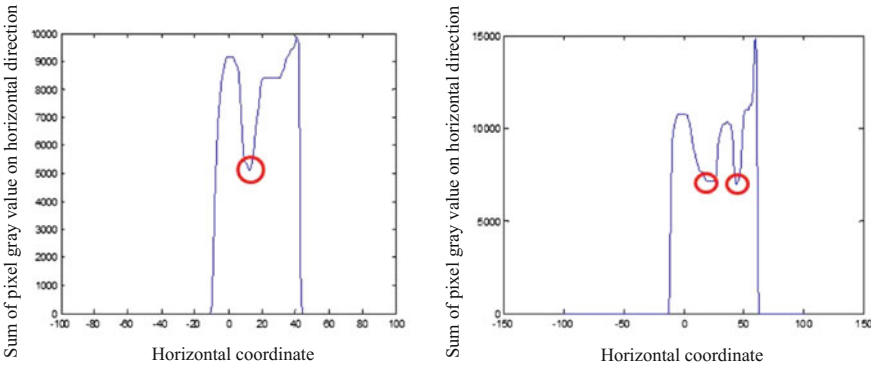

(a) Cumulative grayvalue distribution on the horizontal direction

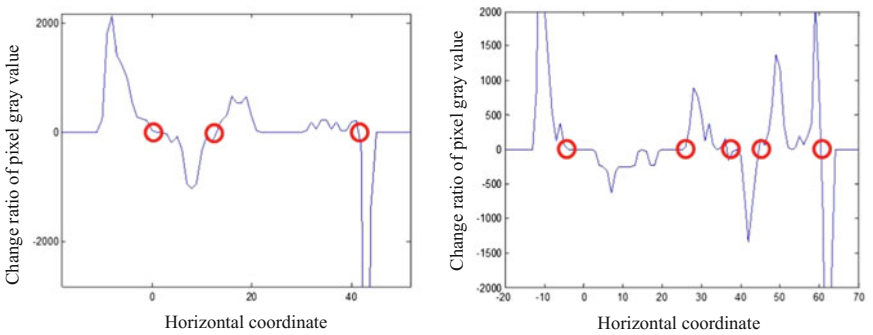

(b) Cumulative difference distribution curve on the horizontal direction

Fig. 6.98 Detection of the loosening fault of screw

Table 6.13 Detection results of diagonal tube

	Total	Number of correct detection	Number of error detection	Detection time (s)
Image number	50	44	0	1.288
Images with diagonal tube	40	38	0	1.318
Images without diagonal tube	10	10	0	1.101
Loosening screw	5	5	0	/
Missing screw	5	5	0	/

6.6 Summary

In recent years, many automatic inspection methods based on image processing and computer vision have been used in railway maintenance. In this chapter, some new detection methods of the safety threatening working state of the insulators, the clevises, and the diagonal tube are presented and discussed in detail.

In order to improve the detection accuracy of non-contact detection for the catenary, some researches should be developed in future [48, 49].

(1) The research and development of pantograph-catenary detection equipment should be in line with the requirements of the 6C standard. On July 1, 2012, this standard has been promulgated and implemented by the Ministry of Railway of China as the general technical specification for the safety inspection and monitoring system (6C system) of the high-speed railway power supply. In the standard, from the technical requirements, system components, communication form, etc., to the specifications of pantograph-catenary detection equipment are given. Therefore, the developed detection equipment should be based on the 6C system standard.

(2) Most of the existing detection equipment in the railway integrated test vehicle must occupy the traffic line, and small portable and hand-held detection equipment has low efficiency outside. With the opening of the low altitude area to the civil aviation, it is possible to realize the detection of pantograph-catenary parameters and faults using the UAV (unmanned aerial vehicle) technology. The short-range aerial line equipment can realize the close multi-angle detection of pantograph-catenary equipment, and effectively prevent the visual dead angle. The long-endurance UAV remote pantograph detection can improve the detection ability to quickly locate the fault point.

(3) With the image detection quality improvement, the possibility to improve the all-weather detection should be considered from the cost and general considerations. The existing image detection devices mostly use the CCD camera, but the visible light detection is vulnerable to ambient light, which can result in exposure, insufficient light, reflective white spot and other issues. Therefore, the quality of image shooting method should be improved for the intelligent recognition in future.

(4) At present, the research of pantograph-catenary image recognition algorithm is based on simple image environment and single parameter detection. But the advantage of image detection is to acquire complex pantograph-catenary image. Therefore, it is an urgent problem to solve for complex image target detection.

(5) The identification ratio of image recognition algorithm can determine the algorithm's practicality. At present, the pantograph-catenary image recognition accuracy still needs to be improved, especially for the complex images with poor clearance and interference parameters. The adaptive detection algorithms need in-depth research to raise the detection accuracy and precision.

(6) 3D technology is becoming more and more important for the design of pantograph-catenary system, but the research is in a preliminary stage. Using a 3D camera, the shooting and 3D image reconstruction for pantograph-catenary components can be realized. For the parameter detection and fault extraction of pantograph-catenary system, the virtual operation simulation and real 3D training will have the important application value.

References

1. Technical requirements of high-speed railway power supply safety detection and monitor system. Railway Transportation (2012) No. 136. Railway Ministry of China, Beijing
2. Yang H, Liu Z, Han Z et al (2013) Foreign body detection between insulator pieces in electrified railway. J China Railw Soc 35(4):30–36
3. Hu MK (1962) Visual pattern recognition by moment invariants. IRE Trans Inf Theor 8: 179–187
4. Petrou M, Kadyrov A (2004) Affine invariant features from the trace transform. IEEE Trans Pattern Anal Mach Intell 26(1):30–44
5. Rahtu E, Salo M, Heikkila J (2005) Affine invariant pattern recognition using multiscale autoconvolution. IEEE Trans Pattern Anal Mach Intell 27(6):908–918
6. Zhou X, Ren X, Zhang G et al (2002) Template update method in target affine tracking. J Image Graphics 7(11):1171–1175
7. Zhang G, Liu Z, Han Y et al (2013) A fast fuzzy matching method of fault detection for rod insulators of high-speed railways. J China Railw Soc 35(5):27–33
8. Cao J, Jie M, Hua T et al (2004) A fast correlation method for image matching using pixels abstract. J Astronaut 25(2):173–178
9. Li W, Salari E (1995) Successive elimination algorithm for motion estimation. IEEE Trans Image Process 4(1):105–107
10. Xie W, Zhou Y, Kou R (2011) An improved fast normalized cross correlation algorithm. J Tongji Univ 39(8):1233–1237
11. Zhang G, Liu Z (2014) Fault detection of catenary insulator damage/foreign material based on corner matching and spectral clustering. Chin J Scientific Instrum 35(6):1370–1377
12. Barnea DI, Silverman HF (1972) A class of algorithms for fast digital image registration. IEEE Trans Comput 21(2):179–186
13. Wu PJ, Chen GM (2005) An improved SSDA in image registration. Comput Eng Appl 41 (33):76–78
14. Bezdek JC, Ehrlich R, Full W (1984) FCM: The fuzzy c-means clustering algorithm. Comput Geosci 10(2–3):191–203
15. Guo X, Liu Z, Zhang G (2015) Fault detection of catenary insulator based on corner matching and image differencing. Proc CSU-EPSA 27(2):8–14
16. Song H, Jiang X, Yang G et al (2007) Application of moving average filter in weak pulse signal detection. Comput Digital Eng 35(10):169–170
17. Mallat S, Hwang WL (1992) Singularity detection and processing with wavelets. IEEE Trans Inf Theor 38(2):617–643
18. Lun DP, Tai-chiu H, Ho Y (2002) Wavelet singularity detection for image processing. IEEE Circ Syst 45(2):156–159
19. Chan TF, Vese LA (2001) Active contours without edges. IEEE Trans Image Proc 10(2): 266–277

20. Chen G (2008) An improved hybrid model for medical image segmentation. In: Proceedings of 11th IEEE Singapore international conference on communication systems, Singapore, pp 367–370
21. Zhang G, Liu Z, Han Y (2016) Automatic recognition for catenary insulators of high-speed railway based on contourlet transform and Chan-Vese model. Optik 127:215–221
22. Shi J, Malik J (2000) Normalized cuts and image segmentation. IEEE Trans Pattern Anal Mach Intell 22(8):888–905
23. Tang J, Peli E, Action S (2003) Image enhancement using a contrast measure in the compressed domain. IEEE Signal Process Lett 10(10):289–292
24. Serra J (1986) Introduction to mathematical morphology. Comput Vis Graphics Image Proc 35(3):283–305
25. Yan X, Lei T (2009) Research of traffic lane detection algorithm based on morphology method. J China Railw Soc 31(1):107–110
26. Han Z, Liu Z, Yang H et al (2013) Insulator fault detection based on curvelet coefficients morphology and zonal energy method. J China Railw Soc 35(3):36–40
27. Li D (2011) The influence of catenary system on high speed railway traffic safety. Chin Railw 2:34–37
28. Lowe DG (1999) Object recognition from local scale-invariant features. In: Proceedings of the 7th IEEE international conference on computer vision, Kerkyra, Greece, pp 1150–1157
29. Lowe DG (2004) Distinctive image features from scale-invariant key points. Int J Comput Vision 60(2):91–110
30. Cheung W, Hamarneh G (2009) SIFT: dimensional scale invariant feature transform. IEEE Trans Image Process 18(9):2012–2021
31. Li C, Ma L (2009) A new framework for feature descriptor based on SIFT. Pattern Recogn Lett 30(5):544–557
32. Battiato S, Gallo G, Puglisi G et al (2007) SIFT features tracking for video stabilization. In: International conference on image analysis and processing, IEEE, 825–830
33. Fischler MA, Bolles RC (1981) Random sample consensus: a paradigm for model fitting with applications to image analysis and automated cartography. Comm ACM 24:381–395
34. Han Y, Liu Z, Han Z et al (2014) Fracture detection of ear pieces of catenary support devices of high-speed railway based on SIFT feature matching. J China Railw Soc 36(2):31–36
35. Bay H, Tuytelaars T, Gool LV (2006) SURF: speeded up robust features. Comput Vis Image Underst 110(3):404–417
36. Juan L, Gwun O (2009) A comparison of SIFT, PCA-SIFT and SURF. Int J Image Proc 3 (4):143–152
37. Yang H, Liu Z, Han Y et al (2013) Defective condition detection of insulators in electrified railway based on feature matching of speeded-up robust features. Power Syst Technol 37 (8):2297–2302
38. Dalal N, Triggs B (2005) Histograms of oriented gradients for human detection. In: IEEE computer society conference on computer vision and pattern recognition, vol 1, pp 886–893
39. Viola P, Jones M (2001) Rapid object detection using a boosted cascade of simple features. In: Proceedings of the 2001 IEEE computer society conference on computer vision and pattern recognition vol 1, pp I-511–I-518
40. Han Y, Liu Z, Geng X et al (2016) Fracture detection of ear pieces in catenary support devices of high-speed railway based on HOG features. J China Railw Soc (in press)
41. Illingworth J, Kittler J (1988) A survey of the Hough transform. Comput Vis Graphics Image Proc 43(2):765–768
42. Lee TS (1996) Image representation using 2D Gabor wavelet. IEEE Trans Pattern Anal Mach Intell 18(10):959–971
43. Lee KC, Ho J, Kriegman DJ (2005) Acquiring linear subspaces for face recognition under variable lighting. IEEE Trans Pattern Anal Mach Intell 27(5):684–698
44. Yang H, Liu Z (2016) Defective condition detection of rotary double ears of support device in electrified railway based on the 2nd generation curvelet transform. J China Railw Soc (in press)

45. Zhong J, Liu Z, Zhang G et al (2016) Condition detection of swivel clevis pins in overhead contact system of high-speed railway. J China Railw Soc (in press)
46. Shai A (2007) Ensemble tracking. IEEE Trans Pattern Anal Mach Intell 29(2):261–271
47. Chen J, Liu Z, Han Y (2016) Location and fault detection of diagonal tube in high-speed railway overhead contact system based on local feature description. J China Railw Soc (in press)
48. Han Z, Liu Z, Zhang G, Yang H (2013) Overview of non-contact image detection technology for the pantograph-catenary monitoring. J China Railw 35(6):40–47
49. Liu Z, Song Y, Han Y et al (2016) Advances of research on high-speed railway catenary. J Southwest Jiaotong Univ 51(3):495–518

Chapter 7
Wire Irregularities Detection of Contact Line

7.1 Introduction

The schematic of the contact line irregularity comparing with ideal condition is shown in Fig. 7.1. Aside from the dynamic interaction between pantograph and catenary and the aerodynamic disturbance caused by pantograph, the contact line irregularity is believed to be another major cause for the fluctuation of pantograph-catenary contact force (PCCF). There are many causes for contact line irregularity given as follows [1, 2].

1. Non-constant height of the contact line above the track plane due to errors of mast and suspension positioning.
2. Difference in the length variation between the contact line and messenger line, due to non-recovered thermal expansion, which causes a variation in catenary geometrical position.
3. Incorrect tension of the wires, due to malfunction of the tensioning devices, which causes a variation of the catenary dynamic response.
4. Errors in dropper length, with wavelengths of the vertical profile of the irregularity of the contact line shorter than the previously considered cases.
5. Wear and manufacturing defects of contact line surface randomly distributed along the railway line.

Although the contact line irregularity can never be completely eliminated, it could be maintained in some feasible conditions if can be detected and localized in advance. There are several attempts on the prediction of contact line wear [3], the simulation of contact line irregularity [2, 4], and the impact study of the contact line irregularity on the current collection [1]. However, in these previous studies, the characterizations of the contact line irregularity were mostly based on the time-domain indicators and power spectrum density (PSD) of irregularity amplitudes, which could not fully reveal the early-stage contact line irregularity. The

Z. Liu, *Detection and Estimation Research of High-speed Railway Catenary*,
Advances in High-speed Rail Technology, DOI 10.1007/978-981-10-2753-6_7

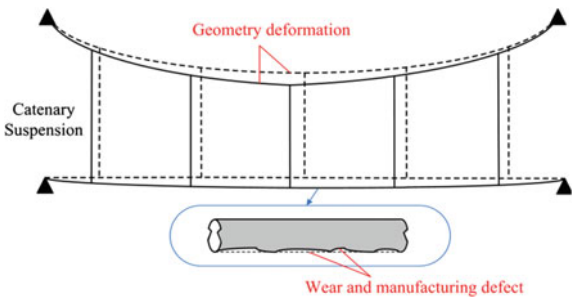

Fig. 7.1 Schematic of the contact line irregularity comparing with ideal condition (*dashed lines*) (Reprinted from Ref. [10], Copyright 2016 with permission from IEEE)

main difficulties of the prediction and detection of contact line irregularity are summarized below.

1. The direct measurement of contact line irregularity requires another set of equipment except the pressure sensors for PCCF measurement, and the accuracy of the measurement should be at the level of 0.1 mm in order to obtain the wear of contact line [5], which can almost be unachievable, and would cost a lot.
2. The current characterization of contact line irregularity can reveal its global condition, but is lack of quantified information, e.g. the wavelength and location of the irregularity, which could be convenient for the maintenance of catenary infrastructure.
3. As the reflection of contact line irregularity, the PCCF or the vertical displacement and acceleration of pantograph is much easy to be measured. But the currently used PSD estimation of the measurements is still a 1-D frequency representation and not able to identify the frequency-domain irregularities. For example, a typical real-life PCCF signal from a section of the Beijing-Guangzhou Railway line in China is depicted in Fig. 7.2a. The PCCF signal is measured under the train speed of about 100 km/h and the sampling interval of 0.5 m. It can be seen that the PCCF shows certain degree of periodicity in an interval cycle of approximately 60 m. The corresponding PSD depicted in Fig. 7.2b shows only one peak at the frequency 0.0156 m^{-1}, i.e. wavelength 64.1 m, which approximately equals to the average span distance of the railway section. Aside from that, no other information on the frequency components can be obtained from the PSD. Besides, the information on the locations of frequency components cannot be provided.

Therefore, this chapter introduces the quadratic time-frequency representation (TFR) to the characterization of PCCF. A detection approach for contact line irregularity is developed based on the TFR of PCCF. Theoretically, the TFR of the PCCF could reveal the contact line irregularity reflected by the PCCF, and as well locate the irregularity components in the measured railway line so that maintenances can be performed accordingly. Some dynamic simulations of pantograph-

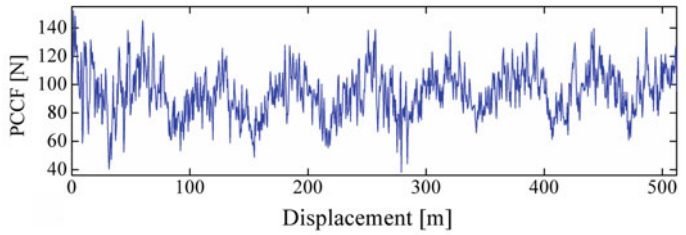

(a) A segment of PCCF measurement.

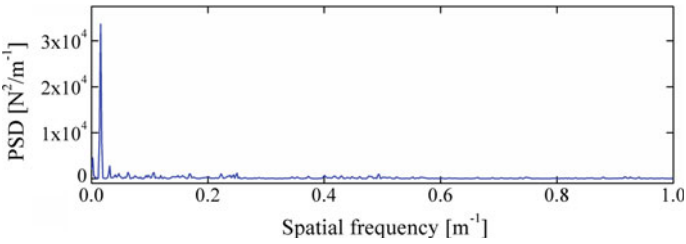

(b) PSD analysis of the PCCF signal.

Fig. 7.2 A real-life PCCF signal and its PSD (Reprinted from Ref. [10], Copyright 2016 with permission from IEEE)

catenary interaction and the contact line irregularity are realized to illustrate the detection approach.

7.2 Times-Frequency Representation of PCCF

The time frequency analysis of non-stationary signals is divided into two categories: linear transformation and nonlinear transform. Linear transformation mainly includes the short-term Fourier transform, Gabor transform and wavelet transform. The time-frequency resolution of short-time Fourier transform and Gabor transform is poor. Wavelet transform is not suitable to decompose signals with several similar frequency components, and the selection requirement of wavelet base is very high. Nonlinear transform adopts the joint time and frequency function to describe the signal energy density changing with the time (mileage), which mainly refers to the Cohen time-frequency distributions [5]. The Cohen class distribution of signal $z(t)$ is defined as follows.

$$C_z(t,\omega) = \int_{-\infty}^{\infty} R_z(t,\tau) e^{-j\omega\tau} d\tau \tag{7.1}$$

where t and ω are the time and frequency of signal $z(t)$, respectively. The time-varying autocorrelation function $R_z(t,\tau)$ of signal $z(t)$ is listed below.

$$\begin{cases} R_z(t,\tau) = \int_{-\infty}^{\infty} z\left(u+\frac{\tau}{2}\right) z^*\left(u-\frac{\tau}{2}\right) \psi(t-u,\tau) du \\ \psi(t,\tau) = \int_{-\infty}^{\infty} \phi(\tau,v) e^{-jvt} dv \end{cases} \tag{7.2}$$

where $\phi(\tau,v)$ is the kernel function, "$*$" denotes complex conjugation, u, τ and v are the position, time and frequency variables in the integration respectively. If $\phi(\tau,v)=1$, the Cohen class distribution is actually the Wigner-Ville distribution.

$$WVD_z(t,\omega) = \int_{-\infty}^{\infty} z\left(t+\frac{\tau}{2}\right) z^*\left(t-\frac{\tau}{2}\right) e^{-j\omega\tau} d\tau \tag{7.3}$$

Wigner-Ville distribution has the best time-frequency concentration, but it suffers from serious cross term phenomenon and negative frequency with no physical meanings. In actual applications, improvements should be made to achieve the maximum cross term suppression with minimum influences on the time-frequency concentration.

In order to suppress the cross terms in Wigner-Ville distribution, some improved distributions have been proposed, including the pseudo Wigner distribution, smoothed pseudo Wigner Ville distribution, Butterworth distribution, Choi-Williams distribution, Born-Jordan distribution and Zhao-Atlas-Mark distribution [6] and so on, whose kernels are shown in Table 7.1.

It is known that different Cohen class distributions are suitable for analyzing the different signals with certain time-frequency characteristics. At present, there is not a kind of distribution that can obtain good time-frequency analysis results for all signals. Since PCCF includes many complex frequency components, and has the characteristic of low-frequency energy concentration, it is very necessary and

Table 7.1 Classical time-frequency distribution kernel functions in Cohen class

Distribution Name	Kernel function $\phi(\tau,v)$
Wigner-Ville distribution (WVD)	1
Pseudo Wigner distribution (PWD)	$\eta\left(\frac{\tau}{2}\right)\eta^*\left(-\frac{\tau}{2}\right)$
Smoothed pseudo Wigner distribution (SPWD)	$\eta\left(\frac{\tau}{2}\right)\eta^*\left(-\frac{\tau}{2}\right)G(v)$
Choi-Williams distribution (CWD)	$e^{-\alpha(\tau v)^2}$
Born-Jordan distribution (BJD)	$\frac{\sin(\tau v/2)}{\tau v/2}$
Butterworth distribution (BUD)	$\frac{1}{1+\left(\frac{\tau}{\tau_0}\right)^{2M}+\left(\frac{v}{v_0}\right)^{2N}}$
Zhao-Atlas-Mark distribution (ZAMD)	$2g(\tau)\frac{\sin(\tau v/2)}{v}$

important to select the appropriate time-frequency analysis method for further analysis.

When the Cohen class time-frequency distribution is used, the real signal should be converted into analytical signal, which can directly eliminate the cross terms between the negative frequency components and the positive frequency components [7]. Hilbert transform can perform the conversion.

The Hilbert transform of signal $x(t)$, namely $y(t)$ is given by

$$y(t) = \frac{1}{\pi} P \int_{-\infty}^{\infty} \frac{x(t')}{t - t'} dt' \tag{7.4}$$

where P indicates the Cauchy principal value. So the analytic version of signal $x(t)$ is formed as

$$z(t) = x(t) + j \cdot y(t) \tag{7.5}$$

The analytic signal $z(t)$ will be used in the following time-frequency analysis instead of real signal $x(t)$.

In this chapter, the used contact pressure data is from the simulation models of Beijing Tianjin high-speed Railway [8], in which the three mass models of pantograph DSA380 and SSS400+ are adopted, respectively. The statistics of PCCF under the different speeds are shown in Table 7.2.

It can be found that the data of each group is in accordance with the basic law, the overall trend of the SSS400+ pantograph contact pressure is smaller, and the DSA380 pantograph contact pressure standard deviation is small. The stable PCCF data from the middle 8 spans in 10 spans are analyzed with time-frequency distribution. The length of data is 384 m (span length is 48 m), and the sampling frequency is 0.5 m, which can satisfy the non-stationarity analysis requirement, namely the data total length is less than 500 m according to Chap. 2. The analysis results with several classical time-frequency distributions for the PCCF data under 300 km/h and DSA380 pantograph are shown in Fig. 7.3.

Table 7.2 Statistics of PCCF

Data type	Speed (km/h)	Mean (N)	Standard deviation (N)	Maximum (N)	Minimum (N)
DSA380	200	102.3	11.1	129.3	65.6
	250	124.3	19.8	191.1	62.5
	300	151.1	26.7	223.4	75.7
	350	182.4	31.7	266.5	90.4
SSS400+	200	88.6	12.3	117.2	43.4
	250	110.3	20.9	167.2	65.5
	300	136.8	32.9	215.4	45.1
	350	168.0	36.0	277.5	62.8

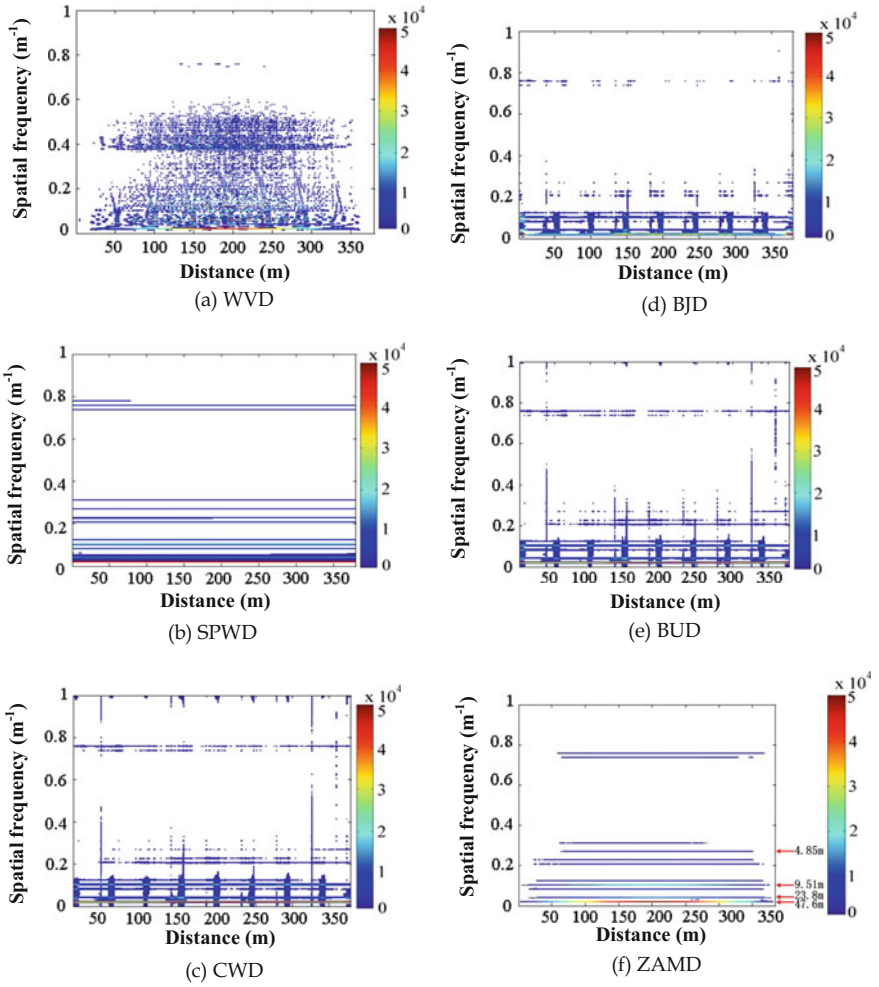

Fig. 7.3 Several classical time-frequency distributions for PCCF (Reprinted from Ref. [10], Copyright 2016 with permission from IEEE)

In Fig. 7.3, six figures are contour maps. The longitudinal coordinate denotes the mileage, and the vertical coordinate denotes spatial frequency. The colors from blue to red mean that the increasing of energy density (shown in energy bands at the right side), and white means no energy. In the time-frequency analysis results of PCCF, if there is energy characterization in the contour map corresponding to a longitudinal coordinate space frequency, it means the existence of the spatial frequency components in PCCF. In addition, the reciprocal of spatial frequency is the wavelength component in PCCF.

In Fig. 7.3, it can be found that the analysis results with WVD, CWD, BJD and BUD are very poor. The situation of cross terms is very severe. In the results of

SPWD and ZAMD, several complete horizontal lines can be clearly identified, which represent the frequency components in the data segment. In these lines, the energy density at spatial frequency 0.021 m^{-1} is the maximum, which can represent the wavelength component 47.6 m corresponding to the period of catenary span. It just accords with the span 48 m in the model, and is the most concentrated wavelength component in PCCF, which is same as the analysis results in [9].

Because the smooth window' width must be set in time domain and frequency domain for SPWD, and the situation of some cross terms in low frequency part is heavy, which results in the poor spatial frequency resolutions, ZAMD is adopted to analyze the PCCF data in this chapter.

7.3 Detection Approach Description Based on ZAMD

The detection and localization approach for contact line irregularity is depicted in the block diagram in Fig. 7.4, in which the Zhao-Atlas-Marks distribution (ZAMD) is adopted for the time–frequency representation (TFR) of PCCF. The purpose of the approach is to identify the irregularity wavelength components caused by contact line irregularity and contained in PCCF, and localize the contact line irregularity that exists in local section. Each procedure in the approach is described in detail below. An illustration of the application of the detection method is given after the approach description.

1. PCCF measurement data

To implement the practical application of proposed method in railway industry, the precise measurement of PCCF should be implemented first as a valid data source.

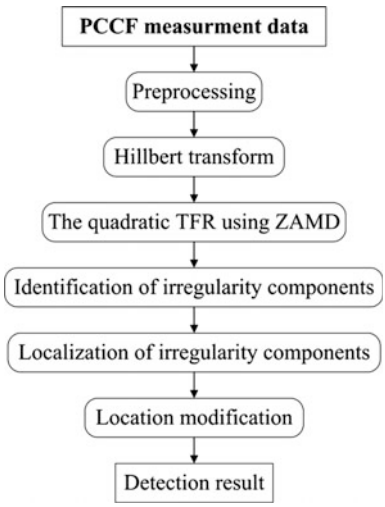

Fig. 7.4 Block diagram of the detection approach (Reprinted from Ref. [10], Copyright 2016 with permission from IEEE)

For reference, the suggested minimum requirement of the basic parameters of measuring sensors, if employed, is given in Table 7.3 where the FS denotes the full scale of sensor. Although the existing measuring methods of PCCF are various in different institutions or companies, the PCCF data are acceptable for the proposed detection method as long as the measurement meets the minimum requirement.

2. Preprocessing

The preprocessing of raw PCCF data must ensure the validity of PCCF and filter the unconcerned frequency ranges. Thus, the preprocessing operations performed on the raw PCCF should depend on the measurement method adopted in the PCCF measurement. Some usual and recommended operations are the eliminating of incorrect measurements, filtering of irrelevant frequency ranges, denoising and so on. When the duration of a PCCF measurement is longer than a tensioning section of the measured railway line, the signal should be divided into several segments.

3. Hilbert transform

The content has been introduced above.

4. Quadratic TFR using ZAMD

The ZAMD has been proven to be valid for the TFR of PCCF signal [10]. It has a cone-shaped kernel defined as [6]

$$\phi(t,\nu) = g(\tau)\frac{\sin(|\tau|\nu/\beta)}{\nu/2} \tag{7.6}$$

where $g(\tau)$ is a time window and parameter β is used to adjust the slopes of the cone-shape kernel with the constraint that $\beta \geq 2$.

5. Identification of irregularity components

Based on the TFR of PCCF, the identification of irregularity components is realized by comparing the TFR with the healthy TFR of the PCCF from the same railway line. In other words, the identification should be based on the priori information on the healthy wavelength components of PCCF in the measured railway line; or at least the catenary structure parameter of the railway line. The identified irregularity wavelengths should be with detection error depending on the resolution of the TFR.

Table 7.3 Minimum requirement of sensor parameters (Reprinted from Ref. [10], Copyright 2016 with permission from IEEE)

Parameter type	Pressure sensor	Acceleration sensor
Measurement range	0.0–500.0 N	$\pm 10.00g$
Measurement accuracy	2 %FS	0.5 %FS
Maximum overload	1000 N	$100g$
Maximum sampling frequency	1000 Hz	1000 Hz

The key to the practical implementation of this procedure is the acquisition of healthy components in PCCF, which is equivalent to the determination of healthy PCCF for a certain railway line. Addressing this problem, three possible ways corresponding to the different stages of pantograph-catenary system are suggested as follows.

(a) If a catenary suspension is in the design stage, the pantograph-catenary system must be verified using simulation before its construction. Based on the simulation results, the TFR of ideal PCCF can be obtained and used as the reference, namely the healthy TFR, for the following acceptance test and operation.
(b) If a pantograph-catenary system is already constructed and in the acceptance stage, the TFR of current PCCF signals can be regarded as the healthy TFR. After the start of normal operation, the deterioration of the TFR of PCCF can be observed by comparing with the healthy TFR, and the contact line irregularities and the severity of irregularities can be obtained.
(c) For an existing railway line with previous data records of PCCF, the earliest record of PCCF signal can be regarded as the relatively healthy one. If there is few or no previous record of PCCF, the new measurement of PCCF can be used as the reference for future measurements, and the structure parameters of catenary suspension can be helpful to determine the healthy components in PCCF.

6. Localization of irregularity components

After the identification of irregularity components, each irregularity component can be localized within a distance range depending on the corresponding energy distribution in the TFR of PCCF. Similarly, the localization results should be with detection error depending on the resolution of the TFR.

7. Location modification

Based on previous experience, the irregularity component with longer wavelength is less detectable because the enormous influence of catenary structure on the PCCF could submerge it. It should be noted that, when using the quadratic TFR of PCCF, there is certain limitation in the localization result given in procedure Step 6 which can be described as follows.

(a) The localization result is closer to actual value when the irregularity wavelength is longer.
(b) The irregularity components detected in long-wavelength range should be properly magnified to obtain the final duration.

Therefore, the duration of the irregularity components in the low-frequency range should be properly magnified. The modification coefficient should be based on the extent of amplitude deviation comparing with healthy condition. In the case of real-life measurement, the modified final durations can be calculated by fitting

the trend of variation ratio versus the irregularity wavelength. The ratio of variation of the start or end point is defined as

$$ratio = \frac{\text{Detected start (end) location}}{\text{Actual start (end) location}} \tag{7.7}$$

and the ratio of the detected start and end points can be obtained by simulation or previous measurement. Then, the cubic polynomial can be used as the fitting formula for the trend of the ratios

$$T(l)=p_1 l^3 + p_2 l^2 + p_3 l + p_4 \tag{7.8}$$

where l is the irregularity wavelength and p_1 to p_4 are the fitting parameters. The fitting curves of the variations of start and end locations can be used to calculate the final durations of certain irregularity components by

$$\text{Final start (end) location} = \frac{\text{Detected start (end) location}}{T(l) \text{ for start (end) location}}. \tag{7.9}$$

As an example, the modification coefficient of the 8 mm-amplitude irregularity, which represents a certain extent of contact line irregularity, is presented in the next section. For future applications of the modification, different modification coefficient should be obtained using different amplitude of irregularity based on a simulation model corresponding to the actual pantograph-catenary system.

8. Detection result

The detection result, namely the output of the detection approach includes the wavelength, duration and midpoint location of irregularity component. Aside from the wavelength and duration, which are the fundamental properties of irregularity component, another indicator that can be used as the reference for localization result is the location of the midpoint of the local irregularity. This indicator is especially useful for the existing railway lines when the severity of the contact line irregularity is unknown due to being lack of previous measurement and monitoring. It provides convenience for determining the actual location of necessary track visit in maintenances.

7.4 Detection Approach Demonstration

To demonstrate the application of the detection approach, a simulation model of pantograph-catenary interaction based on finite element method is employed. The modeling method was validated thoroughly by Bruni et al. [11] and European Committee for Electrotechnical Standardization [12]. The simulations are carried out considering global, local and complex contact line irregularities.

7.4.1 TFR of Healthy PCCF

Concretely, in the simulation model, the catenary span is 48 m and the inter-dropper distances are 5, 9.5, 9.5, 9.5, 9.5 and 5 m, respectively between restriction points and droppers. The pantograph parameters adopt the parameters of the DSA380 pantograph, which is an actual high-speed pantograph in China. A segment of simulation PCCF signal is regarded as the healthy PCCF as shown in Fig. 7.5a. The corresponding TRF using ZAMD is computed according to aforementioned procedures and depicted in Fig. 7.5b. As a result, the TFR shows high time-frequency resolution and all the frequency components are separately distributed in the time-frequency plane. More particularly, the wavelength components marked out by the dashed arrows represent some harmonics that can be identified as the reflections of certain catenary structure parameter. As labeled in Fig. 7.5b, the span wavelength, the half-span wavelength and two inter-dropper distance wavelengths can be observed almost throughout the entire displacement. The two relatively high frequency components far exceed the highest frequency related to the catenary structure, which could be regarded as the result of pantograph vibration.

Note that in the same pantograph-catenary interaction, the TFR of healthy PCCF is different if the operation speed is different. Figure 7.6 depicts the healthy TFRs of PCCF under different operation speed. It can be seen that some wavelength

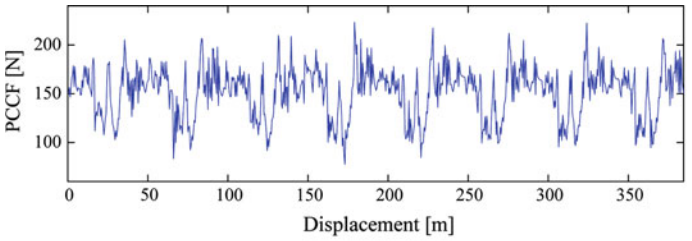

(a) The healthy PCCF signal.

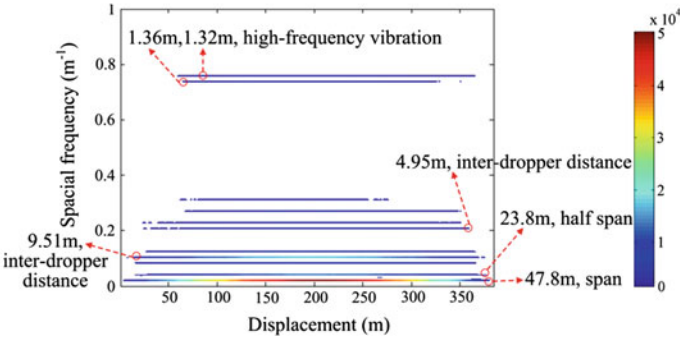

(b) The quadratic TFR of the healthy PCCF signal using ZAMD

Fig. 7.5 The healthy PCCF signal and its quadratic TFR (Reprinted from Ref. [10], Copyright 2016 with permission from IEEE)

components remain the same for PCCF under different speed, especially the marked out components in Fig. 7.5b. Meanwhile, the circled wavelength components in Fig. 7.6 are new and different as the speed changes. The wavelength components tend to be more complex as the speed increases. Thus, it can be concluded that there is a specific healthy PCCF for the pantograph-catenary interaction under a certain speed. The following investigation is carried out based on the PCCF signal under the same speed of 300 km/h.

When the catenary structure and operation speed is the same, but the pantograph type is different, the TFR of healthy PCCF should be different since the interaction is different. Figure 7.7 depicts the TFR of PCCF generated by the SSS400+ pantograph instead of the DSA380 pantograph. It can be seen that most of the wavelength components are still the same comparing with Fig. 7.5b since the catenary structure is the same. But in the circled region, emerging wavelength components appear due to the replacement of pantograph. It can be regarded as the sign of a relatively bad contact quality as the standard deviation of PCCF under the SSS400+ pantograph is 6.2 N larger than the DSA380 pantograph. So, the pantograph type should also be considered when determining the healthy PCCF as the reference for irregularity detection.

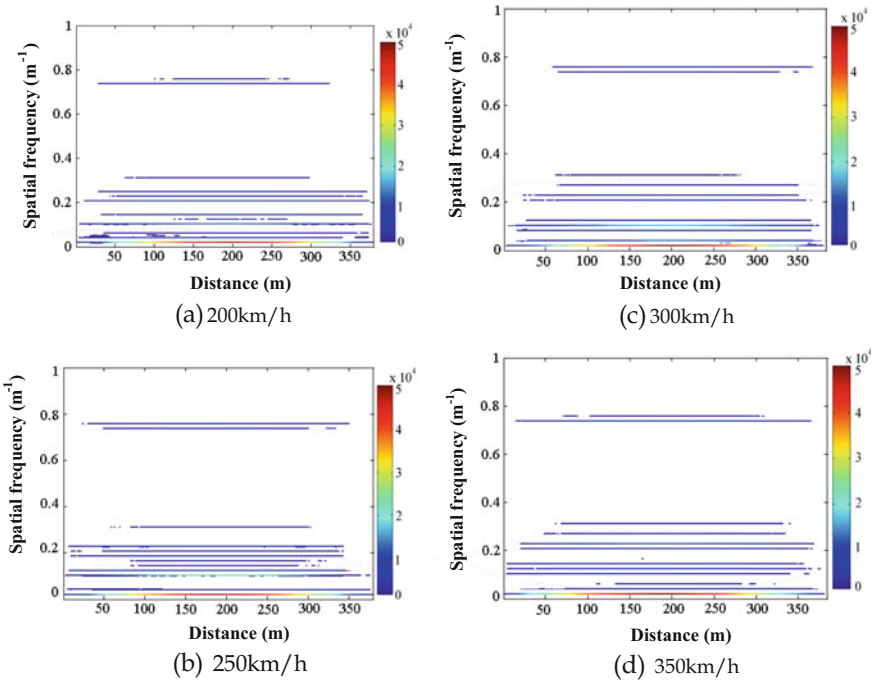

Fig. 7.6 Comparisons of the TFRs of PCCF under different operation speed

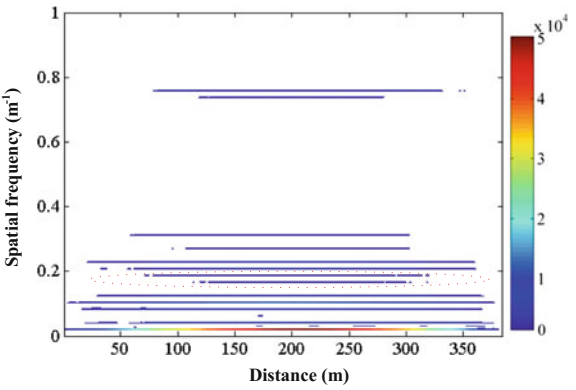

Fig. 7.7 TFR of the PCCF under the SSS400+ pantograph

7.4.2 *Irregularity Detection of Unhealthy PCCF*

Using the quadratic TFR depicted in Fig. 7.4b as the reference of healthy TFR of PCCF, some unhealthy PCCF signals are simulated under the same operation condition with only contact line irregularity in different forms added. Essentially, the irregularity components of the contact line height can be regarded as the combination of harmonic waves with different wavelength, frequency and distance duration. In order to observe the frequency-domain reflection of contact line irregularity in the PCCF signal, simplex waveforms generated by the cosine wave are added to the normal height of contact line to simulate simplified vertical irregularity. More specifically, the global, local and complex irregularities illustrated in Table 7.4 are formed to study the TFR of the PCCF under varies irregularities.

In the case of real-life operation, the synthetic approaches that are more often used to generate real-life contact line vertical irregularity are the inverse Fourier transform [4] and the trigonometric series [13] based on the PSD of the actual contact line height, which are substantially equivalent to the process of harmonic wave superposition. For example, Fig. 7.8a depicts the PSD of measurement data of contact line height from Beijing-Guangzhou Railway line using the maximum entropy method. The solid red line indicates the fitting of the actual PSD, which is used as the input of the trigonometric series method. The contact line irregularity

Table 7.4 Types of simplex contact line irregularity

Type	Schematic
Normal	
Global irregularity	
Local irregularity	
Complex irregularity	

data can be regarded as a zero-mean stationary Gaussian process computed by the sum of cosine functions as follows.

$$s(k\Delta x) = \sum_{n=1}^{N} a_n \cos(\omega_n k + \theta_n) \tag{7.10}$$

where k is the number of the sample point, Δx is the sampling interval, $s(k\Delta x)$ is the irregularity data series, N is the amount of harmonics, θ_n is a random variable uniformly distributed on (0, 2π), and a_n is a normal random variable with zero mean and variance σ_n^2 defined as

$$\sigma_n^2 = 4S(\omega_n)\Delta\omega \tag{7.11}$$

where $S(\omega_n)$ is the fitted PSD of contact line irregularity and $\Delta\omega$ is the frequency interval. The sampling frequency ω_n of the trigonometric series is determined by its upper and lower cut-off frequency ω_u and ω_l as

$$\begin{cases} \Delta\omega = \frac{1}{N}(\omega_u - \omega_l) \\ \omega_n = \omega_u + (n - 0.5)\Delta\omega \end{cases}. \tag{7.12}$$

The synthetic contact line irregularity generated by Eq. (7.10) and the fitted PSD in Fig. 7.8a is depicted in Fig. 7.8b, which shows that as the contact line height

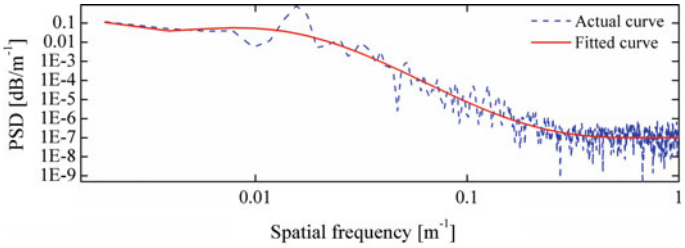

(a) PSD estimation of the measurement of contact line irregularity and its fitting

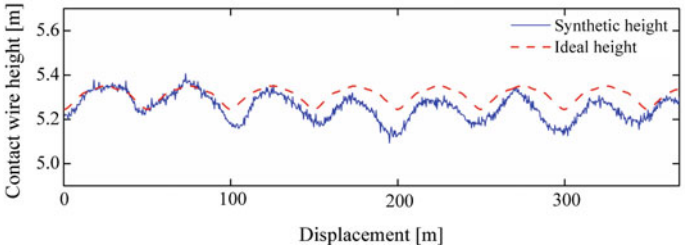

(b) Synthetic contact line irregularity generated by trigonometric seriesmethod.

Fig. 7.8 The generation of synthetic contact line irregularity (Reprinted from Ref. [10], Copyright 2016 with permission from IEEE)

periodically changes in span cycles in general, the irregular components cause observably deviation on the normal contact line height.

The PCCF simulations under simplex and synthetic contact line irregularities are carried out and adopted as unhealthy PCCF for detection approach demonstration. For simplex contact line irregularity, the global, local and complex irregularities are investigated respectively.

Firstly, the PCCF signal under the simplest global irregularity using one cosine function is carried out. The following contours of quadratic TFRs are without colorbar for simplicity. In the TFRs depicted in Fig. 7.9, the quadratic TFRs of the PCCF under different forms of irregularities indicate that, while other components are practically the same as in the TFR of healthy PCCF in Fig. 7.5b, the wavelengths of contact line irregularity can be accurately reflected by the ZAMD. In Fig. 7.9a, b, the global irregularities simulated by a cosine wave with wavelength of 1 and 2 m respectively are both detected and marked out. However, the distance durations of the two global irregularities are not globally distributed. The component with the longer wavelength appears to have a relatively short duration. It is because that the energy of a PCCF signal is mainly concentrated on the low-frequency range, which makes the low-amplitude irregularity harder to reveal itself when its wavelength is closer to the span.

Secondly, some irregularities with limited duration are added to the contact line to investigate the performances of quadratic TFR under local irregularity. For the sake of conciseness, Fig. 7.9 depicts some TFRs of the PCCF signals under different local irregularities in the one contour with all the healthy components grayed and blunted. The local irregularities are existed only in the sixth span, namely from the 240 to 288 m of the displacement in Fig. 7.10, and with independent wavelength from 1 to 5 m with step of 0.5 m, respectively. It can be observed that all the local irregularities are detectable with the wavelengths labeled and approximate distance durations described in the square brackets. However, the distance duration declines as the irregularity wavelength increases, which is the same trend as shown in Fig. 7.9a, b. It confirms that the irregularity component with longer wavelength is less detectable because the enormous influence of catenary structure on the PCCF could submerge it.

Clearly, the duration of local irregularity requires modification. Based on the location modification presented above and Eqs. (7.7) and (7.8), the fitting curves of the variations of start and end locations are shown as the solid lines in Fig. 7.11, which are used to calculate the final durations of corresponding irregularity components. For instance, the apparent start and end locations of the 5 m-wavelength component are 261 and 268 m respectively, and the variation ratios calculated by corresponding fitting formula are 1.075 and 0.942 respectively. So, the final start and end locations are (261/1.088)m and (268/0.931)m respectively according to Eq. (7.7), which is equal to duration [239.9, 287.9 m]. To adopt this modification, the duration of the irregularity should be under 50 % of the total displacement in the low-frequency range, because the irregularity component exceeding half the displacement is highly possible to be global referring to Fig. 7.9.

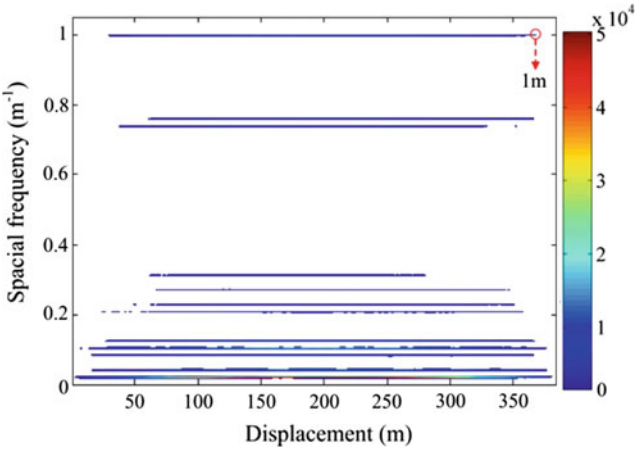

(a) Quadratic TFR of the PCCF under 1m-wavelength global irregularity .

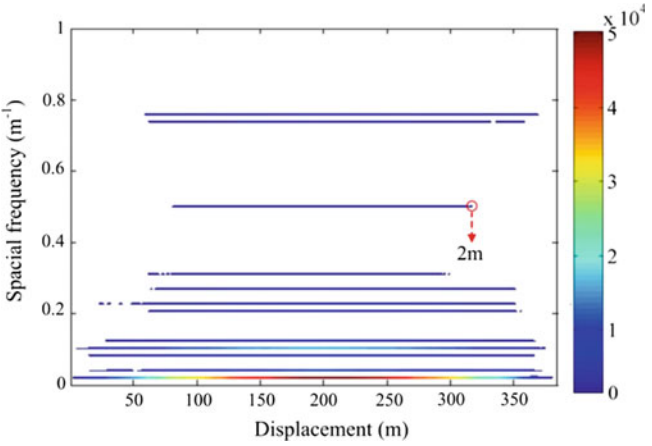

(b) Quadratic TFR of the PCCF under 2m-wavelength global irregularity.

Fig. 7.9 Quadratic TFRs of the PCCF under simplex contact line irregularity (Reprinted from Ref. [10], Copyright 2016 with permission from IEEE)

Thirdly, in the case of complex irregularity, a 3 m-wavelength and 8 mm-amplitude global irregularity and a 2 m-wavelength and 8 mm-amplitude local irregularity in the fifth span are both added to the contact line height, which result in the TFR of PCCF depicted in Fig. 7.12. For the detected local components,

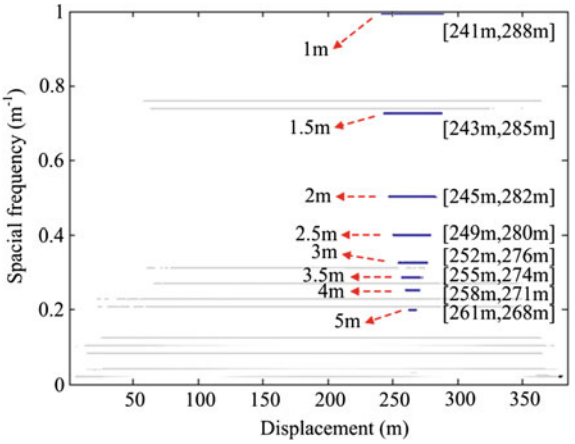

Fig. 7.10 Highlighted quadratic TFRs of PCCF signals under local irregularities with different wavelength (Reprinted from Ref. [10], Copyright 2016 with permission from IEEE)

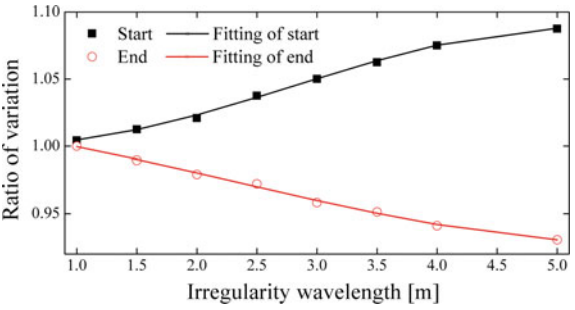

Fig. 7.11 Variation ratios of the start and end location versus the irregularity wavelength and their fitting curves (Reprinted from Ref. [10], Copyright 2016 with permission from IEEE)

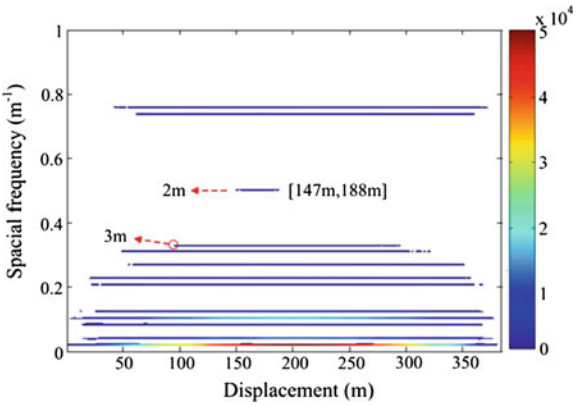

Fig. 7.12 Quadratic TFR of the PCCF under complex irregularity (Reprinted from Ref. [10], Copyright 2016 with permission from IEEE)

the variation ratios for their start and end locations are computed using the fitting curves in Fig. 7.11 by Eq. (7.8). The final duration of the local irregularity is [143.7, 191.8 m], which is approximate to the actual duration [144, 192 m].

Meanwhile, the duration of the global irregularity is non-global but exceeds 50 % of the overall analysis displacement and is close to the essential components of PCCF. It is not suitable for modification and could be inferred to be a global irregularity component.

Fourthly, a synthetic contact wire irregularity is generated by Eq. (7.10) in which the amount of harmonics is 16 and the maximum amplitude is 9.88 mm. The PCCF signal is simulated under the synthetic irregularity with mean 151.0 N and standard deviation 27.7 N that are slightly higher than healthy PCCF. Figure 7.13 depicts the TFR of the PCCF sin which the dashed red lines circle all the irregularity components and the red numbers represent the amount of components in the circle. A total of 12 components are detected in the TFR. The wavelengths and corresponding distance durations of the irregularity components are given in Table 7.5 based on the analysis above, and the intervals of wavelength and duration are given based on the adopted time and frequency smoothing windows. Because of the resolution of TFRs is limited to a certain extent, the values shown in the table are with detection errors. It can be seen that in the frequency range under 0.4 m^{-1}, and three components exceeding half the displacement are recognized as global irregularity. The other components are modified in localization as described above. It is worth mentioning that, in this case, all the irregularity components are not necessarily belonging to the synthetic irregularity. Some of them could be due to the pantograph-catenary vibration frequency indirectly caused by the irregularity.

Lastly, a PCCF signal from a section of Jiaozuo-Liuzhou Railway line in China depicted in Fig. 7.14a is used for detection demonstration. The signal is measured under the train speed of approximately 100 km/h and the sampling interval of 0.5 m. The measurement of the PCCF signal is implemented by installing a pair of pressure sensors and a pair of acceleration sensors on each of the two contact strips of pantograph head. The minimum measurement unit of pressure sensor and acceleration sensor are 0.1 N and 0.01g where the gravitational acceleration $g = 9.81$ m/s^2, respectively. The PCCF is composed of two parts and computed as follows.

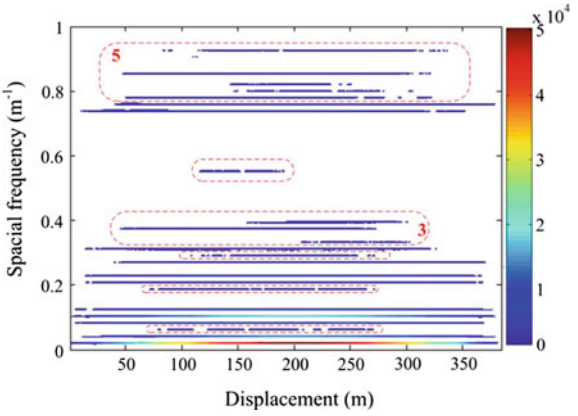

Fig. 7.13 Quadratic TFR of the PCCF under synthetic irregularity with the irregularity components circled by *dashed lines* (Reprinted from Ref. [10], Copyright 2016 with permission from IEEE)

Table 7.5 The detection results of the PCCF under synthetic irregularity

Number	Wavelength (±0.05 m)	Duration [±2, ±2 m]
1	1.05	[79.8, 345.1]
2	1.16	[47.9, 322.2]
3	1.20	[142.3, 251.1]
4	1.24	[146.9, 307.4]
5	1.28	[48.3, 325.8]
6	1.82	[113.7, 200.1]
7	2.54	[149.8, 306.4]
8	2.67	Global
9	3.23	[199.8, 309.2]
10	3.51	[78.6, 284.3]
11	5.49	Global
12	15.38	Global

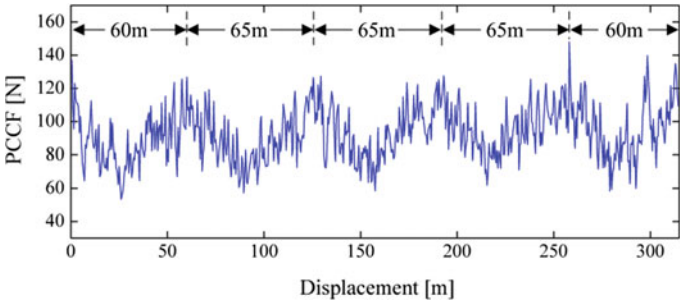

(a) Real-life PCCF measurement.

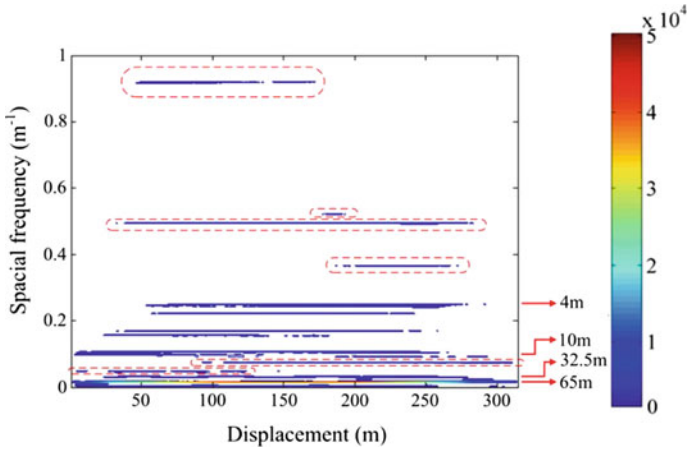

(b) Quadratic TFR of the PCCF measurement with the irregularity components

Fig. 7.14 Real-life PCCF signal and corresponding contact line irregularity detection based on quadratic TFR (Reprinted from Ref. [10], Copyright 2016 with permission from IEEE)

$$F = F_s + F_a = F_s + a \cdot m_{\mathrm{H}} \tag{7.13}$$

where F_s is the resultant force of the measurements of four pressure sensors, F_a is the correction of PCCF, a is the mean value of the measurements of four acceleration sensors, and m_{H} is the mass of pantograph head. The pantograph vertical acceleration is used to modify the dynamic value of PCCF. The PCCF signal shown in Fig. 7.14a is the result using Eq. (7.13) and no further preprocessing operations. It is preselected for a brief demonstration.

As an existing line with limited prior information, the five span distances in the section are given with the fluctuation of the PCCF, and the inter-dropper distances are unevenly distributed from 4 to 10 m in the five spans. Therefore, the wavelength components which are longer than 65 m, approximately equal to half span 32.5 m, and between 4 and 10 m could be regarded as the healthy components referring to the healthy TFR in Fig. 7.5b. It can be seen from the TFR of the PCCF depicted in Fig. 7.14b that the span harmonic, the half-span harmonic and inter-dropper distance harmonics could be observed with minor frequency deviations. Based on the TFR and the exclusion of healthy components, the irregularity components are identified and circled with dashed lines. Consequently, the irregularity components of the PCCF are obtained using the proposed detection approach and given in Table 7.6. In addition, the midpoint location of each local irregularity is presented for reference.

In spite of the unavailable structural parameters and previous condition of the measured catenary infrastructure, the detected irregularity components could be partly confirmed using the vertical acceleration of pantograph that simultaneously measured with the PCCF. Figure 7.15 depicts the PSD of the vertical acceleration in unit of gravitational acceleration. It is notable that the No. 1, 2, 4 and 5 irregularity components have significant and equivalent peaks in the PSD of pantograph vertical acceleration as marked in the figure, while the No. 3 and 6 ones are relatively unconspicuous. As the direct response of contact wire irregularity through the pantograph slide plate, the pantograph vertical acceleration is caused by vehicle vibration, pantograph-catenary coupling vibration and aerodynamic load, and it certainly has multiple frequency components. Among these components, the

Table 7.6 Detection results of the real-life PCCF signal (Reprinted from Ref. [10], Copyright 2016 with permission from IEEE)

Number	Wavelength (±0.05 m)	Duration [±2, ±2 m]	Midpoint (±2 m)
1	1.09	[46.1, 177.8]	112.0
2	1.82	[174.8, 195.2]	184.9
3	2.04	Global	157.5
4	2.70	[177.3, 278.5]	228.1
5	12.82	Global	157.5
6	20.41	[0, 143.6]	67.7

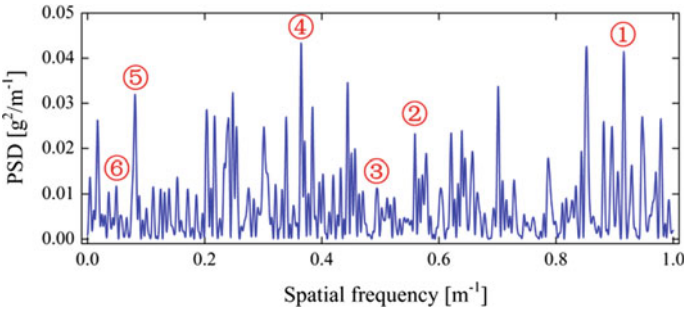

Fig. 7.15 PSD of the vertical acceleration of pantograph (Reprinted from Ref. [10], Copyright 2016 with permission from IEEE)

identification of the exactly same irregularity components contained in the corresponding PCCF can verify the detection results listed in Table 7.6 to a certain extent.

7.5 Summary

The wire irregularity of contact line is one of important factors that influence the current collection quality and stationary operation of trains. PCCF is the most important indicator that estimates the dynamic interaction between pantograph and catenary. In this chapter, first, the times-frequency distributions of PCCF based on different TFRs are analyzed and discussed in detail. The detection of contact wire irregularity in railway catenary is presented. The ZAMD is selected as the best candidate for the quadratic TFR of PCCF. Second, the detection approach description based on ZAMD is presented and the whole detection frame is given. In the end, the detection approach is demonstrated in detail. The quadratic TFRs of healthy and unhealthy PCCF signals show that the wavelengths of contact wire irregularity can be reflected in the TFR. The distance duration of irregularity components can be localized in meter accuracy using the proper modification depending on the irregularity wavelengths. Overall, the approach shows the promising application in contact wire irregularity detection and localization.

Furthermore, the results suggest further improvement in localization accuracy and short-duration irregularity detection in low-frequency range. For example, in order to enhance the reflection of contact wire irregularities in the procedure of preprocessing, the low-frequency energy of PCCF signals can be weakened. In order to enhance the energy of the irregularity components, the frequency components corresponding to catenary structure parameters can be eliminated. Through using a more suitable time–frequency distribution, the time–frequency resolution of the TFR of PCCF signals can be improved.

References

1. Collina A, Fossati F, Papi M et al (2007) Impact of overhead line irregularity on current collection and diagnostics based on the measurement of pantograph dynamics. Proc Inst Mech Eng Part F J Rail Rapid Transit 221(4):547–559
2. Zhang W, Mei G, Wu X et al (2002) Hybrid simulation of dynamics for the pantograph-catenary system. Veh Syst Dyn 38(6):393–414
3. Bucca G, Collina A (2009) A procedure for the wear prediction of collector strip and contact line in pantograph–catenary system. Wear 266(1):46–59
4. Vo Van O, Massat JP, Laurent C et al (2014) Introduction of variability into pantograph–catenary dynamic simulations. Veh Syst Dyn 52(10):1254–1269
5. Cohen L (1995) Time-frequency analysis. Prentice hall
6. Zhao Y, Atlas LE, Marks RJ (1990) The use of cone-shaped kernels for generalized time-frequency representations of nonstationary signals. Acoust Speech Signal Process IEEE Trans 38(7):1084–1091
7. Jones DL, Parks TW (1992) A resolution comparison of several time-frequency representations. IEEE Trans Signal Process 40(2):413–420
8. Liu Z, Hou Y, Han Z et al (2013) Analysis on dynamic characteristics of high-speed railway catenary based on wind filed simulation. J China Railway Soc 35(11):21–28
9. Kim J (2007) An experimental study of the dynamic characteristics of the catenary-pantograph interface in high speed trains. J Mech Sci Technol 21(12):2108–2116
10. Wang H, Liu Z, Song Y, Lu X, Han Z, Zhang J, Wang Y (2016) Detection of contact line irregularities using a quadratic time-frequency representation of the pantograph-catenary contact force. Instrum Measur IEEE Trans. Available: http://dx.doi.org/10.1109/TIM.2016.2518879
11. Bruni S, Ambrosio J, Carnicero A et al (2015) The results of the pantograph–catenary interaction benchmark. Veh Syst Dyn 53(3):412–435
12. European Committee for Electrotechnical Standardization (2002) Railway Applications—Current Collection Systems—Validation of simulation of the dynamic interaction between pantograph and overhead contact line. European Standard EN 50318. CENELEC
13. Zhang W, Shen Z, Zeng J (2013) Study on dynamics of coupled systems in high-speed trains. Veh Syst Dyn 51(7):966–1016

Chapter 8
Estimation of Catenary Based on Spectrum

8.1 Introduction

The track spectrum is the PSD of track irregularities. Track irregularities are classified into several types according to different geometric shapes and positions, such as alignment irregularity, level irregularity, vertical irregularity, gauge irregularity and so forth. From another perspective, they can also be classified into short wavelength and long wavelength irregularities, or periodicity and aperiodicity irregularities through frequency identifications [1]. In practice, instead of using the PSD of track irregularities directly, appropriate formulae are usually used to fit the PSD results and the smoother curves as final track spectrum are obtained [2]. The adopted formulae have various forms for certain type of irregularity in different regions. For example, in Japan, the fitting formula applied to all kinds of irregularities is

$$G(f) = Af^{-1} \tag{8.1}$$

where $G(f)$ is the fitting PSD, f is the spatial frequency, and A is the fitting parameter. In Germany, the fitting formulae for vertical track irregularity, alignment track irregularity and level track irregularity were proposed in the 1980s respectively as follows [3, 4].

$$S_v(\Omega) = \frac{A_v \Omega_c^2}{(\Omega^2 + \Omega_r^2)(\Omega^2 + \Omega_c^2)} \tag{8.2}$$

$$S_a(\Omega) = \frac{A_a \Omega_c^2}{(\Omega^2 + \Omega_r^2)(\Omega^2 + \Omega_c^2)} \tag{8.3}$$

Z. Liu, *Detection and Estimation Research of High-speed Railway Catenary*,
Advances in High-speed Rail Technology, DOI 10.1007/978-981-10-2753-6_8

$$S_l(\Omega) = \frac{A_v b^{-2} \Omega_c^2 \Omega^2}{(\Omega^2 + \Omega_r^2)(\Omega^2 + \Omega_c^2)(\Omega^2 + \Omega_s^2)} \tag{8.4}$$

where $S(\Omega)$ is the fitting PSD, Ω is the spatial circular frequency, b is half of the nominal rolling distance, Ω_c, Ω_r and Ω_s are cutoff frequencies, and A_a and A_v are roughness coefficients for the amplitude of PSD.

In the 1990s, modifications were made to A_a and A_v due to the improvement of track construction. Since then, Eqs. (8.2), (8.3) and (8.4) are widely used in the track spectrum study of European high-speed railway. In general, there are two aspects of applications of the track spectrum. On the one hand, the track condition could be evaluated by comparing the present track spectrum with standard spectrum that is previously established using measurement data. The comparing approach can be an interval criterion by setting an upper and a lower boundary or ranking several boundaries in the standard track spectrum. It provides certain reference and convenient for the track estimation and maintenance. On the other hand, the track spectrum could be used in railway vehicle related study, especially in wheel-track interactions. It is the input function for the theoretical and experimental study of wheel dynamic responses [5].

With the rapid increase of train speed, the early-stage catenary defect will be magnified under high-speed pantograph contact, making the catenary system more vulnerable than ever. High-speed railway catenary requires more advanced estimation method than conventional methods to facilitate the improvement of catenary performance. The conventional threshold criterion and indicators are more likely to be observable after the catenary condition has deteriorated. As a frequency-domain characterization, the track spectrum is proven to be reliable in track condition estimation. Similarly, the catenary spectrum is presented in this chapter as the estimation methodology for catenary. But different from the track irregularity, contact line irregularity is various depending on the design of catenary structure, especially the geometric parameters of contact line, shown in Fig. 8.1. Meanwhile, it is also highly sensitive to external excitations due to the nonlinearity and flexibility of catenary structure. Therefore, the estimation of catenary based on spectrum should consider the current structure of catenary and the influence of external excitations. Thus, as discussed in Chap. 1, the catenary spectrum includes both static and dynamic estimations, which respectively adopt the PSDs of the static catenary data and the dynamic catenary data.

The PSD of static catenary data is similar to the PSD of track irregularity, namely the track spectrum. By mapping the spatial position of contact line into three coordinate planes to quantify these characteristics, the three-dimensional positions of contact line can be described as the height, stagger and longitudinal direction. Thus, three specific types of contact line irregularities that are height irregularity, stagger irregularity and longitudinal irregularity are obtained corresponding to the three-dimensional positions. In a smaller dimension, the irregularity of contact line wear is defined as the distribution of the loss of contact line section

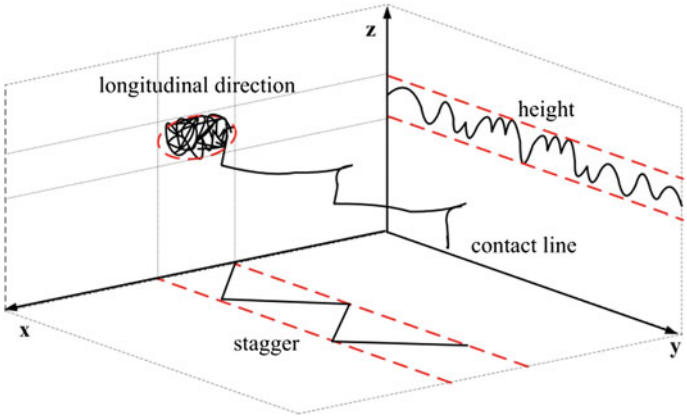

Fig. 8.1 Schematic of the *contact line* spatial position

along the longitudinal direction. The PSDs of all types of contact line irregularity can adequately reflect the static characteristic of contact line.

The PSD of dynamic catenary data mainly include the PSDs of pantograph-catenary contact force (PCCF), pantograph acceleration and dynamic lifting displacement of contact line and pantograph. The PSDs of dynamic data should consider the corresponding catenary structure, operating condition and pantograph type when applied to a certain railway line.

Referring to relevant researches on the track spectrum, the significances and potential applications for the study of catenary spectrums include

(1) For the acceptance and maintenance of catenary, the catenary spectrum can provide more advanced references to estimate the catenary condition comparing with time-domain indicators. It is capable of reflecting early-stage irregularities of contact line as they evolve over time.
(2) For the design of catenary, the catenary spectrum can facilitate the catenary structure optimization, on condition that the corresponding operation condition and pantograph type are determined.
(3) For the studies of pantograph-catenary interaction, the catenary spectrum under different operating conditions can be the input functions for the theoretical and experimental study of pantograph dynamic responses.
(4) The catenary spectrums can be inverted to generate healthy or unhealthy catenary data as data sources for relevant numerical simulations.

At present, PSD analysis is a frequently adopted method to analyze the pantograph-catenary dynamic interaction in the frequency domain [6–10]. It can characterize the both amplitude and frequency information contained in catenary data. Some physical meanings reflected by the PSDs are also discussed. With the help of previous researches, there is certain significance to propose the catenary

spectrum as an alternative for advanced catenary estimation. Since the dynamic catenary data are the direct reflection of the catenary operation performance, this chapter mainly introduces and discusses the catenary estimation based on the PSDs of dynamic data.

8.2 PSD Estimation

The PSD is a statistical function that characterizes the energy distribution of a stationary stochastic process in the frequency domain. In engineering studies, it is frequently adopted to observe the frequency-domain characteristics of a target signal for purpose of fault diagnose and performance evaluation. In the case of catenary data analysis, both the amplitude and frequency information are important for data characterization. The PSD can meet the requirements and fully reflect the statistical characteristic of catenary data. In addition, the PCCF is not always absolute ergodic, especially at restriction point, anchoring region and so on. But in general, long-duration PCCF can be regarded as weak stationary process and applied to PSD analysis.

In track spectrum estimation, the periodogram method and the maximum entropy method are mostly adopted. The periodogram method is a conventional spectrum estimation method based on the Fourier transform. Because it assumes that the autocorrelation function of a signal is equal to zero outside the observed data, and the spectrum resolution of periodogram method is relatively low. The modern spectrum method is commonly based on the parametric model of stochastic process. It can provide much higher frequency resolution than conventional method. Thus, to obtain the accurate PSDs of catenary data, the modern estimation method based on the autoregressive (AR) model is adopted for the PSD analysis of catenary data.

Concretely, assuming a discrete stochastic process has a number N of samples $x(0), x(1), \ldots, x(N-1)$, the periodogram method directly performs the Fourier transform on the process as follows.

$$X(\omega) = \sum_{n=0}^{N-1} x(n) e^{-j\omega n} \tag{8.5}$$

The PSD of the periodogram method is computed by

$$P_x(\omega) = \frac{1}{N} |X_N(\omega)|^2 = \frac{1}{N} \left| \sum_{n=0}^{N-1} x(n) e^{-j\omega n} \right|^2 \tag{8.6}$$

If the discrete stochastic process $\{x(n)\}$ yields the linear difference equation

$$x(n) + \sum_{i=1}^{p} a_i x(n-i) = e(n) + \sum_{i=1}^{q} b_j e(n-j) \tag{8.7}$$

where $e(n)$ is the discrete white noise. Then, the process $\{x(n)\}$ is regarded as the ARMA (Autoregressive Moving Average) process. The coefficients $a_1, \ldots, a_p$ and $b_1, \ldots, b_q$ are for the AR (Autoregressive) process and MA (Moving Average) process, respectively. p and q are the order of AR and MA process, respectively. According to the Wold decomposition theorem, ARMA and MA processes can be described by the AR process, namely

$$\sum_{k=0}^{p} a_k x(n-k) = e(n) \tag{8.8}$$

This is the standard AR model. The PSD estimation is actually the estimation of Eq. (8.8). It is essentially the problem of solving the Yule-Walker equation

$$R = -R_x^{(p)} A \tag{8.9}$$

where $A = (a_1, a_1, \ldots, a_p)^T$, $R = (R_x(1), R_x(2), \ldots, R_x(p))^T$ and

$$R_x^{(p)} = \begin{bmatrix} R_x(0) & R_x(1) & \cdots & R_x(p-1) \\ R_x(1) & R_x(0) & \cdots & R_x(p-2) \\ \vdots & \vdots & \ddots & \vdots \\ R_x(p-1) & R_x(p-2) & & R_x(0) \end{bmatrix} \tag{8.10}$$

is the Toeplitz matrix related to the coefficients. In the PSD estimation based on AR model, the selection of order p is of critical importance. If p is too low, the frequency resolution will be low, whereas if p is too high, the statistical stability will be low. Thus, the well-known Akaike's Information Criterion (AIC) is proposed to determine the order p [11]. When the following information criterion function reaches minimum, the value of p is considered the best selection.

$$AIC(p) = \frac{2p}{N} + \ln J(p) \tag{8.11}$$

where $J(p)$ is the quadratic mean function of estimation error. Another popular criterion is the FPE (Final Prediction Error) criterion. The criterion function is defined as

$$FPE(p) = \frac{N+p}{N-p} \cdot \ln J(p) \tag{8.12}$$

Both criterions are equivalent when the number of samples approaches infinite. The determination of order p for the PSD estimation of PCCF signals is discussed below using both criterions. For a brief illustration, the AIC and FPE values are normalized as follows.

$$\begin{cases} AIC_{norm}(i) = \frac{AIC(i) - \min(AIC)}{\max(AIC) - \min(AIC)} \\ FPE_{norm}(i) = \frac{FPE(i) - \min(FPE)}{\max(FPE) - \min(FPE)} \end{cases} \tag{8.13}$$

where $\max(\cdot)$ and $\min(\cdot)$ denote the maximum and minimum value of corresponding data series, respectively.

As a result, Fig. 8.2a, b respectively depict the normalized AIC and FPE values of PCCF signals from the same pantograph-catenary simulation but under different operation speeds. It can be seen that the results of AIC and FPE are very similar tendency for the same PCCF signal. In general, each curve experiences a rapid decline when the order is under 20 and becomes almost steady beyond order 30. When the order is above 50, all the PCCF signals reach a steady minimum.

Furthermore, the PCCF simulations under the same catenary structure and operation speed, but using different types of pantograph is carried out. In the simulation, the pantograph is regarded as a three-level lumped mass system depicted in Fig. 8.3. It contains three lumped masses M1, M2, and M3 and spring-damper elements between the masses M1 and M2 and M2 and M3 and M3 and the ground. Moreover, three small frictional resistances F1, F2, and F3, which are not strictly necessary depending on the type of the pantograph, are added to each lumped mass to simulate the actuation of the pantograph. The physical parameters of four types are pantograph, namely the SBS81, DSA250, DSA380 and SSS400+ pantographs are given in Table 8.1. The number in the model name represents the designed operation speed of the pantograph. Figure 8.4a, b respectively depict the normalized AIC and FPE values of PCCF signals from the same catenary structure but different pantograph types. Comparing with in the case of different operation speed, the same tendency can be observed from the results of AIC and FPE.

In the case of real-life PCCF measurement data, Fig. 8.5 depicts the normalized AIC and FPE values of PCCF signals measured from the Hukun up line, JingGuang up line and JingGuang down line. It can be seen that, no matter which criterion is adopted, the real-life signals can reach a steady minimum faster than simulation results around order 30. It can simplify the determination of AR model order in practice.

To sum up, the AIC and FPE have equivalent result when dealing with the selection of AR model order of PCCF. Both of them can be adopted in the PSD estimation of PCCF signals based on AR model. Once the model order is obtained, the PSD estimation of PCCF can be realized by solving Eq. (8.9).

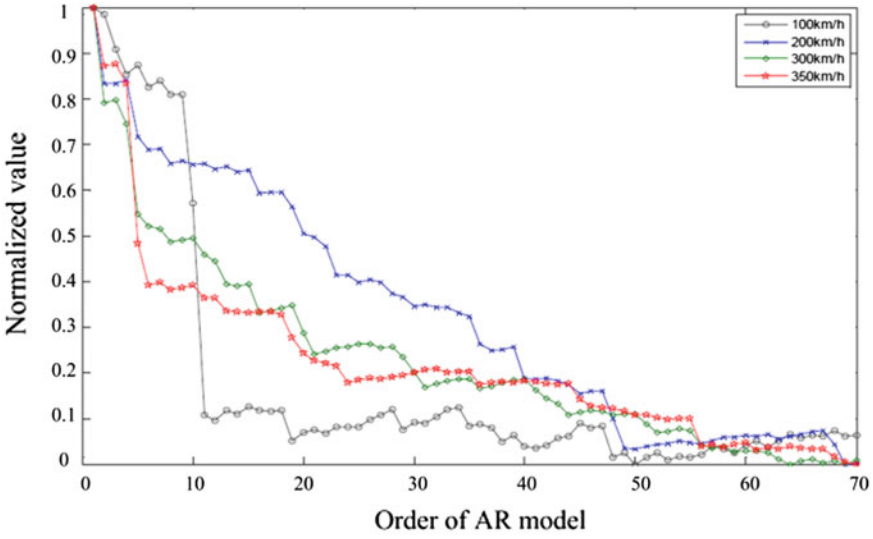

(a) Normalized AIC values w.r.t. the order of AR model.

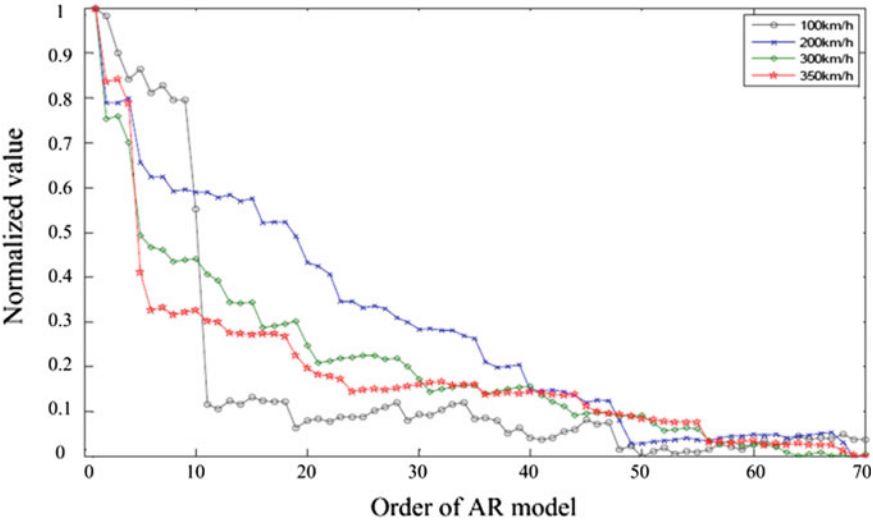

(b) Normalized FPE values w.r.t. the order of AR model.

Fig. 8.2 Normalized criterion values of PCCF under different operation speeds

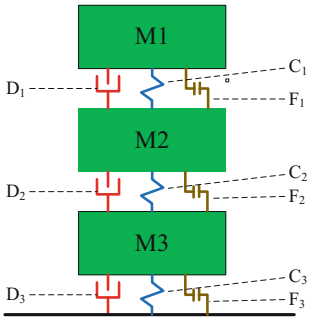

Fig. 8.3 Three-level lumped mass model of pantograph

Table 8.1 Physical parameters of four types of pantograph

Physical parameters	SBS81	DSA250	DSA380	SSS400+
M1 (kg)	10.5	7.51	7.12	6.05
M2 (kg)	8.53	5.855	6.0	6.4
M3 (kg)	10.57	4.645	5.8	14
C1 (N/m)	8400	8380	9430	5813
C2 (N/m)	60,000	6200	14,100	13,600
C3 (N/m)	0	80	0.1	0
D1 (Nm/s)	48	0	0	0
D2 (Nm/s)	0	0	0	0
D3 (Nm/s)	300	70	70	64.9
F1 (N)	0	0	0.5	3
F2 (N)	0	0	3.5	8.5
F3 (N)	6	0	3.5	8.5

8.3 PSD and Catenary Performance

To use the PSDs of catenary data for catenary estimation, the relations between the PSDs and the catenary performance under various circumstances should be understood first. Based on one of the most important dynamic catenary data, namely the PCCF from simulations and measurements, this section investigates the correlation between the PSD and different railway line, operation speed, pantograph type and environmental wind speed.

8.3.1 PSD of PCCF and Railway Line

As an example, two segments of PCCF measurement data (see Fig. 8.6) from the HuKun railway line and the JingHu railway line are adopted for PSD analysis. The two PCCF signal are measured by the same measuring system and under the same

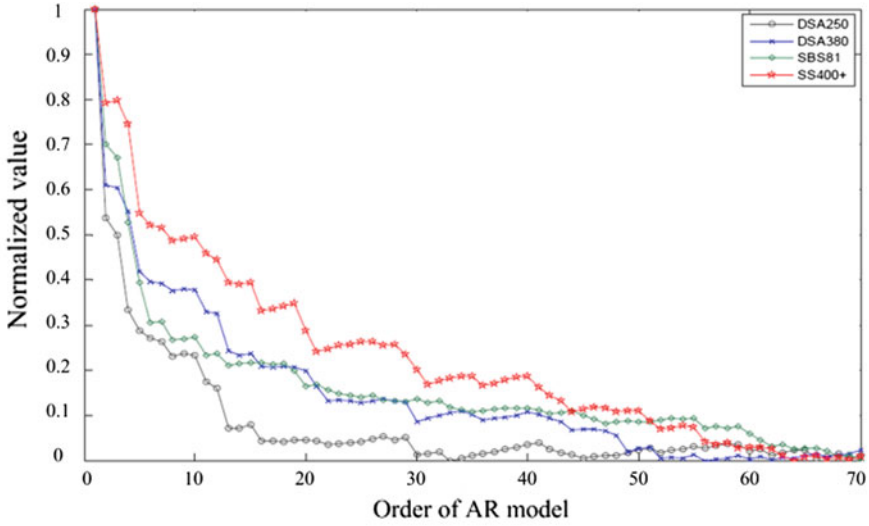

(a) Normalized AIC values w.r.t. the order of AR model.

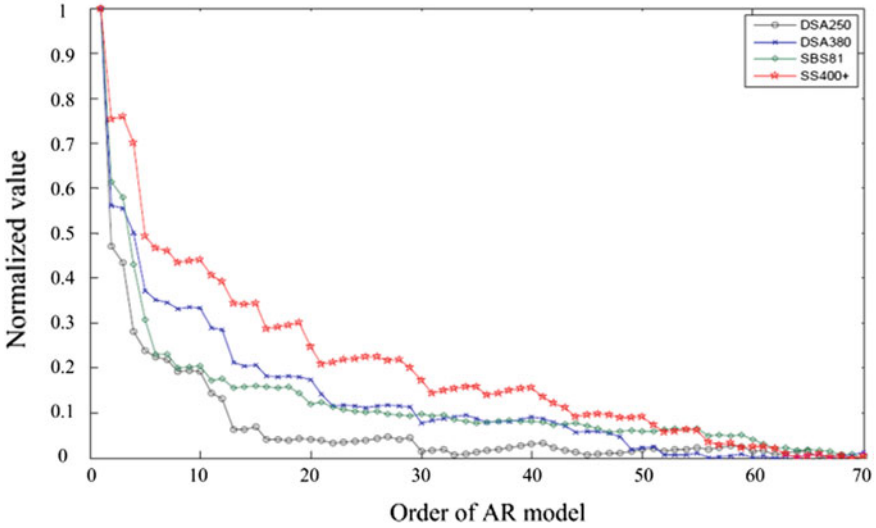

(b) Normalized FPE values w.r.t. the order of AR model.

Fig. 8.4 Normalized criterion values of PCCF with different pantograph type

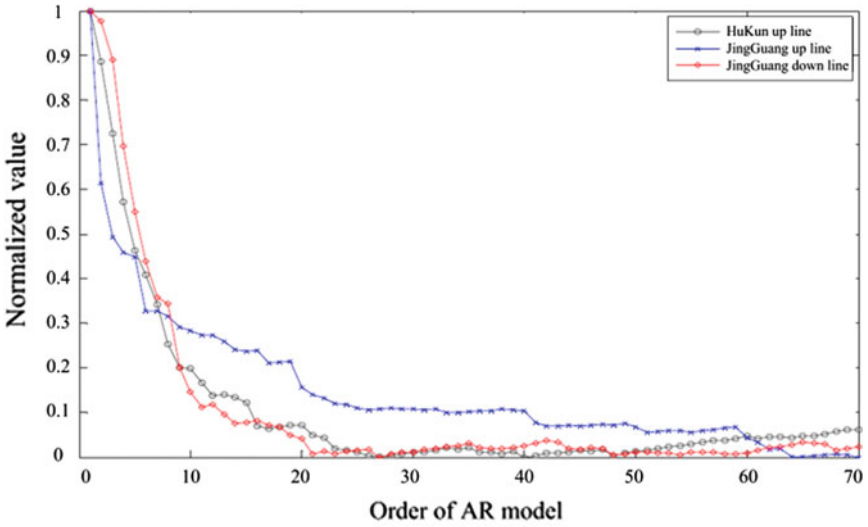

(a) Normalized AIC values w.r.t. the order of AR model.

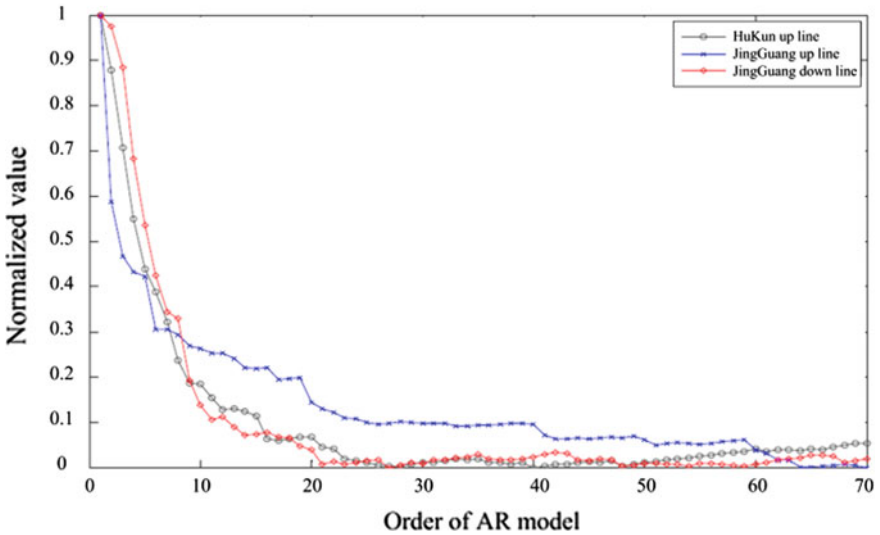

(b) Normalized FPE values w.r.t. the order of AR model.

Fig. 8.5 Normalized criterion values of PCCF from different railway line

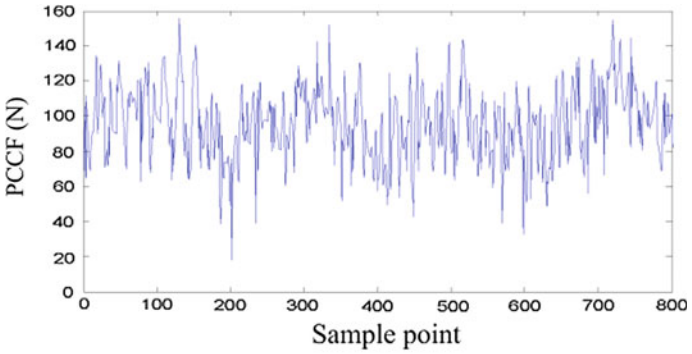

(a) PCCF from HuKun railway line.

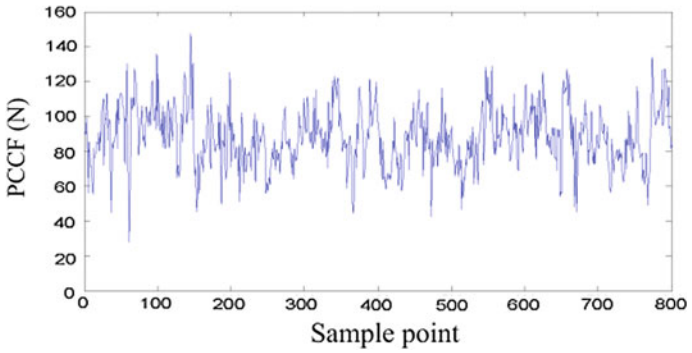

(b) PCCF from JingHu railway line.

Fig. 8.6 PCCF measurement data under 100 km/h operation speed

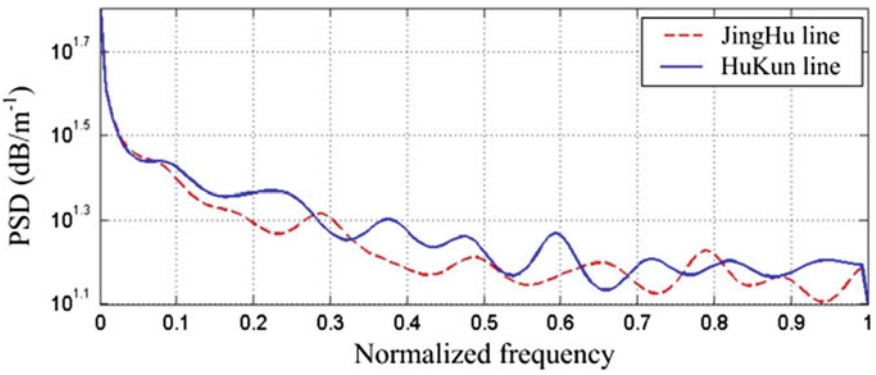

Fig. 8.7 Comparison of the PSDs of PCCF signals from different railway line

operation speed of 100 km/h. Through the PSD estimation based on AR model, the PSDs of the two signals are obtained and depicted in Fig. 8.7 [12].

It can be seen that, under the same operation speed, the PSDs of PCCF from the two railway lines are different. The difference is mainly caused by the different catenary structure, service duration and maintenance level. In addition, although the fluctuations of the PSDs do not match, the overall trends of them are very similar. It indicates that for different railway lines, if the operation speed for measurement is same, the catenary estimation based on PCCF can focus on the fluctuation regardless of the speed, which can be one of the properties and advantages of the utilization of PSD.

8.3.2 PSD of PCCF and Operation Speed

For the same railway line, the PCCF signals under different operation speeds are different. Figure 8.8a, b depicts two segments of PCCF signal measured from the

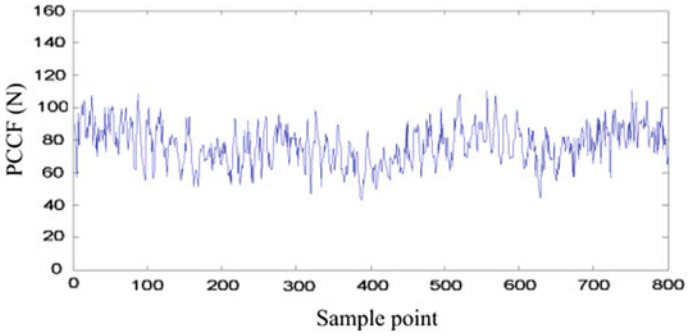

(a) PCCF signal under 50km/h operation speed

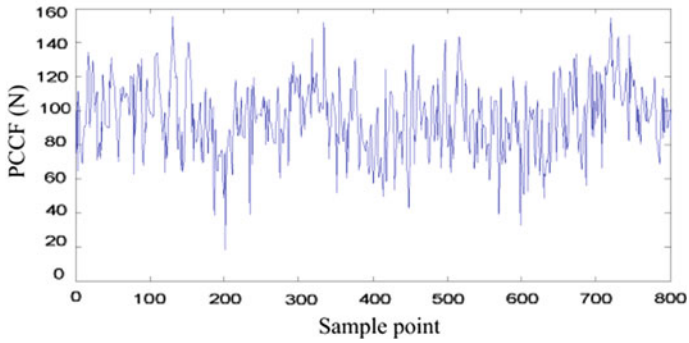

(b) PCCF signal under 100km/h operation speed

Fig. 8.8 PCCF measurement data from the Hukun railway line

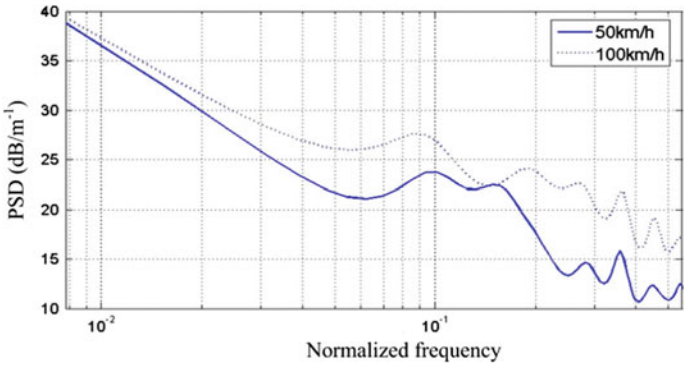

Fig. 8.9 Comparison of the PSDs of PCCF signals under different operation speed

HuKun railway line under the operation speed of 50 and 100 km/h, respectively. The PSDs of the two signals are depicted in Fig. 8.9.

In Fig. 8.9, it can be seen that the general amplitude of the PSD of PCCF under 100 km/h speed is higher than the one under 50 km/h, which can be regarded as the effect of increasing extent of pantograph-catenary vibration as the speed increases. However, the fluctuations of the two PSDs are quite similar. The peaks and valleys of the PSDs appear at the same or near frequency. In Fig. 8.10, the same phenomenon can be obtained from the PSDs of simulation PCCF signals under different speed. These results indicate that for the same railway line, the higher operation speed causes higher amplitude of PSD, which is a property that can be used to classify the standard spectrums into different level by speeds. It means that

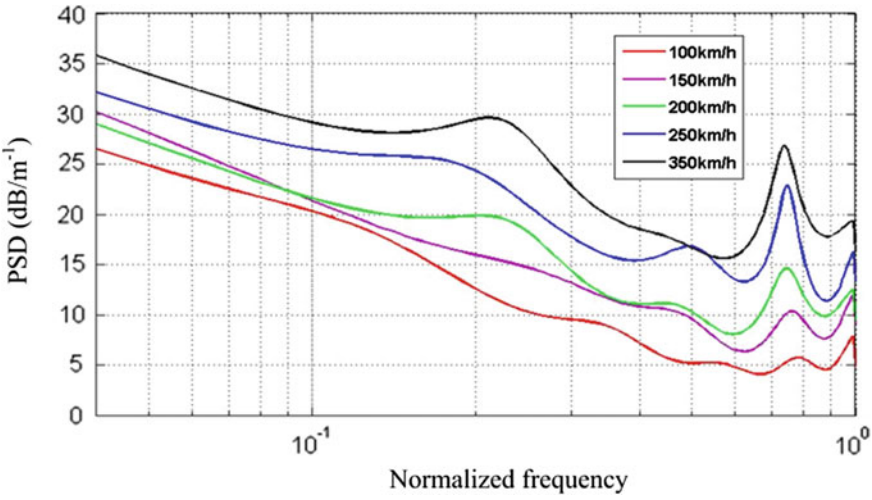

Fig. 8.10 Comparison of the PSDs of simulation PCCF under different speed

for a newly constructed catenary system, the standard spectrums of PCCF can be established for different speed level and employed for future comparison to facilitate maintenance decision.

8.3.3 PSD of PCCF and Pantograph Type

To investigate the influence of pantograph type on the PSD of PCCF, corresponding simulations are carried out using the DSA250 and SSS400+ pantograph given in Table 8.1 with the same catenary structure. As a result, the PCCF signals under the operation speed of 300 km/h are depicted in Fig. 8.11a, b. Figure 8.12a, b depicts the PSD of the PCCF using the two types of pantograph, respectively.

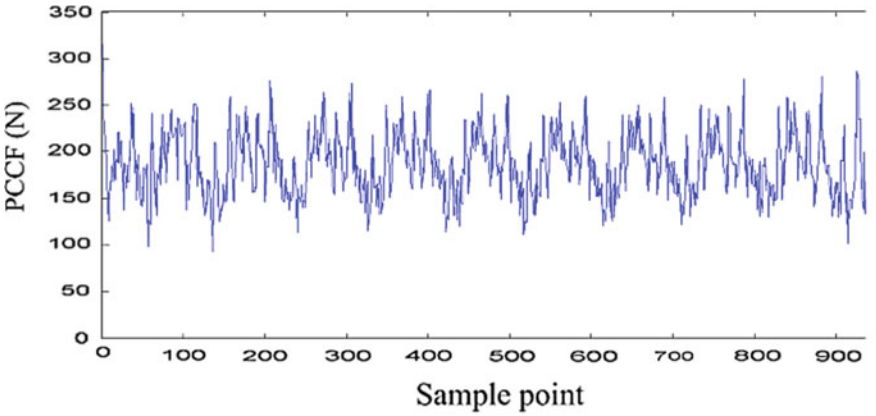

(a) PCCF signal using the DSA250 pantograph.

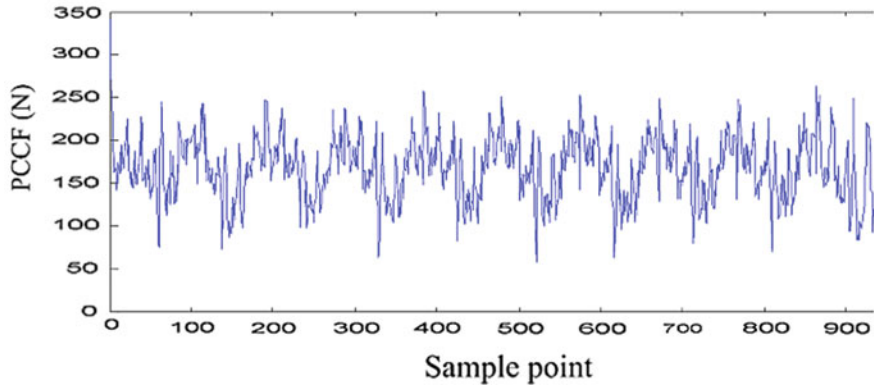

(b) PCCF signal using the SSS400+ pantograph.

Fig. 8.11 Simulation PCCF signals using different pantograph

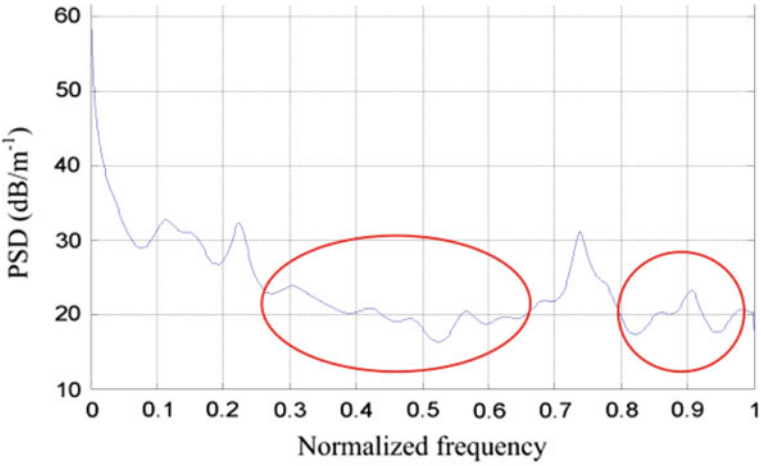

(a) PSD of PCCF using the DSA250 pantograph.

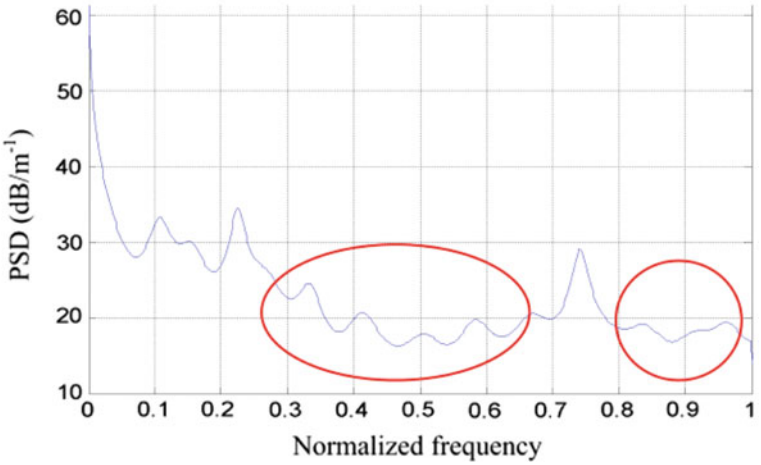

(b) PSD of PCCF using the SSS400+ pantograph.

Fig. 8.12 PSDs of PCCF signals using different pantograph type

In Fig. 8.11, it can be seen that in the time domain, the difference of the two PCCF signals is insignificant. It is hard to decide which pantograph generates the better current collection quality based on just the PCCF itself. However, Fig. 8.12 shows that the different type of pantograph leads to different PSD of PCCF for the same railway line. The PSD of PCCF using the SSS400+ pantograph has better curve smoothness than the other, especially in the high-frequency range, which means less intense high-frequency vibration between pantograph and catenary.

Thus, the PSD of PCCF can be a reference for the performance evaluation of various combinations of pantograph-catenary coupling.

8.3.4 PSD of PCCF and Wind Load

Based on wind simulation technique, the simulation of pantograph-catenary interaction under wind load can be realized. Since the height of catenary structure generally remains the same along a railway line, the influence of height variation in wind simulation can be ignored. Thus, the well-known Davenport wind spectrum [13] is adopted for the stochastic wind simulation in catenary structure. The spectrum is the frequency-domain characterization of observed stochastic wind and commonly used in structural response analysis. It is defined as

$$\begin{cases} S_D(f) = 4kv_{10}^2 \dfrac{x}{n(1+x^2)^{4/3}} \\ x = \dfrac{1200f}{v_{10}} \end{cases} \tag{8.14}$$

where $S_D(f)$ is the wind speed spectrum, f is the frequency, k is the coefficient of terrain roughness depending on the terrain where the wind occurs, v_{10} is the reference mean wind speed at 10 m height depending on the area where the wind occurs, and x is a dimensionless frequency. The stochastic wind speed $v(x,t)$ at a certain spatial position x can be obtained by reversing the spectrum to the time domain using methods such as harmonic superposition, inverse Fourier transform and so on. According to the load code for the design of building structures [14] of China, the wind load exerting on a structural point can be computed by

$$F_w(x,t) = \frac{1}{1600}\beta_z u_s u_z A[v(x,t)]^2 \tag{8.15}$$

where β_z is the wind vibration coefficient, u_z is the variation coefficient of wind pressure, A is the windward area of structure and u_s is the shape factor of wind load, which is considered to be 1.0 for the messenger and contact lines and 1.3 for other supporting devices. Here, the midpoints and both ends of messenger and contact lines in every span are selected to exert the wind loads.

The simulation of pantograph-catenary interaction under the load of stochastic wind with a mean speed of 20 m/s is carried out. Figure 8.13a, b depict the PCCF without and with the wind load exerting on the catenary, respectively [15]. It can be seen that the wind has a severe impact on the interaction that leads to the irregular fluctuation of PCCF.

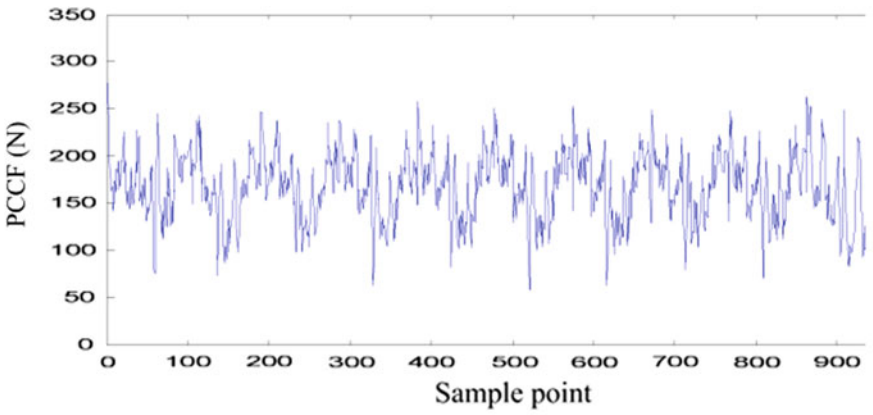

(a) Normal PCCF.

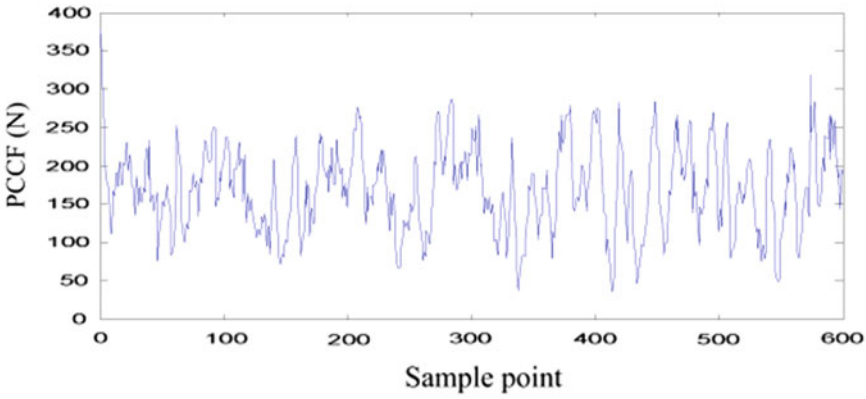

(b) PCCF under wind load

Fig. 8.13 PCCF with and without the influence of wind load on catenary

Figure 8.14a, b depict the PSDs of the two PCCF signals shown in Fig. 8.13. Comparing with the PSD of normal PCCF, the PSD of PCCF influenced by the high-speed wind is similar above normalized frequency of 0.3, but different in the low-frequency range. As circled in the two figures, the spectrum energy around the normalized frequency of 0.1 becomes larger due to the influence of wind, which indicates that the wind largely increases the overall fluctuation of PCCF. The low-frequency parts in the PSD of PCCF can be indicators for the impact of wind on the pantograph-catenary interaction and provide references for the anti-wind performance of catenary.

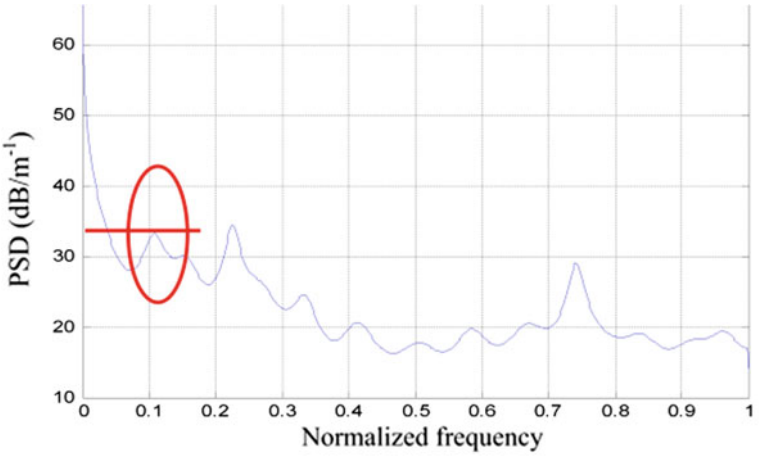

(a) PSD of normal PCCF

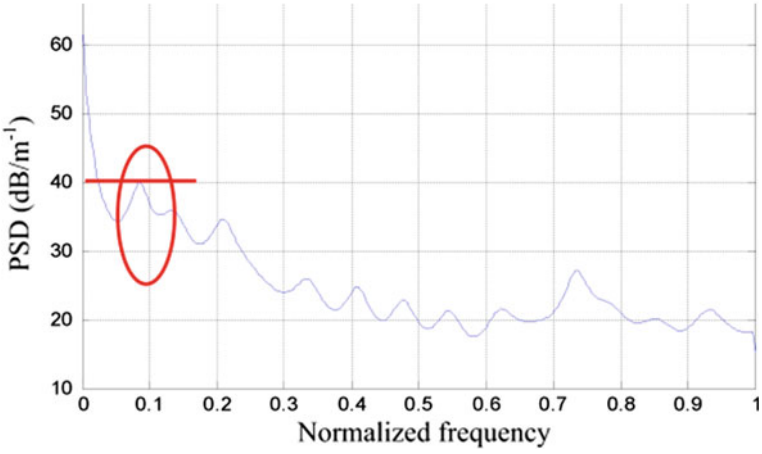

(b) PSD of PCCF under the wind load with 20m/s speed

Fig. 8.14 PSDs of PCCF with and without the influence of wind load

8.4 PSD and Pantograph-Catenary Coupling Performance

The pantograph-catenary couple determines the dynamic performance of pantograph-catenary sliding contact. In theoretical study of the sliding contact, the PCCF computation is commonly realized by adding a virtual spring between the pantograph head and contact wire. As shown in Fig. 8.15, the pantograph and catenary are coupled by the virtual spring with contact stiffness K_C.

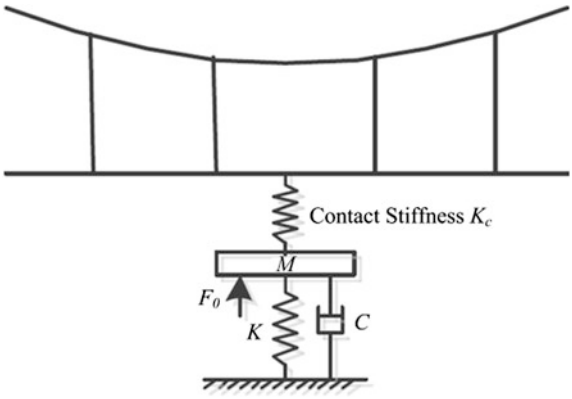

Fig. 8.15 Schematic of the PCCF computation

The PCCF $F_c(t)$ can be computed by

$$F_c(t) = K_c[y_h(t) - y_c(x,t)] \tag{8.16}$$

where $y_h(t)$ is the vertical displacement of the pantograph head, $y_c(x,t)$ is the vertical displacement contact wire, x is the longitudinal position of the contact and t is the computational time. From Eq. (8.16), it can be seen that the fluctuation of PCCF is due to the displacement difference between the contact wire and the pantograph [16]. The pressing and stretching tendencies caused by the nonsynchronous contact wire and pantograph head vibration lead to the repeating fluctuation of PCCF. Thus, the pantograph-catenary coupling performance can be analyzed based on the dynamic difference of contact wire and pantograph head vertical displacement.

8.4.1 PSDs of Vertical Displacements

The contact wire vertical displacement can be essentially expressed as

$$y_c(x,t) = \sum_m A_m \sin\frac{m\pi}{L} \tag{8.17}$$

where m is the number of harmonics, A_m is the amplitude of harmonic and L is the length of anchoring section. The pantograph head has certain following feature during the pantograph-catenary interaction, which makes the pantograph head vertical displacement has the characteristic similar to the contact wire vertical displacement. Therefore, the displacement difference can be characterized in the frequency domain through PSD analysis. The comparison of the PSDs of the displacements can describe the following feature of pantograph head along the entire

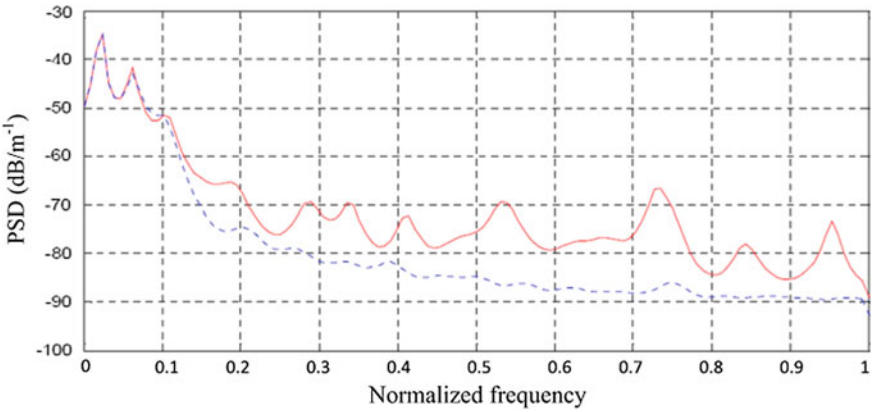

Fig. 8.16 PSDs of the vertical displacements of contact wire (*solid line*) and pantograph head (*dashed line*)

frequency band, which provide a way for evaluating the pantograph-catenary coupling performance.

Figure 8.16 depicts the PSDs of contact wire and pantograph head vertical displacement under 300 km/h operation speed. It can be seen that the two PSDs are identical below the normalized frequency of 0.1, which indicates that the coupling performance is good in general. As the frequency increases, the two PSDs start to split, which indicates that the fluctuation of PCCF is mainly caused by the displacement differences in low and medium frequency ranges. Although there are energy differences in low and medium frequency ranges, the energy differences are relatively low comparing with the low-frequency energy. So, the PCCF fluctuations caused by the energy differences have small amplitudes. They are added to the low-frequency and trend terms of PCCF and results in the complex PCCF signal.

Like the PCCF, the PSDs of the two types of vertical displacement also depend on the different operation conditions. The following sections investigate the correlations between the PSDs and operation speed and pantograph type.

8.4.2 PSDs of Vertical Displacements and Operation Speed

The train operation speeds for different railway line are different. Also, the inspection vehicles have different speed depending on the specific measuring system and measurement condition. Thus, the operation speed is an important factor that should be considered for evaluating the pantograph-catenary coupling performance. Figure 8.17a, b respectively depict the PSDs of the vertical displacement of contact wire and pantograph head under the operation speed of 100, 200, 300 and 350 km/h. In Fig. 8.17a, the high-frequency fluctuations of the PSDs are similar in peaks and valleys, which indicate that when under the interaction with the same

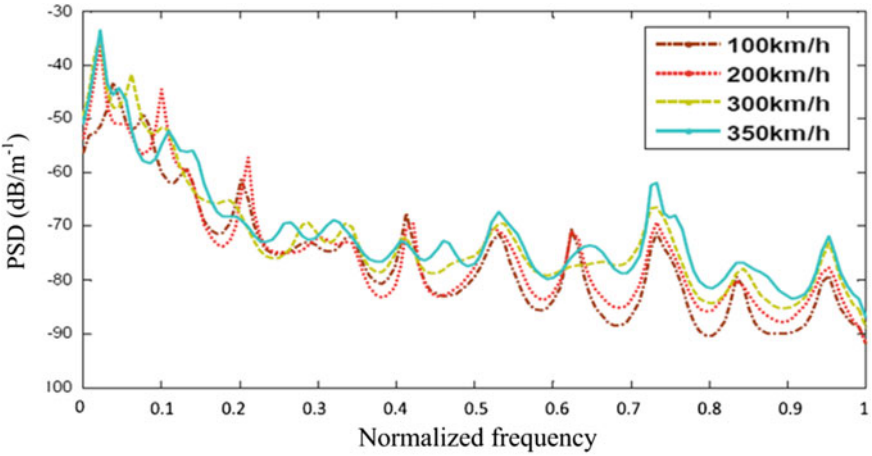

(a) PSDs of contact wire vertical displacement.

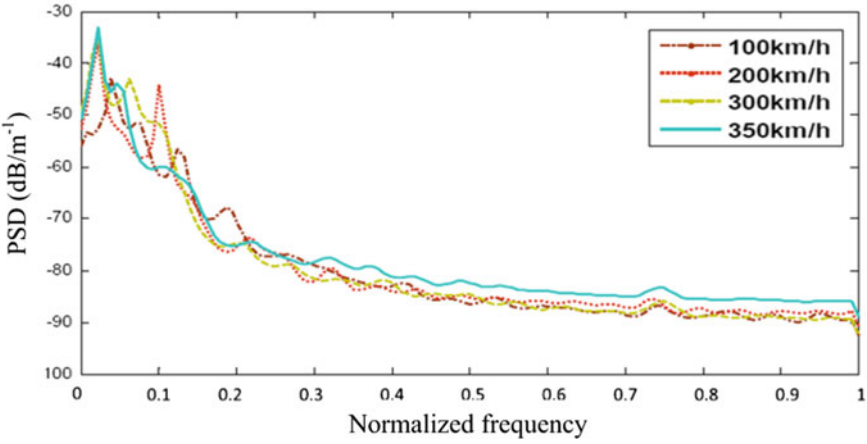

(b) PSDs of pantograph head vertical displacement.

Fig. 8.17 PSDs of vertical displacements under different operation speed

pantograph, the contact wire has similar response for the pantograph impact under different speed. However, in the low-frequency range, as the speed increases, the highest energy caused by the spans appears at a lower frequency with a higher energy, which shows that the contact wire vibration is sensitive to the catenary structure under high operation speed. The higher speed causes more severe low-frequency vibration of contact wire. Comparing with Fig. 8.17a, the PSDs of pantograph head vertical displacement are less sensitive to the operation speed, because the pantograph head is much more stable than contact wire due to the

support of pantograph frame, especially in the medium and high frequency ranges where the spectrums are very smooth [16]. Therefore, the PSDs of contact wire vertical displacement are sensitive to the operation due to the long-span and large-tension structure of catenary.

From above, it can be concluded that the operation speed has more influence on the contact wire than the pantograph head. It conforms to field experiences and reflects the importance of catenary optimization for speed upgrade. In general, the operation speed mainly influences the energy level of the PSDs of vertical displacements. Thus, if the operation speed is the same, the comparison of the fluctuations of PSDs can reveal the frequency-domain characteristics of pantograph-catenary coupling performance.

8.4.3 PSDs of Vertical Displacements and Pantograph Type

Different pantograph types have uneven performances when are coupled with a certain catenary structure. Figure 8.18a, b respectively depict the PSDs of contact wire and pantograph head vertical displacements under 300 km/h speed with three types of pantograph, namely DSA250, DSA380 and SSS400+ pantographs.

In Fig. 8.18a, the amplitude and fluctuation of the PSDs are very similar with just small energy differences at some frequencies. It indicates that, under the same operation speed, the PSD of contact wire vertical displacement is mainly determined by the catenary structure itself, not the pantograph type. In Fig. 8.18b, the PSDs of pantograph head vertical displacement caused by the three types of pantograph are different in amplitude. The pantograph with higher designed operation speed has higher energy through the entire frequency band, which is a sign of better contact quality according to the following discussion.

Figure 8.19a, b depict the comparison of PSDs of the two types of vertical displacements using the DSA250 pantograph and DSA380 pantograph, respectively. As circled in the two figures, the DSA380 pantograph generates perfect fit in the PSDs of contact wire and pantograph head displacement, which indicates a good coupling performance, whereas the DSA250 pantograph results in small energy differences in the same frequency range. The differences in the fitting of PSDs suggest that the DSA250 pantograph has higher fluctuations in long-wavelength periods than the DSA380 pantograph, which means that, in this case the DSA380 pantograph has a better coupling performance. Also, for the DSA380 pantograph, the separation of the PSDs happens at the normalized frequency of 0.1, while it is 0.083 for the DSA250 pantograph, which shows that the DSA380 pantograph can maintain the good coupling performance in a wider frequency band. In the statistics of the corresponding PCCF signals, the average PCCF is higher for the DSA250 pantograph than for the DSA380 pantograph with 155.4 N against 150.9 N, which agrees with the conclusion from the PSDs comparison.

From the above, due to the difference in physical characteristics, the selection of pantograph type is of great importance for the pantograph-catenary coupling

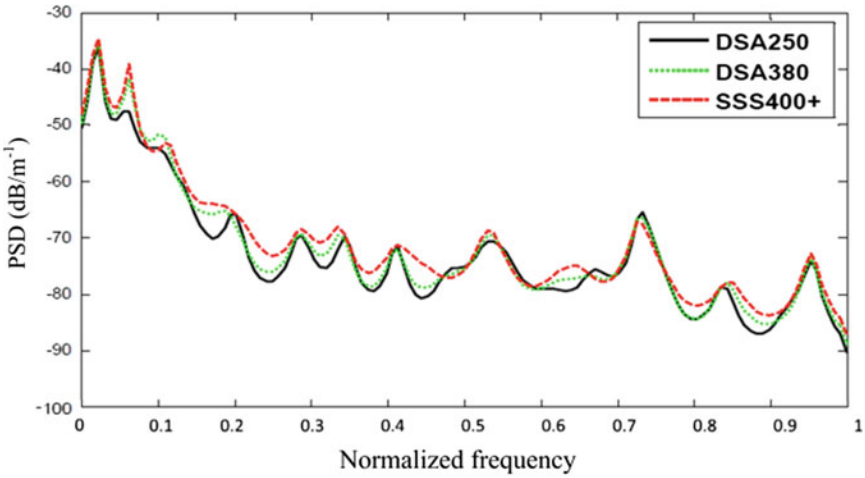

(a) PSDs of contact wire vertical displacement.

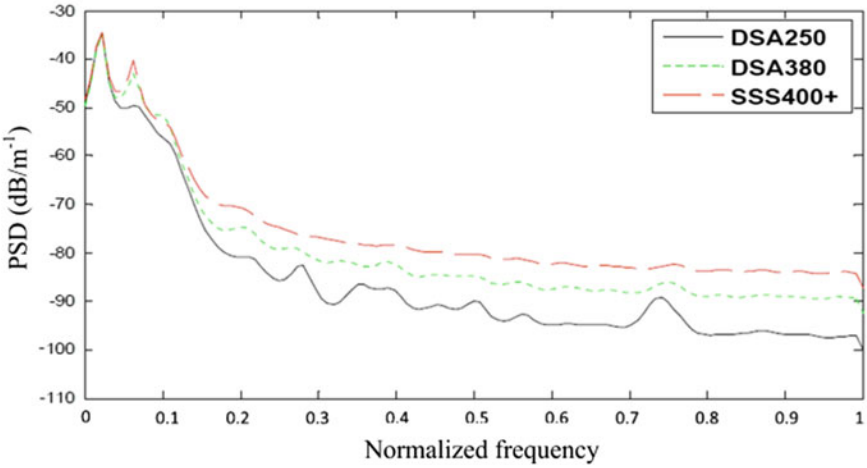

(b) PSDs of pantograph head vertical displacement.

Fig. 8.18 PSDs of vertical displacements using different pantograph type

performance. For the convenience of the utilization of the PSDs correlation, the cross correlation coefficient between the PSD of contact wire and pantograph head vertical displacements is proposed as [16]

$$C_s = \frac{\sum (S_c(i) - \overline{S_c(i)}) \cdot \sum (S_p(i) - \overline{S_p(i)})}{\sqrt{\sum (S_c(i) - \overline{S_c(i)})^2} \cdot \sqrt{\sum (S_p(i) - \overline{S_p(i)})^2}} \tag{8.18}$$

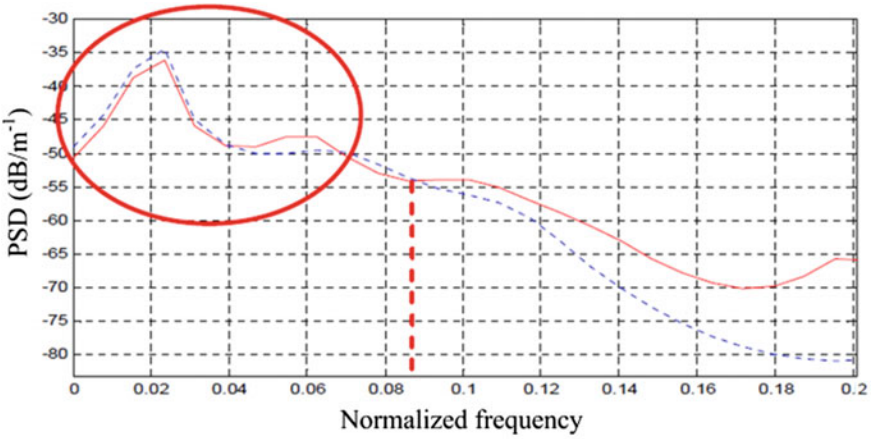

(a) DSA250 pantograph.

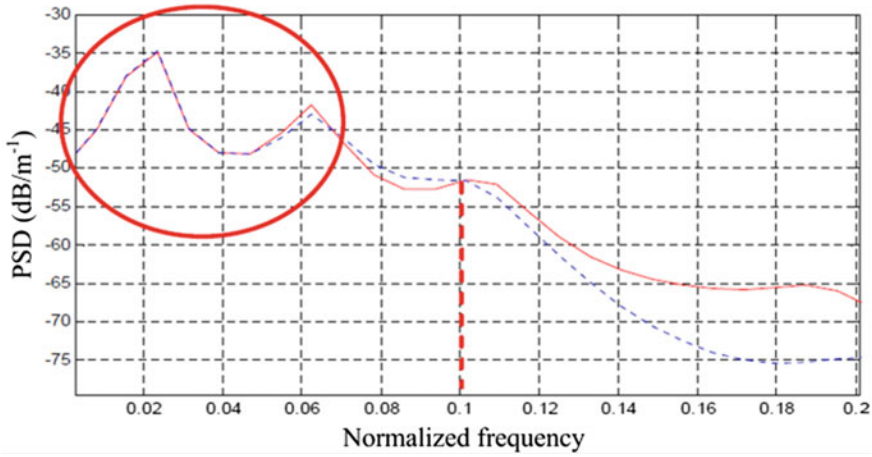

(b) DSA380 pantograph.

Fig. 8.19 Comparisons of the low-frequency PSDs of contact wire (*solid line*) and pantograph head (*dashed line*) vertical displacement using different pantograph

where $S_c(i)$ is the PSD of contact wire vertical displacement, $S_p(i)$ is the PSD of pantograph head vertical displacement, the over line denotes average value.

The cross correlation coefficients for the three types of pantograph are given in Table 8.2. The SSS400+ pantograph, with the highest designed speed, has the highest correlation with the catenary, namely the best coupling performance in all.

Table 8.2 Cross correlation coefficients of different pantograph

Pantograph type	DSA250	DSA380	SSS400+
Coefficient C_s	0.9408	0.9460	0.9581

8.5 PSD Quantification

The above study shows that the PSDs of catenary data can effectively analyze and estimate the catenary-pantograph performance. In the PSDs, the observation and comparison of fluctuation and amplitude is simple, but the qualitative characterizations are not enough for applications. The quantification of the PSDs can make the estimation automatic and help with the standardization of catenary spectrum.

In railway industry, the quantification of the track spectrum is successfully implemented by PSD fitting. Comparing with the track spectrum, the catenary spectrum has the following features.

(1) The catenary spectrum is based on modern spectrum estimation method. The PSDs of catenary data have smooth curves that are conducive to curve fitting.
(2) Due to the influence of span period, dropper arrangement, pantograph contact and environmental perturbation, the PSDs of catenary dynamic data normally have more intensive fluctuation than the track spectrums, which increases the difficulty of curve fitting.

Considering the two features and through a large amount of trials, the fitting of catenary spectrum cannot be realized by fractional polynomial like Eqs. (8.2), (8.3) and (8.4). New formulas must be proposed to fit the PSDs of catenary data to achieve the quantification.

8.5.1 Curve Fitting Method

(1) Gaussian Function Fitting

Due to the particular characteristics of pantograph-catenary interaction, the overall energy of pantograph-catenary vibration smoothly decreases from low to high frequency in general. Meanwhile, the flexible vibration and non-uniform elasticity of catenary cause some fluctuations along with the energy decline, such as shown in Fig. 8.20.

To accurately quantify the particular PSD curve, the Gaussian function is adopted for curve fitting. The kth order Gaussian function is defined as

$$S = \sum_{k=1} a_k \cdot e^{-\left(\frac{x-b_k}{c_k}\right)^2} \tag{8.19}$$

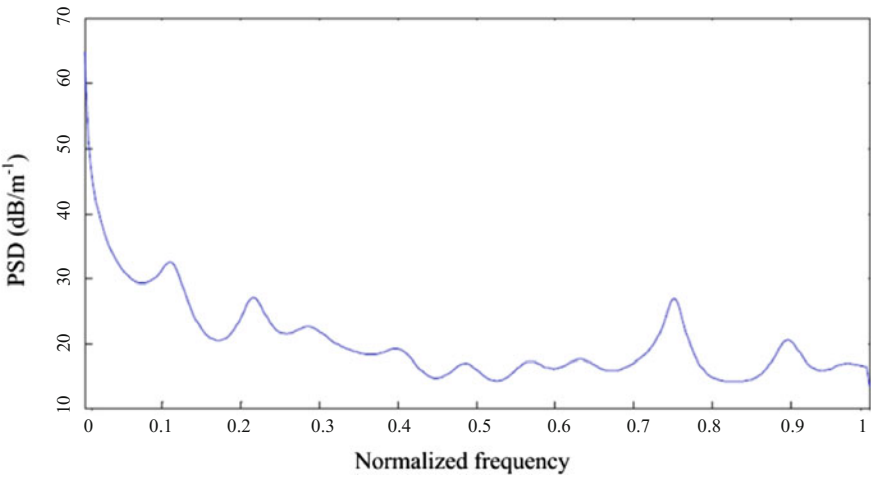

Fig. 8.20 Typical PSD of PCCF

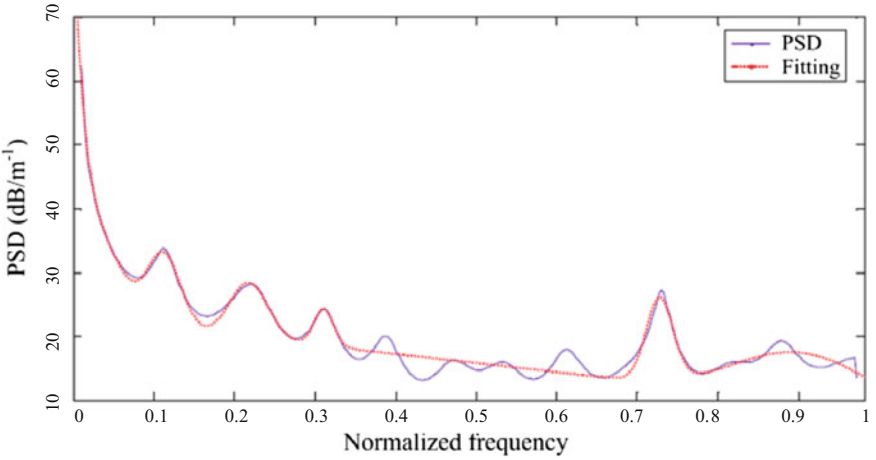

Fig. 8.21 The eighth order Gaussian function fitting of PSD

where a_k, b_k and c_k are the fitting parameters.

To fit the PSD depicted in Fig. 8.20, the eighth order Gaussian function is required to preserve most fluctuations and the fitting result is depicted in Fig. 8.21. It can be seen that the eighth order Gaussian function can almost fit all the peaks and valleys of the PSD. However, the eighth order Gaussian function has 24 parameters, which are too many for the quantification and analysis of catenary spectrum.

(2) Second Order Polynomial Fitting

The extensive fluctuation of the PSD requires too many fitting parameters in the case of Gaussian function. The discussion in Sect. 8.3.2 shows that the trend and amplitude of catenary spectrum have certain law as the operation speed changes. Also, the discussion in Sect. 8.3.3 shows that even for different pantographs, the trend of catenary spectrum is still similar aside from the differences in amplitude. Thus, addressing this issue, the catenary spectrum can be regarded as the combination of the trend part that represents the overall vibration energy and the fluctuation part that represents other harmonics occurred in the interaction. So, the difficulty of fitting can be properly reduced without losing valuable information of the PSD.

The graph of PSD is usually depicted as frequency versus spectrum density in the unit of dB. In the graph, the PSDs have the overall trends similar to the exponential decay, which cannot be fitted with little parameters. Thus, the horizontal axis, namely the frequency can be transformed into logarithmic frequency for fitting first. After the fitting, the reverse transform can restore the PSD and the fitting curve for further study.

The trend of PSD can be described by the lower envelop of the PSD curve. The lower envelop can be obtained by connecting all the valley points using the cubic spline interpolation. As shown in the logarithmic axis in Fig. 8.22, the lower envelop of the PSD is formed.

Through a large number of fitting trails based on simulation and measurement data, the second order polynomial can satisfy the fitting with only three parameters. The fitting formula is simple as

$$S = a \cdot x^2 + b \cdot x + c \tag{8.20}$$

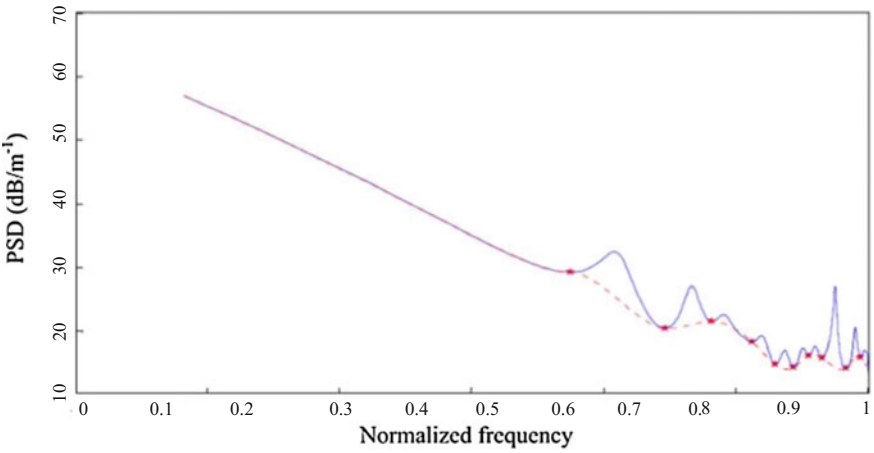

Fig. 8.22 Lower envelop (*dashed line*) of the PSD (*solid line*)

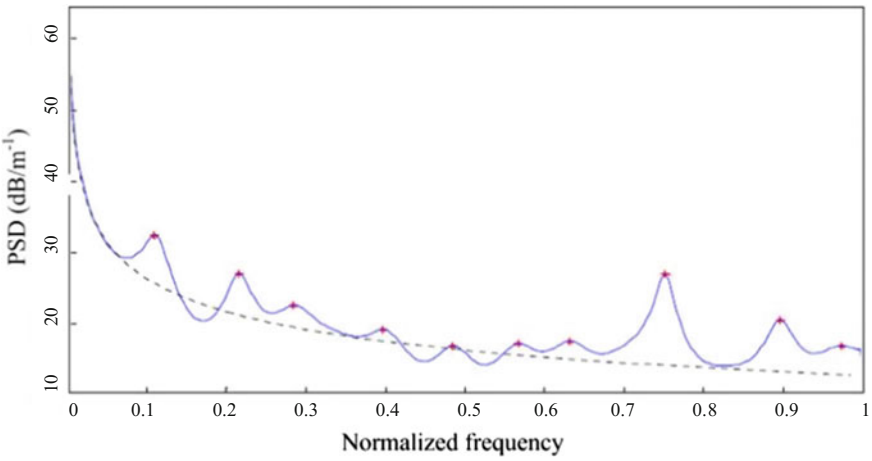

Fig. 8.23 Second order polynomial fitting (*dashed line*) of the trend of PSD

where a, b and c are the fitting parameters. The three parameters describe the curvature, slope and intercept of the PSD respectively, and the parameters have strong regularity. The fitting curve can be transformed to linear axis to fit the original PSD. On the other hand, the fluctuation of PSD can be described by the amplitude and frequency of all peaks in the PSD. In Fig. 8.23, the dashed line is the trend fitting of the PSD and the stars are all the peaks of the PSD.

8.5.2 Fitting Results Analysis

The second order polynomial fitting based on logarithmic transformation of the horizontal axis can properly quantify the PSDs of catenary data. It provides a way for the comparison of pantograph-catenary performance and establishment of standard catenary spectrum. Based on various sources of long-term measurement data of catenary, the data that indicate the good or healthy performance of catenary can be utilized for obtaining the standard catenary spectrum and the corresponding fitting parameters. When the measurement data in current operation deviate from the standardization, it indicates that maintenances must be performed accordingly. The standard parameters can also provide references for the systematic catenary spectrum in different speed levels.

Figure 8.24a depicts the PSDs of PCCF from the same pantograph-catenary couple under different operation speed. Figure 8.24b depicts the corresponding fitting curves based on the second order polynomial fitting. It can be seen that under different speed, the fitting results show a favorable parallel distribution in descending order of the speed. From the values of fitting parameters depicted in Fig. 8.24c, the parameters a, b and c present similar and linear ascending order of

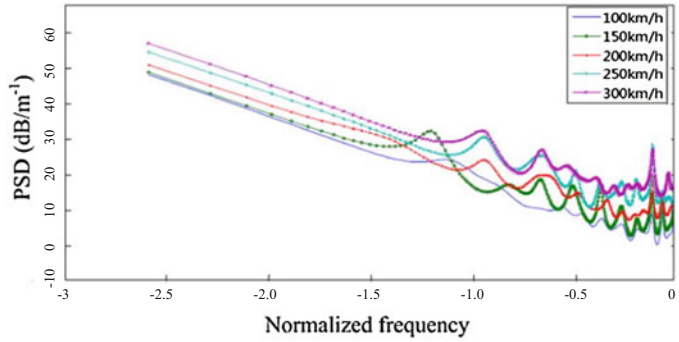

(a) PSDs of PCCF under different speed

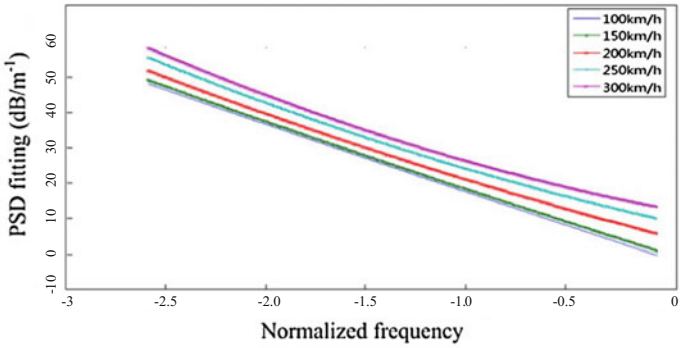

(b) Fitting results of the PSDs

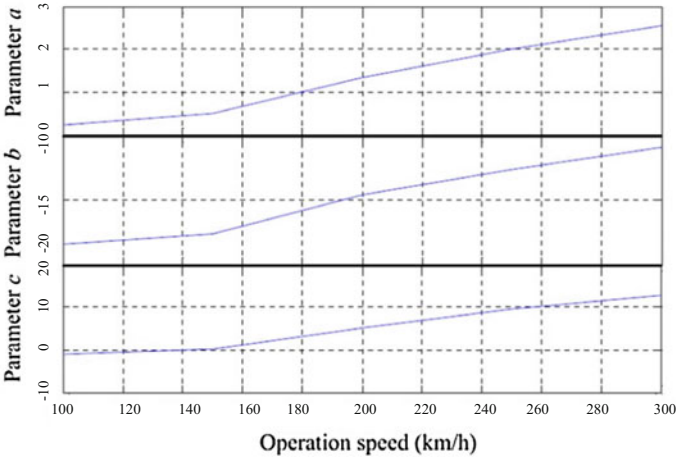

(c) Fitting parameters w.r.t the operation speed

Fig. 8.24 PSDs under different speed and corresponding fitting results

the speed, which prove the regularity of fitting parameters relative to the operation speed [17].

Table 8.3 shows the fitting parameters of PSDs in the case of the same speed but different pantograph types. It can be seen that although the catenary-pantograph couple is different, the values of three parameters show the same regularity in ascending order of the speed. This regularity guarantees the establishment of standardized catenary spectrum.

In addition to the normal operations, the quantifications of PSDs under some bad conditions of catenary also have certain regularity that is helpful to further development. Figure 8.25 depicts the fitting parameters under different contact wire

Table 8.3 Fitting parameters under different pantograph type

Pantograph type		DSA380			SSS400+		
Fitting parameter (km/h)		*a*	*b*	*c*	*a*	*b*	*c*
Speed	100	0.236	−18.412	−1.047	0.1955	−17.538	−17.538
	200	1.333	−14.605	5.208	0.9994	−15.760	3.625
	300	2.556	−10.975	12.810	1.8646	−13.552	11.393

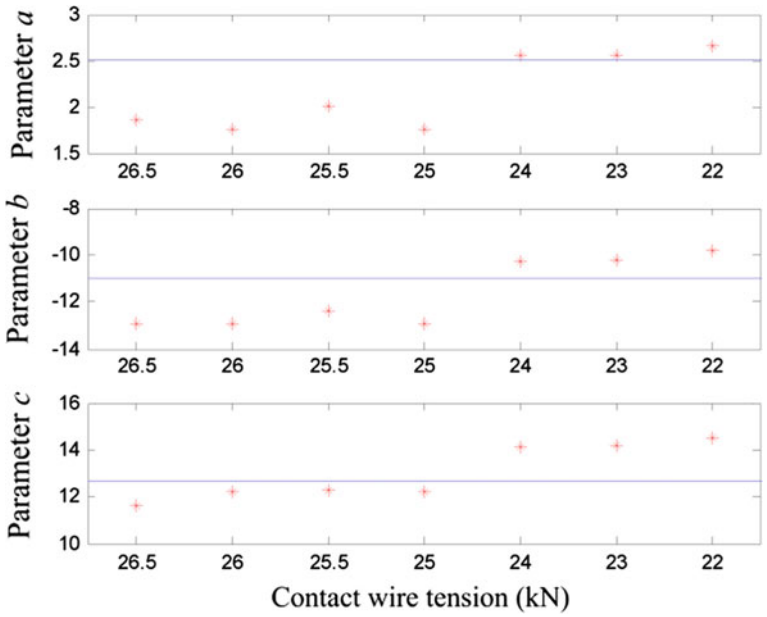

Fig. 8.25 Fitting parameters under contact wire tension losses

tension for which the standard tension designed for the catenary is 27 kN. In the figure, the horizontal lines indicate the fitting parameters under the designed tension, which can be regarded as the standard parameters. The stars indicate the parameter values under different tension loss. It can be seen that three parameters show the same changing tendency relative to the tension. Furthermore, all the parameters exceed further than the standard values when the tension is further below 24 kN. The phenomenon are consistent with the regulations that the percentage of contact wire tension loss must be below 11 % in German [18] or 15 % in China [19]. It means that when the contact wire tension is lower than permission, the corresponding fitting parameters are higher than the standard values, which can be used to establish an interval criterion like in track spectrum evaluation. It further supports the promising application of catenary spectrum for estimating the catenary condition.

In the case of contact wire section loss due to wear, the fitting parameters is depicted in Fig. 8.26 where the horizontal lines indicate the standard values under no section loss. The similar changing law can be seen in the three parameters comparing with in the case tension loss. When the percentage of contact wire section loss is too high, the parameters exceed standard values, which agree with relevant regulation that the section loss must be below 20 %.

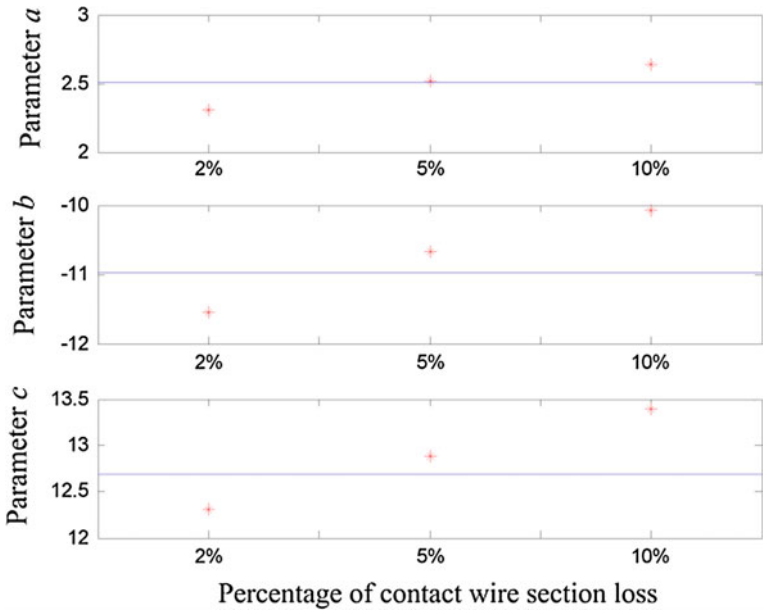

Fig. 8.26 Fitting parameters under contact wire section losses

8.6 Summary

For the better utilization of catenary data in catenary estimation, this chapter introduces the AR model-based PSD estimation to the characterization of catenary dynamic data, particularly the PCCF and vertical displacements of contact wire and pantograph head. First, the selection of AR model order for catenary data is discussed in detail. Then, the correlations between the PSDs and some crucial operation conditions are investigated and a cross correlation coefficient is proposed for evaluating the pantograph-catenary coupling performance. Finally, the quantification method of PSDs is developed based on the second order polynomial. Analyses on some preliminary results show that the quantification can effectively describe the characteristics of the PSDs and provide references for establishing a systematic standardization of catenary spectrum for catenary estimation.

References

1. Luo L, Zhang G, Wangqing W et al (2006) Track smooth state control of wheel/rail system. China Railway Publishing House, Beijing
2. Wang K, Zhai W, Cai Co (2007) Comparison on track spectra of Qinghuangdao-Shenyang passenger railway line and German Railway line. J Southwest Jiaotong Univ 42(4):425–430
3. Chen M (2006) Study on evaluation mthod of power spectrum density (PSD) for the Qinhuangdao-Shenyang dedicated passenger railway line. J China Railway Soc 28(4):84–88
4. Chen M, Wang L, Tao X et al (2008) Study on general track spectrum for Chinese main railway lined. J China Railway Soc 29(5):73–77
5. Wang F, Zhou J, Ren L (2002) Analysis on track spectrum density for dynamic simulations of high-speed vehicles. J China Railway Soc 24(5):21–27
6. Kim JW, Chae HC, Park BS et al (2007) State sensitivity analysis of the pantograph system for a high-speed rail vehicle considering span length and static uplift force. J Sound Vib 303 (3):405–427
7. Van Vo O, Massat JP, Laurent C et al (2014) Introduction of variability into pantograph–catenary dynamic simulations. Veh Syst Dyn 52(10):1254–1269
8. Zhang W, Liu Y, Mei G (2006) Evaluation of the coupled dynamical response of a pantograph—catenary system: contact force and stresses. Veh System Dyn 44(8):645–658
9. Kim JS (2007) An experimental study of the dynamic characteristics of the catenary-pantograph interface in high speed trains. J Mech Sci Technol 21(12):2108–2116
10. Collina A, Fossati F, Papi M et al (2007) Impact of overhead line irregularity on current collection and diagnostics based on the measurement of pantograph dynamics. Proc Inst Mech Eng, Part F: J Rail Rapid Transit 221(4):547–559
11. Akaike H (1976) An information criterion (AIC). Math Sci 14(153):5–9
12. Liu Z, Han Z (2013) Study on electrical railway catenary line spectrum based on AR model. J China Railway Soc 35(12):24–29
13. Davenport AG (1961) The spectrum of horizontal gustiness near the ground in high winds. Q J R Meteorol Soc 87(372):194–211
14. GB50009 M (2012) Load code for the design of building structures. Ministry of housing and urban-rural construction of the People's Republic of China, China
15. Liu Z, Hou Y, Han Z et al (2013) Analysis on dynamic characteristics of high-speed railway catenary based on wind field simulation. J China Railway Soc 35(11):21–28

16. Han Z (2013) The dynamic characteristics assessment of high speed catenary-pantograph based on modern spectrum analysis and intelligent fault image identification. PhD. dissertation, Southwest Jiaotong University, Chengdu
17. Wang H, L Zhigang, Han Z et al (2014) Feature extraction of pantograph-catenary contact force power spectrum of electrified railway. J China Railway Soc 36(11):23–28
18. Kießling F, Puschmann R, Schmieder A et al (1997) Fahrleitungen elektrischer Bahnen. Verlag BG Teubner, Stuttgart-Leipzig
19. Wanju Y (2003) High-speed electrified railway catenary. Southwest Jiaotong University Press, Chengdu, Chengdu